



Search for displaced Supersymmetry in events with two leptons with large impact parameters with the CMS detector at the LHC

Quentin Python

**Proefschrift ingediend met het oog op het behalen van de
academische graad Doctor in de Wetenschappen.**

Published in Faculteit Wetenschappen & Bio-ingenieurswetenschappen
Vrije Universiteit Brussel

Responsible Contact: Quentin Python
Interuniversity Institute for High Energies

Promotor: Prof. Dr. Freya Blekman

Prof. Dr. Jorgen D'Hondt	Chair
Prof. Dr. Stijn Buitink	Secretary
Prof. Dr. Freya Blekman	Promotor
Prof. Dr. Alberto Mariotti	
Prof. Dr. Em. Theo D'Hondt	
Prof. Dr. Giacomo Bruno	
Prof. Dr. Philippe Mermod	

Contents

Introduction	7
1 The Standard Model and Supersymmetry	9
1.1 The Standard Model of particles	9
1.1.1 The elementary particles and their interactions	10
1.1.2 The Standard Model as a quantum field theory	11
1.1.3 Shortcomings of the Standard Model	16
1.2 Supersymmetry	18
1.2.1 Motivation for Supersymmetry	18
1.2.2 Supersymmetry and the minimal supersymmetric Standard Model	19
1.3 Displaced Supersymmetry	22
1.3.1 Mathematical description of Displaced Supersymmetry	22
1.3.2 Constraints on Displaced Supersymmetry	23
2 Experimental Setup	25
2.1 The Large Hadron Collider (LHC)	25
2.1.1 The LHC physics program	26
2.1.2 The LHC design	26
2.1.3 The LHC acceleration procedure	28
2.1.4 The Worldwide LHC Computing Grid	29
2.2 The compact muon solenoid (CMS) detector	31
2.2.1 Overall concept of the CMS detector	31
2.2.2 The CMS coordinate system	31
2.2.3 The CMS tracker	33
2.2.4 The CMS electromagnetic calorimeter	33
2.2.5 The CMS hadronic calorimeter	35
2.2.6 The CMS muon system	36
3 Reconstruction and simulation of proton-proton collisions	39
3.1 Trigger	39
3.2 Physics object reconstruction	41
3.2.1 Track reconstruction	41
3.2.2 Particle-flow algorithm	43
3.2.3 Electron reconstruction and identification	45
3.2.4 Muon reconstruction and identification	45

3.2.5	Other important physics objects	46
3.3	Event simulation	49
3.3.1	Parton density function and hard scattering	49
3.3.2	Parton showering	51
3.3.3	Hadronisation and decay	52
3.3.4	Underlying event	52
3.3.5	Detector simulation	53
3.3.6	Simulation of the pileup	53
3.3.7	Simulating large samples of events	53
3.4	Simulating proton-proton collisions	55
3.4.1	Monte Carlo generators	55
3.4.2	Monte Carlo corrections	55
4	Statistical tools and analysis strategy	57
4.1	How to discover new physics?	57
4.2	Statistical tools	58
4.3	Limit setting	59
4.4	Analysis strategy	60
5	Search for Displaced Supersymmetry in events with an electron and a muon with large impact parameters at 8 TeV	61
5.1	Data and Monte Carlo simulation samples	62
5.1.1	Data samples	62
5.1.2	Standard Model background from simulation	64
5.1.3	Signal process simulation	69
5.2	Corrections to Monte Carlo simulations	74
5.2.1	Event pileup correction	74
5.2.2	Muon reconstruction, identification and isolation corrections	75
5.2.3	Electron reconstruction, identification and isolation corrections	75
5.2.4	Trigger efficiency corrections	75
5.2.5	Tracking efficiency corrections	78
5.3	Event selection and definition of control and signal regions	81
5.3.1	Preselection	82
5.3.2	Prompt lepton control region	86
5.3.3	Displaced lepton control region	87
5.3.4	Hybrid lepton control region	90
5.3.5	Signal regions	90
5.4	Background estimation techniques	92
5.4.1	Background prediction from data-driven technique	92
5.4.2	Background prediction from Monte Carlo simulation	98
5.4.3	Monte Carlo simulation validation in $Z \rightarrow \tau\tau$ control region	98
5.4.4	Background estimation in the signal regions	100
5.5	Systematic uncertainties	102
5.6	Results	104
5.6.1	Event yields	104
5.6.2	Limits	105

6	Parametrisation study	107
6.1	Providing a parametrisation study	107
6.1.1	Procedure	108
6.1.2	Model dependence	110
6.1.3	Results	112
6.1.4	Closure test	114
6.2	Parametrisation: use example	116
6.2.1	Description of models giving rise to long-lived staus	116
6.2.2	Current limits on long-lived staus	117
7	Search for Displaced Supersymmetry in events with same-flavour leptons with large impact parameters at 13 TeV	119
7.1	Data and Monte Carlo simulation samples	120
7.1.1	Data samples	120
7.1.2	Standard Model background from simulation	120
7.1.3	Signal process simulation	124
7.2	Corrections to Monte Carlo simulations	125
7.2.1	Event pileup correction	125
7.2.2	Lepton reconstruction and identification efficiencies corrections	125
7.2.3	Trigger efficiency corrections	125
7.3	Event selection and definition of control and signal regions	127
7.3.1	Preselection	127
7.3.2	Prompt lepton control region	131
7.3.3	Displaced lepton control region	135
7.3.4	Signal regions	135
7.4	Background estimation techniques	137
7.4.1	Background contribution from data-driven technique	137
7.4.2	Background contribution from Monte Carlo simulation	146
7.5	Systematic uncertainties	150
7.5.1	Data-driven estimate systematic uncertainty	150
7.5.2	Displaced tracking efficiency systematic uncertainty	153
7.5.3	Overall systematic uncertainties	153
7.6	Results	155
7.6.1	Event yields	155
7.6.2	Limits	158
7.6.3	Limits combination and comparison	161
8	Conclusion and prospects	167
8.1	Search for Displaced Supersymmetry in events with an electron and a muon with large impact parameters at 8 TeV	168
8.2	Search for Displaced Supersymmetry in events with same-flavour leptons with large impact parameters at 13 TeV	169
8.3	Prospects	169
9	Acknowledgements	171

10 Summary	173
11 Samenvatting	175
Bibliography	177

Introduction

Throughout their evolution, human beings have developed an acute sense for pattern recognition. As hunters and gatherers, being able to predict cycling change of temperature throughout the year and the movement of flocks provide an obvious advantage for survival. In our modern societies, the drive force that pushes people to understand nature is often sheer curiosity. Through the rigorous methods of science, the boundary of human knowledge has never ceased to grow. Nowadays, the discipline that studies the facts about nature, called physics, has expanded way above what a human can experience in his daily life.

The question that has stemmed this thesis was being discussed by ancient Greeks already and can be summarised as follows: “What is the matter made of and how does it interact?” Before science started to answer this question, it was believed that matter was composed of four distinct elements: water, fire, earth and air. It is only over the past two centuries that significant discoveries about the structure of the matter have been made. To the best of our knowledge, matter is composed of fundamental building blocks, called elementary particles, and interact through fundamental forces. The field of physics that unravel the structure of matter and its interaction is called “particle physics” and the theory that describes how is called the Standard Model. It was formulated over decades during the twentieth century and has proven to be an accurate description of nature in various experiments.

Even though the Standard Model has provided a very good description of the subatomic world, it is known that it is not a good candidate to be the ultimate “theory of everything”. Indeed, some observational facts, such as the presence of “dark matter”, cannot be explained within the Standard Model. It is then clear that a more general, or a new, theory has to be found. Many candidate theories are competing to fill the gaps left by the Standard Model. In this thesis, experimental evidence of one of these candidates, called Supersymmetry, will be scrutinised.

The most obvious way to study the structure of matter is to “smash” it to break it down in potential smaller components. This simple idea is at the basis of all particle accelerator experiments, which aim to study the debris created by the collisions of some particles, elementary or not. In this thesis, the information about the collisions of protons accelerated by the Large Hadron Collider is collected by the Compact Muon

Solenoid detector. Ultimately, the goal of this thesis is to answer to the following question or hypothesis : “Is Displaced Supersymmetry an accurate description of nature?” or “Is the Standard Model an accurate description of nature at the TeV scale?”. To do so, the information collected by the Compact Muon Solenoid detector will be analysed using various statistical tools.

Chapter 1 introduces the mathematical descriptions of the Standard Model, generic Supersymmetry, and more specifically, Displaced Supersymmetry. In Chapter 2, the experimental setup is explained. It consists of colliding protons and detecting the product of these collisions. The acceleration and collision of the protons is handled by the Large Hadron Collider, and the data used for this thesis are collected by the Compact Muon Solenoid detector. The algorithm used to interpret the raw information collected by the detector as well as the algorithm to simulate proton-proton collisions is detailed in Chapter 3. Chapter 4 gives a short overview of the strategy to search for Displaced Supersymmetry and some statistical tools used for that purpose. In Chapter 5, a search for Displaced Supersymmetry in events with an electron and a muon at 8 TeV is presented. A study that allows the results of the search at 8 TeV to be reinterpreted for other hypotheses than Displaced Supersymmetry is described in Chapter 6. In Chapter 7, a search for Displaced Supersymmetry in events with same-flavour leptons at 13 TeV is discussed. Finally, a critical discussion of the results as well as possible improvements for future searches are proposed in Chapter 8.

The first four chapters serve as an introduction to my work which is presented in chapters 5 to 7. For the search exposed in Chapter 5, I worked in a collaboration between the Ohio State University and the Vrije Universiteit Brussel. This original work presents a new type of search and was published in Physical Review Letters in 2015 [1]. In addition, I produced the study described in Chapter 6 which extends the impact of the results presented in the paper. In Chapter 7, I present an extension of the published search by using new data, new methods and targeting new phenomena.

Chapter 1

The Standard Model and Supersymmetry

Over the last decades, the predictive power and accuracy of the Standard Model (SM) have been stunning. One of the most striking examples of its accuracy is the measurement of the anomalous magnetic moment of the muon [2]. Despite its tremendous success, the Standard Model is not believed to be the ultimate theory as it falls short to explain few observational facts. In order to accommodate for the weaknesses of the Standard Model, physicists are developing theories that go beyond the Standard Model (BSM). Among these beyond the Standard Model theories, Supersymmetry (SUSY) is probably one of the most popular ones. Supersymmetry takes the Standard Model as a starting point and adds, among other things, an additional symmetry to it.

In Section 1.1, the basic properties of the Standard Model, its mathematical description and its shortcomings will be presented. The general ideas of Supersymmetry will be exposed in Section 1.2. More specifically, the model that inspired this thesis is discussed in Section 1.3.

1.1 The Standard Model of particles

The Standard Model has been built over decades of very intensive work. Many renowned physicists have contributed to its elaboration, and many of these contributions have been awarded the Nobel prize. The current formulation of the Standard Model has been formulated in the mid-1970s and has been unchanged up to now. The successive discoveries of the top quark [3] in 1995, the tau neutrino [4] in 2000 and the Higgs boson [5] in 2012 are just some examples of its tremendous predictive power.

The list of all the fundamental building blocks, as well as the description of the interactions between those, will be exposed in Section 1.1.1. Section 1.1.2 presents the mathematical formulation of the Standard Model along with some fundamental properties. Finally, a list of observed facts that cannot be explained within the Standard Model will be exposed in Section 1.1.3.

1.1.1 The elementary particles and their interactions

Like atoms are organised in the periodic table of elements, it is useful to group the elementary particles depending on their properties. The following properties, or variables, are used to organise elementary particles in a structured way.

Spin

The spin, S , of a particle is a measure of its internal angular momentum. Metaphorically, it is viewed as the rotation of the particle around itself. While the angular momentum can classically take continuous values, elementary particles must obey the laws of quantum mechanics and therefore can only take discrete values of spin. In quantum mechanics, the spin is measured in units of the reduced Planck constant, \hbar . With this unit system, two “types” of particles are distinguished depending on the value of their spin, those who have an half-integer spin, called fermions¹, and those who have an integer spin, called bosons².

Colour charge

Depending on its colour, a particle will or will not interact with the strong force which will be further discussed in Section 1.1.2. The colour is a quantum number that can take six values: red, green, blue and their three corresponding anti-colours, anti-red, anti-green, and anti-blue.

Electric charge

The electric charge of a particle will dictate the interaction of this particle with the electromagnetic force. In particle physics, the electric charge is measured in units of the absolute value of the charge of an electron.

Mass

The mass of a particle corresponds to its energy when this particle is at rest. The SI unit of the mass is the kilogram, kg. However, in particle physics, masses are commonly expressed in GeV/c^2 . In this thesis, the natural unit system is used, by setting $c = \hbar = 1$. By doing so, masses, momenta and energies can all be expressed in GeV. In natural units, a proton has a mass of 0.94 GeV which corresponds to 1.7×10^{-27} kg.

The Standard Model includes twelve fundamental building blocks, also known as elementary particles. These particles are fermions, and they all have spin $1/2$. Among these twelve particles, six of them carry colour charge and are called quarks. The six others do not carry colour charge and are called leptons. Depending on their electric charge, quarks can be further divided in up-type quarks (charge $+2/3$) and in down-type quarks (charge $-1/3$). Finally, they are divided into three generations. The only property that is changing from one generation to an other is the mass of the particle. The leptons can be divided similarly way except that they either carry a charge 0 or a charge -1 . The twelve elementary particles of the Standard Model are listed in Table 1.1. Each of these fermions has a corresponding particle which has the same

¹Fermi was the physicist who described the properties of half-integer spin particles.

²Bose was the physicist who described the properties of integer spin particles.

properties except that the sign of its electric charge is opposite. These oppositely charged particles are referred to as antiparticles. When a particle interacts with its antiparticle, they annihilate into energy. All the known matter is an arrangement of these twelve particles. Moreover, the ordinary matter such as atoms is only composed of u quarks, d quarks, and electrons which are all from the first generation.

Table 1.1: List of the twelve fermions of the Standard Model. They are divided depending on their colour charges (leptons, quarks), their electric charge and into three generations. Each entry of the table contains the full name of the particle and its symbol.

Generation				
		1	2	3
quarks				
Charge	+2/3	up, u	charm, c	top, t
	-1/3	down, d	strange, s	bottom, b
leptons				
Charge	0	electron neutrino, ν_e	muon neutrino, ν_μ	tau neutrino, ν_τ
	-1	electron, e^-	muon, μ^-	tau, τ^-

Fermions interact with each other through the four fundamental forces of nature. These interactions are described by the exchange of integer-spin particles, called gauge bosons. The Standard Model successfully incorporates three of the four fundamental forces of nature. The electromagnetic force is carried by the massless photon, γ , and keeps the electrons in orbit around the nucleus in an atom. The weak force is responsible for the decay of unstable radioactive elements and is carried by three massive gauge bosons, W^+ , W^- and Z^0 . Quarks are “glued” together into hadrons via the strong force which is mediated by eight massless gluons. Table 1.2 summarises the basic properties of the force carriers of the three forces that are incorporated in the Standard Model. Finally, the recently discovered [6, 7] Brout-Englert-Higgs boson, H , commonly referred to as the Higgs boson, completes the list of the Standard Model particles. Section 1.1.2.3 develops the role of this boson in more details.

Table 1.2: List of the forces incorporated in the Standard Model and the gauge bosons associated with them. The masses are taken from the Particle Data Group [8].

Force	Gauge Boson	Mass (GeV)
Strong	gluon, g	0
Electromagnetic	photon, γ	0
Weak	W -boson, W^\pm	80.385 ± 0.015
	Z -boson, Z^0	91.1876 ± 0.0021

1.1.2 The Standard Model as a quantum field theory

Quantum field theory provides a framework in which the Standard Model can be accurately described. While classical field theory successfully described Newtonian grav-

itation and classical electromagnetism, it falls short to describe the microscopic world. In quantum field theory, particles are treated as excitation of a physical field. Like in classical field theory, the Lagrangian formalism is used to describe the system. The equation of motion of the field can be found by using the principle of least action, $\delta\mathcal{S} = 0$, where the action is defined as the integral over spacetime coordinate, x , of the Lagrangian, \mathcal{L}

$$\mathcal{S} = \int \mathcal{L}(x) d^4x. \quad (1.1)$$

The challenge of coherently describing the Standard Model is now reduced to finding the appropriate Lagrangian for each possible interaction. Using gauge symmetry as a guiding principle, the Lagrangian of the Standard Model will be derived starting from the experimentally verified Dirac equation in the following section.

1.1.2.1 The Dirac approach

The interaction between fermions is successfully described by the relativistic Dirac equation. The Lagrangian density of a free fermion is the sum of a kinetic term and a mass term,

$$\mathcal{L}_{Dirac} = i\bar{\psi}\gamma^\mu\partial_\mu\psi - m\bar{\psi}\psi, \quad (1.2)$$

where the γ^μ are the Dirac matrices and the ψ ($\bar{\psi}$) is associated with the fermion (anti fermion) field. Using the principle of least action, Equation 1.2 becomes

$$i\gamma^\mu\partial_\mu\psi - m\psi = 0. \quad (1.3)$$

Using the principle of gauge symmetry, the Lagrangian must be invariant under some transformation for it to agree with what is observed in nature. Since the physically meaningful part of the field is its modulus, $|\psi|^2$, adding a phase might preserve the invariance of the Lagrangian. Adding an additional phase to the field, one gets:

$$\psi \rightarrow \psi' = e^{-i\vec{\alpha}(x) \cdot \frac{\vec{\tau}}{2}} \psi. \quad (1.4)$$

Here the $\vec{\alpha}(x)$ are the rotations parameters and $\vec{\tau}$ are the generators of the Lie-group. However, using only the transformation of the field, the modified Lagrangian is not invariant. The invariance can be restored by replacing the derivative by the covariant derivative defined as

$$D_\mu = \partial_\mu - ig\frac{\vec{\tau}}{2} \cdot \vec{A}_\mu \quad (1.5)$$

where \vec{A}_μ is a vector field that couples with the fermion with the coupling strength g . Introducing Equation 1.5 in Equation 1.2, the new Lagrangian becomes

$$\mathcal{L}_{Dirac} = i\bar{\psi}\gamma^\mu\partial_\mu\psi - m\bar{\psi}\psi + g\bar{\psi}\gamma^\mu\frac{\vec{\tau}}{2} \cdot \vec{A}_\mu\psi. \quad (1.6)$$

The invariant Lagrangian does now incorporate a field which is interacting with the fermion. It is important to notice that this new field has become necessary as a consequence of enforcing the gauge invariance. In other words, the gauge invariance seems to give rise to the interacting field.

1.1.2.2 Symmetries of the Standard Model

In Section 1.1.1, the interactions of the Standard Model were explained by the exchange of bosons. However, the example above has shown that the interactions can be seen as a consequence of gauge symmetry. Comparing these two observations, a one to one correspondence can be made between boson and gauge symmetry. For that reason, the bosons that are the carriers of a force are called gauge bosons. Including the three fundamental forces, the full group symmetry of the Standard Model, G_{SM} , is given by

$$G_{SM} = SU(3)_c \times SU(2)_L \times U(1)_Y. \quad (1.7)$$

The $SU(3)_c$ symmetry is associated to the strong force, while the electroweak forces are represented by the $SU(2)_L \times U(1)_Y$ group.

Strong interaction

The strong interaction, or strong force, acts only on particles that carry a colour charge, namely the quarks. The theory which explains these interactions is known as quantum chromodynamics³ (QCD). Using the same procedure as in Section 1.1.2.1, eight fields are introduced in the covariant derivative⁴.

$$D_\mu = \partial_\mu - ig_s \frac{\lambda_\alpha}{2} G_\mu^\alpha \quad (1.8)$$

where G_μ^α represents the eight gluons fields ($\alpha = 1, \dots, 8$), λ_α are Gell-Mann matrices and g_s the coupling constant of the strong interaction. It occurs that $SU(3)$ is a non-Abelian group which allows the gluon to couple to itself. As a consequence, the strong force increases when two quarks are being pulled apart. In nature, quarks cannot be seen on their own and they are always grouped into so-called hadrons. A hadron is a non-elementary particle which has 0 as colour charge. This is (mostly) achieved in two ways: mesons are composite particles of two quarks of opposite colour and baryons are composite particles of three quarks of different colour. However, a combination of more quarks is also allowed. For example, four quarks and one antiquark can form a bound state resulting in a so-called "pentaquark". In 2015, the LHCb collaboration discovered a pentaquark [9].

electroweak interaction

The electroweak interaction puts the electromagnetic interaction and the weak interaction within the same framework. Even though these two forces seem to have a very different effect at low energy, it was shown that they are two manifestations of the same force [10–12]. It occurs that the difference in their strength can be explained by the mass of the force carrier, which is massless in the case of the electromagnetic interaction.

³Chroma means colour in greek.

⁴The number of fields associated with a symmetry is given by the number of parameters minus the number of constraints. $U(n)$ symmetry is represented by a $n \times n$ complex matrix, leading to $2n^2$ parameters. Requiring unitarity implies n^2 constraint. $SU(n)$ group adds an additional constraint by requiring the determinant of the matrix to be 1. The number of fields associated with $SU(n)$ is then given by $2n^2 - n^2 - 1 = n^2 - 1$.

As mentioned previously, the symmetry group of the electroweak interaction is $SU(2)_L \times U(1)_Y$. The first part, $SU(2)_L$, has three generators and acts on particles with so-called “weak isospin”, T_3 . The three fields associated with this symmetry are W_μ^α with $\alpha = 1, 2, 3$. The weak isospin is related to the electric charge, Q , and the “weak hypercharge”, Y , as follows

$$Q = T_3 + Y. \quad (1.9)$$

Likewise, the electromagnetic symmetry, $U(1)_{EM}$, introduces a single field, B_μ . Altogether, the covariant derivative that keeps the invariance of the electroweak Lagrangian is

$$D_\mu = \partial_\mu - ig \frac{\sigma^\alpha}{2} W_\mu^\alpha - ig' \frac{Y}{2} B_\mu, \quad (1.10)$$

where g (g') is the coupling constant associated with the $SU(2)$ ($U(1)$) gauge group, and σ^α are the Pauli Matrices.

Once again, the four fields introduced in the covariant derivative are connected to the four bosons mediating the electromagnetic force introduced in Section 1.1.1. Let W_μ^\pm , Z_μ and A_μ be the fields associated with the physical W^\pm , Z and γ respectively. These fields can be expressed as linear combinations of the fields introduced in Equation 1.10 as follows:

$$\begin{aligned} W_\mu^\pm &= \frac{1}{\sqrt{2}}(W_\mu^1 \mp iW_\mu^2) \\ A_\mu &= W_\mu^3 \sin \theta_W + B_\mu \cos \theta_W \\ Z_\mu &= W_\mu^3 \cos \theta_W - B_\mu \sin \theta_W \end{aligned} \quad (1.11)$$

where the mixing angle, θ_W , is defined as:

$$\tan \theta_W = \frac{g'}{g}. \quad (1.12)$$

All the forces of the Standard Model are coherently embedded within a unified theory. However, at this stage, the non-zero mass of the bosons mediating the weak force cannot be explained. Indeed, if one tries to add explicit mass term to the Lagrangian, the gauge symmetry is broken. In 1964, Brout and Englert [13] and Higgs [14] described the mechanism handling the problem of the massive bosons. This mechanism will be presented in the next section.

1.1.2.3 The Brout-Englert-Higgs mechanism

If the symmetry of the electroweak interaction were preserved, the masses of the W^\pm bosons and the Z boson would be zero. However, the masses of these bosons have been measured to be non-zero. This implies that the electroweak symmetry must be spontaneously broken by the addition of an additional scalar field which preserves the

invariance of the Lagrangian but has a non-zero vacuum expectation value (VEV). A candidate field fulfilling this criterion, ϕ , can be written as an electroweak doublet,

$$\phi = \begin{pmatrix} \phi^+ \\ \phi^0 \end{pmatrix} \quad (1.13)$$

where ϕ^+ and ϕ^0 are complex scalar fields. The Lagrangian attached to this field is

$$\begin{aligned} \mathcal{L}_\phi &= (D^\mu \phi)^\dagger (D_\mu \phi) - V(\phi) \\ &= (D^\mu \phi)^\dagger (D_\mu \phi) - \mu^2 (\phi^\dagger \phi) - \lambda (\phi^\dagger \phi)^2 \end{aligned} \quad (1.14)$$

where μ^2 is a mass parameter, $\lambda > 0$ is the coupling constant of the field interacting with itself and \dagger indicates the hermitian conjugate. When μ^2 is less than zero, the minimum of this field is non-zero and is given by

$$\langle \phi^\dagger \phi \rangle = v^2 = \frac{|\mu^2|}{\lambda}. \quad (1.15)$$

Making an expansion about a particular choice of the minimum one gets,

$$\frac{1}{\sqrt{2}} \begin{pmatrix} 0 \\ v + h(x) \end{pmatrix} \quad (1.16)$$

where $h(x)$ is associated with the physical field of the Higgs boson. The masses of the bosons are all proportional to the vacuum expectation value and one gets the following relations

$$m_H = \sqrt{2\lambda}v, \quad (1.17)$$

$$m_W^\pm = \frac{1}{2}|g|v, \quad (1.18)$$

$$m_Z = \frac{1}{2}\sqrt{g'^2 + g^2}v. \quad (1.19)$$

The mass of the Higgs boson was recently measured by ATLAS and CMS [15] to be :

$$m_H = 125.09 \pm 0.21 (stat.) \pm 0.11 (syst.) \text{ GeV}. \quad (1.20)$$

This mechanism does not directly provide mass to the fermions. However, an additional gauge invariant coupling between the fermions and the Higgs field can explain their masses. The mass of the fermions is directly proportional to its Yukawa coupling [16]. Its Lagrangian has the following form

$$\mathcal{L}_{Yukawa} = -Y_{ij} \bar{\psi}_{L,i} \phi \psi_{R,j}, \quad (1.21)$$

where Y_{ij} is a matrix filled with new coupling constants.

1.1.3 Shortcomings of the Standard Model

The Standard Model is currently the best theory of the particle content of our world and its interactions. With the recent discovery of the Higgs boson particle, all the particles predicted by the theory have been discovered. However, there are still observational facts that cannot be explained. It is believed that the Standard Model is a low energy effective field theory, which means a theory that is valid only if the energy coming into play is smaller than a certain value. Hereafter, some of the most important problems of the Standard Model will be revealed.

Gravity

The Standard Model successfully incorporates three of the four fundamental forces of nature. Gravity, which is the force that acts on objects with mass, is accurately described by Einstein’s general theory of relativity. Within this description, gravitation is not described as a force but by a distortion of space-time itself. This theory predicted gravitational waves, which have recently been discovered [17] by the LIGO collaboration. Unfortunately, the theory of general relativity cannot be embedded within the Standard Model without drastic extensions.

Neutrino masses

In the Standard Model, neutrinos are massless. However, various experiments [18–20] have shown that a neutrino of generation x can transform itself into a neutrino of an other generation, y and that the transition probability depends on distance and energy. This phenomenon is commonly referred to as neutrino oscillation. The oscillation probability from generation x to generation y is proportional to the square of neutrino mass difference, $\mathcal{P}_{x \rightarrow y} \propto (m_x - m_y)^2$. Hence, in the Standard Model, this probability must be zero, and it fails to explain the experimentally observed neutrino oscillation.

Dark matter and dark energy

The matter that is described by the Standard Model is referred to as baryonic matter. However, results from galaxy rotation curves [21], for example, strongly indicate the presence of a new type of matter. Unlike baryonic matter, this new type of matter does not interact with the electromagnetic force and hence is “invisible” and is referred to as “dark matter”. It is believed that dark matter should interact with the gravitational force and another force not included in the Standard Model. An ideal candidate for this matter would be a weakly interacting massive particle (WIMP) [22]. Furthermore, results from the Planck satellite [23] suggest a new form of energy, referred to as “dark energy”. The Standard Model seems to provide an explanation for about 5% of the total energy in the universe while 95% would be explained by dark matter and dark energy.

Naturalness, fine tuning and the hierarchy problem

The recently discovered Higgs boson has a mass of about 125 GeV. It is common to express the mass of a particle as the sum of its bare mass and some corrections.

For the Higgs boson mass, one gets:

$$M_H^2 = (M_H)_0^2 + \delta m^2, \quad (1.22)$$

where $(M_H)_0^2$ is the bare mass of the Higgs boson squared and δm^2 arises from loop correction diagrams due to the coupling between the Higgs boson and quarks, gauge bosons, and Higgs boson itself. Since these diagrams are all proportional to the mass of the particle interacting with the Higgs boson, the top quark contribution is dominating since it is the heaviest. At first order and taking into account only the contribution of the top quark, one gets:

$$\delta m^2 = -\left(\frac{\lambda_t}{4\pi}\right)^2 2\Lambda_{cut}^2, \quad (1.23)$$

where λ_t stands for the Yukawa coupling defined in 1.21 of the top quark and Λ_{cut} is the ultraviolet cut-off scale up to which the theory is valid. If the Standard Model is the proper description of the world, or in absence of beyond the Standard Model physics, Λ_{cut} is of the order of the Planck scale ($\approx 10^{18}$ GeV). In order to have the equality of Equation 1.23 to be correct, the bare mass of the Higgs boson should take an extremely precise value near the Planck scale. The ratio $\frac{M_W^2}{M_{Planck}^2} = 10^{-32}$ is a measure of how accurately the bare mass of the Higgs boson should be chosen to fit the observation. While, in principle, this could be due to sheer randomness, it seems extremely “unnatural” to have this level of fine-tuning. This problem is commonly referred to as fine-tuning, hierarchy or naturalness and suggests that there must be a new theory near the electroweak scale.

Supersymmetry provides an elegant way to solve the hierarchy problem. In the next section, the generic ideas of Supersymmetry will be presented as well as the more specific type of Supersymmetry that has motivated this research.

1.2 Supersymmetry

Some problems of the Standard Model have been highlighted in section 1.1.3. Since many observational facts cannot possibly be explained by the current theory, physicists know that a new one has to be found. Supersymmetry [24] is one of the good candidates that can solve some of the shortcomings of the Standard Model.

Section 1.2.1 will show that the hierarchy problem can be elegantly solved by adding an additional symmetry to the Standard Model. In Section 1.2.2 the new set of particles introduced by Supersymmetry and the most simplistic supersymmetric model will be reviewed.

1.2.1 Motivation for Supersymmetry

In Equation 1.22, there are three terms. The first term is the mass of the Higgs boson, the second term is a free parameter, and the third term can be calculated by the theory. Within the Standard Model, the δm^2 term is of the order of the Planck scale which requires an extremely fined-tuned value of the bare mass of the Higgs. Naturalness arguments suggest that the δm^2 should be of the same order as the $(M_H)_0^2$ term. The idea is now to find a new theory which would imply a small δm^2 and solve the hierarchy problem. Imagine a beyond the Standard Model theory that predicts new particles to couple to the Higgs, so that the δm^2 term can be written as the sum of two terms

$$\delta m^2(Sum) = \delta m^2(SM) + \delta m^2(BSM). \quad (1.24)$$

It is useful to further divide these contributions into their bosonic and fermionic parts as they pick up an opposite sign,

$$\delta m^2 \propto \Lambda_{cut}^2(boson - fermion). \quad (1.25)$$

Combining Equations (1.24) to (1.25), one gets

$$\delta m^2(Sum) \propto \Lambda_{cut}^2[boson(SM) - fermion(SM) + boson(BSM) - fermion(BSM)]. \quad (1.26)$$

It is easy to notice that the δm^2 term vanishes if the following equalities hold

$$boson(SM) = fermion(BSM) \quad (1.27)$$

$$fermion(SM) = boson(BSM). \quad (1.28)$$

For this cancelation to happen, each particle in the Standard Model should be related by a symmetry to a "partner" in the beyond the Standard Model theory. The symmetry that transforms bosons into fermions and vice versa is commonly referred to as Supersymmetry. In the next section, some aspects of the most simplistic supersymmetric model will be discussed.

1.2.2 Supersymmetry and the minimal supersymmetric Standard Model

Supersymmetry introduces a new operator, \mathcal{Q} , which transforms bosonic states into fermionic states and vice-versa, as,

$$\begin{aligned}\mathcal{Q}|boson\rangle &= |fermion\rangle \\ \mathcal{Q}|fermion\rangle &= |boson\rangle.\end{aligned}\tag{1.29}$$

Since this operator transforms the spin of the state it is called a "spinor" and it satisfies some commutation and anti-commutation relations. The commutation relation of two operators A and B is written as

$$[A, B] := AB - BA\tag{1.30}$$

and the anti-commutation relation is written as

$$\{A, B\} := AB + BA.\tag{1.31}$$

Hence, the two operators commute if $[A, B] = 0$ and anti-commute if $\{A, B\} = 0$. The commutation and anti-commutation relation that the operator \mathcal{Q} must satisfy are written as follows,

$$\{\mathcal{Q}, \mathcal{Q}\} = \{\mathcal{Q}^\dagger, \mathcal{Q}^\dagger\} = 0\tag{1.32}$$

$$\{\mathcal{Q}^\dagger, \mathcal{Q}\} = P^\mu\tag{1.33}$$

$$[P^\mu, \mathcal{Q}] = [P^\mu, \mathcal{Q}^\dagger] = 0,\tag{1.34}$$

where P^μ is the four-component momentum operator. One of the consequences of these relations is that a supersymmetric state, or "supermultiplet", should contain an equal number of degrees of freedom for the bosonic part as for the fermionic part. Furthermore, if Supersymmetry were a preserved symmetry, it would imply that the mass of each superpartner should be equal to their Standard Model counterparts. Since no such particles have been yet discovered, Supersymmetry, if it exists, should necessarily be a broken symmetry. It is useful to write the full Lagrangian as the sum of two terms,

$$\mathcal{L} = \mathcal{L}_{SUSY} + \mathcal{L}_{BREAK}\tag{1.35}$$

where the first term preserves the symmetry and the second term breaks it. However, in order to preserve the partial cancelation of the quadratic divergence of the Higgs boson mass, the term that breaks the symmetry should be added with care. The Lagrangian that has the desired properties is referred to as the "soft SUSY breaking" term and is written as

$$\begin{aligned}\mathcal{L}_{SOFT} = & -\frac{1}{2}M_a\lambda^a\lambda^a \\ & -(m^2)_j^i\phi^{*j}\phi_i \\ & -\frac{1}{2}b^{ij}\phi_i\phi_j \\ & +\frac{1}{6}a^{ijk}\phi_i\phi_j\phi_k\end{aligned}\tag{1.36}$$

where M_a is the gaugino⁵ mass term, $(m^2)_j^i$ and b^{ij} are scalar-squared terms, and a^{ijk} is a scalar³ term. The Lagrangian of the supersymmetric theory with the desired properties is obtained by combining equations 1.35 and 1.36 and can generally be written as

$$\mathcal{L} = \mathcal{L}_{SUSY} + \mathcal{L}_{SOFT} \quad (1.37)$$

The description of the world is now related to the values of all the free parameters introduced in the soft SUSY breaking term. A specific choice of these parameters will be discussed in the following section.

1.2.2.1 Minimal supersymmetric Standard Model

The minimal supersymmetric Standard Model (MSSM) can solve the fine tuning problem while keeping the number of free parameters as low as possible. As mentioned previously, a supermultiplet has the same number of fermionic and bosonic degrees of freedom. For any fermions, which have spin 1/2, there are two degrees of freedom. In order for the supermultiplet to be consistent with the supersymmetric algebra, it must necessarily contains two bosonic degree of freedom. One way to achieve this is to combine a two-component Weyl fermion with a complex scalar field. Supermultiplets with this form are commonly referred to as "chiral supermultiplets."

The following conventions are used to refer to the superpartners of a Standard Model particle. The superpartner of a fermion is named by adding a "s" in front of the Standard Model particle name. For example, quarks become squarks and top quark becomes top squark, or "stop". For the superpartners of the bosons, the name is constructed by adding a "ino" at the end of the Standard Model particles' name. All superpartners are referred to as "sparticles" and a "~" is noted on top of each of them to distinguish them from their Standard Model counterparts.

The list of all possible chiral supermultiplets within the minimal supersymmetric Standard Model is shown in Table 1.3. In a similar fashion, the gauge bosons are grouped with their superpartner into "gauge supermultiplets" as displayed in Table 1.4 where the W^0 and the B^0 correspond to the A_μ and Z_μ fields introduced in Equation 1.11. Inspecting the particle content of the minimal supersymmetric Standard Model, one can notice that each Standard Model particle has acquired a superpartner. Furthermore, it is also worth noting that in the minimal supersymmetric Standard Model, the Higgs boson is required to be a doublet. The observed Higgs boson is compatible with a spin 0 particle so it cannot possibly be embedded in a gauge supermultiplet. For that reason, the Higgs boson resides in a chiral supermultiplet. However, it turns out that it is necessary to have two Higgs boson doublets in order to have a consistent theory. The observed Higgs boson is then expressed as linear combination of the newly introduced H_u and H_d .

The minimal supersymmetric Standard Model introduces an additional symmetry, called "R-parity", defined as follows,

$$R_p = (-1)^{3(B-L)+2S}. \quad (1.38)$$

⁵The gauginos are the superpartners of the gauge bosons.

Table 1.3: List of all the chiral supermultiplets within the minimal supersymmetric Standard Model. The table is shown only for one family but the other families exhibit similar properties.

Names		spin 0	spin 1/2
squarks, quarks 3 families	Q	$(\tilde{u}_L \quad \tilde{d}_L)$	$(u_L \quad d_L)$
	\bar{u}	\tilde{u}_R^*	u_R^\dagger
	\bar{d}	\tilde{d}_R^*	d_R^\dagger
sleptons, leptons 3 families	L	$(\tilde{\nu} \quad \tilde{e}_L)$	$(\nu \quad e_L)$
	\bar{e}	\tilde{e}_R^*	e_R^\dagger
Higgs, higgsinos	H_u	$(H_u^+ \quad H_u^0)$	$(\tilde{H}_u^+ \quad \tilde{H}_u^0)$
	H_d	$(H_d^0 \quad H_d^-)$	$(\tilde{H}_d^0 \quad \tilde{H}_d^-)$

Table 1.4: List of all the gauge supermultiplets within the minimal supersymmetric Standard Model.

Names	spin 1/2	spin 1
gluino, gluon	\tilde{g}	g
winos, W	$\tilde{W}^\pm \quad \tilde{W}^0$	$W^\pm \quad W^0$
bino, B	\tilde{B}^0	B^0

where B stands for the baryon number, L for the lepton number, and S for the spin. With this definition, all particles have $R_p = 1$ while sparticles have $R_p = -1$. For each interaction, the overall R_p is calculated by multiplying the R_p of all the particles. It follows that an interaction preserves the R-parity if, and only if, the difference between the number of sparticles in the final state and the number of sparticles in the initial state is zero or a multiple of two. This also implies that the lightest supersymmetric particle (LSP) cannot decay and hence must be stable. In that regard, supersymmetric models which preserve R-parity might provide an ideal candidate for weakly interacting massive particles. In the next section, the specific model that has motivated this research, in which R-parity is not conserved, will be briefly exposed.

1.3 Displaced Supersymmetry

Many of the searches at the LHC for Supersymmetry, for example [25, 26] have been inspired by the minimal supersymmetric Standard Model and have been optimised for this scenario. However, up to now, no hints of Supersymmetry have been found, and the naturalness-inspired minimal supersymmetric Standard Model is less and less likely to be an accurate description of nature. As a consequence, alternative models of Supersymmetry have become more and more appealing over the past years. “Displaced Supersymmetry” [27] is a model in which R-parity is violated (RPV), which allows the lightest supersymmetric particle to decay into Standard Model particles. Depending on the values of the R-parity violating couplings, the lightest supersymmetric particle may acquire a sufficient lifetime so that its decay can be measurably displaced from its production.

The mathematical description of the model will be exposed in Section 1.3.1. Section 1.3.2 catalogues some of the experimental constraints on this model.

1.3.1 Mathematical description of Displaced Supersymmetry

As it can be seen in Equation 1.38, R-parity is related to the baryon number and the lepton number. The introduction of baryon and/or lepton-violating terms can be done through the supersymmetric potential, the “superpotential”, W . There is only one renormalizable operator violating the baryon number, ($\Delta B \neq 0$),

$$W_{\Delta B \neq 0} = \frac{1}{2} \lambda''_{ijk} U_i D_j D_k \quad (1.39)$$

and three lepton-violating operators, ($\Delta L \neq 0$),

$$W_{\Delta L \neq 0} = \frac{1}{2} \lambda_{ijk} L_i L_j E_k + \lambda'_{ijk} L_i Q_j D_k + \epsilon_i L_i H_u \quad (1.40)$$

where i, j and k run over the three families of fermions.

However, many of these parameters are highly constrained. Especially, simultaneous lepton and baryon-violating terms give rise to proton decay which is known to be stable, as it will be discussed in more details in the next section. In order to avoid clashing with proton decay, this specific scenario considers lepton-violating operators only. Especially, it is assumed that the dominant R-parity violating are the superpotential bilinears

$$W \supset \mu_{L,i} L_i H_u. \quad (1.41)$$

In the mass basis, it becomes

$$W \supset \epsilon_i y_{jk}^d L_i Q_j D_k + \epsilon_i y_{jk}^e L_i L_j E_k \quad (1.42)$$

where $\epsilon_i = \frac{\mu_{L,i}}{\mu}$ are the lepton-Higgs mixing angles. This superpotential predicts that the sparticles will mainly decay into fermions of the third generation. In the specific scenario considered in this thesis, the lightest supersymmetric particle is the top squark and it will decay through a R-parity violating operator into a bottom quark and a lepton.

1.3.2 Constraints on Displaced Supersymmetry

Even though the R-parity violating operator considered in this thesis only violates lepton number, ultra-violet completion can introduce baryon-number violating operator as well. The most stringent constraint on R-parity violating models is provided by the non-observation of the proton decay. If R-parity is violated, many Feynman diagrams could contribute to the decay of the proton and Figure 1.1 represents the $p \rightarrow e^+ \pi^0$ case. For this model, the strongest constraint comes from the study of the $p \rightarrow \nu K^+$ decay.

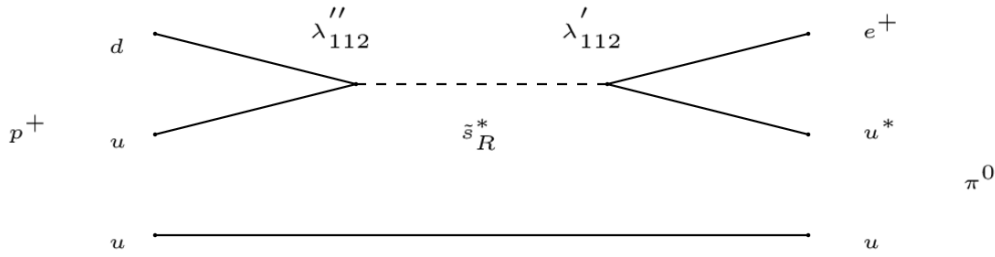


Figure 1.1: Feynman diagram example of the the proton decay involving R-parity violating interaction.

Since the lifetime of a particle can be expressed as function of its total width, Γ , as follows

$$\tau = \frac{\hbar}{\Gamma} = \frac{\hbar}{\sum_i \Gamma_i}, \quad (1.43)$$

a higher bound on each partial width, Γ_i , can be deduced. Using the $\Gamma_{p \rightarrow \nu K^+}$ decay, the partial lifetime of the proton was measured to be higher than 6.7×10^{32} yr at 90% confidence level [28]. With this model the partial width can be roughly estimated by

$$\Gamma_{p \rightarrow \nu K^+} \approx \frac{1}{8\pi} \frac{\Delta m^5}{m_{s_R}^4} (\lambda''_{112} \epsilon_i y_s \sec \beta)^2, \quad (1.44)$$

where y_s is the Standard Model Yukawa coupling of the strange quark, Δm the mass difference between the proton and the Kaon, and β is the ratio of the vacuum expected value of the Higgs doublet. Using the experimental bound and combining eqs. (1.43) and (1.44) together, one can deduce the upper bound on the coupling

$$\lambda''_{112} < 7 \times 10^{-21} \left(\frac{m_{s_R}}{300 \text{ GeV}} \right)^2 \left(\frac{10^{-3}}{\epsilon_i} \right) \left(\frac{5}{\sec \beta} \right). \quad (1.45)$$

In the last equation, the terms have been rearranged so that the coupling is multiplied by unitless terms that are all close to one for some reasonable parameters of the model.

The ATLAS and CMS collaborations have an extensive search program aiming at discovering Supersymmetry. However, the bounds on this specific model are rather

weak for mainly two reasons. In order to understand the first of these reasons, it is important to remember that searches cannot directly detect sparticles but only their Standard Model decay products such as electrons, muons, and jets. In addition, these "physics objects" are not detected but are inferred after combining the information of different detectors into complex algorithms. It turns out that these algorithms are usually tuned in such a way that reconstruction efficiency for physics objects that are produced far from the interaction point is suboptimal. The other reason is that, when the minimal supersymmetric Standard Model is assumed, the lightest supersymmetric particle is stable and hence escapes the detector. A wide range of these searches are using a variable that is very powerful in such a scenario but that is not well suited when assuming Displaced Supersymmetry. It follows that this model is very weakly constrained.

The main goal of this thesis is to design a search that is sensitive to the Displaced Supersymmetry scenario. However, before explaining the search itself, it is crucial to understand the experimental setup which is exposed in Chapter 2 and the algorithms which are explained in Chapter 3.

Chapter 2

Experimental Setup

One of the most fundamental principles of the scientific method is known as "hypothesis testing". For a hypothesis to be testable, the hypothesis should have some predictive power that can be experimentally verified. In the current case, the statistical analysis of a very large amount of proton-proton collisions can provide a good test for the existence of Displaced Supersymmetry.

Schematically, the experiment can be divided into two parts. The first part consists of creating a machine that can collide protons. The Large Hadron Collider [29] (LHC) at the “european organisation for nuclear research” (CERN), is the most powerful accelerator ever built by humankind and some of its properties will be exposed in Section 2.1. The second part consists of collecting the information of all the particles that are eventually created after the collisions of the protons. Gigantic detectors are built around the point where the collisions take place, called the interaction points. The detector used for this research is called the Compact Muon Solenoid [30] (CMS), and its characteristics will be exposed in Section 2.2.

2.1 The Large Hadron Collider (LHC)

The LHC is located in the same tunnel that previously hosted the Large Electron-Positron (LEP) collider. The 26.7 km tunnel is situated at the border of France and Switzerland and lies between 45 m and 170 m underground. The designed centre of mass energy, \sqrt{s} , of the LHC is 14 TeV which is approximately seven times larger than the previously most powerful accelerator, the Tevatron [31]. The installation of the LHC was completed in September 2008, and the first recorded collisions occurred in November 2009.

Section 2.1.1 lists the experiments built around the LHC along with their corresponding physics program. The design of the LHC will be discussed in Section 2.1.2 and its operation in Section 2.1.3. Finally, the computing scheme put into place to handle the huge amount of data collected will be explained in Section 2.1.4.

2.1.1 The LHC physics program

As it was highlighted in Section 1.1.3, many aspects of the Standard Model or its possible extension need in-depth scrutiny. Depending on which problem one wants to tackle, the information needed to be recorded can vary drastically and dedicated detectors are built to serve these specific purposes. The main motivation for building the LHC was to discover the Higgs boson which was investigated by the LEP up to roughly 115 GeV. The branching fractions of the Higgs depend strongly on its mass so that multiple final states have to be considered. For these reasons, the ATLAS [32] and CMS [30] were designed as general-purpose detectors. The data used in this thesis was collected by the CMS detector which will be described in more detail in Section 2.2. The main goal of the LHCb experiment [33] is to shed some light on matter-antimatter asymmetry by making precise measurements on hadrons containing a b quark. It is believed that shortly after the Big Bang, the energy density was so high that a so-called quark-gluon plasma was formed. This state of matter can be achieved by colliding heavy ions such as lead and the ALICE detector [34] aims at studying the properties of this state. Each of these four experiments is located at one of the interaction points of the LHC whose operation will be explained in the next section.

2.1.2 The LHC design

The design of the LHC was mostly driven by the search for the Higgs boson. In order to have a chance to discover it, it should be ensured that a significant number of Higgs bosons should be produced when colliding two protons. The number of Higgs bosons expected is proportional to its production probability and the number of times the experience of colliding two protons is repeated. More specifically, the rate at which a certain particle, X , is produced can be expressed as

$$\frac{dN_X}{dt} = L \sigma_X(\sqrt{s}), \quad (2.1)$$

where L is the instantaneous luminosity and is related to the number of trials per unit of time, and σ_X is the production cross-section and is related to the production probability. The LHC designed peak luminosity is $L = 10 \times 10^{34} \text{cm}^{-2}\text{s}^{-1}$ and its designed centre of mass energy is 14 TeV. With these parameters, a Higgs boson is produced roughly every 5 seconds.

In order to satisfy the high energy requirement with an accelerator using the same tunnel as LEP, it was decided to collide protons instead of electrons. The advantage of colliding heavier particles is straightforward when one keeps in mind that, in a circular accelerator, particles lose energy through synchrotron radiation. Indeed, the loss of energy per turn, ΔE , is proportional to the energy to the fourth power as

$$\Delta E \propto \frac{E^4}{Rm^4}. \quad (2.2)$$

Since protons are roughly 2×10^3 times heavier than electrons, the energy loss per turn is roughly 2×10^{13} smaller, which is an obvious advantage because the total amount

of energy necessary to accelerate a proton at the designed energy is smaller than what it would require for an electron.

It is technically extremely challenging to reach the designed luminosity using proton and antiproton beams. Indeed, an antiproton beam is harder to produce at first hand and also harder to maintain at high density while being accelerated. For that reason, the LHC uses two proton beams. In order to collide these beams, they must circulate inside the LHC with an opposite direction. To be maintained in their circular orbit, the Lorentz force, written as

$$\frac{d\vec{p}}{dt} = q\vec{v} \times \vec{B} \quad (2.3)$$

has to be centripetal. Since the velocity, \vec{v} , is equal in norm but different in sign for both beams, the same has to be true for the magnetic field, \vec{B} . As the space in the pre-existing tunnel is limited to roughly four meters, it was impossible to have two well separated pipes in two different support structures. This problem was solved by putting the two pipes in the same support structure, each of the pipes being surrounded by a separate superconducting coil to generate the desired magnetic field. Figure 2.1 shows one of these dipole magnets in the plane transverse to the beam pipe.

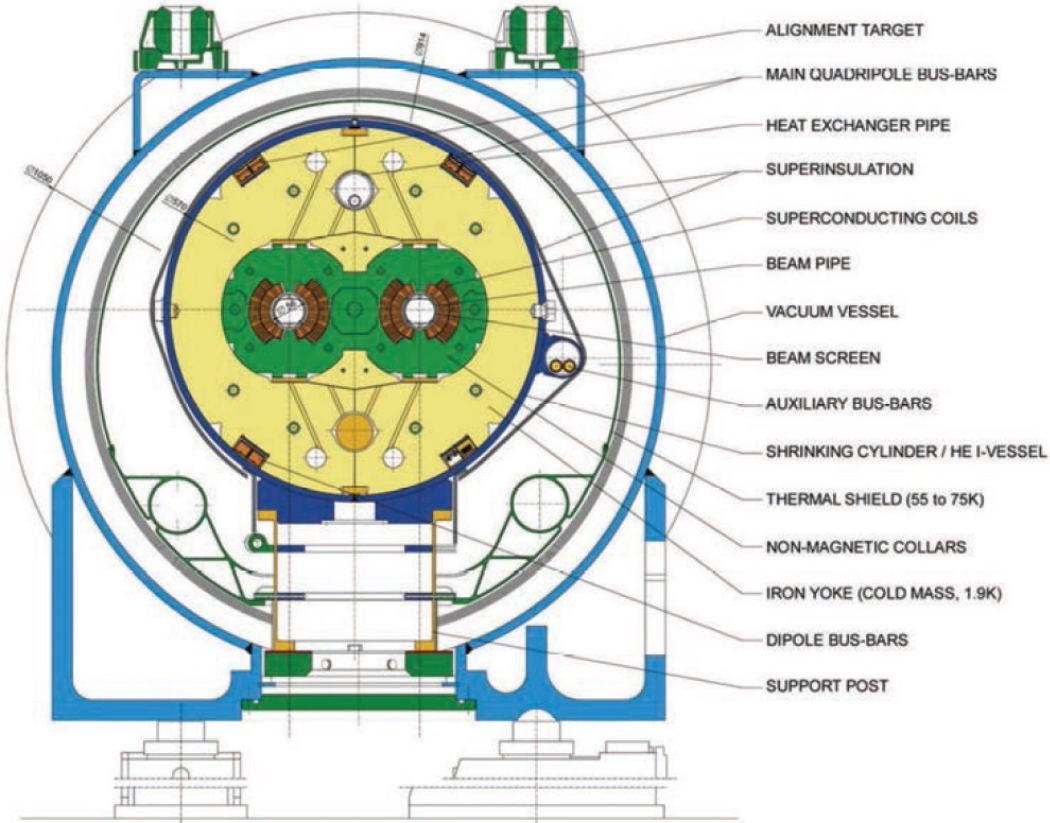


Figure 2.1: Cross-section view of a typical dipole magnet [35] used to maintain the protons in the desired trajectory. The magnetic field generated by the superconducting coils goes as high as 8.33 T.

At this point, the luminosity and the energy requirement of the LHC have been

defined. In the next section, more detailed technical information on how to achieve these figures will be given.

2.1.3 The LHC acceleration procedure

The protons are accelerated to the desired energy in many steps [29] using accelerators previously built and used by the LEP. Firstly, their energies are increased to 50 MeV by a linear accelerator, the LINAC2. Then, their energies are incrementally increased by successive circular accelerators: The BOOSTER complex sets their energies to 1 GeV, the proton synchrotron (PS) to 26 GeV and the super proton synchrotron (SPS) to 450 GeV. At this stage, the protons from the SPS are fed inside the LHC ring which will further increase their energies up to 7 TeV and also guides the beams so that they cross each other at the place where the detectors are built. Figure 2.2 shows a schematic representation of the multiple accelerators that are used to reach the energy of 7 TeV.

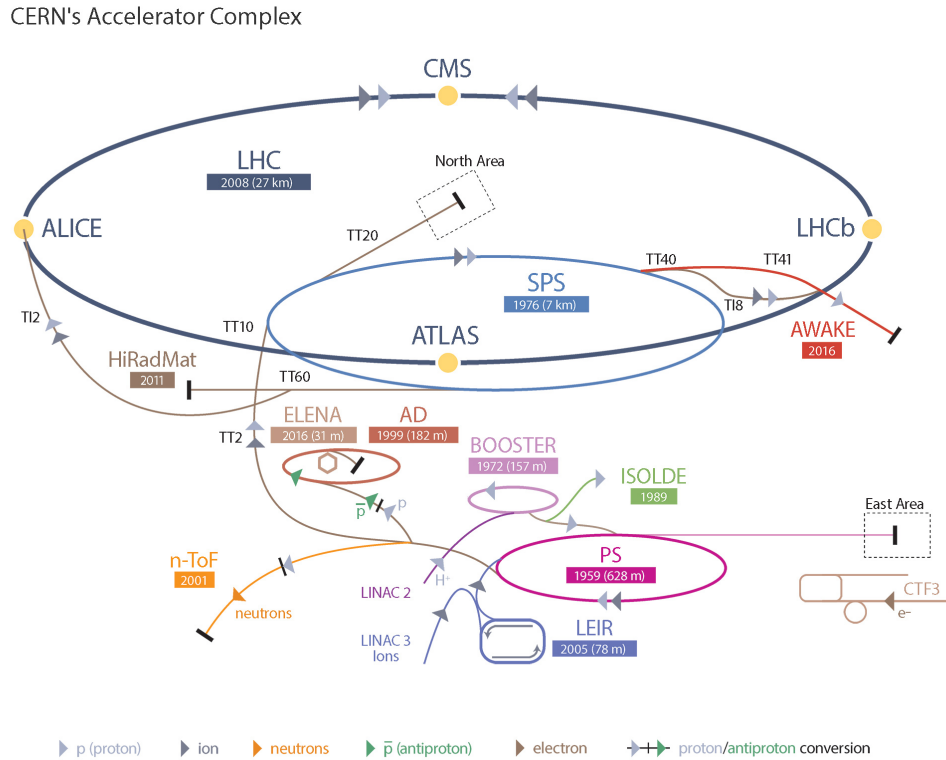


Figure 2.2: Schematic of the LHC complex [36]. To reach their designed energy of 7 TeV, protons are accelerated, step by step, by a chain of accelerators. The four yellow dots represent the four interaction points around which the detectors have been built.

The LHC complex is a quasi-circular ring where the protons are accelerated by the electrical field generated by radio-frequency (RF) cavities. The electrical field varies at a frequency of 40 MHz. During the acceleration process, protons are clustered together

in so-called "bunches". Each bunch contains up to 10^{11} protons and each beam is composed of 2808 bunches. The time between two consecutive bunches is 25 ns while the bunch length is roughly 1 ns at 7 TeV. The protons are maintained in their quasi-circular orbit thanks to the 1232 dipole magnets as depicted in Figure 2.1. Each of these dipoles measures about 15 meters and weighs almost 30 tons and can generate a magnetic field up to 8.33 T. This magnetic field is created by superconducting coils which are cooled down to 1.8 K.

The instantaneous luminosity can now be expressed as follows:

$$L = \frac{n_b f N^2}{A} \quad (2.4)$$

where n_b is the number of bunches per beam, f the frequency at which a bunch is crossing another bunch, N the number of protons per bunch and A is the area of interaction. The area of interaction is obviously related to the bunch size in the plane perpendicular to the proton's velocity. High luminosity is achieved by squeezing the bunch as tightly as possible, making A from Equation 2.4 small, and this squeezing is achieved by quadrupole magnets. Higher order multipoles are used to stabilise and focus the beams. In total, the LHC is composed of more than 9000 magnets.

2.1.4 The Worldwide LHC Computing Grid

In the previous section, the design of the LHC was reviewed so that it can accomplish its scientific goals. One of the key features is to achieve a very high luminosity. While high luminosity gives a reasonable chance to produce rare particles such as a Higgs boson, it comes with some drawbacks. At each bunch crossing, multiple proton-proton interactions may occur resulting in an increase of the complexity to distinguish which particles were created by which interaction. These additional proton-proton interactions are commonly referred to as "pileup". Furthermore, a huge amount of information is necessary to be processed in a very short time. In order to handle the data as efficiently as possible, the physicists put into place a computing infrastructure called the worldwide LHC computing grid (WLCG) which will be succinctly described hereafter.

The worldwide LHC computing grid is organised in three different layers, or "Tiers", from Tier-0 to Tier-2. Each of these Tiers has different purposes and may store different types of information.

Tier-0

There are two Tier-0 centres located at CERN in Geneva and at the Wigner Research Centre for Physics in Budapest. The entirety of the data collected at CERN goes through the Tier-0 centres before being eventually distributed to higher Tiers centres. The Tier-0 centres store the raw data (digital information) collected by each detector and transforms this information into a format that may be used in physics analyses. This step is known as the "reconstruction". In addition, the Tier-0 centres distribute the raw data and its reconstructed output to Tier-1 sites. When data are not being taken, the Tier-0 resources are used to perform re-reconstruction using improved calibrations.

Tier-1

All of the 13 Tier-1 centres are connected to the Tier-0 sites with optical-fibre links working at 10 gigabits per second. They may store part of the raw and reconstructed data as well as some simulations. In addition, they perform large data reprocessing and distribute the information to Tier-2 centres.

Tier-2

There are 155 Tier-2 centres spread over the world, one of which is located in Brussels. They provide data that can be used for physics analyses. Furthermore, the computing resources of the Tier-2 sites are widely used to produce simulations that will eventually be compared with the data.

2.2 The compact muon solenoid (CMS) detector

The CMS detector is one of the four main experiments located around the LHC. Like the ATLAS detector, it was designed as a general-purpose experiment which means that it can be used for a wide range of physics analyses. To achieve this goal, each variable of interest should be reconstructed with good precision. For example, the projection of the momentum of a particle in the plane transverse to the beam pipe, p_T , is a powerful variable to search for rare events and is accurately measured by CMS thanks to the strong magnetic field of 3.8 T generated by its solenoid.

First, the overall concept of the CMS detector [30] will be exposed in Section 2.2.1. The coordinate system convention used by the CMS collaboration will be discussed in Section 2.2.2. Then, each sub-detector will be reviewed, from the closest to the beam pipe to the farthest. The tracker which aims at detecting the trajectory of the electrically charged particles will be explained in Section 2.2.3. The electromagnetic calorimeter (ECAL) which measures the energy deposit left by particles that interact through the electromagnetic force, such as electrons and photons, will be exposed in Section 2.2.4. The energy deposit of the hadrons, which interact through the strong force, is measured by the hadronic calorimeter (HCAL) which will be reviewed in Section 2.2.5. Finally, in Section 2.2.6, details about the outer most sub-detector, the muon system, will be provided.

2.2.1 Overall concept of the CMS detector

The collision of two protons can give rise to a wide variety of particles. Due to the vastly different properties of these particles, different materials should be placed in the detector to increase the chance that a given particle will interact with at least a part of the detector. It is very common for these kinds of detectors to be built in layers, each of these layers having a different purpose. It is only by looking at the information of all the layers, or sub-detectors, that the full picture of what happened can be deduced. Additionally, to allow precise measurement of the particles with high p_T , a strong magnetic field is required. The CMS cylindrical solenoid can generate a magnetic field of 3.8 T. Inside the solenoid, the magnetic field is roughly uniform while it decreases rapidly outside it. Since the layers are wrapped around the beam pipe, CMS has quite naturally a cylindrical shape as it can be seen in Figure 2.3. Its overall length is about 29 m, and its diameter is roughly 15 m. With a weight of almost 15 000 tons, CMS is the heaviest detector at the LHC.

2.2.2 The CMS coordinate system

It is well known that most of physics problems start with the choice of a coordinate system. Since the results are independent of this choice, in principle, every physicist should be able to choose his or her favourite one. However, CMS is a very large collaboration, and communication amongst physicists would become very hard if multiple

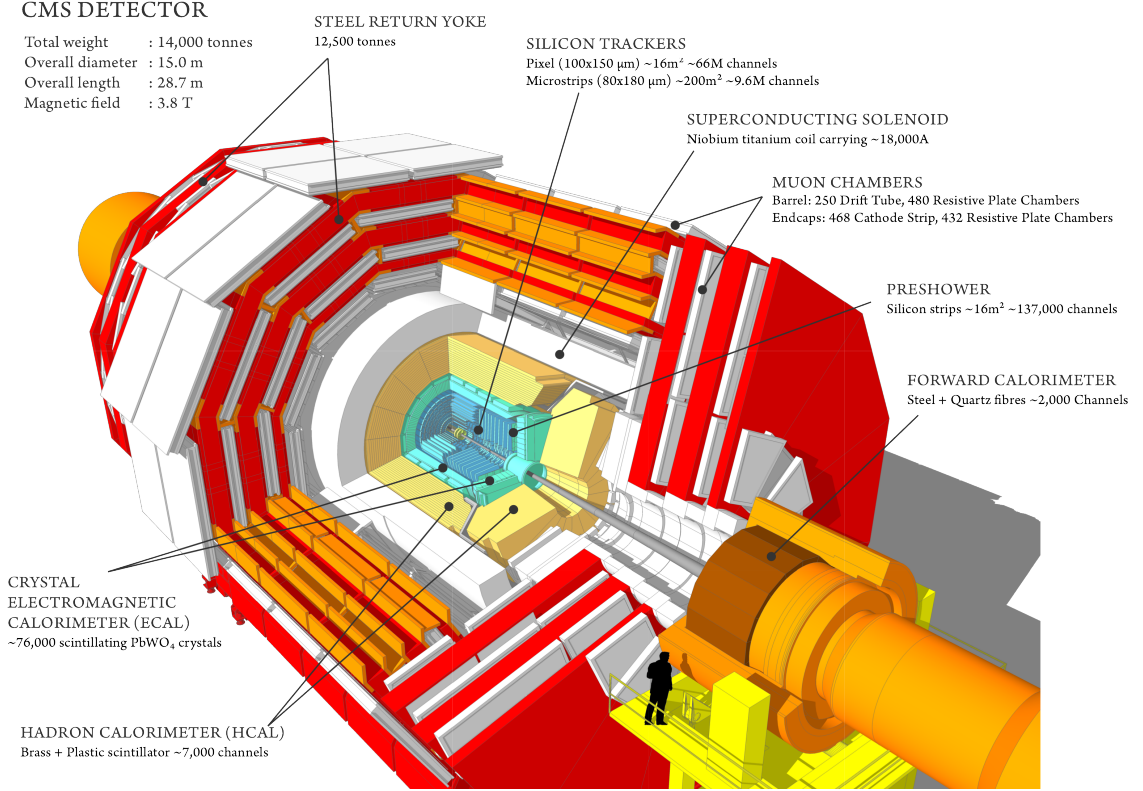


Figure 2.3: Schematic of the whole CMS detector [37].

coordinate systems were used simultaneously. For this reason, the CMS collaboration has agreed on a unique coordinate system that is used by all its collaborators.

The origin of this coordinate system is in the centre of the CMS detector where the proton-proton collisions occur. The x-axis points towards the centre of the LHC and the y-axis points upward, toward the sky. At the origin, the z-axis is tangent to the beam pipe, and its direction is set so that the system defines a right-handed coordinate system. Due to the cylindrical shape of the CMS detector, it is very natural to add a cylindrical coordinate system so each point of the space can be characterised by two angles and one length. The radial coordinate of a point, r , is the distance between this point and the z-axis. The azimuthal angle of a point, ϕ , is defined as the angle between this point and the x-axis in the (x-y) plane and ranges from 0 to 2π . Finally, the polar angle of a point, θ , is the angle measured from the z-axis to this point and ranges from 0 to π . However, the polar angle has not the same value in the rest-frame as compared to the frame of the particle. For that reason, it is useful to introduce a new variable that is related to θ , but that is Lorentz invariant under boost along the z-axis. The rapidity, y , defined as

$$y = \frac{1}{2} \ln \frac{E + p_z}{E - p_z} \quad (2.5)$$

satisfies the Lorentz invariance. In practice, the pseudorapidity defined as

$$\eta = -\ln\left(\tan\frac{\theta}{2}\right) \quad (2.6)$$

is more commonly used instead of the rapidity. The pseudorapidity is the approximation of the rapidity in the case where the mass of the particle is negligible compared to its energy.

2.2.3 The CMS tracker

The main goal of the tracker [38] is to reconstruct tracks of charged particles. This is achieved by using a complex algorithm that fits the hits left by these charged particles when traversing the sensors that compose the tracker. Because CMS is a general-purpose detector, the tracker is required to perform well in various domains. For example, depending on the analysis, the following criteria should be matched: good p_T resolution, efficient track reconstruction for low p_T , and, most importantly for this thesis, excellent spatial resolution. Because of the high luminosity achieved at the interaction region, around which the CMS detector is located, the number of charged particles produced per bunch-crossing is high. To ensure that a sensor will not be traversed by multiple charged particles at the same time, the granularity of the tracker should be as high as possible. This is especially true for the sensors close to the beam pipe as the rate decreases with the distance to the beam pipe. For that reason, the tracker uses two different technologies.

The pixel tracker is located as close as possible to the beam pipe. It is composed of three concentric sensor layers, placed at a radius of 4.4 cm, 7.3 cm and 10.2 cm, and two pairs of endcap disks at a $|z|$ of 34.5 cm and 46.5 cm. Figure 2.4 is a schematic of the pixel tracker. The pixel tracker is composed of about 66 million cells with dimension $150 \times 100 \mu\text{m}$. The single hit resolution obtained with this configuration is $10 \mu\text{m}$ in the $r\phi$ dimension and ranges from 15 to $20 \mu\text{m}$ in the z dimension.

The strip tracker is surrounding the pixel tracker and can be divided into four different subsystems. The tracker inner barrel (TIB) is composed of four concentric layers and covers the region up to a radius of 55 cm. The η coverage is extended thanks to the tracker inner disk (TID), which is composed of three disks on each side and go up to a $|z|$ of 118 cm. The tracker outer barrel (TOB), composed of 6 layers, covers $r > 55 \text{ cm}$ and $|z| < 118 \text{ cm}$. Finally, the tracker endcap (TEC), covers the region between $|z|$ of 124 cm and $|z|$ of 282 cm using nine disks. Altogether, the strip tracker contains 9.2 million strips and the resolution in the $r\phi$ ranges from 13 to $47 \mu\text{m}$. Figure 2.5 represents the top half of the entire CMS tracker projected in the $r - z$ plane.

The algorithm that is used to link the hits coming from the same track will be explained in Section 3.2.1.

2.2.4 The CMS electromagnetic calorimeter

The electromagnetic calorimeter [40] aims at measuring the energy of particles that interact through the electromagnetic force, namely, the electrons and the photons.

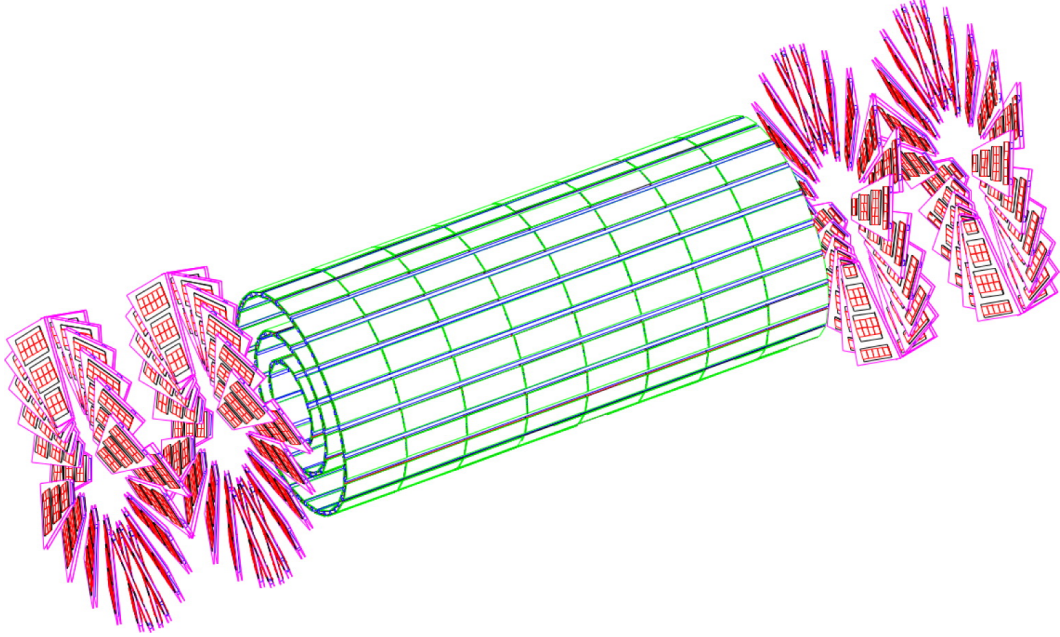


Figure 2.4: Schematic representation of the pixel tracker [30] composed of three concentric layers and four endcaps, two on each side.

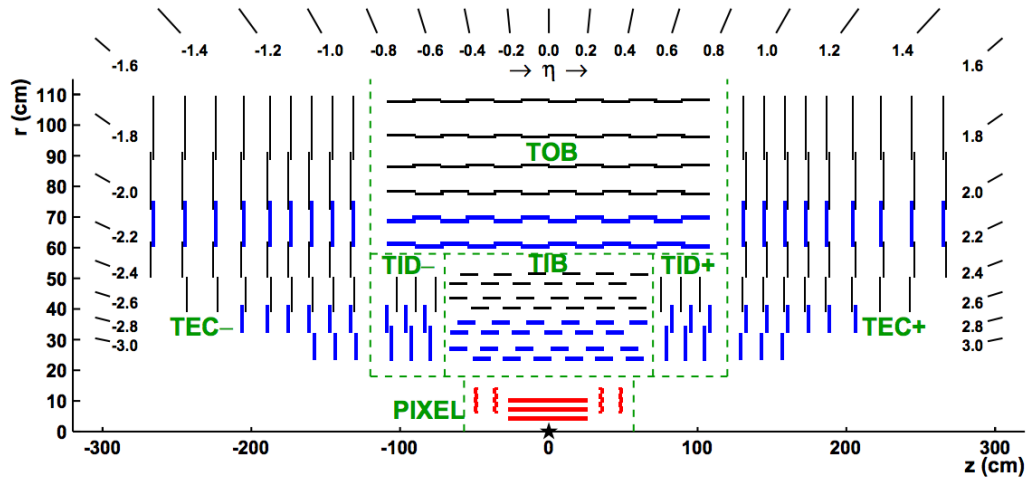


Figure 2.5: Schematic view of the entire CMS tracker [39]. The pixel part is depicted in red and is the closest to the beam pipe. For the strip tracker, the modules that provide 2D hits resolution are depicted in black while the ones that provide 3D hit resolution are in blue. The green dashed lines do not represent any sensor but are here to help the reader to distinguish the different parts of the tracker.

Again, it is divided into two parts, the electromagnetic calorimeter barrel (EB) and the electromagnetic calorimeter endcap (EE) as depicted in Figure 2.6. Scintillating lead tungstate crystals (PbWO_4) are used in both regions. The choice of lead tungstate

is motivated by the following properties: high density (8.28 g cm^{-3}), good radiation tolerance, small radiation length ($X_0 = 0.89 \text{ cm}$), small Moliere radius¹ ($r_M = 2.19 \text{ cm}$), and a fast response [30]. As a consequence, the shower will be narrow, short enough, the electromagnetic calorimeter will keep functioning for a long time without being too much damaged by radiation, and most of the light ($\approx 80\%$) will be collected before the next bunch crossing.

The ECAL barrel covers the region up to $\eta = 1.48$ using more than 60 thousand crystals. Each of the crystals has a dimension of $2.2 \times 2.2 \text{ cm}^2$ and a length of 23 cm which corresponds to almost 26 radiation lengths. The electromagnetic calorimeter endcap extends the η coverage up to a value of 3. Its crystals have a dimension of $2.9 \times 2.9 \text{ cm}^2$ and are 22 cm long. There are a bit more than seven thousands crystals in each of the electromagnetic calorimeter endcaps. In order to distinguish π^0 from photons, a detector called the preshower detector is placed in front of the electromagnetic calorimeter endcap between $\eta = 1.653$ and $\eta = 2.6$. This sub-detector contains lead interleaved with silicon strips.

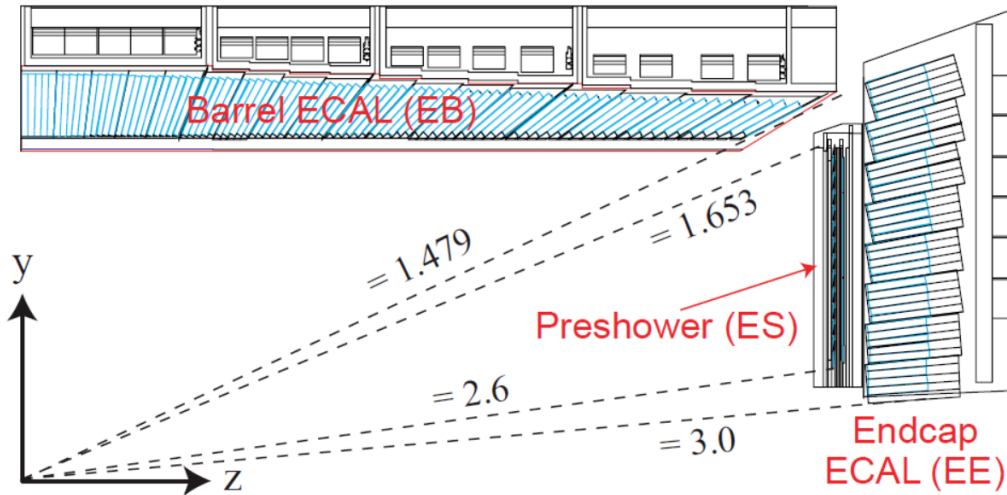


Figure 2.6: Schematic of the electromagnetic calorimeter detector [30]. The central region ($|\eta| < 1.48$) is covered by the EB while the most forward regions is covered by the EE up to $\eta = 3.0$.

2.2.5 The CMS hadronic calorimeter

The hadronic calorimeter [30] aims at measuring the energy from the hadrons created by the proton-proton collisions. Because this sub-component of the detector is not crucial for the analysis presented in this thesis, it will be only briefly described. Most of the hadronic calorimeter is composed of multiple layers of brass absorbers interleaved with plastic scintillators. The layers are arranged so that they form "towers" of fixed

¹The Moliere radius is the radius of the cylindre that contains on average 90% of the shower's energy deposition.

size in the (η, ϕ) space. The hadronic calorimeter is surrounding the electromagnetic calorimeter and is divided into four sub-components.

The central part of the hadronic calorimeter is the hadronic calorimeter barrel (HB) and is placed between the electromagnetic calorimeter barrel and the magnet coil. Due to this space restriction, hadronic showers might not be entirely contained in the hadronic calorimeter barrel, and a complementary sub-detector is placed outside the magnet coil, the hadronic calorimeter outer barrel (HO). Together they cover the region up to $|\eta| = 1.4$. The hadronic calorimeter endcap (HE) extends the η coverage with a slight overlap with the HB, $1.3 < |\eta| < 3.0$. Finally, a fourth sub-detector is placed in order to extend the coverage for large values of η , called the forward region. This sub-detector is called the hadronic calorimeter forward (HF).

A schematic of the four sub-detectors of the hadronic calorimeter is shown in Figure 2.7. The energy resolution of the hadronic calorimeter was measured using π^- beams with an energy ranging from 20 GeV to 300 GeV [41]. It was shown that the relative error on the energy decreases with increasing energy. For pions with an energy of 20 GeV (300 GeV), the energy resolution is about 27% (10%).

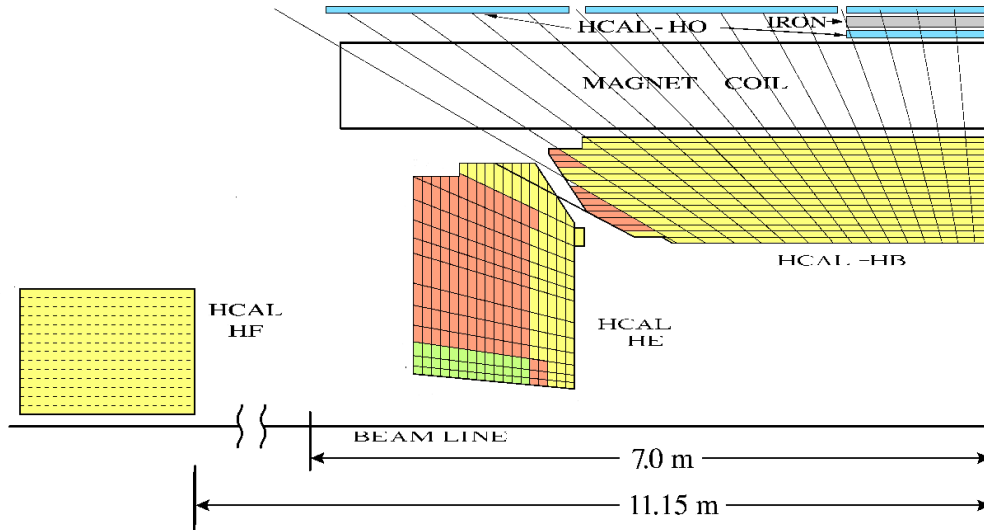


Figure 2.7: Layout of the four components of the hadronic calorimeter system in the $r-z$ plane [42]. Because of the symmetry of the hadronic calorimeter with these axes, only one of the four quadrants is shown. The two curly lines indicate that a part of the z axis is removed in order to keep the figure compact.

2.2.6 The CMS muon system

The outermost sub-detector of the CMS detector is the muon system. All of the components of the muon system lie outside the magnet coil, within the magnet's return yoke. It was designed to be able to measure the properties of the muons with high accuracy. The central part ($|\eta| < 1.2$) of the detector is covered using four layers of

drift tubes (DT). For the most forward part ($0.9 < |\eta| < 2.4$), the muons will be detected by up to four layers of cathode strip chambers (CSC). In addition, resistive plate chambers (RPC) are covering the region up to $|\eta| < 1.6$. Resistive plate chambers are used because of their very fast time response which improves the time resolution down to 1 ns.

Figure 2.8 shows part of the CMS detector where the different parts of the muon system are highlighted. The p_T resolution obtained with the muon system does largely depend on its p_T . A resolution better than 10% is achieved for muons with p_T as high as 2000 GeV.

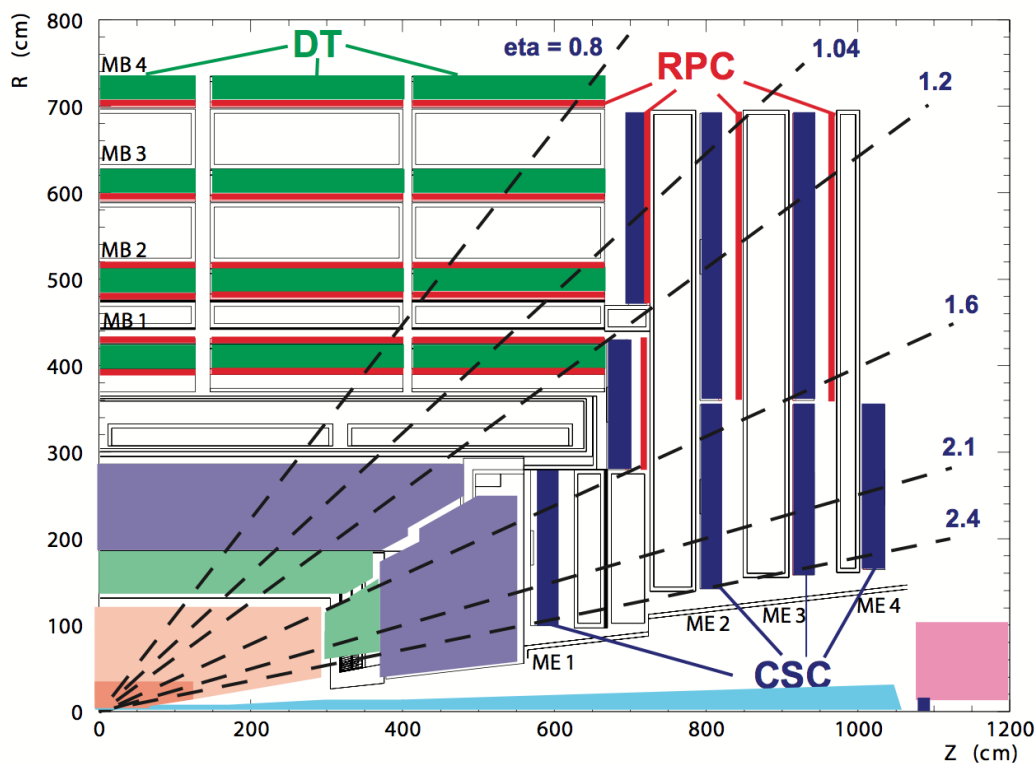


Figure 2.8: Layout of all the components of the CMS detector in $r - z$ plane [43]. Because of the symmetry of the CMS detector with this choice of axes, only one of the four quadrant is shown. Only the sub-detectors that are part of the muon system are labelled but the tracker, the electromagnetic calorimeter and the hadronic calorimeter are also displayed in orange, green and purple, respectively.

At this stage, all the information that one could gather about proton-proton collisions is collected by one (or more) of the sub-detectors. The algorithms used to convert this information into more meaningful one will be explained in the next section.

Reconstruction and simulation of proton-proton collisions

To be able to assess the validity of the Standard Model, or any other model, three ingredients are necessary. Firstly, the information collected by all the detectors described in the previous section should be converted into information about the final state, i.e. four-vectors of particles that are called physics objects. Secondly, due to the limitation of the storage capacity, only potentially interesting events are selected to be saved. Finally, the number of events with a particular final state should be compared with the number expected from the Standard Model processes which can be estimated thanks to simulation.

The trigger system, which aims to select the fraction of events that can be saved for later use, is described in Section 3.1 In Section 3.2, the algorithms crucial for the reconstruction and the identification of physics objects will be discussed. This includes the tracker algorithm, the particle-flow algorithm, and electrons and muons identification. The Standard Model processes can be estimated thanks to the use of Monte Carlo (MC) simulations. All the steps necessary in the simulation chain will be explained in Section 3.3. In Section 3.4, the correction applied to the simulations to improve the agreement between Monte Carlo and data is reviewed.

3.1 Trigger

The physics programs of the LHC experiments require to have a very high luminosity to produce rare events at a decent rate. In 2015, the bunch-crossing frequency was 40 MHz with an average of roughly 20 proton-proton collisions per bunch crossing yielding slightly less than 10^9 collisions per second. Because the rate at which information can be stored is limited by the technology used, only a small fraction of the events can be saved. The goal of the trigger is to select the most interesting events only and reduce the event rate so that all of these events can be stored. This is achieved using two trigger levels: the Level-1 (L1) trigger, and the high-level trigger (HLT).

The Level-1 trigger

The L1 trigger takes as input the raw information collected by the calorimeters and the

muon chambers. At this stage, physics objects, such as electrons, muons, photons, jets, and missing transverse energy are not reconstructed, and only a coarse L1 algorithm is used to decide whether to keep an event. The events that have been kept by the L1 trigger are then fed into the next trigger level with a rate of roughly 100 kHz.

The high level trigger

The reduced event rate after L1 allows the HLT to perform a partial reconstruction of each event using all the sub-detectors, tracker included. Physics objects are partially reconstructed and the decision on whether to keep an event can be made. To be able to store all the events passing the HLT, the output event rate of the HLT is required to be lower than 400 Hz [44].

The potentially interesting events vary greatly from analysis to analysis. The full dataset recorded and stored is divided into multiple sub-datasets depending on the object on which selections are imposed. For example, all the HLT algorithms that contain a selection of one single electron, irrespective of the exact cut, are grouped under the “SingleElectron” dataset. It is also possible to store events when no proton-proton collisions are occurring. These events are grouped under the “NoBPTX” dataset. The list of dataset names used for this thesis is given in Table 3.1 as well as the physic objects on which the selection is applied.

Table 3.1: List of dataset names as well as the physic objects on which the selection is applied.

dataset name	physic object(s)
SingleElectron	One electron
DoubleEG	Two electrons or photons
SingleMu	One muon
DoubleMu	Two muons
MuEG	One muon and one electron or photon
MET	missing transverse energy
NoBPTX	no proton-proton collisions

3.2 Physics object reconstruction

At the luminosity reached at the LHC in 2012, roughly twenty proton-proton collisions occur for each bunch crossing. Each of these collisions will create many particles. To be able to disentangle all the particles, identify each of the collisions individually, and reconstruct physics objects that can be used for physics analyses, powerful algorithms must be used. All the algorithms used to reconstruct the physics objects relevant for this thesis will be discussed in this section.

Firstly, the tracking algorithm, responsible for converting hits in the tracker into tracks, will be described in Section 3.2.1. In Section 3.2.2, the particle-flow algorithm that uses the information provided by all sub-detectors in order to reconstruct all the stable particles will be reviewed. The quality requirement imposed on electrons and muons to ensure a better purity will be discussed in Section 3.2.3 and Section 3.2.4, respectively. The reconstruction of more complicated objects, such as jets, is introduced in Section 3.2.5.

3.2.1 Track reconstruction

The raw input of the tracking algorithm [38] is the hits detected by each of the sensors composing the tracker system described in Section 2.2.3. Its goal is to find which of these hits can be associated to the same track and give a list of tracks as output. The algorithm used by CMS to execute this challenging task is commonly referred to as the combinatorial track finder. It is using a Kalman filter [45–47] technique and more specifically a combinatorial Kalman filter [48]. The main idea of the algorithm is to use an iterative procedure during which the easiest tracks to find are identified first. When a track is found, all of its hits are removed from the hit collection, which reduces the complexity to find the next ones. The combinatorial track finding is divided into four steps: seed generation, track finding, track fitting and track selection. Each of these steps will be described in the following paragraphs.

Seed generation

The very first step of the tracking algorithm is called the seed generation. Seeds are searched for in the innermost part of the tracker and will eventually be extrapolated outward. This approach, also referred to as the "inside-out" approach, is more efficient than the "outside-in" counterpart thanks to the high granularity of the pixel tracker. Indeed, even if the density of tracks is higher in the inner region, the channel occupancy, defined as the fraction of the channels with a hit over the number of channels, is lower. Finally, since the hit inefficiency (the probability to miss a real hit) is proportional to the channel occupancy, a low channel occupancy yields a better hit efficiency. For tracks originating from the prompt region, the optimal seed, which corresponds to the zeroth iteration, is obtained if three pixel hits, or a "pixel triplet", are compatible with each other. Also the track parameters must satisfy the conditions on p_T , d_0 and z_0 that can be seen in Table 3.2, where d_0 is defined, in the transverse plane of the z coordinate, as the distance of closest approach of the extrapolated lepton track to the

center of the luminous region and z_0 is the analogous of d_0 but measured along the z-axis.

When all the seeds of the zeroth iteration have been found, seeds satisfying criteria of the first iteration are searched for, and so on for all the iterations. In general, the later iterations allow for more displaced tracks to be found which is of crucial importance for the analysis in this thesis. Specifically, iteration 4 and 5 do not require any pixel hits and the requirement on the d_0 is significantly relaxed.

Table 3.2: List of selections applied for each seed iteration [38].

Iteration	Seeding layers	p_T (GeV)	d_0 (cm)	$ z_0 $
0	Pixel triplets	> 0.8	< 0.2	$< 3 \text{ SD}$
1	Mixed pairs with vertex	> 0.6	< 0.2	$< 0.2 \text{ cm}$
2	Pixel triplets	> 0.075	< 0.2	$< 3.3 \text{ SD}$
3	Mixed triplets	> 0.375	< 1.2	$< 10 \text{ cm}$
4	TIB 1+2 TID/TEC ring 1+2	> 0.5	< 2.0	$< 10 \text{ cm}$
5	TOB 1+2 & TEC ring 5	> 0.6	< 5.0	$< 30 \text{ cm}$

Track finding

Track finding is the process of finding collections of hits produced by individual particles. It is in this step that the Kalman Filter method is used. At each iteration, the track is extrapolated to the next layer assuming an helical trajectory and taking into account the information gathered up to that point (track parameter and related uncertainty) as well as multiple scattering effects, forming a list of track candidates. This procedure is repeated until a stable condition is satisfied, most commonly when the outermost layer is reached. At this stage, hits can be shared by multiple track candidates. The ambiguity is removed using a "trajectory cleaner" that uses the fraction of shared hits by two different track candidates as input. This parameter, f_{shared} , reads

$$f_{shared} = \frac{N_{shared}^{hits}}{\min(N_1^{hits}, N_2^{hits})}, \quad (3.1)$$

where N_1^{hits} (N_2^{hits}) is the number of used hits to form the first (second) track candidate. If f_{shared} goes above a certain threshold, the candidate with the lowest number of hits is removed from the candidate list.

Track fitting

In order to improve the track parameters found up to this stage, a specific treatment is applied. A Kalman filter is initialised from the innermost hit to the outer most hit as well as from the outer most hit to the innermost hit. Then, a weighted average is used to define the most accurate values of the track parameters. The trajectory is no more helical in the case of a non-uniform magnetic field, and a more accurate equation is solved using a Runge-Kutta propagator [49]. Further more, a search for spurious hits (hits that are wrongly associated with the track) is performed.

Track selection

The last stage consists of removing fake tracks which are defined as tracks that are not coming from a charged particle. This is performed by applying cuts such as the number of layers that have hits, the track quality and the compatibility of the track with the primary vertex. The track quality is defined as χ^2/ndof where χ^2 is the sum of squares of the difference between the fitted values and the hit values over the known uncertainties and ndof is the number of degrees of freedom of the track. The values of the cuts vary with the iteration number. At the end of the track selection, the tracks found by each of the six iterations are merged into a single list of tracks. This list of tracks is of crucial importance for the particle-flow algorithm which will be discussed in the next section.

3.2.2 Particle-flow algorithm

All the particles that are created by the proton-proton collisions may interact differently with some of the sub-detectors. For most particles, looking at the information of any of the sub-detectors individually does not provide sufficient information to identify which particle traversed it. However, by looking at the signal, or lack thereof, of all the sub-detectors simultaneously, particle identification can be achieved better than with just one sub-detector. For example, the tracker cannot easily distinguish between a pion and an electron. However, an electron will deposit its energy in the electromagnetic calorimeter while the pion will do so mostly in the hadronic calorimeter. If one can connect the information of the tracker with the information of the electromagnetic calorimeter or hadronic calorimeter, pions can easily be distinguished from electrons. The particle-flow algorithm aims at reconstructing all stable particles by identifying potential links between the tracker, the electromagnetic calorimeter, the hadronic calorimeter and the muon system. The types of particles that can be distinguished from each other with this principle are muons, electrons, charged hadrons, neutral hadrons, and photons. Figure 3.1 shows the typical interaction of these particles with the detector.

The particle-flow algorithm [50] takes as input fundamental "elements" such as tracker tracks, electromagnetic calorimeter clusters (defined as 5×5 cells), hadronic calorimeter clusters, and muon tracks. The following pairing of elements are considered: tracker track - electromagnetic calorimeter cluster, tracker track - hadronic calorimeter cluster, electromagnetic calorimeter cluster - hadronic calorimeter cluster, and tracker track - muon track. When a match is found, elements are grouped within a so-called "block" which consist of at least two elements.

The blocks constitute the input of the next step, which is the individual particle reconstruction and identification. Similar to the iteration procedure in the tracking, the most distinguishable objects are resolved first. When this is done, all the elements that are related to the reconstructed particle are removed from the block, decreasing the complexity of the next step. The muons are the easiest particles to reconstruct as they are the only ones to traverse the detector up to the muon system, so they are reconstructed first. Afterwards, the electrons are identified and reconstructed. Next, charged hadrons are reconstructed by searching for a tracker track element as well as hadronic calorimeter cluster element. The total energy deposit in the calorimeters is

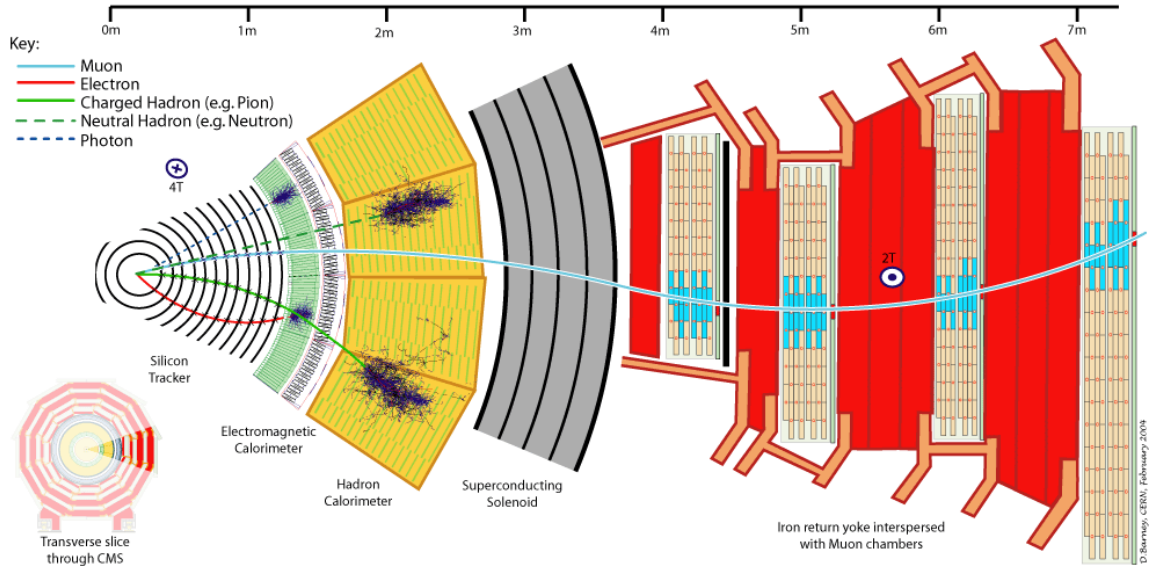


Figure 3.1: Typical interaction between particles and the CMS sub-detectors shown in the transverse view.

compared to the sum of all the matching track momenta, where the momentum of each track is calculated by measuring the radius of curvature of the track. If these values agree within three standard deviations, a charged hadron is identified. If the sum of the track momenta exceeds the energy deposit, neutral hadrons and photons are searched for. When all charged hadrons have been identified, none of the remaining blocks should contain a track element. All the remaining electromagnetic calorimeter clusters are assigned to photons while the remaining hadronic calorimeter clusters are assumed to be associated with neutral hadrons.

After the reconstruction of the physics objects, further requirements are typically applied to decrease potential ambiguities. This step is commonly referred to as "identification", and its definition depends on the physics object considered and even depends on the analysis scenario. In order to facilitate the discussion, imagine that one is interested in identifying electrons. The exact selection criteria applied to pass the identification may vary from one analysis to another. Indeed, a loosening of the requirement would increase the efficiency of selecting genuine electrons as well as the fraction of false positives, commonly known as the fake rate, which is defined as the fraction of non-electrons that have passed the selection criteria. A trade-off between the efficiency of selecting genuine electrons and the purity of the selected electrons has to be made. The CMS collaboration prepares a few options, and the analysts are responsible to choose the option that satisfies their needs or develop a new selection. It is very common to refer these various options as "working points". In most cases, three working points are available: "loose", "medium", and "tight" where the loose working point yields the best efficiency while the tight working point has the highest purity. The definition of these working points can also change when data are being taken under new conditions or when more recent studies are performed.

3.2.3 Electron reconstruction and identification

As already mentioned previously, an electron is created by linking a tracker track with an electromagnetic calorimeter cluster. It turns out that, depending on the momentum and the detector location of the electron, the information of one sub-detector will be more reliable than the other. The sub-detector providing the more reliable information will be used as the seed and a match in the other sub-detector will be searched for.

A very energetic and well isolated (not surrounded by other particles) electron will be seeded using information from the electromagnetic calorimeter. In this case, a "super cluster" is formed by combining clusters with high energy deposit ($E_T > 4 \text{ GeV}$). The direction of the electron is calculated using the barycentre of the super cluster, which is the average position of the clusters weighted by the energy deposit. Then, the position of the hits expected in the tracker is inferred. This method will be referred to as the "electromagnetic calorimeter-driven" approach.

For an electron which is not well isolated, the electromagnetic calorimeter-driven approach described previously is inadequate. Indeed, particles surrounding the electron may deposit their energy in the same super cluster as the electron, introducing a bias in the estimation of the electron position. Furthermore, when an electron is produced inside a jet, many tracks could be associated with the extrapolation from the electromagnetic calorimeter if the electromagnetic calorimeter-driven procedure was used. The electromagnetic calorimeter-driven approach also fails for very low p_T electrons. In that case, the tracks of the electrons are highly bent in the magnetic field and photons emitted by bremsstrahlung are spread over many electromagnetic calorimeter clusters which render the estimation of the electron position inaccurate. For both these cases, the most trustworthy information is provided by the tracker. In this method, referred to as the "tracker-driven" approach, all the tracks found by the tracker are seeds for potential electron candidates.

Various variables are then used in order to identify this track as a track coming from an electron. As mentioned already in the previous subsection, various working points are defined and their definitions depend on the data-taking period. The exact definition used will be discussed in chapters 5 and 7.

The seeds produced by the electromagnetic calorimeter-driven and the tracker-driven methods are then merged into a single collection of seeds which are fed into the full Gaussian-sum filter tracking algorithm [51]. In the Kalman filter algorithm, which is used in the standard tracking algorithm, it is assumed that the energy loss distribution is Gaussian which is not appropriate for particles which radiate a large amount of energy through bremsstrahlung such as electrons. In the Gaussian-sum filter algorithm, a mixture of Gaussians is used in order to estimate the energy loss by Bremsstrahlung instead of a single Gaussian. The momentum resolution is improved when using the Gaussian-sum filter algorithm with respect to the simpler Kalman filter approach.

3.2.4 Muon reconstruction and identification

Due to their properties, muons can be very efficiently reconstructed and identified by the CMS detector. Electrons and photons are absorbed by the electromagnetic

calorimeter, the hadronic calorimeter absorbs hadrons, and tau leptons have a too short lifetime to reach the muon system. The neutrinos are the only other Standard Model particles that can travel up to the muon system, but they cross them without giving any hint of their presence. Using these facts, it can be deduced that only a muon can generate a signal in the muon system. However, not all the muons will be able to reach the muon system. Indeed, low p_T muons are highly bent by the magnetic field, and, due to energy loss, might never reach the muon system. Since muons are charged particles, the tracker can also provide insightful information. Using the fact that a muon should at least be detected by either the tracker or the muon system, three "types" of muons are defined. Thanks to the complementarity of the tracker and the muon chambers, about 99% of the muons produced by proton-proton collisions are either reconstructed in the tracker or the muon system.

- **Standalone muons:** The muon system is composed of sensors that can provide the information about whether or not this specific sensor was traversed (hit). The hits registered by each drift tubes or cathode strip chambers are then matched to form track segments, called track stubs. These tracks are the seeds of the standalone muon tracks which use the hits of the drift tubes, cathode strip chambers and resistive plate chambers.
- **Tracker muons:** All tracks with $p_T > 0.5 \text{ GeV}$ are potential candidates for muon tracks. These tracks are extrapolated towards the muon chambers taking into account the usual effects. If a tracker track has at least one match with a stub track, either from the drift tubes or the cathode strip chambers, the track becomes a tracker muon track.
- **Global muons:** For each standalone muon track, an inward extrapolation will be performed to find an eventual tracker track. If the extrapolation of a tracker muon track at a given surface, matches the one of a standalone muon track, a global muon is formed. The global muon track parameters are extracted by a fit combining the information of both sub-detectors. At low p_T , the tracker provides the most insightful information while the muon system can improve the p_T resolution for larger value, typically above 200 GeV . This is the most commonly used definition and the one used in this thesis.

To enhance the purity of the muons, additional identification selections are applied. The exact definition used will be discussed in chapters 5 and 7.

3.2.5 Other important physics objects

Jet reconstruction

Quarks and gluons cannot be directly detected by the detector. Indeed, before binding into hadrons, quarks and gluons undergo fragmentation which will create multiple particles forming a "jet" of particles. The anti- k_t algorithm [52] aims at clustering jets of particles inside a unique object, henceforth referred to as a "jet". Two particle-flow objects, i and j , are either merged into a single jet or not depending on the comparison

of two parameters. The first parameter is related to the distance between the two objects, d_{ij} ,

$$d_{ij} = \min\left(\frac{1}{k_{ti}^2}, \frac{1}{k_{tj}^2}\right) \frac{\Delta R_{ij}^2}{R^2}, \quad (3.2)$$

where $k_t = p_T$, R is a parameter of the jet which is called the "jet cone radius", $\Delta R_{ij} = \sqrt{\Delta y_{ij}^2 + \Delta \phi_{ij}^2}$, ϕ is the azimuthal angle introduced in Section 2.2.2, and y is the rapidity as defined in Equation 2.5. The second parameter is

$$d_i = \frac{1}{k_{ti}^2}. \quad (3.3)$$

First, all the d_{ij} couples are calculated as well as all the d_i parameters. Then if the smallest d_{ij} is smaller than the smallest d_i , the two objects are merged inside a single jet and are removed from the list of inputs. On the contrary, if d_{ij} is larger than d_i , the two objects belong to two different jets. This procedure is repeated until the list of objects is exhausted. Like for the electrons and the muons, some additional identification cuts can be applied to reduce the fake rate.

b-jet reconstruction

Jets originating from a b quark, hereafter called "b-jets", can be distinguished from jets originating from lighter quarks or gluons. Because b quarks hadronise and form B-mesons, that have a lifetime of the order of few picoseconds, their decay products are sufficiently displaced from the proton-proton vertex to allow to reconstruct a secondary vertex. The most commonly used algorithm to identify, or "tag", a b-jet in CMS is the combined secondary vertex (CSV) algorithm [53]. Many variables can provide discriminating power such as the presence of a secondary vertex, the flight distance significance in the transverse plane, the vertex mass, etc. However, instead of cutting on one or more of these variables separately, a more subtle approach is used. This approach is commonly referred to as multivariate analysis (MVA) technique and consist of combining together all the variables and their correlations in order to produce a single variable called the discriminator. This procedure allows having better discrimination power between genuine jets and fake jets that can arise from noise in the hadronic calorimeter or problems in the reconstruction of the pileup. Three working points are defined by the CMS collaboration enabling to choose between high b-jet efficiency or high purity.

Missing transverse energy reconstruction

Despite the large thickness of the CMS detector, some particles might not interact with any of its components. For example, this is the case for the neutrinos as already mentioned in Section 3.2.4. Furthermore, when assuming R-parity conserved Supersymmetry, the lightest supersymmetric particle does not interact with Standard Model particles and will also escape the detector. However, using momentum conservation, the presence of particles escaping the detector can be deduced. Indeed, when a collision produces only Standard Model particles without any neutrinos, the sum of the

momenta of all reconstructed particles should be null as in the following equation,

$$\Sigma \vec{p} = \vec{0}. \quad (3.4)$$

When this sum is not equal to zero, a new variable, referred to as missing momentum, \vec{p}^{miss} , is introduced in order to recover the momentum conservation as

$$\Sigma \vec{p} + \vec{p}^{\text{miss}} = \vec{0}. \quad (3.5)$$

In practice, it is more convenient to have a scalar value and it is common to use the norm of the vector projected in the transverse plane, the missing transverse momentum, $P_{\text{T}}^{\text{miss}}$. Finally, for a collision at centre of mass energy of few TeV, the mass of a neutrino is negligible as compared to its momentum, it is customary to use the missing transverse energy, $E_{\text{T}}^{\text{miss}}$, also referred to as "MET". This variable provides a very good sensitivity for R-parity conserved Supersymmetry and has been used in various searches in which the minimal supersymmetric Standard Model scenario was assumed.

3.3 Event simulation

In the previous section, a brief overview of the algorithms used to reconstruct a final state from the digital information collected by the sub-detectors has been discussed. However, it is crucial to understand that the information that is analysed by physicists is the output of these algorithms and hence relies on their accuracy. In some sense, the reconstruction algorithms can be viewed as a very complicated function that takes "reality" as input and gives the best possible "hypothesis" of this reality as output. In data, the reality is not directly accessible but is inferred from this hypothesis. To have a grip on how accurate the hypothesis is, or equivalently how performant the algorithms are, simulations of proton-proton collisions are used. These simulations are passed through exactly the same reconstruction procedure as the one used for data, and the output can be directly compared with the input, providing valuable information about the accuracy of the algorithms. In this section, all the steps necessary to produce simulation of the LHC collisions [54, 55] will be explained.

The first element of the simulation procedure is the description of the proton-proton collision itself which depends on the distribution of the components inside each proton, called partons. Both the parton density function (PDF) and the hard interaction will be discussed in Section 3.3.1. In Section 3.3.2, a process called "parton showering" during which each parton can radiate another parton is described. The recombination of the partons into hadrons, called "hadronisation", and the potential decay of these hadrons are reviewed in Section 3.3.3. In Section 3.3.4, the effect of the parton showering initiated by the partons not involved in the hard scattering is taken into account. After the generation steps, the interaction of the particles with the detector material will be simulated, which is described in Section 3.3.5. The handling of the pileup interactions is discussed in Section 3.3.6. Finally, the way that the CMS collaboration handles the simulation of various processes is described in Section 3.3.7.

3.3.1 Parton density function and hard scattering

The first step of the full generation chain, which is sketched in Figure 3.2, aims at calculating the probability of producing any final states when colliding two protons. When two composite objects, like protons, interact with each other, it is assumed that the hard scattering occurs between one of the constituents, or partons, of each proton. The centre-of-mass energy of the proton-proton collision, \sqrt{s} , gets reduced to the centre-of-mass energy of the two interacting partons, $\sqrt{\hat{s}}$. This reduced centre-of-mass energy is related to the energy scale, Q^2 , and can be expressed as:

$$\sqrt{Q^2} \equiv \sqrt{\hat{s}} = \sqrt{x_i x_j s} , \quad (3.6)$$

where x_i is the momentum fraction carried by the parton i in the first proton and x_j is the momentum fraction carried by the parton j in the second proton. Now, the differential cross-section of any process, $d\sigma_{pp \rightarrow X}$, is given by the sum of all the possible partonic differential cross-sections, $d\hat{\sigma}_{ij \rightarrow X}$, weighted by the corresponding

PDF, $f_i(x_i, Q^2)$ and $f_j(x_j, Q^2)$:

$$d\sigma_{pp \rightarrow X} = \sum_{i,j} \int f_i(x_i, Q^2) dx_i \int f_j(x_j, Q^2) dx_j d\hat{\sigma}_{ij \rightarrow X}. \quad (3.7)$$

Here, the sum runs over all the possible configurations of spins, colours, and parton-flavour of each parton. For each process, the cross-section can be inferred from the PDF and the partonic differential cross-section.

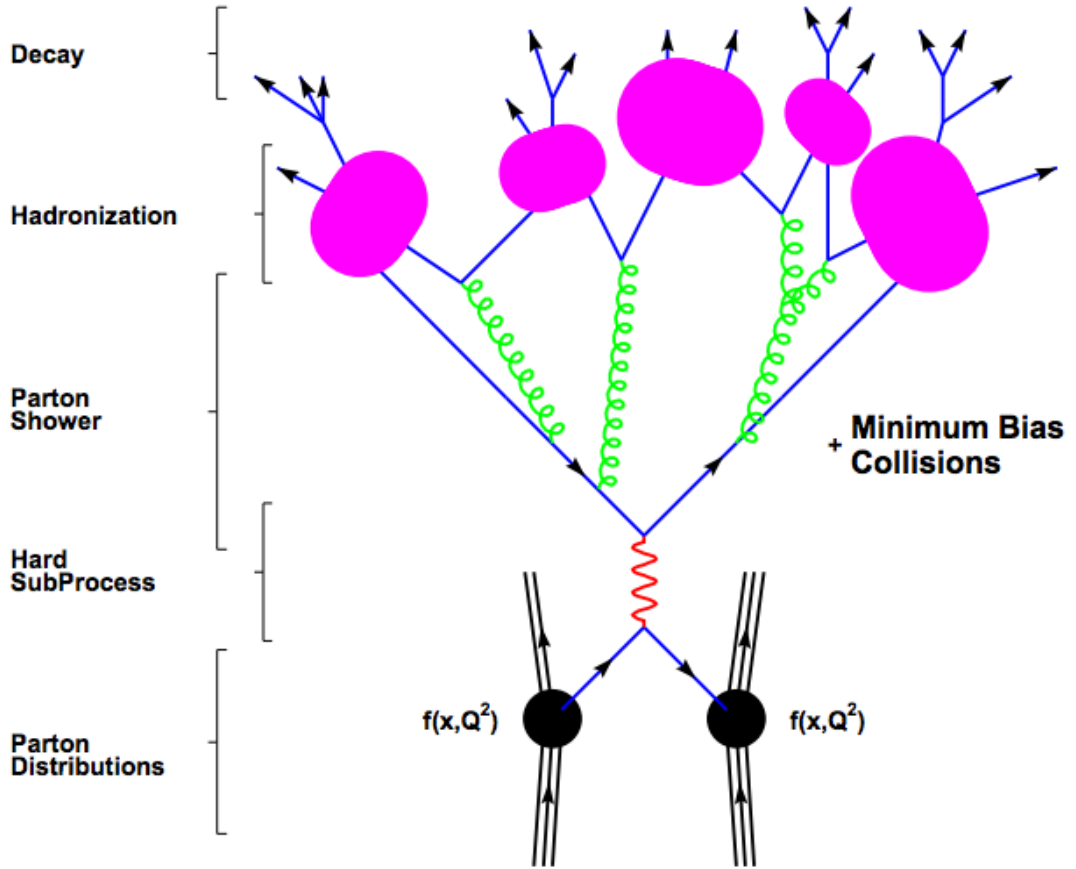


Figure 3.2: Schematic representation [54] of the simulation of a proton-proton hard scattering. The two black dots are the protons, the green wavy lines are partons created during the parton showering and the magenta blob are (meta-)stable hadrons.

The PDFs are obtained empirically, mostly from deep inelastic scattering between a proton and an electron or a positron. In this thesis, the most valuable information about the proton's PDF is extracted from the results of the HERA experiments [56], where deep inelastic electron-proton collisions were studied. Since the energy available at this accelerator was much lower than the one at the LHC, the PDFs are typically extrapolated to higher Q^2 .

The partonic differential cross-sections involve matrix elements that can be computed by using the corresponding Feynman diagrams. These diagrams include the strong coupling constant, α_s , which becomes smaller at large scale. In the regime where $\alpha_s \ll 1$, the Feynman diagrams of higher order in α_s become negligible, and the matrix elements can be calculated up to a certain order. Leading order (LO) calculations of a $2 \rightarrow 2$ partons process include terms in α_s^2 , next-to-leading order (NLO) adds the α_s^3 terms, next-to-next-to-leading order (NNLO) goes as high as the fourth power in α_s . The accuracy increases with the orders up to which terms are included, but so does the computational time as well, and calculations are not possible yet to all orders. Once again, a trade-off between the accuracy and the computing time has to be made.

Also, when adding loop corrections, divergent integrals may arise. There are mostly two types of divergence, one called "ultraviolet divergence" and the other called the "infrared divergence". In the high energy limit, the ultraviolet divergence is solved by the introduction of a new scale, μ_R which renders the integral finite. At low energy, the infrared divergence is solved by the introduction of another scale, the factorisation scale, μ_F . The physical results should be independent of the choices of these scales, and alternative choices are used as a systematic uncertainty.

3.3.2 Parton showering

The quarks and gluons produced in the collision are carrying a colour charge and thus will undergo interaction through the strong force. Each parton can radiate another parton which, in turn, can also radiate, creating parton showering. The processes that can generate an additional parton are the following: gluon radiation from a quark, $q \rightarrow qg$, gluon radiation from a gluon, $g \rightarrow gg$, and gluon annihilation into quark and anti-quark, $g \rightarrow q\bar{q}$. In each of these scenarios, one particle, "the parent", decays into two particles, called "children". Next, the children created in the first step might also create a pair of children which, in turn, can also decay. The decay chain is repeated down to a certain energy scale after which the α_s becomes too large for accurate perturbation calculation. Typically around 1 GeV, the rest of the chain is handled by the hadronisation process, described in the next section.

Let a be the parent particle and b and c the two children. The energy conservation of the interaction of a into b and c is

$$E_a = E_b + E_c. \quad (3.8)$$

Let z be the energy fraction carried by the child b . It follows that

$$E_b = zE_a \quad (3.9)$$

$$E_c = (1 - z)E_a. \quad (3.10)$$

Now, the probability of interaction, known as the DGLAP¹ equation [57–59], can be expressed as follows

$$d\mathcal{P}_{a \rightarrow bc} = \frac{\alpha_s}{2\pi} \frac{dQ^2}{Q^2} P_{a \rightarrow bc}(z) dz \quad (3.11)$$

¹DGLAP stands for the name of the five physicists that contributed to the elaboration of this equation: Dokshitzer, Gribov, Lipatov, Altarelli and Parisi.

where the probability $P_{a \rightarrow bc}(z)$ depends on which of the three processes mentioned before is considered. Finally, the probability of a particle to decay at a given time, t , depends on the interaction probability at that time but also on the non-interaction probability up to this time. The probability of non-interaction, known as the Sudakov form factor, has to be multiplied by the probability found in Equation 3.11, resulting in

$$d\mathcal{P}_{a \rightarrow bc} = \frac{\alpha_s}{2\pi} \frac{dQ^2}{Q^2} P_{a \rightarrow bc}(z) dz \exp\left(- \sum_{b,c} \int_{Q^2}^{Q_{max}^2} \frac{dQ'^2}{Q'^2} \frac{\alpha_s}{2\pi} P_{a \rightarrow bc}(z') dz'\right). \quad (3.12)$$

3.3.3 Hadronisation and decay

When the partons generated by the parton showering process reach an energy of the order of Λ_{QCD} , the procedure breaks down. At lower scales, the procedure is completed by the hadronisation described in this section. All the partons, which carry a colour, will bind with other surrounding partons to form colour-neutral objects, called hadrons. Since perturbative calculations are not suitable at low scales, hadronisation is described by phenomenological models.

The model used in PYTHIA, a general-purpose Monte Carlo generator widely used in CMS, is known as the "Lund string model" [60]. In this model, the potential energy, V , generated on a quark-antiquark pair by the strong field, is proportional to the distance between them, r , like if a string was binding them together. The energy stored can be written as $V(r) = kr$, where k is a constant with value of the order of 1 GeV/fm. If the quarks are pulled apart, the energy increases and might be converted into another quark-antiquark pair. This process is known as "fragmentation" and will occur until all the partons have bound into hadrons. The hadrons created might be short-lived, and their decays are also handled during this stage.

The hadronisation uses a phenomenological model with some free parameters. These parameters are tuned to match the experimental data [61, 62]. In general, this model seems to reproduce the data quite well, but the quality of the prediction depends on the process.

3.3.4 Underlying event

In the hard scattering, the assumption is that only one parton of each proton is colliding. Since the proton is colour-neutral, the "leftovers" of the protons are also carrying a colour-charge after the parton taking place in the hard scattering is removed. This so-called "beam remnant" will also generate a parton shower which will eventually overlap with the partons created by the hard scatter.

Moreover, in some rare cases, two partons of each proton can collide, giving rise to two hard scatterings. This phenomenon is referred to as double parton scattering. The combined effects of the hadronisation of the beam-remnant and the double parton scattering is known as "underlying event". These effects cannot be calculated perturbatively and, once again, a phenomenological model is used.

The parameters of this model were tuned using data from the CDF collaboration [63] at the Tevatron accelerator. Then, the value of the parameters was adjusted using data

provided by the LHC experiments and the agreement between data and simulation was shown to be good [64]. In Chapter 5, the $Z2^*$ [62] tune is used, while, mostly because the change of the centre of mass energy, the CUETP8M1 tune [61] is used in Chapter 7.

3.3.5 Detector simulation

The full event generation chain has been explained in sections 3.3.1 to 3.3.4. The next step is to simulate the interactions of the generated particles with the full CMS detector. This step is handled by the GEANT4 program [65] which includes the geometry of all the detectors and a detailed map of the magnetic field. Effects such as photon radiation through bremsstrahlung, photon conversion into an electron-positron pair, and energy loss due to ionisation with some of the material are all incorporated in this simulation step. The response of all the sub-detectors collecting the information necessary for the reconstruction is also simulated. After the generation and the simulation step, simulated samples are reconstructed with the same algorithms as the data. However, for the simulated samples, not only the reconstructed objects are stored but also the generated objects which do not exist for the data. The comparison of the generated collections with the reconstructed collections provides very crucial information about the reconstruction algorithm performance.

3.3.6 Simulation of the pileup

Finally, the effect of the pileup should be taken into account as well. The particles created by the pileup interaction also deposit energy in the calorimeters and leave tracks in the tracker. In this thesis, the effect of pileup is taken into account by generating additional "minimum-bias" interactions. The effect of the additional particles on the detector response is superimposed with the detector response from the hard scattering. It is quite obvious to note that the number of permutations increases with the number of particles which increases with the number of pileup interactions. As a consequence, the ability of the reconstruction algorithm to disentangle all the particles decreases with the number of pileup interactions. With this consideration, it is important that the simulations have the same pileup distribution as in the data. However the Monte Carlo simulations are typically produced about one year before the data-taking period, and the pileup distribution of the data is hard to estimate accurately until the data-taking period starts. The pileup distribution in the Monte Carlo simulations is estimated to the best of our knowledge and is then corrected to improve the agreement with the data.

3.3.7 Simulating large samples of events

Typically, the simulation of one event can take up to 100 seconds. For Standard Model processes with a large cross-section, a very large amount of events should be simulated in order to match the integrated luminosity of the data. For example, making the sum of all the simulated events as shown in Table 5.4 and Table 5.5, a bit more than 700 million events are simulated which would require roughly two millennia for a single computer. For that reason, a large amount of computers is necessary to simulate all

these events, which is costly. Because many beyond the Standard Model searches share common Standard Model backgrounds, it would be very inefficient if every search group would have to produce their own samples. For that reason, Standard Model samples are centrally produced by physicists of the CMS collaboration and are available for all members of the collaboration who need the samples for their analysis.

3.4 Simulating proton-proton collisions

As discussed in the previous section, to get a full event description, various assumptions or choices have to be made. Depending on the target processes one wants to generate, some assumptions yield more accurate results than others. Quite naturally, multiple Monte Carlo generators emerged concurrently as a consequence. Also, when it is known that Monte Carlo simulation does not reproduce the data perfectly, additional corrections are applied to the simulation in order to increase the agreement with the data.

The list of Monte Carlo generators used in this thesis is discussed in Section 3.4.1. The methods to extract the corrections are described in Section 3.4.2.

3.4.1 Monte Carlo generators

In this section, the list of all the Monte Carlo generators used in this thesis is listed. It contains general purpose Monte Carlo generators as well some programs which are specialised in one part of the generation step and have to be combined with more generic Monte Carlo generators. The Monte Carlo generators used in this thesis are, PYTHIA [66], MADGRAPH [67], POWHEG [68], MC@NLO [69] and TAUOLA [70]. The choice of the samples used in Chapters 5 and 7 is mostly driven by the known accuracy of the generator used to create them. In the case where multiple choices yield similar accuracy, the sample with the largest amount of generated events is preferred.

3.4.2 Monte Carlo corrections

After considerable effort to have as accurate simulations as possible, the Monte Carlo simulation reproduces the data to within few percent. Because this difference will impact the physics result, additional corrections are required. To mitigate the remaining difference, various corrections, referred to as correction factors (CF), are applied to the Standard Model samples. Correction factors are frequently used by CMS collaborators, and dedicated studies are performed to derive them. Typically, they are derived by comparing Monte Carlo simulation from Standard Model processes in well-understood data and are applied to simulated Standard Model processes as well as simulated signal.

3.4.2.1 Pileup correction factors

In order to reduce the time between the data collection and the data analysis, the Monte Carlo samples are frequently produced before the data taking period. The exact evolution of the LHC conditions is impossible to foresee exactly, and so is the instantaneous luminosity. As the number of interactions per bunch crossing increases with the instantaneous luminosity of the LHC, it is expected that the distribution of the number of interactions per bunch crossing will differ between data and Monte Carlo. However, since the detector performance is related to the number of events per bunch crossing, it is important that it is well modelled.

When a given data taking period is over, the simulation is corrected using the estimated true number of interactions of the data. For each Monte Carlo sample, after normalising each distribution to unit area, the correction factor to be applied as a function of the number of interactions per bunch crossing is the ratio of the true data distribution derived from luminosity information to the true number of pileup interactions in the simulation.

3.4.2.2 Lepton correction factors

The method used to derive the correction factors for lepton-related selections is called the “tag and probe” method [71, 72]. The idea of the method relies on the ability to obtain a pure sample of leptons. In $Z \rightarrow ll$ processes, two leptons are produced which invariant mass is close to the mass of the Z -boson. In data, such events are reconstructed with tight identification on one of the leptons (tag) and a looser identification on the other one (probe). Then, the efficiency of the selection of interest is defined as the number of passing probes divided by the number of total probes. In the searches presented in this thesis, only well identified and isolated leptons are selected. These leptons will be further referred to as “good” leptons. Schematically, the selection of good leptons involves three sequential selection, and its efficiency can be factorised as:

$$\varepsilon_{lepton} = \varepsilon_{\text{RECO}} \cdot \varepsilon_{\text{ID/RECO}} \cdot \varepsilon_{\text{ISO/ID}}, \quad (3.13)$$

where $\varepsilon_{\text{RECO}}$ is the reconstruction efficiency, $\varepsilon_{\text{ID/RECO}}$ the identification efficiency for reconstructed leptons, and $\varepsilon_{\text{ISO/ID}}$ the relative isolation (I_{rel}) efficiency for identified (and reconstructed) leptons. These efficiencies are calculated for Monte Carlo and data, and the ratio of these efficiencies defines the correction factors to be used. They are derived as a function of η and p_T , and for each lepton, the global correction factor is the product of all the correction factors.

Statistical tools and analysis strategy

In all science experiments, a hypothesis is tested with respect to another one. In this thesis, the first hypothesis can be formulated as "is the Standard Model compatible with the observation?" and the second "is Displaced Supersymmetry compatible with the observation?". To do so, it is common to use a statistical method that provides numerical information about the validity of both hypotheses.

In Section 4.1, the basic strategy to adopt to be able to provide sensible information about the validity of the two hypotheses is exposed. The statistical tools used in order to do so are shortly reviewed in Section 4.2. Finally, Section 4.3 explains how to convert statistical information into limits on a hypothetical model.

4.1 How to discover new physics?

The total number of events, N , of any process, X , is given by integrating the Equation 2.1 over time, yielding

$$N_X = L_{int} \sigma_X \quad (4.1)$$

where the integrated luminosity, L_{int} , over the time, t , is defined as

$$L_{int} = \int L dt \quad (4.2)$$

In this thesis, the goal is to asses the existence of Displaced Supersymmetry, which predicts the occasional production of a pair of top squarks. It is common to refer to as "signal" the assumed process one wants to discover or constrain while the known standard Standard Model is referred to as "background". Using Equation 4.1, the number of expected signal events, N_s , becomes

$$N_s = L_{int} \sigma_s, \quad (4.3)$$

and the number of expected background events is

$$N_b = L_{int} \sum_i \sigma_b^i = L_{int} \sigma_b^{tot} \quad (4.4)$$

where i runs over all the known Standard Model processes. It is quite intuitive that any signal is more likely to be discovered if the number of expected signal events is

large and the number of background events is small. For the sake of argument, let us introduce the signal over background ratio, s/b ,

$$s/b = \frac{N_s}{N_b} = \frac{\sigma_s}{\sigma_b^{tot}}. \quad (4.5)$$

Typically, this fraction is very small, and in that case, not much can be said about the signal hypothesis. However, one can apply a selection to retain only a fraction of the events and the former equation becomes

$$s/b = \frac{\sigma_s}{\sigma_b^{tot}} \frac{A_s}{A_b}, \quad (4.6)$$

where A stands for the average acceptance and is proportional to the selection efficiency. With this definition, the signal over background ratio can be increased if the cuts applied have a high efficiency for signal and a low efficiency for at least one of the backgrounds so if $A_b \ll A_s$. This can be achieved by applying a cut on a variable that has a very different distribution for background compared to the signal. Such variables are called "discriminating variables". Using a discriminating variable, it is then possible to have a much larger signal over background ratio which renders an analysis more efficient on testing the validity of the existence of a certain signal.

4.2 Statistical tools

The Poisson probability density function describes the number of data events observed in a counting experiment. The probability of observing exactly n occurrences over an interval of time if the average rate, λ , is known and given by:

$$Poisson(n) = \frac{e^{-\lambda} \lambda^n}{n!}. \quad (4.7)$$

In the most simple case, the probability of observing n events while exactly b events are expected is given by the likelihood function

$$L(n|b) = \frac{e^{-b} b^n}{n!}. \quad (4.8)$$

In practice, the uncertainty related to b should be taken into account as well. This is done by adding a set of nuisance parameters, $\vec{\theta}$, where each of the component, θ_j , is related to one of the systematic uncertainty. Hence, the new likelihood function is the product of Poisson distributions:

$$L(n|b) = \frac{e^{-b} b^n}{n!} \prod_j^{N_p} p_j(\tilde{\theta}_j | \theta_j), \quad (4.9)$$

where N_p is the number of nuisance parameters, and $\tilde{\theta}_j$ is the maximum value of the function p_j .

In this thesis, two searches are presented in which a selection is applied to the data, and the event yield is compared to the background expectation. In the case where the number of events in the data is compatible, within the uncertainties, with the expected background, limits are set on the signal. The hypothesis H_0 where the background and signal are assumed is compared to the hypothesis H_1 which corresponds to the background-only hypothesis. The question one wants to answer can be formulated as "Given the observed number of events, the expected number of background events, and the uncertainty attached to these numbers, how likely is it for the signal to exist? This answer is typically given using the signal strength, μ , which quantifies by which number the assumed cross-section of the signal should be multiplied to match the observation. A signal strength of $\mu = 0$ corresponds to the background-only hypothesis and a signal strength of $\mu = 1$ corresponds to the nominal signal hypothesis. To do so, a test statistic is introduced using the previously defined likelihood function.

Firstly, two likelihood functions are introduced. The "maximum likelihood function", $L(\hat{\mu}, \hat{\theta})$, is used to find the values of the nuisance parameters, θ_j , and the signal strength, μ that maximise its value when both are fitted simultaneously. Now, the "conditional maximum likelihood" function, $L(\mu, \hat{\theta}(\mu))$, is also used to find the values of θ_j and μ that maximise its value but when a certain value of μ is assumed and fixed. The "profile likelihood ratio", $\lambda(\mu)$, is defined as the ratio of the two likelihood functions as

$$\lambda(\mu) = \frac{L(\hat{\mu}, \hat{\theta})}{L(\mu, \hat{\theta}(\mu))}, \quad (4.10)$$

and depends on the parameters of interest, μ .

4.3 Limit setting

When no excess over the background prediction is observed, limits on the assumed signal can be set. Typically, one-sided limits on the signal strength are set using the test statistic, q_μ , defined as:

$$q_\mu = \begin{cases} -2 \ln \lambda(\mu) & \hat{\mu} \leq \mu \\ 0 & \mu < \hat{\mu} \end{cases}$$

The probability density function, f , of the test statistic can be evaluated for both hypotheses, $f(q_\mu|H_0)$ and $f(q_\mu|H_1)$, for instance by generating MC pseudo-data. Alternatively, it was shown that the generation of a large amount of pseudo-experiments could be avoided by using asymptotic formulae [73] to approximate the probability density function of q_μ .

The p-value defines the fraction of cases that are more extreme than the observed one and hence indicate the compatibility of an hypothesis with the observation. For example, the p-value of the hypothesis H_0 is defined as:

$$p_{H_0} = P(q_\mu^{obs} < q_\mu|H_0) = \int_{q_\mu^{obs}}^{\infty} f(q_\mu|H_0) dq_\mu. \quad (4.11)$$

A low p-value indicates poor compatibility between the hypothesis and the observation. Finally, the confidence level value, CLs [74], compares the p-value of both hypotheses simultaneously and is defined as,

$$CLs = \frac{p_{H_0}}{1 - p_{H_1}}. \quad (4.12)$$

The H_0 hypothesis is excluded at $1-\alpha$ confidence level if the observed CLs is lower or equal to α . In this thesis, $\alpha = 0.05$ is used so 95% confidence level limits are set. This value is commonly chosen in particle physics and picking the same value will allow this work to be compared to other measurements. An expected exclusion limit can also be defined by considering the median of the H_1 hypothesis only. Uncertainty bands of -2, -1, +1, and +2 standard deviation can also be attached to the expected exclusion limit by considering the 5%, 32%, 68%, and 95% quantiles of the H_1 hypothesis.

4.4 Analysis strategy

Before starting a search, one has to figure out if it has a good discovery potential. As already hinted previously, a search has a good discovery potential, or "sensitivity", if the signal can be clearly distinguished from all sources of background. In the current case, as already discussed in 1.3, the most striking feature of the signal is the fact that the particles emerging from the decay of the sparticles should be displaced with respect to the collision point. The selection applied in the following searches will rely upon this feature. However other criteria have to be taken into account when designing a new search, such as potential overlap with other searches and the simplicity of the objects used in the selection. With these considerations, a first search is presented in Chapter 5 in which one displaced electron and one displaced muon are selected. Requiring that the leptons do not have the same flavour reduces the signal acceptance, but it should affect more substantially the a priori unknown background contribution from Drell-Yan¹ processes in which the two leptons do have the same flavour. In Chapter 7, the search is extended to same-flavour leptons final states. The addition of same-flavour states does not only complement the opposite-flavour state analysis, but it also provides sensitivity to a wider range of beyond the Standard Model models.

¹At high energy, a process in which a photon decays into a pair of opposite sign leptons is indistinguishable from a process in which a Z -boson decays into a pair of opposite sign leptons. The Drell-Yan process is the name of the process that encapsulates both possible decays.

Search for Displaced Supersymmetry in events with an electron and a muon with large impact parameters at 8 TeV

For decades, the Standard Model has been describing the particles and their interactions with huge success and accuracy. Nevertheless, as described in chapter 1.1.3, the Standard Model has its shortcomings, and it is believed to be a low-energy effective theory. Many extensions to the Standard Model are being investigated, and Supersymmetry is probably one of the most famous of them. While a broad range of supersymmetric searches have been conducted by the ATLAS and the CMS collaborations, some sets of models have been neglected. In 2014, models in which the lightest supersymmetric particle has a lifetime that would produce a macroscopic displacement of its potential child particle were almost unconstrained. In this chapter, a search for new physics in events with one electron and one muon whose trajectory are displaced from the interaction region is presented. This search uses a data sample obtained from proton-proton collisions at a centre of mass energy of 8 TeV, hereafter referred to as the Displaced $e\mu$ search at 8 TeV, and was published in the journal Physical Review Letters [1]. Limits on a specific model of the Displaced Supersymmetry scenario are set, but the selection has been purposefully designed to retain sensitivity to a wide range of beyond the Standard Model models with displaced particles, which will be exploited in Chapter 6.

In Section 5.1, basic information on the list of samples used for this search is given. The correction factors (CF) applied in this search are explained in Section 5.2. The selection of the events is described in Section 5.3. The background estimation methods are explained in Section 5.4. In Section 5.5, the list of all systematic uncertainties taken into account in this search is given. Finally, the results are presented in Section 5.6.

5.1 Data and Monte Carlo simulation samples

Following the argumentation given in Section 4.1, the list of all the samples can be divided into three categories, data, signal and background. Then, the data has to be compared with the background only hypothesis as well as the background plus signal hypothesis. The background samples and the signal samples are produced by Monte Carlo simulation as explained in sections 3.3 and 3.4.

The data samples used are described in Section 5.1.1, the Standard Model background samples are listed in Section 5.1.2, and the signal samples are exposed in Section 5.1.3.

5.1.1 Data samples

This analysis uses proton-proton collisions data collected in 2012 at $\sqrt{s} = 8$ TeV, corresponding to an integrated luminosity of $19.7 \pm 0.5 \text{ fb}^{-1}$. The search is done using the dataset that requires one muon and one electron or photon which will henceforth be referred to as the MuEG dataset. Background estimation and other cross-checks are performed using datasets requiring one electron (**SingleElectron**), one muon (**SingleMu**), two electrons (**DoubleElectron**), and two muons (**DoubleMu**). All the data used in the following analysis were reconstructed with the same software version and using the latest calibrations available. The integrated luminosity of these datasets, as well as their main purpose, are summarised in Table 5.1.

Table 5.1: List of data samples used for the analysis. The **MuEG** dataset is used for discovery purposes, the **SingleElectron** and the **SingleMu** datasets are used in order to determine the properties of the QCD in control regions, and the **DoubleElectron** and **DoubleMu** datasets are used to check the accuracy of the correction factors of the leptons.

Dataset	Integrated luminosity (fb^{-1})	Purpose
/MuEG/Run2012A-22Jan2013-v1/AOD	0.87	
/MuEG/Run2012B-22Jan2013-v1/AOD	4.41	
/MuEG/Run2012C-22Jan2013-v1/AOD	7.04	
/MuEG/Run2012D-22Jan2013-v1/AOD	7.33	
MuEG	19.7	discovery
/SingleElectron/Run2012A-22Jan2013-v1/AOD	0.88	
/SingleElectron/Run2012B-22Jan2013-v1/AOD	4.25	
/SingleElectron/Run2012C-22Jan2013-v1/AOD	6.77	
/SingleElectron/Run2012D-22Jan2013-v1/AOD	7.19	
SingleElectron	19.1	QCD cross check
/DoubleElectron/Run2012A-22Jan2013-v1/AOD	0.88	
/DoubleElectron/Run2012B-22Jan2013-v1/AOD	4.29	
/DoubleElectron/Run2012C-22Jan2013-v1/AOD	6.94	
/DoubleElectron/Run2012D-22Jan2013-v1/AOD	7.23	
DoubleElectron	19.3	electron CF
/SingleMu/Run2012A-22Jan2013-v1/AOD	0.87	
/SingleMu/Run2012B-22Jan2013-v1/AOD	4.39	
/SingleMu/Run2012C-22Jan2013-v1/AOD	6.79	
/SingleMu/Run2012D-22Jan2013-v1/AOD	7.27	
SingleMu	19.3	QCD cross check
/DoubleMuParked/Run2012A-22Jan2013-v1/AOD	0.88	
/DoubleMuParked/Run2012B-22Jan2013-v1/AOD	4.41	
/DoubleMuParked/Run2012C-22Jan2013-v1/AOD	6.77	
/DoubleMuParked/Run2012D-22Jan2013-v1/AOD	7.37	
DoubleMu	19.4	muon CF

5.1.2 Standard Model background from simulation

To find potential discrepancies which might be hints of new physics, the observed data must be compared to the expected background, which is created by the Standard Model processes. In practice, the Monte Carlo samples are split depending on the physics process at stake. The reason is that, depending on the search and the final states of interest, some processes do not contribute and are hence not necessary to process. All the backgrounds that can produce an event with exactly one electron and one muon in the final state are considered. This includes samples where there is actually only one genuine lepton and one fake lepton. The samples are grouped into two main subgroups, referred to as QCD samples in Table 5.2 and non-QCD samples in Table 5.3. Furthermore, it is often convenient to group related samples together within the same "composite dataset" name. Tables 5.4 and 5.5 exhibit the list of the composite dataset names used in this analysis with the colour used to depict them in the figures of this chapter, the list of the individual dataset names composing them, the number of events generated, the cross-section, and the event weight to be applied in order to match the integrated luminosity of the data. For a given process, X , the event weight, w , has a value such that the following equation holds.

$$N_X = w_X N_X^{gen} \quad (5.1)$$

Inserting Equation 5.1 in Equation 4.1, one gets,

$$w_X = \frac{L_{int} \sigma_X}{N_X^{gen}}. \quad (5.2)$$

Inspecting this equation, one can deduce that the event weight is proportional to the total integrated luminosity and the cross-section of its process and inversely proportional to the number of simulated events. Obviously, the uncertainty on the number of expected events of a given background is proportional to the event weight so that one wants to get the event weight as low as possible. Since the total integrated luminosity is fixed by the experiment, it means that, in order to keep an event weight as low as possible, the number of simulated events should be large for a process with a large cross-section. However, as already mentioned in 3.3.5, the simulation of an event is time-consuming, and processes with large cross-sections require that a very large amount of events are simulated to have a low event weight, which is not always feasible. As it can be seen in Table 5.4, the event weight of QCD samples is typically very large which means that a very large uncertainty is attached to the background expectation for these samples.

Table 5.2: Dataset names for simulated samples used to model multi-jet events.

Individual Dataset Nickname	Individual Dataset Source Name
<i>EM QCD</i> p_T 20 – 30	QCD_Pt_20_30_EMEnriched*_pythia6_***-v1_AODSIM
<i>EM QCD</i> p_T 30 – 80	QCD_Pt_30_80_EMEnriched*_pythia6_***-v1_AODSIM
<i>EM QCD</i> p_T 80 – 170	QCD_Pt_80_170_EMEnriched*_pythia6_***-v1_AODSIM
<i>EM QCD</i> p_T 170 – 250	QCD_Pt_170_250_EMEnriched*_pythia6_***-v1_AODSIM
<i>EM QCD</i> p_T 250 – 350	QCD_Pt_250_350_EMEnriched*_pythia6_***-v1_AODSIM
<i>EM QCD</i> p_T 350 – ∞	QCD_Pt_350_EMEnriched*_pythia6_***-v1_AODSIM
<i>BCtoE QCD</i> p_T 20 – 30	QCD_Pt_20_30_BCtoE*_pythia6_***-v1_AODSIM
<i>BCtoE QCD</i> p_T 30 – 80	QCD_Pt_30_80_BCtoE*_pythia6_***-v1_AODSIM
<i>BCtoE QCD</i> p_T 80 – 170	QCD_Pt_80_170_BCtoE*_pythia6_***-v1_AODSIM
<i>BCtoE QCD</i> p_T 170 – 250	QCD_Pt_170_250_BCtoE*_pythia6_***-v1_AODSIM
<i>BCtoE QCD</i> p_T 250 – 350	QCD_Pt_250_350_BCtoE*_pythia6_***-v1_AODSIM
<i>BCtoE QCD</i> p_T 350 – ∞	QCD_Pt_350_BCtoE*_pythia6_***-v2_AODSIM
μ <i>QCD</i> p_T 20 – 30	QCD_Pt-20to30_MuEnrichedPt5*_pythia6_***-v1_AODSIM
μ <i>QCD</i> p_T 30 – 50	QCD_Pt-30to50_MuEnrichedPt5*_pythia6_***-v1_AODSIM
μ <i>QCD</i> p_T 50 – 80	QCD_Pt-50to80_MuEnrichedPt5*_pythia6_***-v1_AODSIM
μ <i>QCD</i> p_T 80 – 120	QCD_Pt-80to120_MuEnrichedPt5*_pythia6_***-v1_AODSIM
μ <i>QCD</i> p_T 120 – 170	QCD_Pt-120to170_MuEnrichedPt5*_pythia6_***-v1_AODSIM
μ <i>QCD</i> p_T 170 – 300	QCD_Pt-170to300_MuEnrichedPt5*_pythia6_***-v1_AODSIM
μ <i>QCD</i> p_T 300 – 470	QCD_Pt-300to470_MuEnrichedPt5*_pythia6_***-v1_AODSIM
μ <i>QCD</i> p_T 470 – 600	QCD_Pt-470to600_MuEnrichedPt5*_pythia6_***-v1_AODSIM
μ <i>QCD</i> p_T 600 – 800	QCD_Pt-600to800_MuEnrichedPt5*_pythia6_***-v1_AODSIM
μ <i>QCD</i> p_T 800 – 1000	QCD_Pt-800to1000_MuEnrichedPt5*_pythia6_***-v1_AODSIM
μ <i>QCD</i> p_T 1000 – ∞	QCD_Pt-1000_MuEnrichedPt5*_pythia6_***-v1_AODSIM
<i>B</i> → μ <i>QCD</i> p_T 15 – 30	QCD_pt15to30_bEnriched_MuEnrichedPt14*_pythia6_***-v1_AODSIM
<i>B</i> → μ <i>QCD</i> p_T 30 – 50	QCD_pt30to50_bEnriched_MuEnrichedPt14*_pythia6_***-v1_AODSIM
<i>B</i> → μ <i>QCD</i> p_T 50 – 150	QCD_pt50to150_bEnriched_MuEnrichedPt14*_pythia6_***-v1_AODSIM
<i>B</i> → μ <i>QCD</i> p_T 150 – ∞	QCD_pt150_bEnriched_MuEnrichedPt14*_pythia6_***-v1_AODSIM
<i>B</i> <i>QCD</i> p_T 15 – 30	QCD_Pt-15To30_bEnriched*_pythia6-evtgen_***-v1_AODSIM
<i>B</i> <i>QCD</i> p_T 30 – 50	QCD_Pt-30To50_bEnriched*_pythia6-evtgen_***-v1_AODSIM
<i>B</i> <i>QCD</i> p_T 50 – 150	QCD_Pt-50To150_bEnriched*_pythia6-evtgen_***-v1_AODSIM
<i>B</i> <i>QCD</i> p_T 150 – ∞	QCD_Pt-150_bEnriched*_pythia6-evtgen_***-v1_AODSIM

* TuneZ2star_8TeV

*** Summer12_DR53X-PU_S10_START53_V7A

Table 5.3: Dataset names for simulated samples used to model Standard Model processes other than multi-jet events.

Individual Dataset Nickname	Individual Dataset Source Name
$Z \rightarrow \tau\tau$	DYToTauTau_M-20_CT10_**-powheg-tauola-pythia6_***-v2_AODSIM
$W \rightarrow l\nu$ (0 Jets)	WJetsToLNu_*-madgraph-tarball_***-v2_AODSIM
$W \rightarrow l\nu$ (1 Jet)	W1JetsToLNu_*-madgraph_***-v1_AODSIM
$W \rightarrow l\nu$ (2 Jets)	W2JetsToLNu_*-madgraph_***-v1_AODSIM
$W \rightarrow l\nu$ (3 Jets)	W3JetsToLNu_*-madgraph_***-v1_AODSIM
$W \rightarrow l\nu$ (4 Jets)	W4JetsToLNu_*-madgraph_***-v1_AODSIM
WW	WW_*.pythia6_tauola_***-v1_AODSIM
WZ	WZ_*.pythia6_tauola_***-v1_AODSIM
ZZ	ZZ_*.pythia6_tauola_***-v1_AODSIM
$Z\gamma$	ZG_Inclusive_8TeV-madgraph_v2_***-v1_AODSIM
$W\gamma$	WGToLNuG_*-madgraph-tauola_***-v1_AODSIM
$Z \rightarrow ee$	DYToEE_M-20_CT10_**-powheg-pythia6_***-v1_AODSIM
$Z \rightarrow \mu\mu$	DYToMuMu_M-20_CT10_**-powheg-pythia6_***-v1_AODSIM
t (s - channel)	T_s-channel_*-powheg-tauola_***-v1_AODSIM
t (t - channel)	T_t-channel_*-powheg-tauola_***-v1_AODSIM
t (tW - channel)	T_tW-channel-DR_*-powheg-tauola_***-v1_AODSIM
\bar{t} (s - channel)	Tbar_s-channel_*-powheg-tauola_***-v1_AODSIM
\bar{t} (t - channel)	Tbar_t-channel_*-powheg-tauola_***-v1_AODSIM
\bar{t} (tW - channel)	Tbar_tW-channel-DR_*-powheg-tauola_***-v1_AODSIM
$t\bar{t}$ (hadronic)	TTJets_HadronicMGDecays_8TeV-madgraph_***_ext-v1_AODSIM
$t\bar{t}$ (semi - leptonic)	TTJets_SemiLeptMGDecays_8TeV-madgraph-tauola_***-v1_AODSIM
$t\bar{t}$ (leptonic)	TTJets_FullLeptMGDecays_8TeV-madgraph-tauola_***-v2_AODSIM
* TuneZ2Star_8TeV	
** TuneZ2star_v2_8TeV	
*** Summer12_DR53X-PU_S10_START53_V7A	

Table 5.4: Relevant information for simulated samples used to model QCD multi-jet events. Cross-sections are calculated using leading order diagrams.








Composite Dataset Color	Composite Dataset Nickname	Individual Dataset Nickname	Generated Events	Cross Section (pb)	Weighting Factor for 19.7 fb^{-1}
	<i>electron QCD</i>	<i>EM QCD</i> p_T 20 – 30	35 034 466	2 915 000.0	1 640
		<i>EM QCD</i> p_T 30 – 80	33 071 082	4 616 000.0	2 750
		<i>EM QCD</i> p_T 80 – 170	34 495 358	183 300.0	105
		<i>EM QCD</i> p_T 170 – 250	31 572 364	4 587.0	2.86
		<i>EM QCD</i> p_T 250 – 350	34 385 490	556.8	0.319
		<i>EM QCD</i> p_T 350 – ∞	33 716 597	89.1	0.052
		<i>BCtoE QCD</i> p_T 20 – 30	1 739 931	167 400.0	1 890
		<i>BCtoE QCD</i> p_T 30 – 80	2 047 601	167 000.0	1 610
		<i>BCtoE QCD</i> p_T 80 – 170	1 943 542	12 980.0	131
		<i>BCtoE QCD</i> p_T 170 – 250	1 941 568	632.0	6.41
		<i>BCtoE QCD</i> p_T 250 – 350	2 014 017	103.3	1.01
		<i>BCtoE QCD</i> p_T 350 – ∞	1 927 989	23.92	0.244
	μ QCD	μ QCD p_T 20 – 30	8 456 771	1 866 000.0	4 340
		μ QCD p_T 30 – 50	8 768 369	806 300.0	1 810
		μ QCD p_T 50 – 80	9 321 405	176 200.0	372
		μ QCD p_T 80 – 120	8 870 825	40 450.0	89.7
		μ QCD p_T 120 – 170	8 002 619	7 464.0	18.4
		μ QCD p_T 170 – 300	7 583 138	2 300.0	5.97
		μ QCD p_T 300 – 470	6 915 839	151.8	0.432
		μ QCD p_T 470 – 600	3 715 206	11.8	0.062 5
		μ QCD p_T 600 – 800	4 022 822	2.69	0.013 2
		μ QCD p_T 800 – 1000	3 994 239	0.368 8	0.001 82
		μ QCD p_T 1000 – ∞	3 795 858	0.084 91	0.000 44
	$B \rightarrow \mu$ QCD	$B \rightarrow \mu$ QCD p_T 15 – 30	5 566 351	39 820.0	141
		$B \rightarrow \mu$ QCD p_T 30 – 50	5 003 344	41 400.0	163
		$B \rightarrow \mu$ QCD p_T 50 – 150	4 862 679	22 450.0	90.9
		$B \rightarrow \mu$ QCD p_T 150 – ∞	5 151 090	579.1	2.21
	B QCD	B QCD p_T 15 – 30	4 742 750	63 810 000.0	265 000
		B QCD p_T 30 – 50	4 901 203	5 422 000.0	21 800
		B QCD p_T 50 – 150	2 476 927	894 300.0	7 110
		B QCD p_T 150 – ∞	472 619	8 478.0	353

Table 5.5: Relevant information for simulated samples used to model Standard Model processes other than QCD multi-jet events. Unless noted otherwise, cross-sections are calculated using leading order diagrams. The higher-order cross-sections are tabulated in [75]. The “other EWK” composite dataset is composed of all the samples involving electroweak processes other than $Z \rightarrow \tau\tau$ and processes where at least a top quark (top) is produced.

Composite Dataset Color	Composite Dataset Nickname	Individual Dataset Nickname	Generated Events	Cross Section (pb)	Weighting Factor for 19.7 fb ⁻¹
	$Z \rightarrow \tau\tau$	$Z \rightarrow \tau\tau$	47 883 953	1 966.7 [†]	0.808
		$W \rightarrow l\nu$ (0 <i>Jets</i>)	57 673 265	27 186	9.28
		$W \rightarrow l\nu$ (1 <i>Jet</i>)	23 136 036	6 519.6	5.55
		$W \rightarrow l\nu$ (2 <i>Jets</i>)	34 391 822	2 112.8	1.21
		$W \rightarrow l\nu$ (3 <i>Jets</i>)	15 124 797	626.61	0.815
		$W \rightarrow l\nu$ (4 <i>Jets</i>)	13 363 033	258.37	0.381
	other EWK	WW	9 993 617	56.0*	0.110
		WZ	9 993 251	33.593*	0.066 2
		ZZ	9 792 744	17.0*	0.034 2
		$Z\gamma$	6 320 039	123.9	0.386
		$W\gamma$	4 801 097	461.6	1.89
		$Z \rightarrow ee$	42 457 198	1 966.7 [†]	0.912
		$Z \rightarrow \mu\mu$	47 593 026	1 966.7 [†]	0.813
		t (s – channel)	259 657	3.79**	0.287
	top	t (t – channel)	3 754 544	56.4**	0.296
		t (tW – channel)	496 918	11.1**	0.440
		\bar{t} (s – channel)	139 835	1.76**	0.248
		\bar{t} (t – channel)	1 933 504	30.7**	0.312
		\bar{t} (tW – channel)	492 779	11.1**	0.443
		$t\bar{t}$ (<i>hadronic</i>)	30 545 753	112.32***	0.072 4
		$t\bar{t}$ (<i>semi – leptonic</i>)	24 891 262	107.67***	0.085 1
		$t\bar{t}$ (<i>leptonic</i>)	11 993 263	25.803***	0.042 3

* NLO calculated with MCFM 6.1

** approximate NLO calculated in [76]

*** NNLO calculated in [77]; branching ratios calculated from $W \rightarrow l\nu$ fraction from [78]

[†] NNLO calculated with FEWZ 3.1

5.1.3 Signal process simulation

In this search, samples of the process $pp \rightarrow \tilde{t}_1 \tilde{t}_1^*$, with the top squarks decaying via $\tilde{t}_1 \rightarrow bl$ are used as a benchmark model. These samples were produced using the PYTHIA 8 event generator [79] and it was assumed that the branching fraction for all lepton flavours is the same. This assumption is inspired by Standard Model lepton universality but not all models do not make this assumption. Samples were generated with a top squark mass, $m_{\tilde{t}}$, ranging from 200 GeV to 1200 GeV. In each simulated sample, the width of the top squark was modified, enabling different lifetimes. Five different widths were picked to generate five $\langle c\tau_{\tilde{t}} \rangle$ values ranging from 0.1 cm to 1000 cm. The list of signal samples is summarised in Table 5.6.

Table 5.6: List of signal samples.

Individual Dataset name	Individual Dataset Full Name
$\tilde{t}\tilde{t}$ $M(200) < c\tau > (*)$	DisplacedSUSY_StopToBL_M-200_CTau-*_v†\$_MINIAODSIM
$\tilde{t}\tilde{t}$ $M(300) < c\tau > (*)$	DisplacedSUSY_StopToBL_M-300_CTau-*_v†\$_MINIAODSIM
$\tilde{t}\tilde{t}$ $M(400) < c\tau > (*)$	DisplacedSUSY_StopToBL_M-400_CTau-*_v†\$_MINIAODSIM
$\tilde{t}\tilde{t}$ $M(500) < c\tau > (*)$	DisplacedSUSY_StopToBL_M-500_CTau-*_v†\$_MINIAODSIM
$\tilde{t}\tilde{t}$ $M(600) < c\tau > (*)$	DisplacedSUSY_StopToBL_M-600_CTau-*_v†\$_MINIAODSIM
$\tilde{t}\tilde{t}$ $M(700) < c\tau > (*)$	DisplacedSUSY_StopToBL_M-700_CTau-*_v†\$_MINIAODSIM
$\tilde{t}\tilde{t}$ $M(800) < c\tau > (*)$	DisplacedSUSY_StopToBL_M-800_CTau-*_v†\$_MINIAODSIM
$\tilde{t}\tilde{t}$ $M(900) < c\tau > (*)$	DisplacedSUSY_StopToBL_M-900_CTau-*_v†\$_MINIAODSIM
$\tilde{t}\tilde{t}$ $M(1000) < c\tau > (*)$	DisplacedSUSY_StopToBL_M-1000_CTau-*_v†\$_MINIAODSIM
	†:= PU25nsData2015v1_76X_mcRun2_asymptotic_v12
	\$:= RunIIFall15MiniAODv2
	$< c\tau >$ in cm, either 0.1, 1, 10, 100, or 1000

The production cross-section [80] for each mass hypothesis is given in Table 5.7. For $m_{\tilde{t}} = 200$ GeV the production cross-section of a pair of top squarks is comparable to the very rare process of the production of two W-bosons. For $m_{\tilde{t}} = 1000$ GeV the production cross-section drops by roughly five orders of magnitude as compared to $m_{\tilde{t}} = 200$ GeV. This implies that a very discriminating variable must be found to have a decent signal over background ratio. As discussed already, the most striking feature of the Displaced Supersymmetry is the long lifetime of the top squark. Indeed, particles with long lifetime are not produced by Standard Model processes and a selection related to the lifetime of the produced particles offers an excellent discriminating power between signal and background.

Figure 5.1 shows some generator-level distributions for signal samples with different values of $m_{\tilde{t}}$ and $\langle c\tau_{\tilde{t}} \rangle$. The top figure shows the ϕ distribution of the top squark. Because the physics is independent of this variable, all the samples exhibit a flat distribution. The overall normalisation is proportional to the production cross-section and the samples with higher $m_{\tilde{t}}$ yield lower event count, as expected. In the middle figure,

Table 5.7: Production cross-section of the signal processes for a centre of mass energy of 8 TeV.

Dataset Name	Cross-section (pb ⁻¹)
$\tilde{t}\tilde{t} M(200) < c\tau > (*)$	18.5 ± 2.2
$\tilde{t}\tilde{t} M(300) < c\tau > (*)$	2.00 ± 0.29
$\tilde{t}\tilde{t} M(400) < c\tau > (*)$	0.356 ± 0.051
$\tilde{t}\tilde{t} M(500) < c\tau > (*)$	0.085 ± 0.013
$\tilde{t}\tilde{t} M(600) < c\tau > (*)$	0.0248 ± 0.0041
$\tilde{t}\tilde{t} M(700) < c\tau > (*)$	0.0081 ± 0.0015
$\tilde{t}\tilde{t} M(800) < c\tau > (*)$	0.00289 ± 0.00059
$\tilde{t}\tilde{t} M(900) < c\tau > (*)$	0.00109 ± 0.00026
$\tilde{t}\tilde{t} M(1000) < c\tau > (*)$	0.00043 ± 0.00012

*: $< c\tau >$ in cm, either 0.1, 1, 10, 100, or 1000

one can observe that the peak of the top squark p_T increases with the increase of $m_{\tilde{t}}$. This is also expected since the energy available for the two top squarks is larger when the mass of the top squark increases. Finally, the bottom figures show the distribution of the top squark $c\tau$, which is proportional to the flight distance which is the distance separating the creation vertex of the top squark with its decay one. Using log-scale for the y-axis, the distributions resemble linear functions as expected for falling exponential decay where the slope is given by $-\frac{1}{\langle c\tau_{\tilde{t}} \rangle}$.

However, precise information about the creation vertex of the top squark and its decay is not necessarily available at the reconstructed level. Because the lifetime of the top squark is the most crucial feature of the set of models under investigation in this thesis, a variable that is connected to the flight distance but that is available at reconstructed level is used. The transverse impact parameter, d_0 , defined in Section 3.2.1 will be used as the discriminating variable between signal events and background events. Figure 5.2 is a graphical representation of the d_0 definition. Inspecting this figure, the positive correlation between the lifetime of the top squark and the lepton's d_0 is obvious. Hereafter, d_0 will invariably be used as $|d_0|$. Figure 5.3 illustrates the discriminating power of the leptons' d_0 . Indeed, while the Standard Model backgrounds cluster at small values of d_0 , the signal spreads almost equally in the 2D plane of electron d_0 and muon d_0 . The d_0 variable will play a key role in the selection of the events as will be explained in the next section.

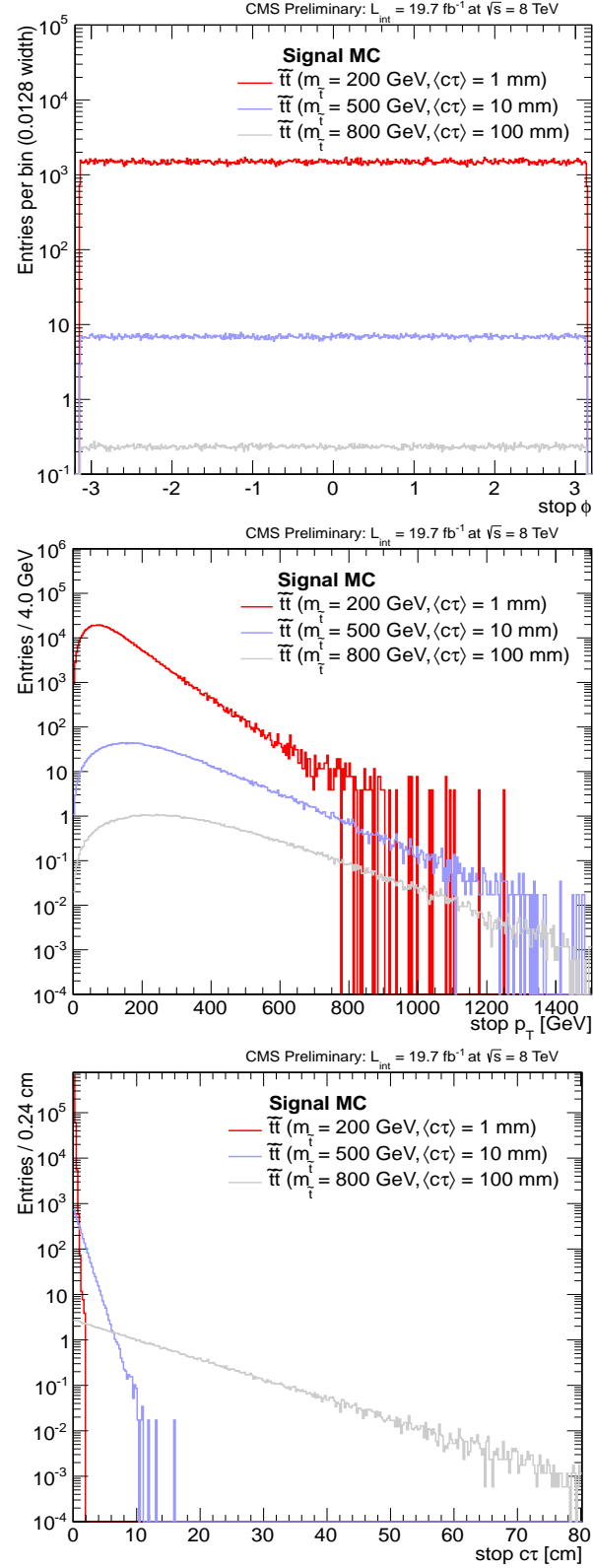


Figure 5.1: Examples of generator-level quantities for the top squarks in three signal samples with different top squark masses and lifetimes.

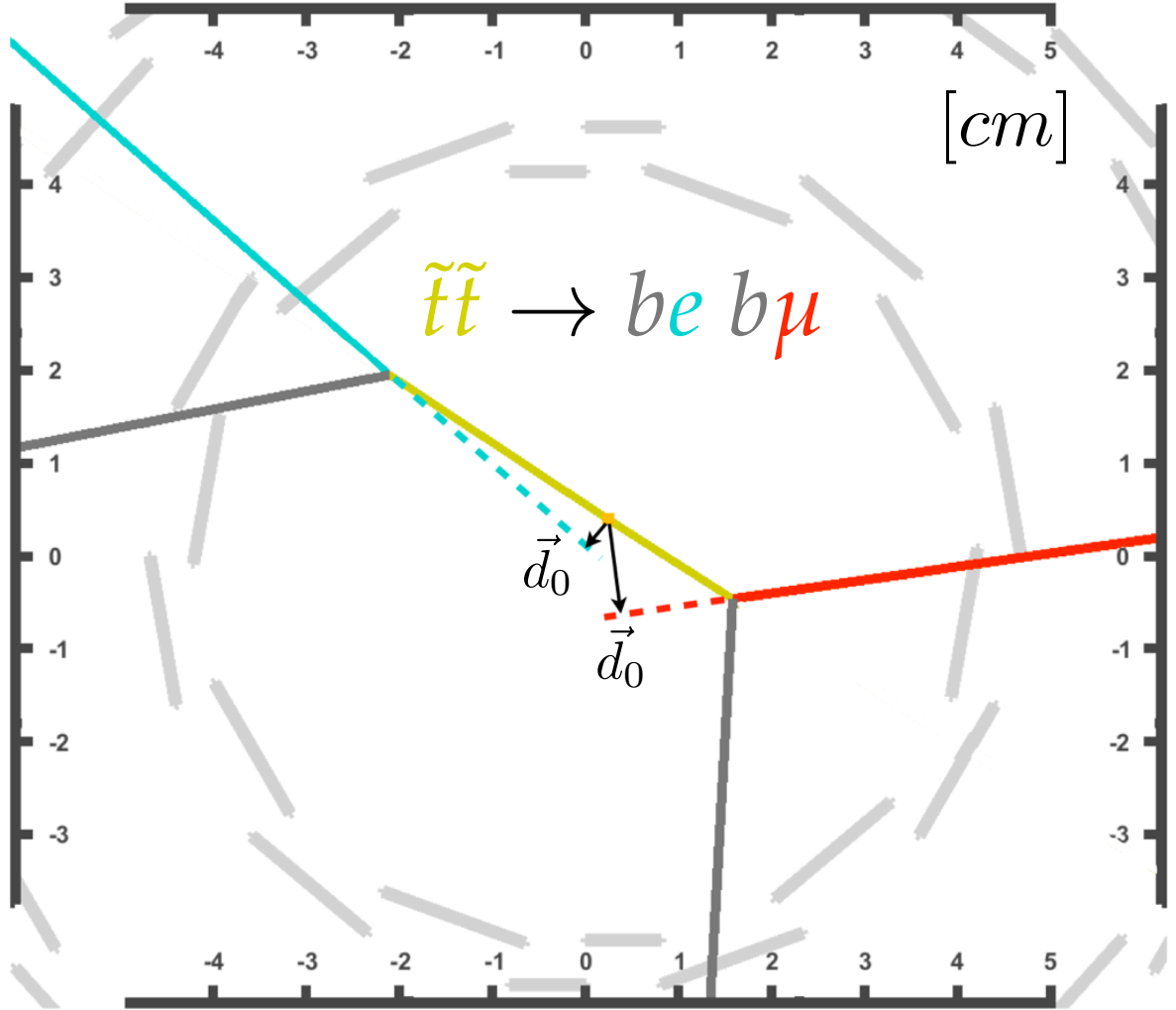


Figure 5.2: Transverse view of the CMS interaction point, showing a typical event from the signal process $\tilde{t}\tilde{t} \rightarrow b b l l$. The definition of the leptons' impact parameters are shown by the black arrows.

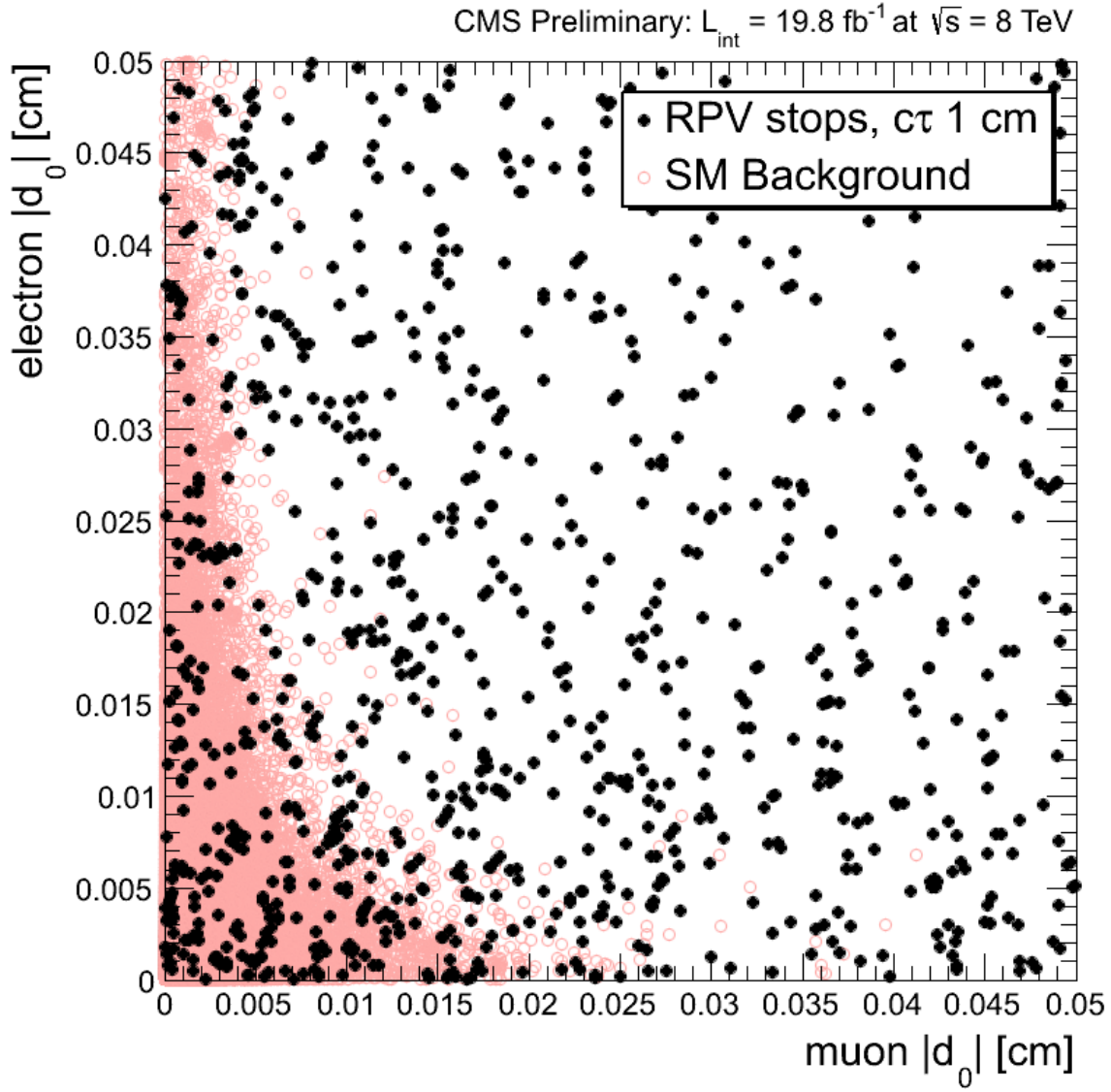


Figure 5.3: Distributions of signal (black solid markers) and background Monte Carlo (open pink markers) in the 2D plane of electron $|d_0|$ versus muon $|d_0|$.

5.2 Corrections to Monte Carlo simulations

In this section, the corrections applied to enhance the Monte Carlo versus data agreement are reviewed. It includes all the correction factors provided by the CMS collaboration described in Section 3.4.2, and correction factors specific to this search.

The correction factors that account for the difference in pileup scenario between Monte Carlo and data will be set out in Section 5.2.1. The muon correction factors are discussed in Section 5.2.2 and the electron correction factors in Section 5.2.3. The trigger correction factor will be shown in Section 5.2.4. Finally, the correction factor related to the displaced tracking efficiency is presented in Section 5.2.5.

5.2.1 Event pileup correction

The method described in Section 3.4.2 is used here. Figure 5.4 compares the distribution of the number of reconstructed vertices in data and Monte Carlo before and after the corrections were applied. Even though some minor disagreements remain, the agreement is significantly improved by the reweighting, validating the technique used. In addition, it was checked that events populating the region where the agreement is the worst have low d_0 . As d_0 is the most discriminating variable of this analysis, it is expected that the residual disagreement will have little to no effect on the final results.

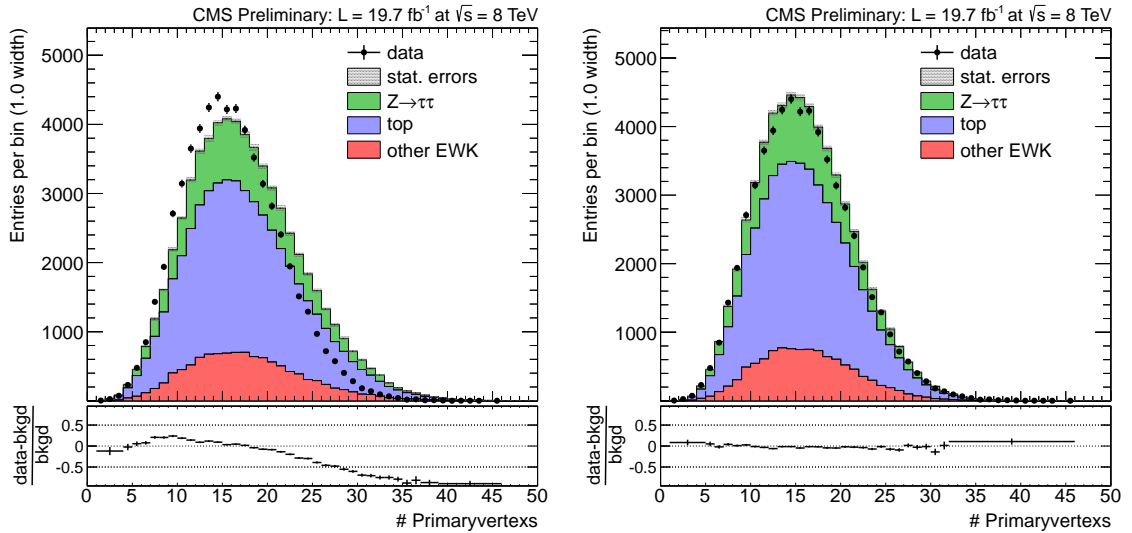


Figure 5.4: The distribution of the number of reconstructed vertices before (left) and after (right) the simulation was corrected to match the data. The data (black dots) is compared to the sum of expected Standard Model backgrounds split into different sources, $Z \rightarrow \tau\tau$ (green), top (blue), and other EWK (red). The grey shaded area represents the statistical and systematic uncertainties on the sum of the MC simulations. In the ratio plots, the bin size is automatically chosen so that the relative uncertainty remains constant in each bin.

5.2.2 Muon reconstruction, identification and isolation corrections

As explained already, the CMS collaboration provides centrally-produced correction factors for the whole collaboration that can be used in the majority of physics analyses. However, in this analysis, the selection of the muons has been slightly modified which implies that the correction factors produced by the CMS collaboration are not suitable for use in this analysis. For this reason, analysis-specific correction factors were derived using the same method as explained in Section 3.4.2 but with the displaced selection used in this thesis.

Using Equation 3.13, the efficiency to select a good muon can be factorised as follows:

$$\varepsilon_{\mu} = \varepsilon_{\text{TRK}} \cdot \varepsilon_{\text{ID/TRK}} \cdot \varepsilon_{\text{ISO/ID}}, \quad (5.3)$$

where ε_{TRK} is the track reconstruction efficiency, $\varepsilon_{\text{ID/TRK}}$ is the identification efficiency for reconstructed muons, and $\varepsilon_{\text{ISO/ID}}$ the isolation efficiency for identified (and reconstructed) muons. The track reconstruction efficiency has been shown to be very close to unity for Monte Carlo and data so that no correction is required to be used. The correction factors for the identification efficiency and the isolation efficiency obtained for the analysis-specific cuts are shown in Figure 5.5. As it can be observed in this figure, all the correction factors are close to one which signifies that the data is well reproduced by the Monte Carlo simulations. In addition, this confirms that the correction factors obtained with the small change in the selection are consistent with the official correction factors [81].

5.2.3 Electron reconstruction, identification and isolation corrections

As for the muons, the selection applied to the electrons is different from the official one. Following the same procedure, the correction factors relevant to the electrons selected by this analysis are computed using the tag and probe method. The relative difference between the values obtained with the correction factors obtained for this analysis and the official ones are shown in Figure 5.6. As it can be observed in this figure, the correction factors are compatible with each other within the uncertainties. The largest relative difference occurs for electrons with p_T between 10 and 20 GeV and with η close to 1.5 and amounts to less than 10%. When the η and/or the p_T of the lepton exceeds the upper range of the correction factor histogram, the value of the closest bin is taken and, its uncertainty is doubled.

5.2.4 Trigger efficiency corrections

The goal of this section is to estimate if the efficiency to pass the analysis trigger is similar for data and Monte Carlo. To do so, a sample containing a muon and a photon is needed. However, to have a sample that is independent of the sample used for the search, the sample used for this study should not be collected by triggers applying a requirement on muons or photons. In addition, as will be explained in the next

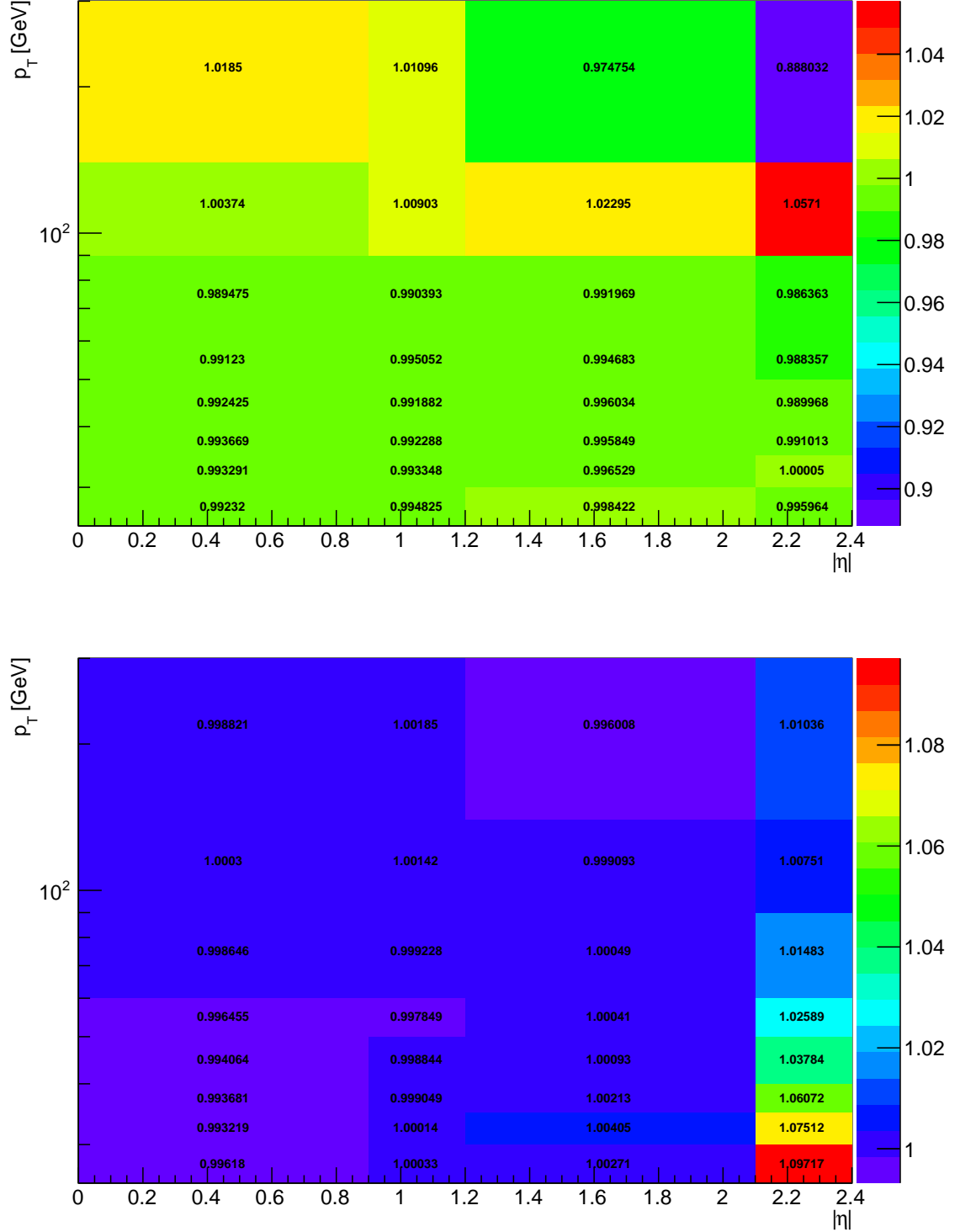


Figure 5.5: Muons correction factors as function of p_T and η for the identification (top) and isolation (bottom) for muons collected using the tag and probe method.

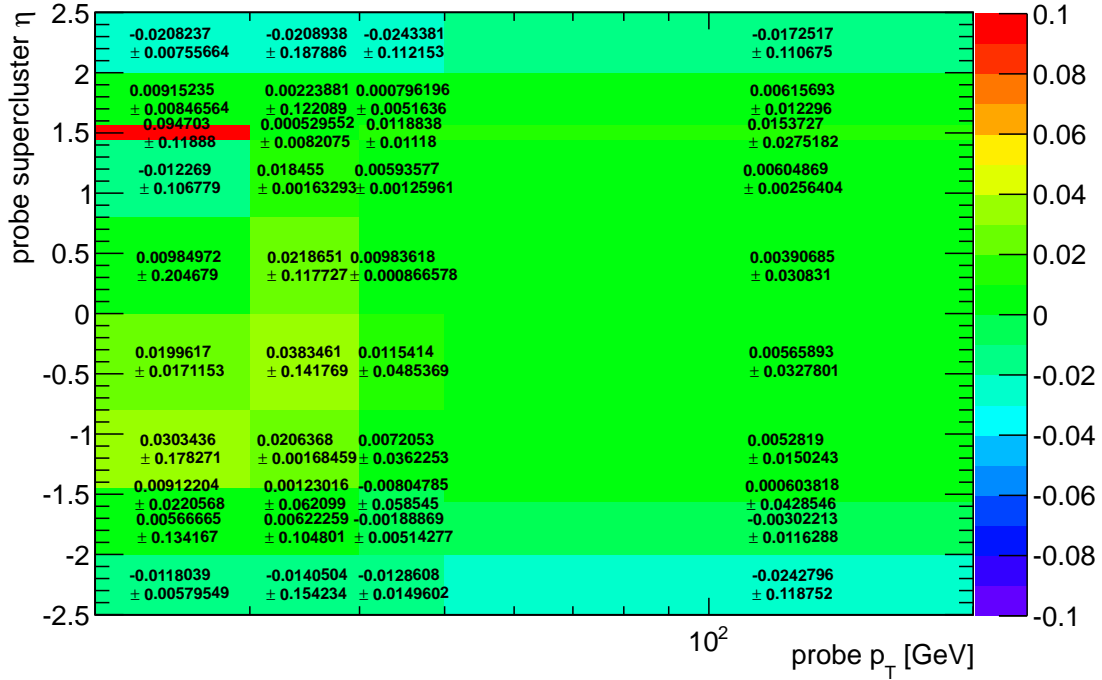


Figure 5.6: Relative difference between the correction factors derived with the modified identification selections and the official correction factors as function of η and p_T .

section, the events coming from QCD processes are estimated from the data, so it is not necessary to derive a correction factor for these events. From Table 5.14, the most dominant background after QCD is given by events coming from processes involving the production of a top quark. For that reason, a $t\bar{t}$ Monte Carlo sample is used and a $t\bar{t}$ enriched selection is applied to the data to enhance the purity of $t\bar{t}$ processes. The leptons in the final state are produced through $t\bar{t} \rightarrow WWb\bar{b}$ where both W bosons decay into a lepton and a neutrino, $W \rightarrow l\nu$. The final state then contains two b-jets and two leptons. The two leptons are selected using the same selection than in the analysis. Additionally, the events are required to contain two jets with $p_T > 30$ GeV and $|\eta| < 2.4$. At least one of the jets should pass the medium CSV b-tag working point (>0.679).

Sometimes, the exact requirement defining a trigger may differ in Monte Carlo and in data. The reason is that Monte Carlo samples are produced before the data taking and that some change in the definition of the trigger can happen in between. To avoid this, only triggers that have not been updated after the Monte Carlo production are used in this study. Furthermore, only triggers that have a high efficiency for $t\bar{t}$ events are used. This includes triggers which make requirements either on a jet or on the E_T^{miss} . The list of the triggers is shown in Table 7.5.

The trigger correction factor is the ratio of the data trigger efficiency to the Monte Carlo trigger efficiency,

$$SF_{trig} = \epsilon_{Data}^{MET/jet} / \epsilon_{MC}^{t\bar{t}}. \quad (5.4)$$

Table 5.8: List of trigger names used in order to select $t\bar{t}$ enriched sample.

Trigger name
HLT_DiCentralJetSumpT100_dPhi05_DiCentralPFJet60_25_PFMET100_HBHENoiseCleaned
HLT_DiCentralPFJet30_PFMET80_BTagCSV07
HLT_MET120_HBHENoiseCleaned

The data trigger efficiency is defined as the number of events passing the $E_T^{\text{miss}}/\text{jet}$ trigger, the preselection and the HLT_Mu22_Photon22_CaloIdL trigger over the number of events that pass the $E_T^{\text{miss}}/\text{jet}$ trigger and the preselection. The Monte Carlo trigger efficiency is defined in the same way but using $t\bar{t}$ events. Using this definition, the trigger correction factor obtained is 0.981 ± 0.004 and is applied to correct the Monte Carlo events.

As an additional sanity check, the trigger efficiencies were also derived as a function of p_T (top), η (middle) and d_0 (bottom) as depicted in Figure 5.7. The data trigger efficiency can be compared with the Monte Carlo $t\bar{t}$ events and for some signal samples. A good agreement is observed in all six graphs over the whole range of the variables of interest.

Moreover, using Equation 5.4, the correction factors were derived as a function of the lepton p_T . Figure 5.8 displays the p_T dependent correction factors. The parameter extracted from a straight line χ^2 fit is consistent with the single correction factor previously derived. Because there is no obvious dependency of the correction factor with respect to the variables tested, the single correction factor value of 0.981 ± 0.004 is used.

5.2.5 Tracking efficiency corrections

In this section, the goal is to try to estimate how well the simulation models displaced tracks. The CMS tracking system has been optimised to reconstruct prompt leptons, $d_0 < 0.02$ cm. In this analysis, the focus is placed on displaced leptons, and it is worth checking how well the tracking efficiency is simulated for such particles. To do so, a very similar technique as the one explained in [82] is used which is briefly explained hereafter. The same software and samples were used, but the d_0 range has been modified to $0.02 < d_0 < 2.0$ cm so that it matches the definition of the signal regions of this analysis. To get genuinely displaced leptons, events from good cosmic runs, collected in summer 2012 for the data are used. A dedicated sample of cosmic rays was used for the Monte Carlo. As the reconstruction algorithm is designed to reconstruct events occurring from a proton-proton collision, the beginning of a track is assumed to come close to the interaction point. This implies that a cosmic muon traversing the whole detector should produce two different tracks. Two standalone muons will eventually be combined by the “cosmic1LegMuon” algorithm in a single cosmic muon event. To calculate the tracking efficiency, the number of reconstructed tracker tracks is divided by twice the number of cosmic muons, as each muon should produce two different tracks. Figure 5.9 shows the track finding efficiency for data

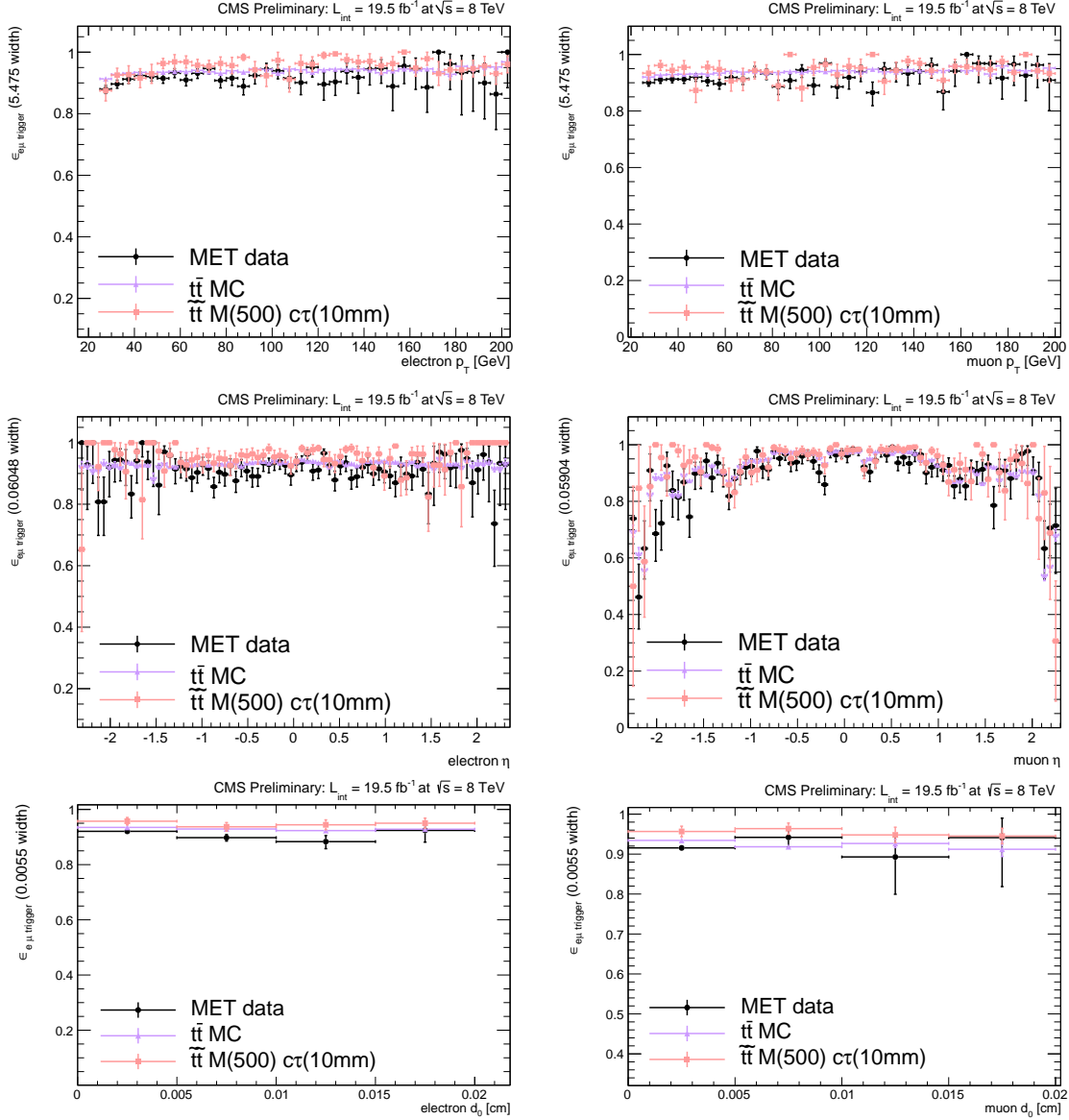


Figure 5.7: Trigger Efficiency as a function of the p_T (top), η (middle) and d_0 (bottom) for electrons (left) and muons (right) for the data (black), $t\bar{t}$ Monte Carlo (purple), and signal Monte Carlo (red).

and Monte Carlo, as well as the ratio SF_{trk} of these efficiencies. For that range, a very similar behaviour for the tracking efficiency in Monte Carlo and data is observed. Since no clear dependence on d_0 is seen, a single correction factor is used for $0.02 < d_0 < 2.0$ cm to correct the Monte Carlo. This correction factor is measured to be 0.960 ± 0.014 .

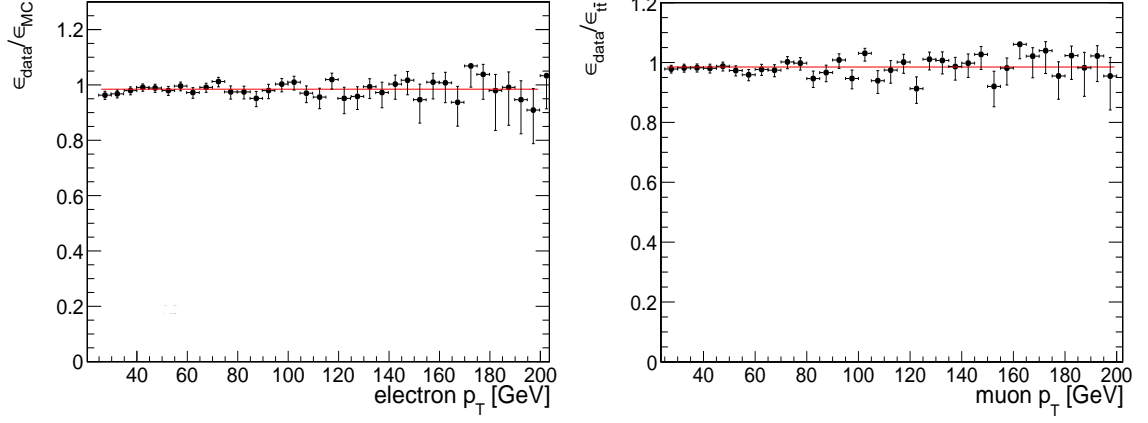


Figure 5.8: Correction factors as a function of the p_T , for electrons (left) and muons (right). The straight line represents the fit to the trigger correction factors.

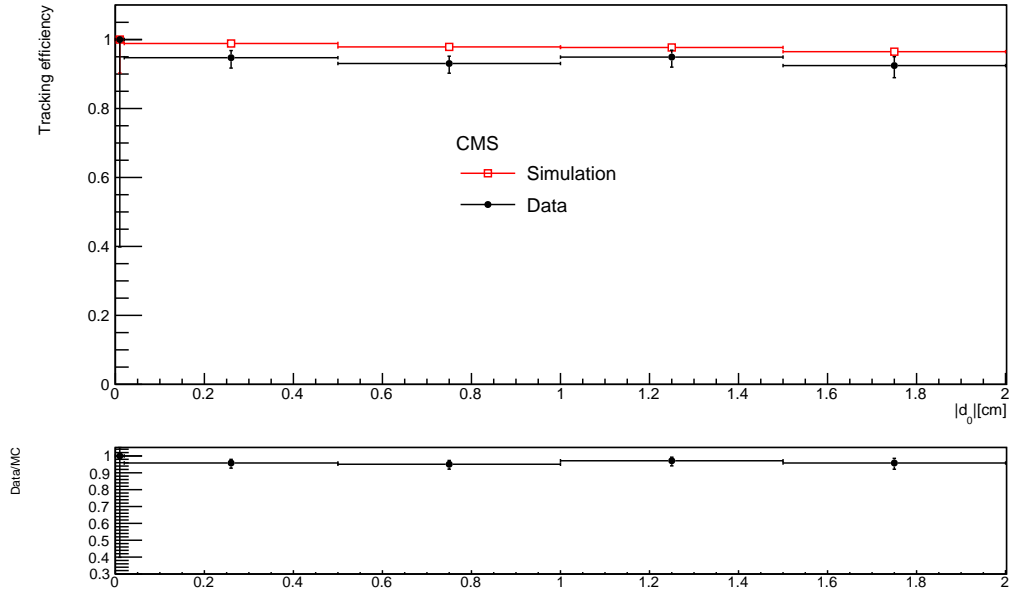


Figure 5.9: Track-finding efficiency when a cosmic ray muon has been reconstructed for data (black) and Monte Carlo (red). The first d_0 bin extends from 0-200 μm . The bottom shows the ratio of data to Monte Carlo which corresponds to the SF_{trk} .

5.3 Event selection and definition of control and signal regions

The event selection of this analysis can be divided into two stages. Firstly, events should contain exactly one well identified and isolated electron and muon in the final state. After this stage, hereafter referred to as the "preselection", the number of events should still be large enough to allow some simulation versus data comparison. The second stage, applied on top of the first stage, categorises each event depending on the lepton d_0 of the events. By doing so, multiple regions are defined, all designed for a specific purpose which will be detailed in this section. Table 5.9 summarises the list of all the regions defined in this analysis. It contains a short description, the name, the list of requirement, the purpose and the section in which these regions are described.

Table 5.9: List of all the regions defined in this analysis. Each line contains a short description, the name, the list of requirements, the purpose and the section of description of the corresponding region.

description	name	selection	purpose	section
prompt lepton control region	PCR	preselection and $d_0 < 0.01$ cm	checks the normalisation and accuracy of MC simulation	5.3.2
displaced control region	DCR	preselection and $0.01 < d_0$ $d_{01} < 0.02$ cm	gets the normalisation of the QCD for the data-driven method	5.3.3
hybrid control regions	HCRs	preselection and $0.02 < d_{01}$ $d_{02} < 0.01$ cm	validates contribution from QCD processes in half displaced region	5.3.4
signal regions	SRs	preselection and 0.02 cm $< d_0$	signal enriched region, split in three sub-regions	5.3.5
$Z \rightarrow \tau\tau$ enriched control region	$Z \rightarrow \tau\tau$	preselection and $Z \rightarrow \tau\tau$ enriching cuts	validates MC in region mostly depleted of background from QCD processes	5.4.2

The preselection cuts are set out in Section 5.3.1. The "prompt control region" (PCR) aims to check the Monte Carlo versus data agreement and is outlined in Section 5.3.2. The "displaced control region" (DCR) has been designed to estimate the contribution of QCD and is explained in Section 5.3.3. The QCD estimation method

is validated in a control region where one lepton is prompt and one is displaced. This region will be referred to as the "hybrid control region" (HCR), and is discussed in Section 5.3.4. Finally, Section 5.3.5 details the definition of the three signal regions (SRs) used in this analysis. Figure 5.10 shows a schematic representation of all the regions using the preselection.

Prompt Control Region (PCR):

2 Good leptons with both d_0 in $[0; 0.01]$ cm
 $\Delta R(\text{lepton1}, \text{lepton2}) > 0.5$; $q_1 \cdot q_2 = -1$

Hybrid Control Region (HCR):

2 Good leptons with one d_0 in $[0.01; 2]$ cm
and one d_0 in $[0; 0.02]$ cm
 $\Delta R(\text{lepton1}, \text{lepton2}) > 0.5$; $q_1 \cdot q_2 = -1$

Displaced Control Region (DCR):

2 Good leptons with both $d_0 > 0.01$ cm but at
least one $d_0 < 0.02$ cm
 $\Delta R(\text{lepton1}, \text{lepton2}) > 0.5$; $q_1 \cdot q_2 = -1$

Signal Region (SR):

2 Good leptons with both d_0 in $[0.02; 2]$ cm
 $\Delta R(\text{lepton1}, \text{lepton2}) > 0.5$; $q_1 \cdot q_2 = -1$

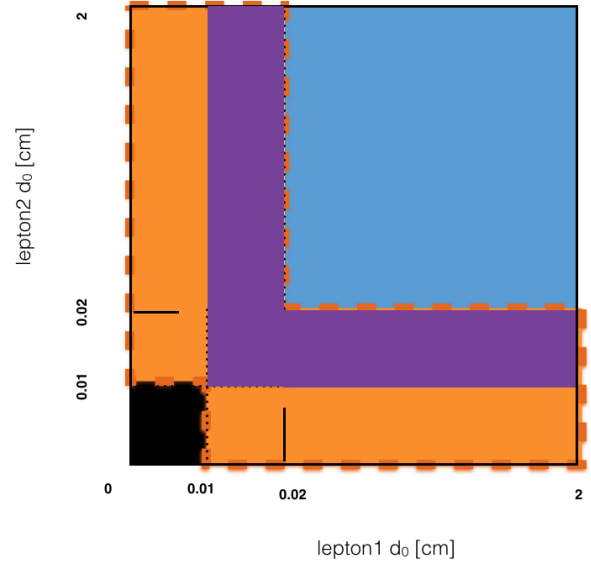


Figure 5.10: Schematic of various regions defined in the 2D plane of the leptons' d_0 after the standard preselection. Because the hybrid control region overlaps with displaced control region, the edges of the former are drawn explicitly.

5.3.1 Preselection

All the events are required to be selected by a trigger. The trigger used is the HLT_Mu22_Photon22_CaloIdL trigger. This trigger requires the presence of a muon and a photon both with $p_T > 22$ GeV. Requiring the event to pass a photon trigger instead of an electron trigger significantly increases our sensitivity to displaced electrons because of the tighter requirement on the electron's track in electron trigger. The efficiency to pass this trigger for signal events that passed the preselection is shown in Figure 5.11. All the samples have an almost constant trigger efficiency of about 95%. A more detailed trigger study, where efficiencies are derived as a function of p_T and d_0 , is presented in Section 5.2.4.

The goal of the preselection is to select events with exactly one electron and one muon, all of which are well identified and well isolated. These leptons are reconstructed with the standard particle flow algorithm as explained in 3.2.2. To be within the CMS tracker acceptance, leptons are required to have their $|\eta|$ smaller than 2.5. A requirement of $p_T > 25$ GeV is applied to ensure that the leptons transverse momentum is above the trigger threshold.

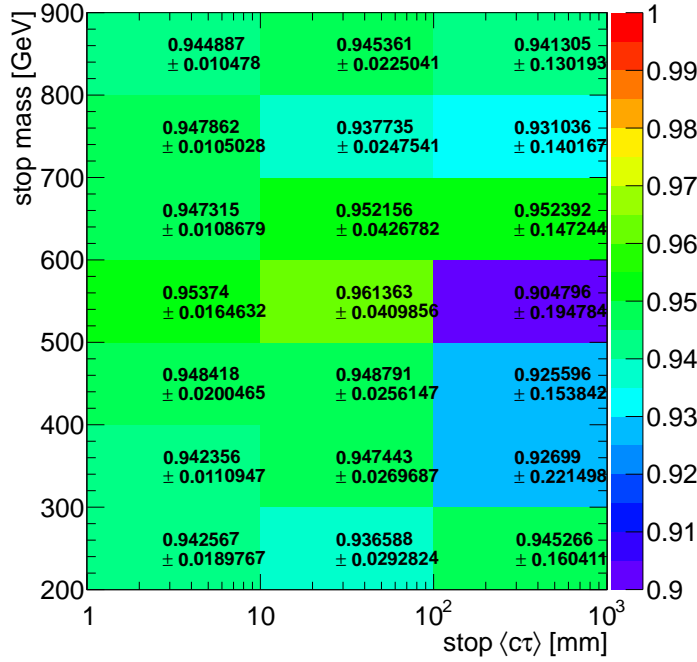


Figure 5.11: Trigger efficiencies in signal Monte Carlo for events passing the preselection.

In this analysis, the identification (ID) of the electron is performed using a boosted decision tree (BDT). The general idea of a BDT is to combine multiple variables into a single variable, called the discriminant. The interested reader can find more details on BDT [83]. In this case, informations about the tracking and the shower-shape are used, as well as some kinematic and geometrical matching between the electron track and its supercluster. In this search, the "non-triggering" BDT was used as it was designed to retain a good efficiency for electrons with large impact parameter. The selection to be applied to the electron candidate depends on its $|\eta|$, and the used values are shown in Table 5.10. For the isolation, the cone size used is 0.3 around the electron, and the I_{rel} should be smaller than 0.1 which corresponds to the tight working point.

Table 5.10: The requirements made on the output of the electron identification BDT.

Electron $ \eta $	Discriminant Value
0 – 0.8	> -0.34
0.8 – 1.479	> -0.65
1.479 – 2.5	> 0.60

As the official muon identification selection includes cuts on the d_0 and the d_z , the selection was modified by removing these cuts. Table 5.11 displays the cuts used to identify a muon in this analysis. A muon is isolated if I_{rel} , using a cone of 0.4 around

Table 5.11: Selections applied in the analysis for the muon identification after the removal of the cuts on $|d_0| < 2$ mm and $|d_z| < 5$ mm.

Selection Description
passes global muon reconstruction
$\chi^2/\text{ndof} < 10$ for the track fit
at least one muon chamber hit included in the track fit
muon segments in at least two muon stations
at least one pixel hit in the tracker
at least six tracker layers with hits

the muon, is smaller than 0.12 corresponding to the official tight working point.

For both leptons, the efficiency to be reconstructed and selected as a function of the generated lepton's d_0 becomes very small for a d_0 of about 2 cm, as can be seen in Figure 5.12. Figure 5.13 displays the same efficiencies when a reconstructed lepton can be found close to the generated lepton. By doing so, the only difference between these two figures lies in the reconstruction efficiency so that one can conclude that the shape of the full selection efficiency is dominated by the performance of the reconstruction which, in turn, is driven by the track finding efficiency. More specifically, the list of tracks is composed of all the different seed iterations. As already discussed in Section 3.2.1, the different seed iterations require a different selection on the d_0 variable. As it can be seen in Table 3.2, the first three seed iterations require the d_0 variable to be smaller than 0.2 cm, the fourth seed iteration requires $d_0 < 1.2$ cm and the fifth seed iteration selects only tracks with d_0 smaller than 2 cm. These values correspond to the efficiency drops observed in Figure 5.12.

For the muons and the electrons, the full efficiency is almost negligible for d_0 larger than 2 cm. These efficiency drops are attributed to an explicit cut at the trigger level in the muon case, and a low track reconstruction efficiency in the electron case. For these reasons, the search is limited to leptons with $d_0 < 2$ cm and an explicit cut at this value is applied. Note that other searches [84–86] are focusing on much more displaced signatures so to be complementary and avoid duplication, this analysis aims to be sensitive to moderate lifetimes that are also what is predicted by Displaced Supersymmetry.

At the top of the standard isolation, the leptons are required to not be near any jet. Jets of $p_T > 10$ GeV are considered and leptons should not lie within a cone of $\Delta R < 0.5$. This additional cut is necessary to reject rare events in which leptons from B and D mesons are wrongly isolated due to a feature of the pileup correction algorithm used to calculate I_{rel} . In this algorithm, the energy within a cone around the lepton is added, but the energy of the particles that can be attributed to pileup events is removed.

The electron and the muon of the events are required to be separated by $\Delta R > 0.5$ and to have opposite charge. The list of all cuts that correspond to the analysis preselection is summarised in Tables 5.12 and 5.13.

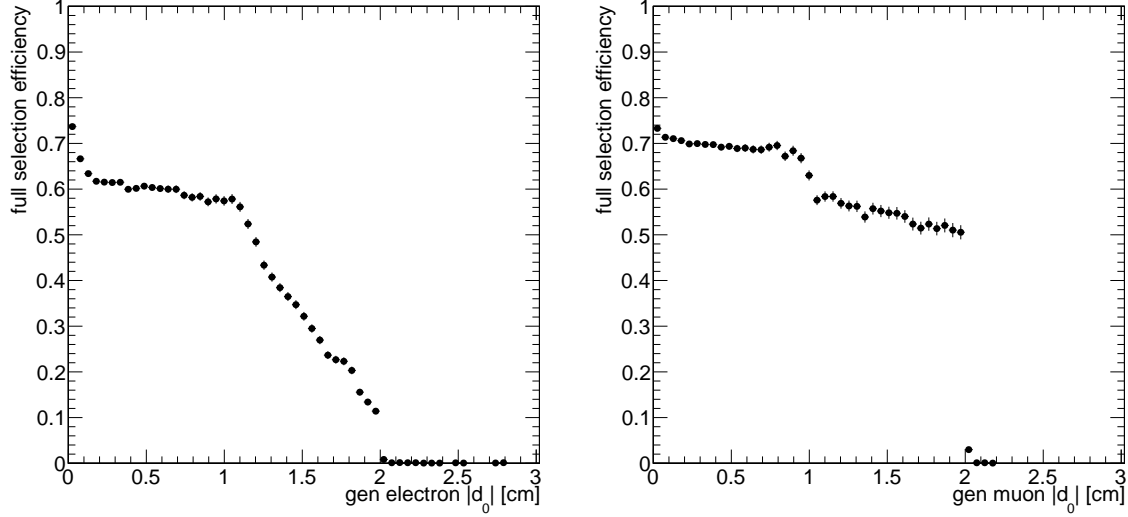


Figure 5.12: Full efficiencies as a function of $|d_0|$ for the electron (left) and muon (right) leg of our preselection, including effects from tracking, reconstruction, identification, and isolation.

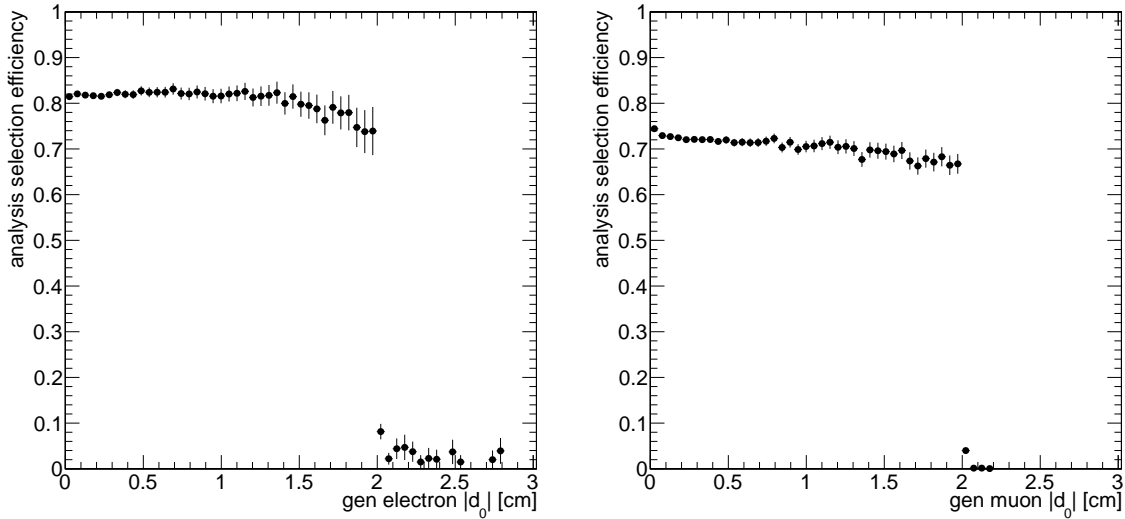


Figure 5.13: Analysis selection efficiencies as a function of $|d_0|$ for the electron (left) and muon (right) leg of our preselection. These are the same as the full efficiencies but with the reconstruction of the leptons factored out.

Table 5.12: Summary of lepton-related cuts.

cut parameter	electron	muon
$ \eta $	$ \eta < 2.5$	$ \eta < 2.5$
p_T	$p_T > 25 \text{ GeV}$	$p_T > 25 \text{ GeV}$
Particle ID	non-triggering BDT & conversion veto	modified tight ID
Isolation	ρ -corrected iso. < 0.10	$\Delta\beta$ -corrected iso. < 0.12
Additional Iso.	$\Delta R_{e,\text{jet}} > 0.5$	$\Delta R_{\mu,\text{jet}} > 0.5$
Impact Parameter	$ d_0 < 2 \text{ cm}$	$ d_0 < 2 \text{ cm}$

Table 5.13: Summary of lepton pair cuts

cut parameter	cut value
$\Delta R_{\mu,e}$	> 0.5
$q_e * q_\mu$	$= -1$

At this stage of the selection, a potential signal would be indistinguishable from the background contribution. It is for this reason that a variable that helps to discriminate between Standard Model background and signal should be used. The main feature of our signal is that the top squark has a moderate lifetime and hence the lepton decaying from it will be displaced with respect to the origin of the top squark. The d_0 of the leptons, as defined in the previous section, is now used to categorise the events in various regions with increasing signal purity.

5.3.2 Prompt lepton control region

The prompt control region is populated by a subset of the preselected events in which both leptons have a d_0 smaller than 0.01 cm. This region is dominated by prompt Standard Model backgrounds while being almost depleted of the signal. For that reason, this region is perfectly suited to compare the accuracy of our Monte Carlo simulation with the data. In all the figures of this section, the standard correction factors discussed in Section 5.2 have been applied to the Monte Carlo samples to correct known discrepancies. Furthermore, unless specifically mentioned, all the Monte Carlo simulations are "normalised" to the integrated luminosity which means that the event weight is calculated using Equation 5.2.

Table 5.14 shows the expected numbers of events in the prompt control region. Figure 5.14 shows the p_T , η , and d_0 distributions of both leptons. Figure 5.15 shows the invariant mass spectrum for the dilepton pairs in the events. In all these figures, a good data-Monte Carlo agreement is observed. Indeed, inspecting the ratios displayed on the bottom of each graph, one can observe that the majority of the bins are compatible

with unity. This suggests that the Monte Carlo simulations are accurately describing the prompt data and that they can be relied upon. The agreement in the d_0 distribution is definitely worse than for the other variables. This is a known effect that is due to the miss-modelling of the detector alignment in the Monte Carlo simulations. Like in the pileup scenario case, Monte Carlo simulations are produced with an a priori guess of what will be the alignment scenario of the detector. This difference in alignment scenarios results in a difference in resolution between Monte Carlo simulation and data. Since this search relies on the d_0 variable to discriminate between Standard Model backgrounds and the signal, it is important that it is well understood. It can be argued that the discrepancy dissipates when d_0 is becoming larger which implies that it is not affecting the displaced control region and even less the signal regions. Indeed, for the sake of argument, let us consider that the resolution in data and in Monte Carlo is well described by a single Gaussian probability density function. Thanks to the fact that a probability density function is always normalised, the ratio of data to Monte Carlo, represented by two Gaussians with slightly different standard deviation, will be first slightly lower than one, then will increase to a maximum value and then will decrease asymptotically toward one. When considering large d_0 ($d_0 \gg SD_{d_0}$), the ratio is close to one which is the case for the signal regions. In addition, as it will be seen in Section 5.6, the background contribution is largely dominated by events coming from QCD processes which is determined from data and hence not impacted by the resolution difference between Monte Carlo and data. Finally, the d_0 distribution of signal events can be considered as roughly flat over a range of few SD_{d_0} , and hence the impact of the resolution on the event yield in the signal regions is minor.

Table 5.14: Numbers of expected events in the prompt lepton control region. The "—" signifies that the statistical uncertainty is negligible compared to the systematic one which is discussed in Section 5.5. However, these uncertainties are incorporated in the calculation of the total statistical uncertainty.

Event Source	Event Yield \pm 1SD (stat.) \pm 1SD (syst.)
other EWK	$9300 \pm \text{—} \pm 1100$
top	$35300 \pm \text{—} \pm 2800$
$Z \rightarrow \tau\tau$	$10550 \pm 90 \pm 850$
Total expected background	$55300 \pm 100 \pm 3100$
Observation	52720

5.3.3 Displaced lepton control region

The displaced control region is defined as a subset of the preselected events in which both leptons have a d_0 larger than 0.01 cm but at least one of them smaller than 0.02 cm. With this definition, the displaced control region does not overlap with the signal regions and looks like an "L-shape" in the electrons' d_0 versus muons' d_0 as can be seen in Figure 5.10. This requirement is designed to remove promptly decaying Standard

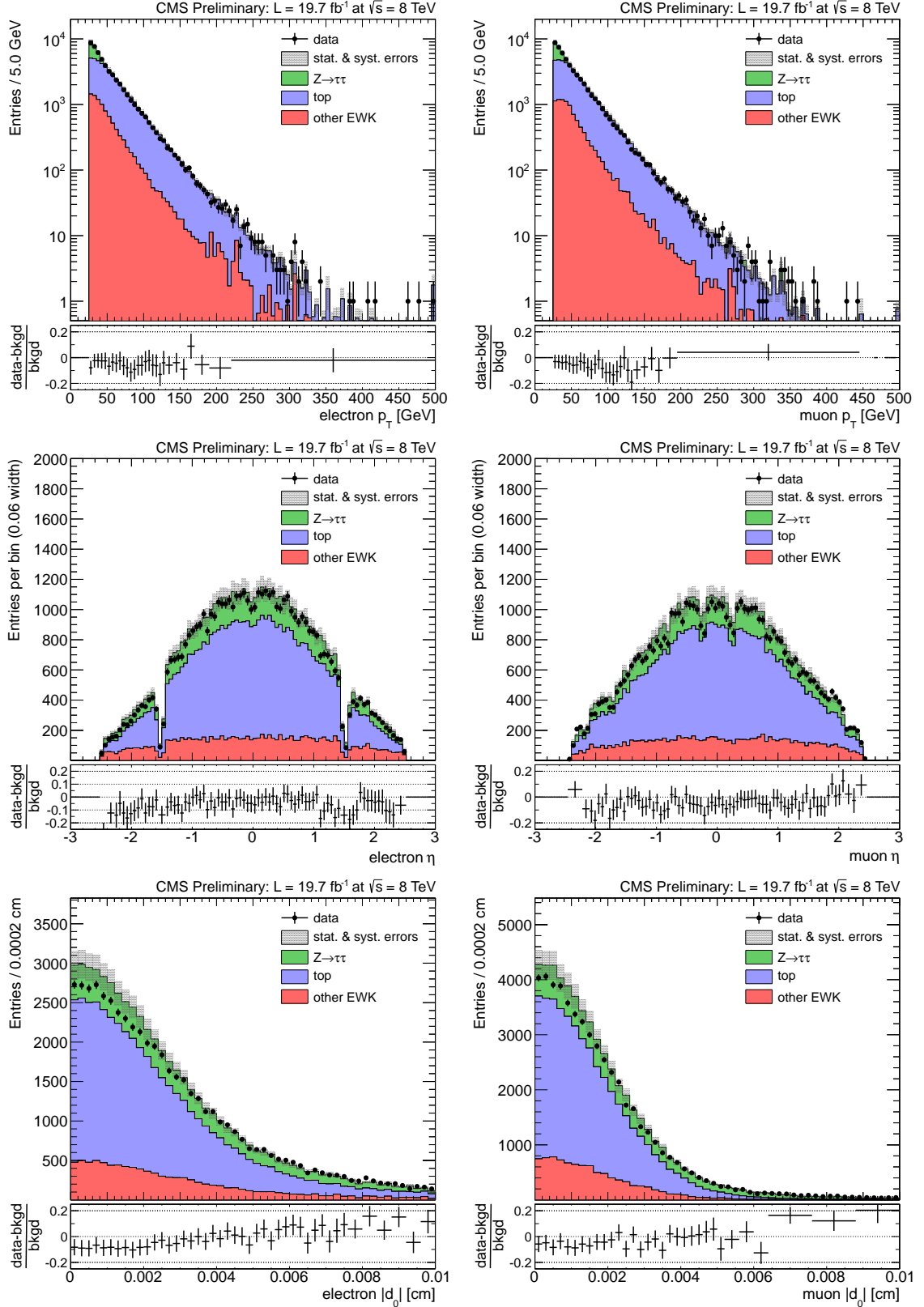


Figure 5.14: Lepton p_T (top), η (middle), and $|d_0|$ (bottom) spectra in the prompt lepton control region, for electrons (left) and muons (right). The data (black dots) is compared to the sum of expected Standard Model backgrounds split into different sources, $Z \rightarrow \tau\tau$ (green), top (blue), and other EWK (red). The grey shaded area represents the statistical and systematic uncertainties on the sum of the MC simulations. In the ratio plots, the bin size is automatically chosen so that the relative uncertainty remains constant in each bin.

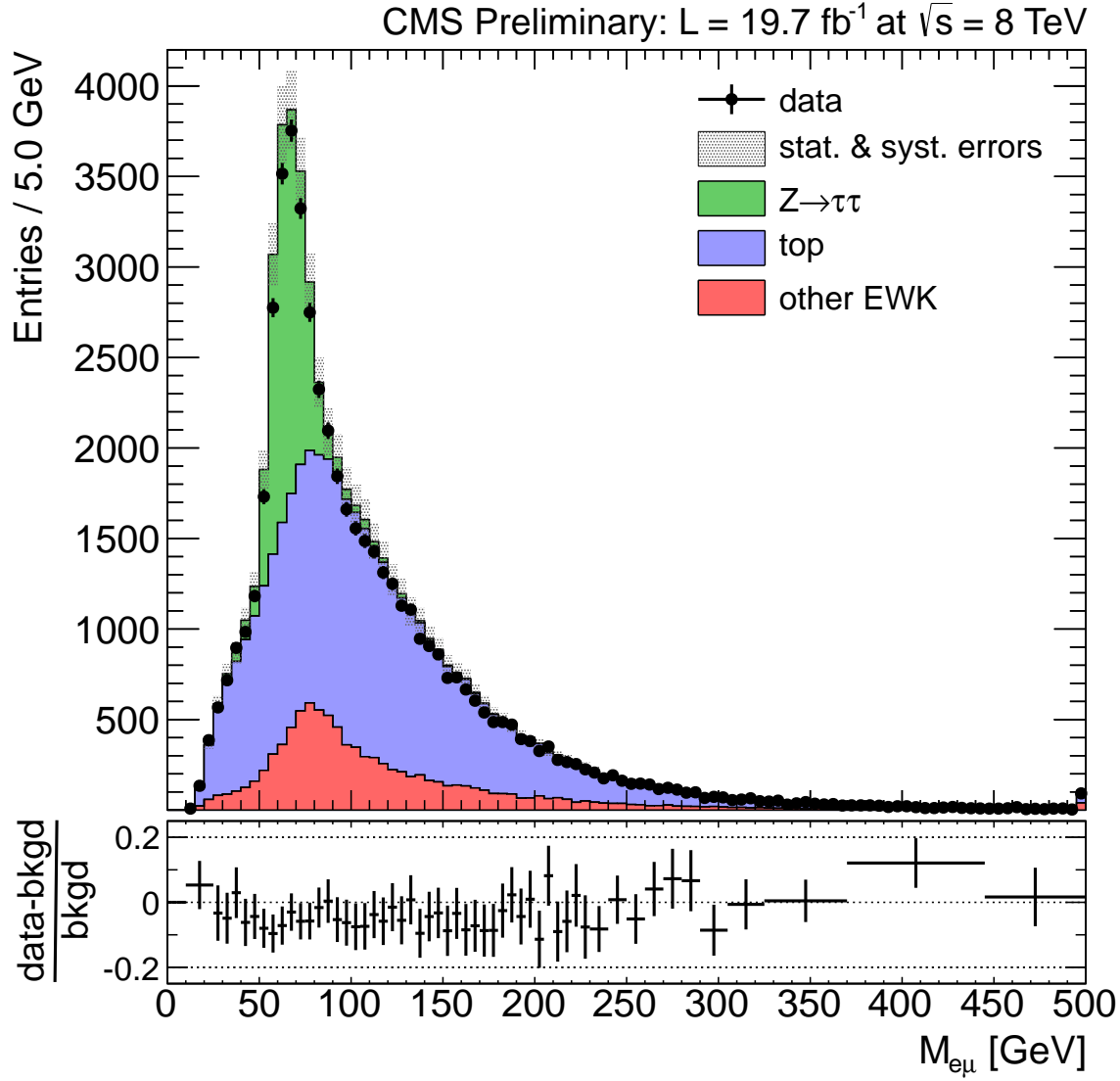


Figure 5.15: Dilepton invariant mass spectrum of events in the prompt lepton control region. The data (black dots) is compared to the sum of expected Standard Model backgrounds split into different sources, $Z \rightarrow \tau\tau$ (green), top (blue), and other EWK (red). The grey shaded area represents the statistical and systematic uncertainties on the sum of the MC simulations. In the ratio plots, the bin size is automatically chosen so that the relative uncertainty remains constant in each bin.

Model backgrounds such as "Other EWK" and, to a lesser extent, backgrounds from top decays. Therefore, the events populating this region are coming from Standard Model processes that produce truly displaced leptons such as QCD and $Z \rightarrow \tau\tau$ processes. This region will be used to estimate the background contribution from QCD processes in the signal regions. The procedure used will be presented in detail in Section 5.4.1.

5.3.4 Hybrid lepton control region

The hybrid control region is composed of the preselected events in which one lepton satisfies $d_0 > 0.01$ cm and the other has $d_0 < 0.02$ cm. Having one prompt lepton and one displaced lepton allows us to have a sufficient number of events with displaced leptons but does not overlap with the signal regions. This region was specifically designed to validate the method used to estimate the background coming from QCD processes.

5.3.5 Signal regions

Events that are preselected and that have both leptons satisfying $0.02 \text{ cm} < d_0 < 2$ cm populate one of the signal regions. By requiring both leptons to have large d_0 , these regions will be largely free of any leptons from prompt Standard Model backgrounds. However, since the efficiency of the leptons' d_0 cut is highly correlated to the lifetime of the leptons' parent, the optimal cut on d_0 will depend on the lifetime of the top squark. To have regions optimised for various top squark lifetimes, the signal region is split into three inclusive signal regions. An event enters the loose signal region (LSR), if both leptons have $0.02 \text{ cm} < d_0 < 2$ cm. Events that have both leptons with $0.05 \text{ cm} < d_0 < 2$ cm populate the medium signal region (MSR). Finally, the tight signal region (TSR) contains events with both leptons satisfying $0.1 \text{ cm} < d_0 < 2$ cm. In principle, dividing further the signal regions would have been possible. Additional checks have shown that the expected limits are not greatly improved when the number of regions exceeds three due to low statistics.

With the current definition, the three signal regions are overlapping as the events of the loose signal region are included in the medium signal region and the tight signal region, and the events of the medium signal region are included in the tight signal region. When setting limits, this would yield to double counting, so three new signal regions are defined so that they do not overlap. The signal region 3 (SR3) is equated to be the tight signal region. The signal region 2 (SR2) is populated by all the events entering the medium signal region minus the events in the tight signal region. Finally, the events entering the signal region 1 (SR1) are all the events entering the loose signal region that do not enter the medium signal region. Figure 5.16 shows the definition of the three inclusive signal regions (left) and the three exclusive signal regions (right).

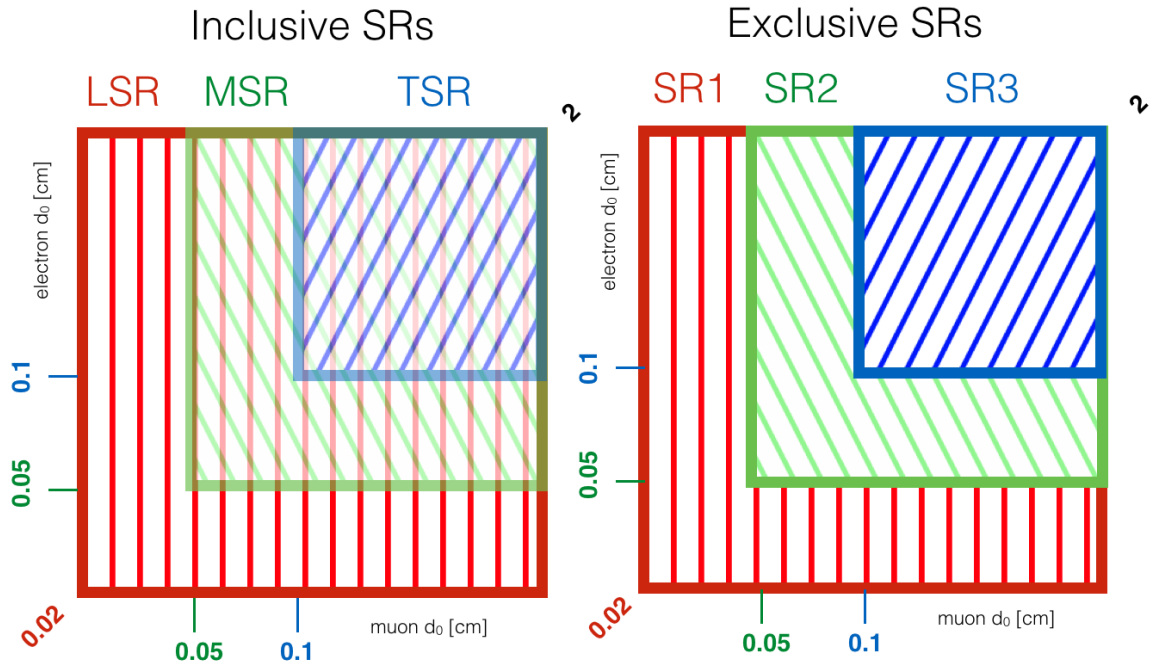


Figure 5.16: Schematic representation of the three inclusive signal regions (left) and the three exclusive signal regions (right) in the 2D plane of the leptons' d_0 .

5.4 Background estimation techniques

The purpose of this section is to explain the procedure used to estimate the contribution from Standard Model processes in the three signal regions defined previously. To end up in one of the signal regions, any event should satisfy two criteria. Firstly, it should contain exactly one isolated electron and one isolated muon. Secondly, these leptons should have a large d_0 . Any Standard Model processes that can produce two different-flavour leptons, genuine or fake, are considered as a source of background. This includes $Z \rightarrow \tau\tau$, top and other EWK processes and leptonic decays from QCD processes. Among these backgrounds, only three of them will produce truly displaced leptons, QCD, top and $Z \rightarrow \tau\tau$ processes. The QCD and the top processes can produce displaced lepton after the decay of B mesons which have a lifetime of $c\tau_B \approx 500 \mu\text{m}$. As the τ also has a substantial lifetime ($c\tau_\tau \approx 87 \mu\text{m}$), $Z \rightarrow \tau\tau$ can also produce leptons with significantly large d_0 . The production cross-section of QCD processes is so large that an accurate description of this process would require gigantic simulated samples. As these samples are not available, one cannot rely on simulation for QCD processes. In addition, the theory uncertainty on the cross-section production is typically fairly large. For that reason, the background contribution from QCD processes will be estimated using data in control regions.

The method used to estimate the background contribution from QCD processes will be exposed in Section 5.4.1. The background contribution from non-QCD processes, are estimated using Monte Carlo simulation via a technique that is explained in Section 5.4.2.

5.4.1 Background prediction from data-driven technique

In this search, the signal can be efficiently isolated from the background thanks to the displacement, its unique feature. The selection applied is tight enough that very little background is expected while keeping a significant amount of signal. For this kind of search, background contributions from QCD processes cannot be accurately estimated by Monte Carlo simulation. Indeed, the events in the $EM \text{ QCD } p_T 80 - 170$ sample would be multiplied by a factor of 2750 to provide yields equivalent to the data, as shown in Table 5.4. This leads to a huge statistical uncertainty and unrealistic event numbers expected, which is obviously not desired and would negatively impact the sensitivity of the search. For that reason, the background contribution from QCD processes is estimated using control regions in data. It is common to refer to such a method as a "data-driven" method.

The purpose of this section is to estimate the QCD contribution in each signal region and explain the method used for that matter. It is sufficient to derive the d_0 distribution, along with its normalisation, of leptons coming from QCD processes when the preselection cuts are applied. Once this is achieved, the yield in each signal regions can be estimated by applying the corresponding cut on the d_0 of the electron and the muon.

The name of the method used hereafter to estimate the QCD contribution in the

signal regions is called the "ABCD method" after the four yields considered, and is illustrated in Figure 5.17. The idea is that, applying a cut on two variables, one can define four non-overlapping regions. Then, assuming that these variables are relatively uncorrelated, one can estimate the yield in a region, knowing the contribution in the three other regions. Indeed, one can write :

$$N_B = \frac{N_A}{N_C} \times N_D \quad (5.5)$$

where N_i is the number of events in region i .

The I_{rel} as introduced in Section 3.4.2.2 and the charge product between the two leptons were chosen as the two variables of interest for this study. The most signal-like region should have the same requirement as the preselection, which included isolated leptons and opposite charge sign (OS) leptons (region B). Region A contains isolated leptons, but the charge requirement is reversed so that the leptons have the same sign charge (SS). Region C is populated by non-isolated leptons and opposite charge sign leptons. Finally, events with non-isolated leptons and same charge sign leptons compose region D. For the non-isolated regions, the cut on the I_{rel} of the leptons was not simply inverted but instead sideband regions as defined in Table 5.15 were defined. This ensures a better separation between the isolated and the non-isolated regions as well as removes events in the tails of the isolation spectra, which are less well understood. In addition to changing the cut on the isolation, the $\Delta R_{l,jet} > 0.5$ requirement is removed because it is part of the isolation. The definition of the four regions is summarised in Figure 5.17.

Table 5.15: Definition of the isolation sideband used to define regions C and D.

	standard I_{rel} requirement	sideband I_{rel} requirement
electron	< 0.1	$[0.2, 1.0]$
muon	< 0.12	$[0.24, 1.5]$

In each region except region B, the contribution from QCD processes is equated to be the difference of the data and the other backgrounds that are taken from the simulation. In order to get the d_0 distribution of the leptons in region B, the d_0 distribution in region D is scaled by the ratio of the QCD yield in region A to the QCD yield in region C. The validity of the method is checked in the displaced control region, as defined in Section 5.3.3, which does not overlap with the signal regions. Figure 5.18 (5.19) shows the d_0 distribution¹ for electrons (muons), in the four regions defined in the ABCD method in the displaced control region. For all the regions but region B, only nonQCD processes are included and thus agreement between data and Monte Carlo is not expected. In region B, the QCD contribution is added on top of all the non-QCD backgrounds and is calculated as explained above using the three other regions.

¹In these figures, the d_0 range for which the distribution is shown has been adapted according to the statistic available so that the upper range is not always 2 cm. The same statement holds for all the other figures of this section in which the d_0 distribution is displayed.

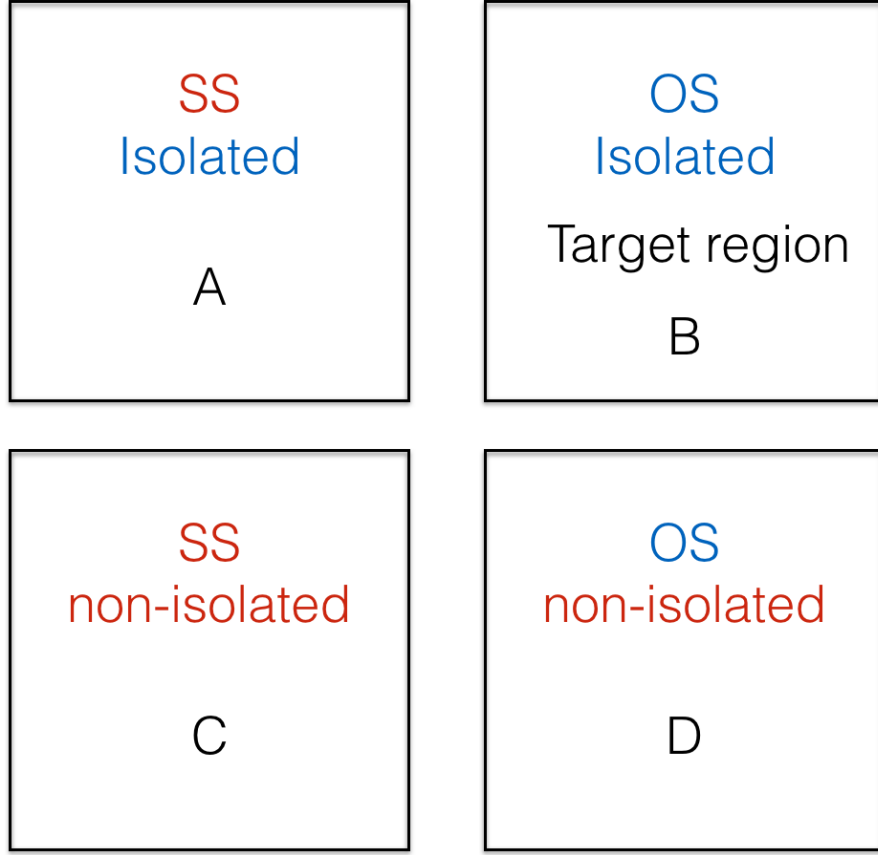


Figure 5.17: Schematic of the definition of the four regions used in the ABCD method. When the cut is the same as in the preselection the cut name is in blue, it is in red otherwise.

Figure 5.20 shows the invariant mass distribution in the displaced control region with the QCD contribution estimated with the data-driven method. The corresponding yields can be found in Table 5.16. Inspecting the values of the table, it is clear that the contribution from QCD is necessary to have a better agreement between the data and the sum of the background. Indeed the observed number of events is 154 which is compatible with the expected background if one includes the QCD contribution which amounts to 50 events.

Additionally, the validity of the prediction provided by the data-driven method is checked in the hybrid control region as defined in Section 5.3.4 which contains one displaced and one prompt lepton. Figure 5.21 shows the leptons' d_0 distribution in the equivalent of the B region but in the hybrid control region instead of the displaced control region. Again, the agreement between background and data is enhanced thanks to the addition of the QCD contribution, which further validates the methodology used.

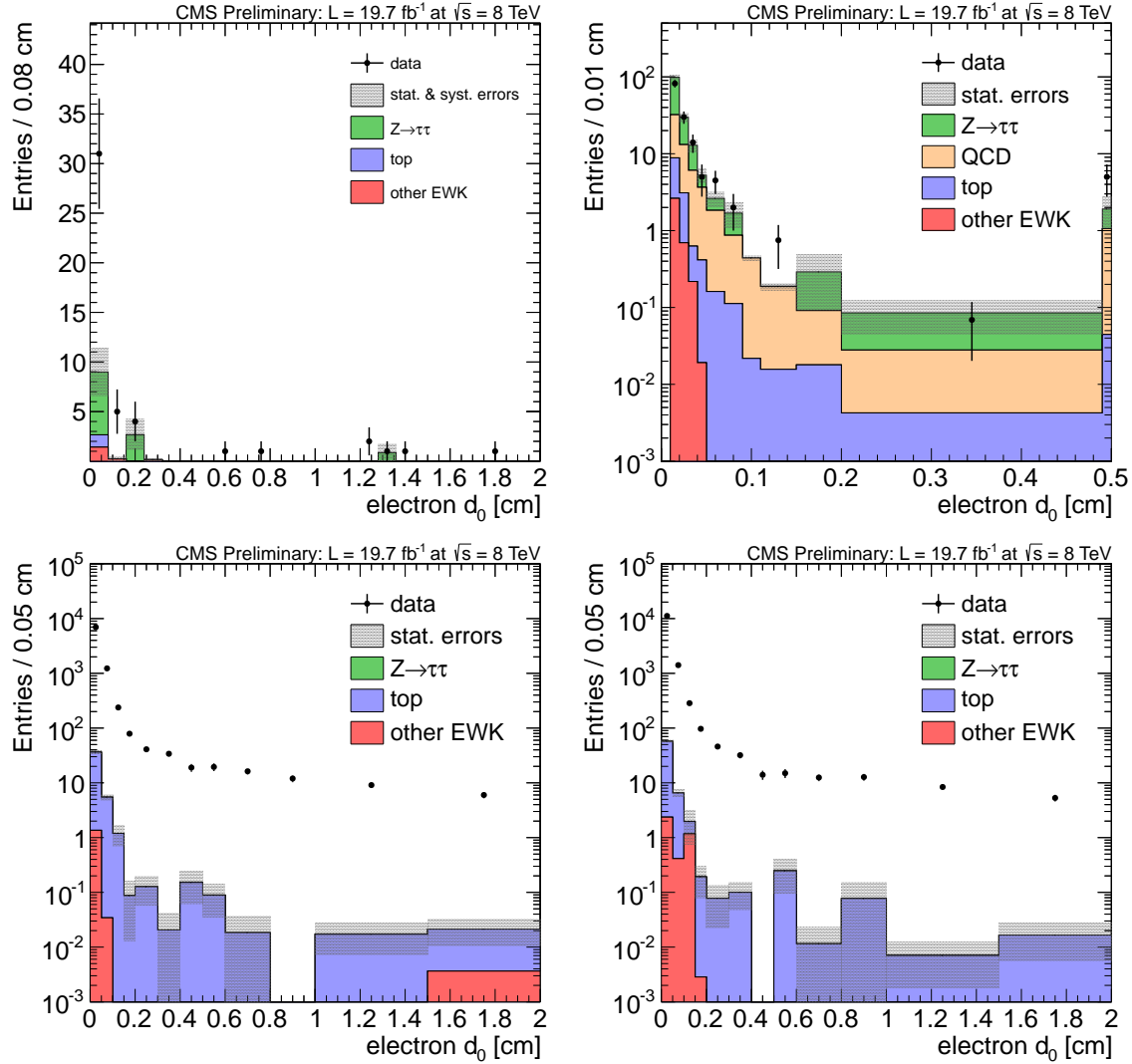


Figure 5.18: Electron impact parameter distributions in the regions used in the ABCD method in the displaced control region. The figures correspond to region A (upper left), the target region B (upper right), the region C (lower left), and the region D (lower right). In region B, the QCD contribution is extracted with the ABCD method explained in the text using information from the three other regions. In these regions, all the difference between data and Monte Carlo is attributed to QCD processes.

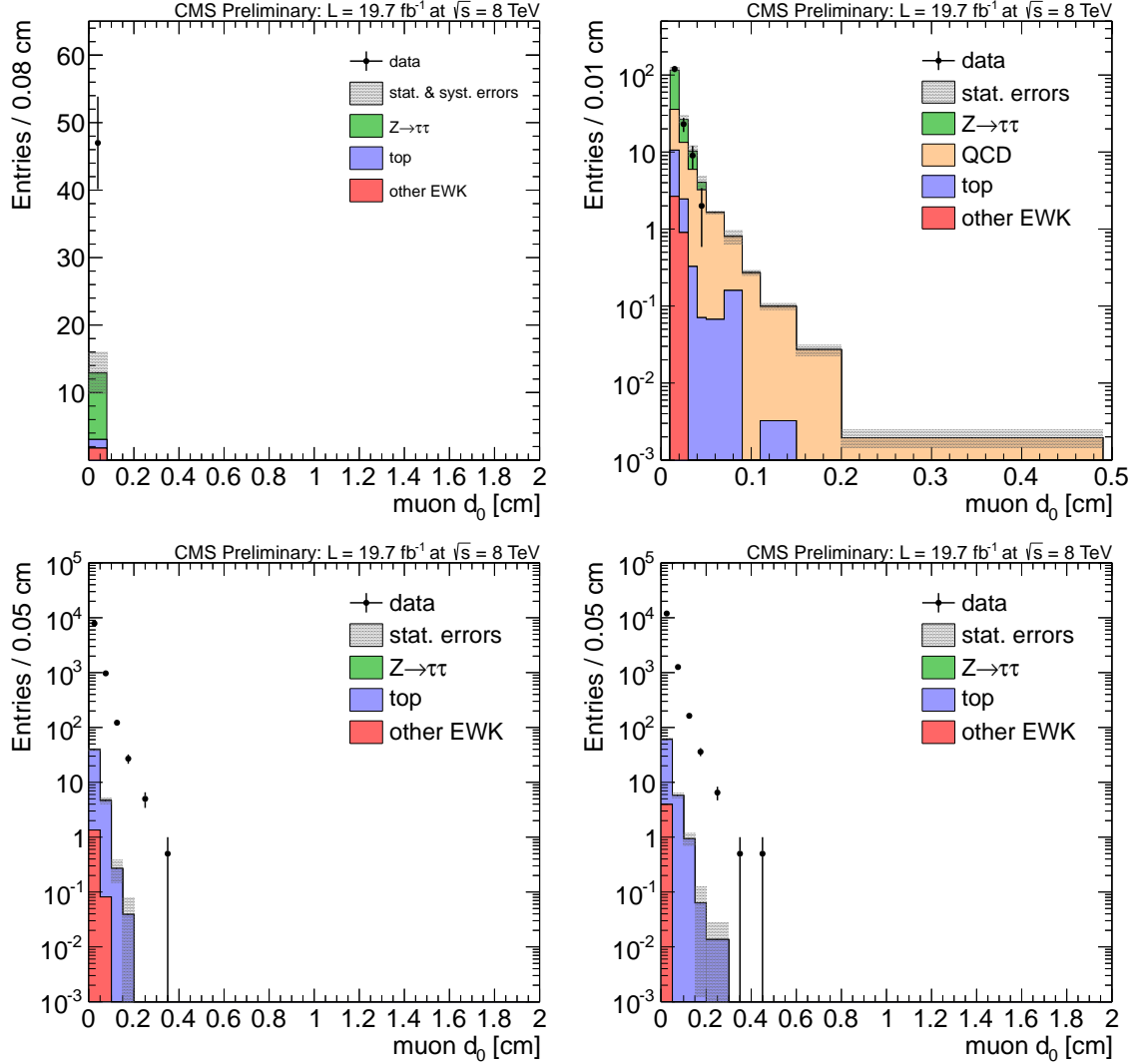


Figure 5.19: Muon impact parameter distributions in the regions used in the ABCD method. The figures correspond to region A (upper left), the target region B (upper right), the region C (lower left), and the region D (lower right). In region B, the QCD contribution is extracted with the ABCD method explained in the text using information from the three other regions. In these regions, all the difference between data and Monte Carlo is attributed to QCD processes.

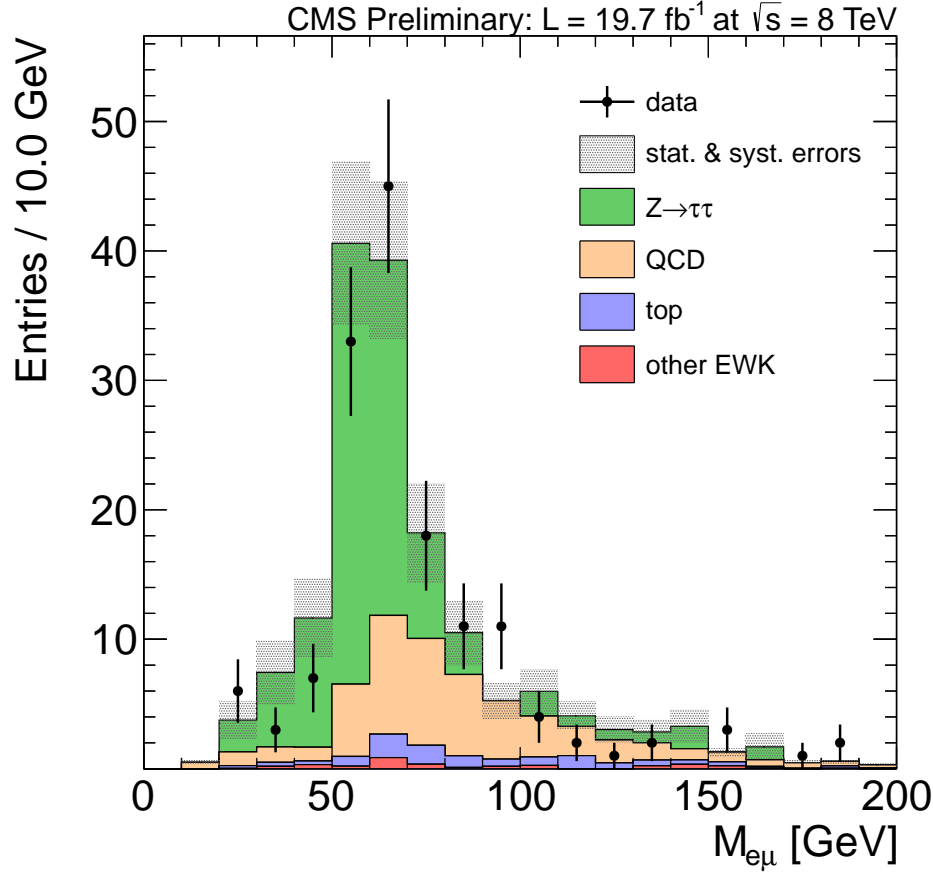


Figure 5.20: Dilepton invariant mass spectrum of events in the displaced lepton control region where the QCD contribution is calculated with the data-driven method.

Table 5.16: Numbers of expected events in the displaced control region. Two significant digits are displayed for the uncertainties of each background, while the total uncertainties are rounded to a single significant digit.

Event Source	Event Yield $\pm 1\text{SD (stat.)} \pm 1\text{SD (syst.)}$
other EWK	$3.56 \pm 0.99 \pm 0.43$
top	$10.3 \pm 1.0 \pm 0.8$
QCD	$50 \pm 0.0 \pm 15$
$Z \rightarrow \tau\tau$	$98.2 \pm 9.2 \pm 8.0$
Total expected background	$162 \pm 9 \pm 17$
Observation	154

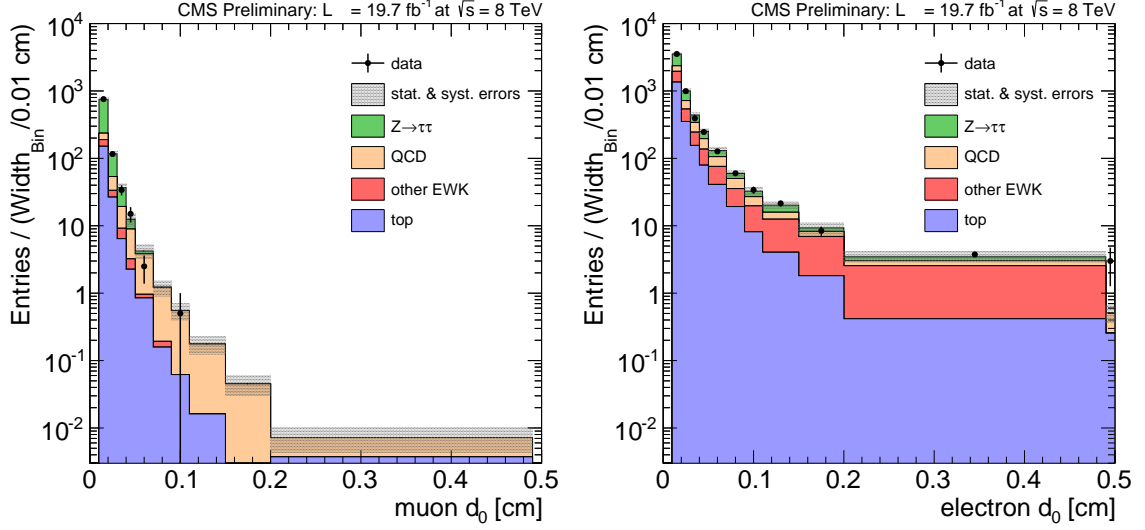


Figure 5.21: Muon (left) and electron (right) impact parameter distributions in the B region in the hybrid control region. The contents of the overflow bin are added to the rightmost bin of the figure.

5.4.2 Background prediction from Monte Carlo simulation

As already mentioned above, all the backgrounds but the QCD contribution can be derived safely from Monte Carlo simulation as the event weight is much closer to one. However, it is import to check if the Monte Carlo simulations are accurately reproducing the d_0 variable for larger values of it. As $Z \rightarrow \tau\tau$ produces genuine displaced leptons, this topology is a good candidate to check the accuracy of Monte Carlo simulation.

5.4.3 Monte Carlo simulation validation in $Z \rightarrow \tau\tau$ control region

A new control region is defined by applying the standard analysis preselection, at the top of which $Z \rightarrow \tau\tau$ enriching cuts are applied. These cuts have a high efficiency for the events coming from the $Z \rightarrow \tau\tau$ process and a low one for the other ones. Using the fact that $W \rightarrow l\nu + \text{jets}$ processes contain a neutrino, its contribution is largely suppressed by requiring low missing energy. Events are rejected if at least one of the lepton plus E_T^{miss} is higher than 50 GeV. The QCD and $t\bar{t}$ contributions are reduced when removing events with a total scalar sum of transverse jet energy, $\sum p_{T,jet}$, bigger than 100 GeV. Finally, leptons are required to be nearly back to back in ϕ , to further reduce the possibility of contamination from signal events. Table 5.17 contains the list of all the cuts applied in order to define the $Z \rightarrow \tau\tau$ control region. The d_0 spectra are shown in Figure 5.22 for Monte Carlo simulation and data. As it can be seen in this figure, this region is highly dominated by $Z \rightarrow \tau\tau$ processes, as intended by the selection applied. A good agreement is observed for muons as well as for electrons that provides confidence that the Monte Carlo simulation can be used to estimate the background contribution from non-QCD processes.

Table 5.17: $Z \rightarrow \tau\tau$ enriching cuts.

$Z \rightarrow \tau\tau$ Selections
analysis preselection
exactly one electron with $M_T < 50$ GeV
exactly one muon with $M_T < 50$ GeV
exactly one electron-muon pair with $\Delta\phi > 2.5$
$\sum p_{T,jet} < 100$ GeV

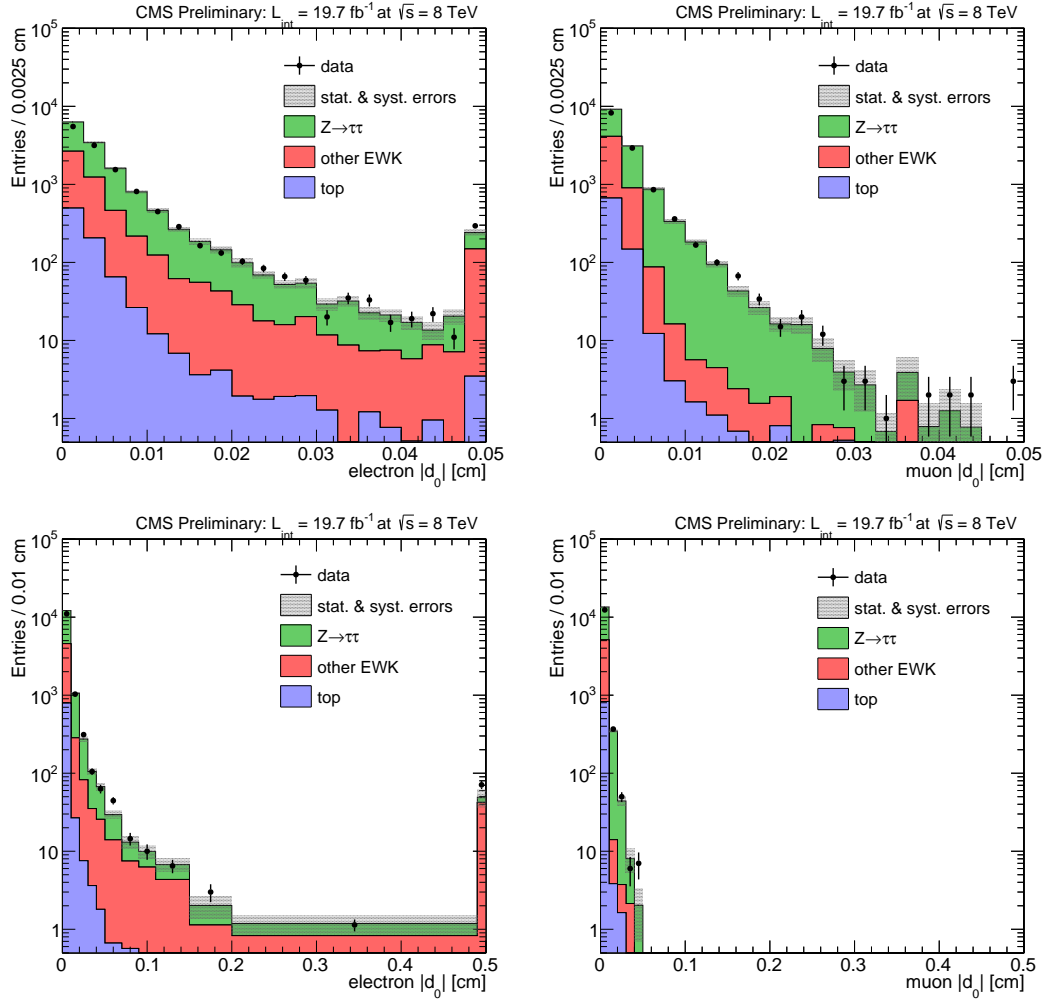


Figure 5.22: Impact parameter spectra of electrons (left) and muons (right) in $Z \rightarrow \tau\tau$ enriched control region, up to 0.05 cm (top) and 0.5 cm (bottom).

5.4.4 Background estimation in the signal regions

By requiring high d_0 for both leptons, the three signal regions have been purposefully designed to be as much background-free as possible. While this is a good feature for the sensitivity of the search, it might be slightly inconvenient to have exactly zero events as the Monte Carlo prediction for mostly one reason: it is hard to assess the statistical error related to zero events prediction. To avoid this, the background contribution from non-QCD processes for large d_0 is extended by calculating the efficiency separately to pass the electron's d_0 cut and the muon's d_0 cut, as shown in Figure 5.23, for events in the prompt control region. Then, assuming that these efficiencies are uncorrelated, assumption which is tested in the next paragraph, one can estimate the contribution in any signal region by multiplying the yield obtained in the prompt control region with the two efficiencies at the d_0 that corresponds to the definition of the signal region of interest as described by the following equation:

$$N_{SR} = N_{PCR} \epsilon_{\mu}(SR) \epsilon_e(SR). \quad (5.6)$$

This method will hereafter be referred to as the "factorisation method". When the background prediction is zero even using the factorisation method, the prediction from the looser neighbouring signal region with non-zero prediction is used as a conservative estimate.

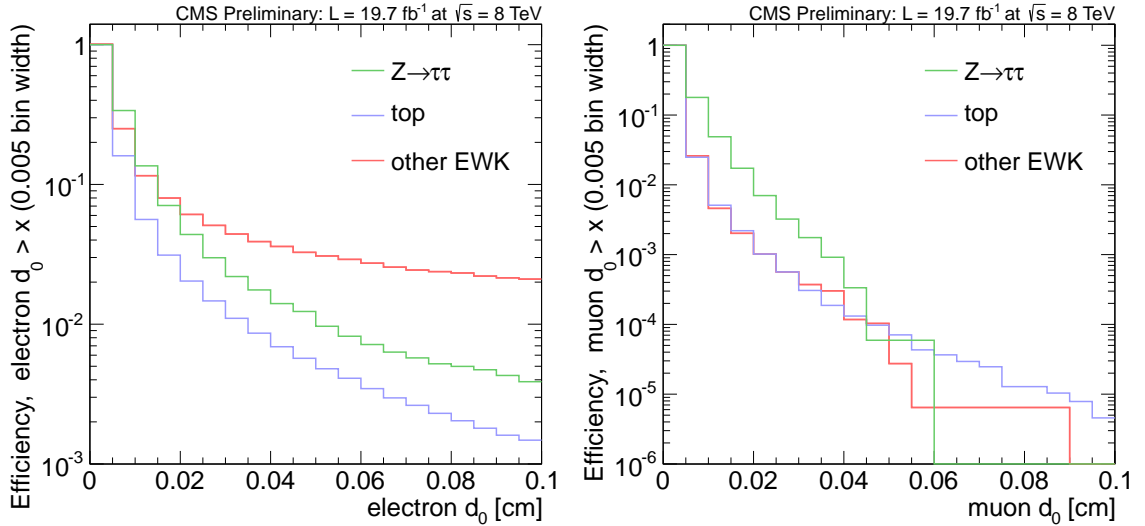


Figure 5.23: Efficiency curves as a function of the minimum $|d_0|$ requirement, for the selected electrons (left) and muons (right) in events passing the analysis preselection, for the three different background processes estimated using Monte Carlo.

The accuracy of the factorization method is checked by comparing its background estimate with the one gotten from applying the cuts on both leptons d_0 . The two methods can be compared only where the "cut and count" method, gives non-zero prediction while the goal of the factorisation method is to extend the non-zero prediction. Figure 5.24 illustrates the good agreement observed between these two methods over

the whole d_0 range except for "other EWK" background. In that case, the factorisation method overestimates the background contribution, suggesting a negative correlation between the leptons' d_0 . However, the contribution from this process remains small as compared to the other background. For this reason, the yield given by the factorisation method can be used as a conservative estimate.

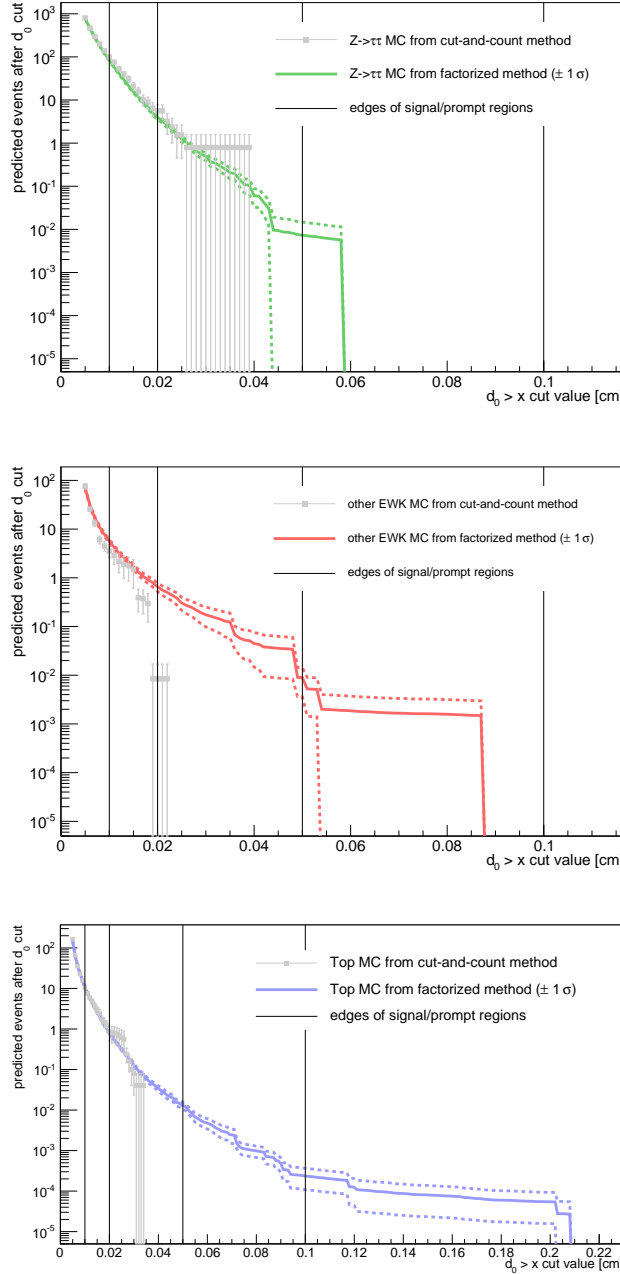


Figure 5.24: Comparison of the cut and count method (grey squares) and the factorisation method (coloured bands) for the three different background processes estimated using Monte Carlo.

5.5 Systematic uncertainties

The purpose of this section is to assess the effect of all the systematic uncertainties on the assumption and methods that led to the result of this search. In addition to the uncertainties related to all corrections discussed in Section 5.2, the uncertainty related to the signal and background cross-section and the PDF are considered.

The uncertainty on the pileup assumption is derived using the standard CMS recommendation. By varying the total inelastic cross-section by \pm one standard deviation, two additional inelastic scattering distributions were created. The mean central value for the total inelastic cross-section is derived by the CMS collaboration in an independent measurement and is found to be $69.4 \text{ mb} \pm 5\%$ [87]. The analysis was rerun with each of the three different distributions shown in Figure 5.25 and the resulting change on the event yield is found to be smaller than 0.3% for all the background samples while being less than 5% for the signal samples.

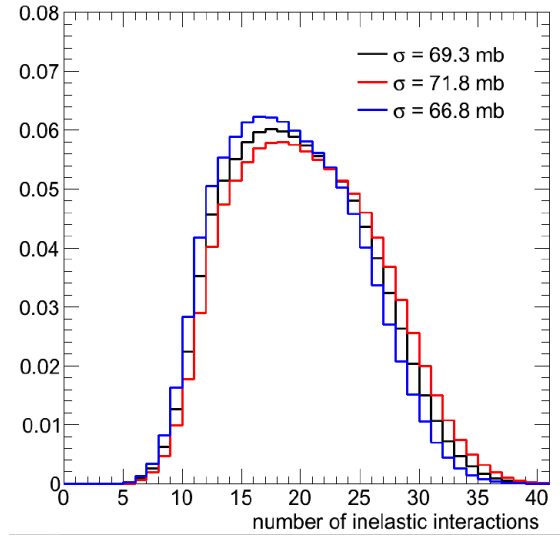


Figure 5.25: Distributions used for pileup reweighting uncertainties.

The uncertainty on the leptons identification and isolation efficiency is calculated by varying each correction factor used in sections 5.2.2 and 5.2.3 by one standard deviation. The standard deviation includes both statistical uncertainty and systematic uncertainty related to the tag and probe method where both uncertainties are added in quadrature.

The trigger uncertainty is calculated by shifting by 2% the trigger correction factor. The effect on the final results is quoted as the trigger uncertainty and does not depend on the sample used.

For each process, the cross-section is a function of the PDF as expressed in Equation 3.7. For this reason, the choice of PDF used may impact the cross-section and in turn the number of expected background. To assess the effect on the final results, alternative PDFs are considered. Following the official PDF4LHC recommendation [88], the PDF related uncertainty can be calculated using the suggested envelope of the CTEQ, MSTW and NNPDF PDF sets. The value of the uncertainties ranges from 0.1%-2.1% for the background samples while it ranges from 0.6%-4.6% for the signal samples.

The resulting relative systematic uncertainty affecting the background contribution is the squared sum of all the systematic uncertainties. Table 5.18 summarises the list of systematic uncertainties considered in the analysis and the resulting overall systematic uncertainty. The effect of each systematic uncertainty is reported for each sample and uncertainties that do not depend on the sample are not quoted in the table. For the signal samples, the lowest and the highest fluctuations are reported. Generally, the uncertainty is increasing with the top squark mass while being almost independent of the top squark lifetime. Because the contribution from QCD processes is estimated using a data-driven technique, none of the correction to the Monte Carlo simulation affects it. In that case, the systematic uncertainty is related to the number of events used in the regions A, C, and D. The rightmost column shows the total uncertainty including all the uncertainties, even the ones not figuring in the table.

Table 5.18: List of systematic uncertainties considered in this search. The rightmost column includes all the relevant systematic uncertainties, including the ones not explicitly mentioned in the table.

Dataset	Cross-section	Pileup	e ID/ I_{rel}	μ ID/ I_{rel}	PDF	Total
$W \rightarrow l\nu$	$\pm 3.5\%$	$\pm 0.07\%$	$\pm 0.42\%$	$\pm 0.61\%$	$\pm 0.66\%$	$\pm 11.0\%$
diboson	$\pm 6.2\%$	$\pm 0.28\%$	$\pm 0.35\%$	$\pm 0.63\%$	$\pm 0.59\%$	$\pm 9.0\%$
single top	$\pm 6.9\%$	$\pm 0.17\%$	$\pm 0.29\%$	$\pm 0.64\%$	$\pm 2.15\%$	$\pm 9.4\%$
$t\bar{t}$	$\pm 4.3\%$	$\pm 0.19\%$	$\pm 0.49\%$	$\pm 0.56\%$	$\pm 0.11\%$	$\pm 8.0\%$
$Z \rightarrow ll$	$\pm 4.6\%$	$\pm 0.21\%$	$\pm 0.29\%$	$\pm 0.64\%$	$\pm 1.66\%$	$\pm 8.1\%$
QCD	—	—	—	—	—	$\pm 30\%$
signal	$\pm 15\text{-}28\%$	$\pm 0.1\text{-}5.4\%$	$\pm 0.13\text{-}0.29\%$	$\pm 0.9\text{-}3.8\%$	$\pm 0.06\text{-}4.6\%$	$\pm 15\text{-}28\%$

5.6 Results

5.6.1 Event yields

The yield in each of the three inclusive signal regions is shown in Table 5.19. When the number of predicted events is zero, the value from the first non-zero preceding region is conservatively quoted. In this case, a "<" sign is prefixed to the value to denote that an upper bound as the actual estimate is used. By comparing the values of total expected backgrounds with the observed number, one can conclude that there is no significant excess. The expected signal yields using a mass hypothesis of 500 GeV and for three different average lifetime values are listed in the last three rows. Inspecting these last three rows and comparing it to the total expected background, the advantage of having multiple regions becomes obvious. Indeed for a low lifetime, the less displaced signal region contains most of the signal events while the sensitivity shifts toward more displaced signal regions for increasing lifetime. The expected background is about 1 for the signal region 2 and 0 for the signal region 3. It is interesting to note that for the signal with $\langle c\tau \rangle = 1.0$, the yield is roughly constant over the three signal regions while it can be argued that the d_0 distribution is described by an exponential function. This is explained by the fact that the difference between two bounds defining the signal regions is not constant and the more displaced regions cover a larger d_0 range.

Table 5.19: Numbers of expected and observed events in the three signal regions. Background and signal expectations are quoted as $N_{exp} \pm SD(\text{stat}) \pm SD(\text{sys})$. A "<" preceding a yield denotes that that raw estimate was null and that the yield is taken from the previous signal region.

Event Source	SR1	SR2	SR3
other EWK	$0.65 \pm 0.13 \pm 0.08$	$(0.89 \pm 0.53 \pm 0.11) \times 10^{-2}$	$< (89 \pm 53 \pm 11) \times 10^{-4}$
top	$0.767 \pm 0.038 \pm 0.061$	$(1.25 \pm 0.26 \pm 0.10) \times 10^{-2}$	$(2.4 \pm 1.3 \pm 0.2) \times 10^{-4}$
$Z \rightarrow \tau\tau$	$3.93 \pm 0.42 \pm 0.32$	$(0.73 \pm 0.73 \pm 0.06) \times 10^{-2}$	$< (73 \pm 73 \pm 6) \times 10^{-4}$
QCD	$12.7 \pm 0.2 \pm 3.8$	$(98 \pm 6 \pm 30) \times 10^{-2}$	$(340 \pm 110 \pm 100) \times 10^{-4}$
Total expected			
background	$18.0 \pm 0.5 \pm 3.8$	$1.01 \pm 0.06 \pm 0.30$	$0.051 \pm 0.015 \pm 0.010$
Observation	19	0	0
<hr/>			
$gg \rightarrow \widetilde{t}_1 \widetilde{t}_1^*$			
M = 500 GeV			
$\langle c\tau \rangle = 0.1$ cm	$30.1 \pm 0.7 \pm 1.1$	$6.54 \pm 0.34 \pm 0.24$	$1.34 \pm 0.15 \pm 0.05$
$\langle c\tau \rangle = 1.0$ cm	$35.3 \pm 0.8 \pm 1.3$	$30.3 \pm 0.7 \pm 1.1$	$51.3 \pm 1.0 \pm 1.9$
$\langle c\tau \rangle = 10.0$ cm	$4.73 \pm 0.30 \pm 0.17$	$5.57 \pm 0.32 \pm 0.20$	$26.27 \pm 0.70 \pm 0.93$

5.6.2 Limits

In the absence of any significant excess over the background, 95% CL upper limits are set, as explained in Section 4.3, on the cross-section for the top squark pair production at 8 TeV. Using a simplified model to calculate the top squark cross-section as a function of its mass, the upper limit on the cross-section is converted into an upper limit on the mass of the top squark. This procedure is repeated for all the lifetimes and masses hypothesis that have been considered.

To combine the limits extracted from the three exclusive signal regions, the "Higgs combine" tool is used [89]. The expected limits are calculated using the Bayesian method that employs Markov Chain Monte Carlo technique. The resulting observed and expected limits graph is shown in Figure 5.26 where the region left to the contours is excluded by this search.

It can be noted that the limits on the top quark mass depend on its $\langle c\tau_t \rangle$. This is due to the combination of two factors: the expected background is decreasing for a higher value of $\langle c\tau_t \rangle$ and the signal acceptance is also decreasing for a higher value of $\langle c\tau_t \rangle$. The most stringent limits at 95% CLs are set for a $\langle c\tau_t \rangle$ of 2 cm/ c where top squark masses up to 790 GeV are excluded. These limits are the most stringent limits on the Displaced Supersymmetry model.

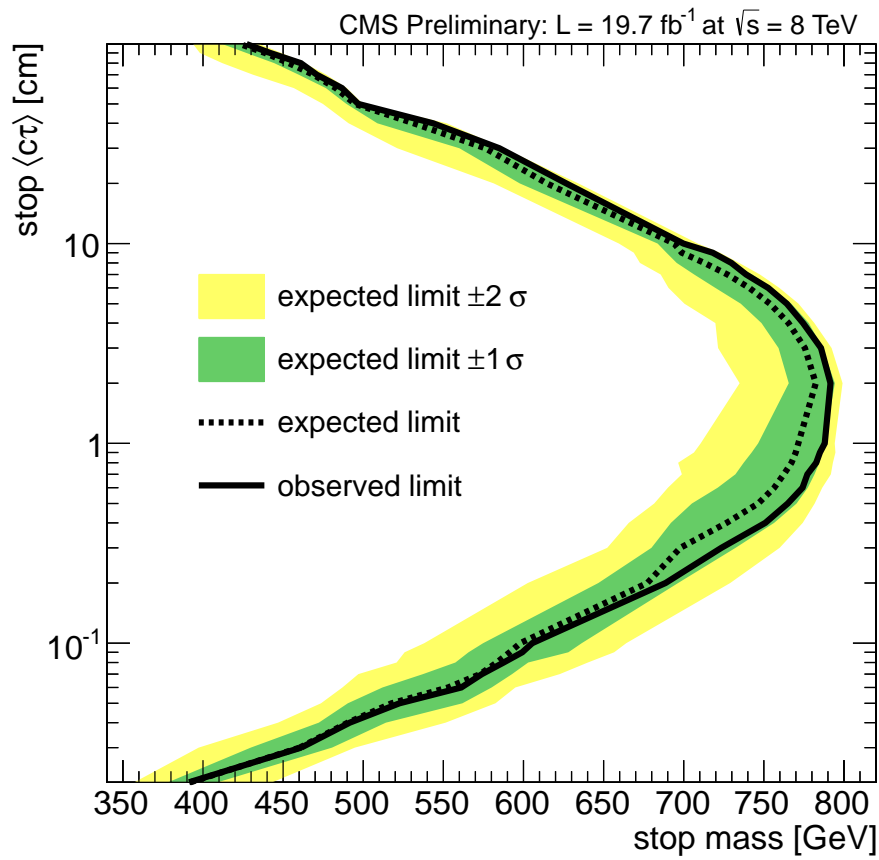


Figure 5.26: Expected and observed 95% exclusion contours for top squarks pair production in the plane of top squark average lifetime and mass. The region to the left of the contours is excluded by this search.

Parametrisation study

In the previous chapter, the event yield of Table 5.19 has been used to set limits on the Displaced Supersymmetry model. However, as it was already mentioned, the selection applied to separate signal events from background has not been highly customised for this specific model. The advantage of this strategy is that this search retains sensitivity to a broad range of alternative models involving one displaced electron and one displaced muon. More specifically, the event yields obtained can be used to set limits on other models providing that dedicated Monte Carlo simulations of the CMS detector are available for these other models and assuming that simulations are available in order to calculate the acceptance. In practice, as already mentioned in Section 3.3.7, these CMS-specific simulations are extremely time-consuming and not easily reproduced by anyone outside the CMS collaboration. The goal of the following study is to provide the tools to "emulate" the CMS reconstruction algorithms. By no means these tools can replace the full CMS reconstruction, but they can provide invaluable help to model builders to assess how the limits on the one model can translate in a limit for their specific models, allowing to constrain some model without doing a new dedicated search.

In Section 6.1, the necessary steps to provide a useful tool outside the CMS collaboration using the results of the Displaced $e\mu$ search will be revealed. A paper where the parametrisation was used to set limit on a vast variety of models will be discussed in Section 6.2.

6.1 Providing a parametrisation study

In this section, the necessary steps to create a useful parametrisation study will be explained. It is really necessary for the potential user to have a clear explanation of what exactly was done to create the tool, what is its domain of applicability and how accurate the prediction is.

The exact procedure of this study will be explained in Section 6.1.1. In Section 6.1.2 the model dependence of the parametrisation will be tested using different values of the mass and the lifetime of the top squark. The resulting efficiencies which are meant to

be used by physicists are shown in Section 6.1.3. The accuracy of the parametrisation will be assessed in Section 6.1.4.

6.1.1 Procedure

This study intends to provide a recipe that can be used by physicists to allow them to translate the event yield obtained in Chapter 5 into the model of their choice. In the search in this thesis, an event will end up in one of the signal regions defined in Section 5.3.5 if it was reconstructed, triggered and selected. The reconstruction algorithm involves detector specific variables which are not available for model builders. The reconstruction efficiency of a lepton depends strongly on the flight distance. However, as already mentioned in Section 5.1.3, the flight distance is not necessarily available at the reconstructed level. For these reasons, the reconstruction efficiency will be derived as a function of a variable that is highly correlated with this distance. In this study, the reconstruction efficiency will be derived as a function of the d_0 of each generated lepton separately. As shown in Figure 5.11, the trigger efficiency seems to be similar for all lifetime and mass hypotheses so will be emulated by a single number. The set of cuts applied in the preselection of the search presented in the previous chapter is summarised in Tables 5.12–5.13. They include requirements on the isolation and the identification of the leptons. As these variables are also constructed using some detector-specific variables, it is impossible for model builders to apply them directly on the generated sample they have produced. The selection efficiency will be derived as a function of the p_T ¹ of each generated lepton, separately.

From Equation 4.1, the yield obtained in a signal region is proportional to the acceptance of the preselection cuts and the d_0 cuts defining this region. One can write,

$$Y_{SR}^R = \sigma L_{int} A_P^R A_{SR}^R, \quad (6.1)$$

where Y stands for the yield, A the acceptance, R for reconstructed and P for preselection. Splitting the acceptance of the preselection cuts into two components, one gets

$$Y_{SR}^R = \sigma L_{int} A_{P'}^R A_{P''}^R A_{SR}^R, \quad (6.2)$$

where $A_{P'}^R$ is the component that can be directly translated from the reconstruction level to the generated level and $A_{P''}^R$ is the component that contains cuts which require detector specific information. With this definition, replacing the acceptance of the preselection cuts at reconstructed level by its analogue at generated level, one gets

$$Y_{SR}^R = \sigma L_{int} A_{P'}^G A_{P''}^G W_{P''}^{G \rightarrow R} A_{SR}^R, \quad (6.3)$$

where $W_P^{G \rightarrow R}$ is the weight to be applied to account for the differences between generated level and reconstructed level quantities related to the preselection cuts. Assuming that the d_0 is perfectly well reconstructed, one gets

$$Y_{SR}^R = \sigma L_{int} A_{P'}^G A_{P''}^G W_{P''}^{G \rightarrow R} A_{SR}^G. \quad (6.4)$$

¹The performance of the parametrisation was tested using η as an additional variable. This study has shown that the performance was similar than with d_0 and p_T .

The last equation implies that it is possible to get an estimate of the yield at reconstructed level using cuts on generated level and the appropriate weight. Following the discussion above, the acceptance of the preselection containing CMS-specific cuts combined with the weight to take into account the difference between generated level and reconstruction level quantities can be split into three components as follows:

$$A_{P''}^G W_{P''}^{G \rightarrow R} := \varepsilon^{event} = \varepsilon_{reco}^{event} \varepsilon_{trigger}^{event} \varepsilon_{sel}^{event}. \quad (6.5)$$

Furthermore, the reconstruction efficiency and the selection efficiency are the product of the electron and the muon components

$$\begin{aligned} \varepsilon_{reco}^{event} &= \varepsilon_{reco}^{electron}(d_0) \varepsilon_{reco}^{muon}(d_0) \\ \varepsilon_{sel}^{event} &= \varepsilon_{sel}^{electron}(p_T) \varepsilon_{sel}^{muon}(p_T). \end{aligned} \quad (6.6)$$

Combining Equation 6.5 and Equation 6.6, one gets

$$\varepsilon^{event} = \varepsilon_{reco}^{electron}(d_0) \varepsilon_{sel}^{electron}(p_T) \varepsilon_{reco}^{muon}(d_0) \varepsilon_{sel}^{muon}(p_T) \varepsilon_{trigger}. \quad (6.7)$$

To calculate the final efficiency, each of the terms on the right-hand side of the previous equation has to be determined. Generally, the efficiency to pass any cut can be defined as follows,

$$\varepsilon_{cut} = \frac{N_{passed}}{N_{tot}}, \quad (6.8)$$

where N_{tot} is the total number of events in the sample and N_{passed} is the number of events that successfully satisfy the requirement. For each lepton, two efficiencies have to be calculated which can be done by introducing three inclusive sets of cuts and making the appropriate ratios. These sets of cuts will be referred to as "stage", and the following stages are introduced: "Initial", "Reconstructed", and "Selected". The two efficiencies of interest can now be defined as the ratio of the yield of two consecutive stages. For each lepton, the reconstruction efficiency is

$$\varepsilon_{reco} = \frac{N_{Reconstructed}}{N_{Initial}} \quad (6.9)$$

and the selection efficiency is

$$\varepsilon_{sel} = \frac{N_{Selected}}{N_{Reconstructed}}. \quad (6.10)$$

The fifth and last term of the right-hand side of Equation 6.7 is the trigger efficiency, defined as

$$\varepsilon_{trig} = \frac{N_{Preselection+trigger}}{N_{Preselection}}. \quad (6.11)$$

As mentioned above, this efficiency is roughly constant for all the samples and has a value of about 0.95.

The first stage, referred to as 'Initial', includes the loosest set of cuts. It requires one generated electron (muon) coming from a top squark. This lepton must have $p_T > 10$ GeV and $|\eta| < 2.5$. It also requires that the secondary vertex is inside the first layer

of the CMS pixel detector. This corresponds to 30 cm in the axis parallel to the beam pipe and 4 cm in the transverse plane. While the requirement on secondary vertex location is necessary to make the efficiency independent of the top squark lifetime, it also removes events with a longer lifetime. This is acceptable since flight distances beyond 30 cm are well covered by other analyses [84–86].

The second stage, referred to as 'Reconstructed', incorporates all the cuts of the Initial stage, on top of which a reconstructed lepton is required to be within a cone of $\Delta R < 0.5$ with respect to a generated lepton. This cut ensures that the reconstructed lepton is coming from the generated one.

Finally, the 'Selected' stage adds, on top of the Reconstructed one, all the cuts that contain detector-specific variables of the relevant lepton. The list of all the cuts defining the three stages is shown in Table. 6.1.

Table 6.1: Definition of the three inclusive stages. In the Initial stage, all the cuts are applied either on the generated electron (GenElectron), or on the generated muons (GenMuon).

electron	muon
Initial	
1 GenElectron coming from a top squark	1 GenMuon coming from a top squark
1 GenElectron with $v_0 < 4$ cm	1 GenMuon with $v_0 < 4$ cm
1 GenElectron with $\text{abs}(v_z) < 30$ cm	1 GenMuon with $\text{abs}(v_z) < 30$ cm
1 GenElectron with $p_T > 10$ GeV	1 GenMuon with $p_T > 10$ GeV
Reconstructed	
1 electron-GenElectron pair with $\text{deltaR} < 0.05$	1 muon-GenMuon pair with $\text{deltaR} < 0.05$
Selected	
1 electron with $p_T > 25$ GeV	1 muon with $p_T > 25$ GeV
1 electron with non triggering ID	1 muon with tightIDdisplaced
1 electron with $\text{relPFrhoIso} < 0.1$	1 muon with $\text{relPFdBetaIso} < 0.12$

In principle, one has to check that different top squark lifetimes or top squark masses do not yield different efficiencies. More generally, checking the invariability of some values while assuming different inputs is referred to as model dependence testing and this the topic of the next section.

6.1.2 Model dependence

The purpose of this section is to estimate how much the efficiencies are varying with the top squark mass, $m_{\tilde{t}}$, and its average lifetime, $\langle c\tau_{\tilde{t}} \rangle$. Obviously, if there is a non-negligible dependence of the efficiencies with the top squark parameters, it is hard to claim that these efficiencies can also be used for models not involving top squark at all. For this study to be as useful as possible, the efficiencies should not vary too much with the change of the top squark parameters.

The samples used here are the same as the ones used in the Displaced $e\mu$ search. The details on how they were generated and reconstructed can be found in Section 5.1.3. In this chapter, samples with $m_{\tilde{t}}$ of 200, 600 and 1000 GeV and with $\langle c\tau_{\tilde{t}} \rangle$ of 1, 10, 100 and 1000 mm are used, for a total of twelve samples.

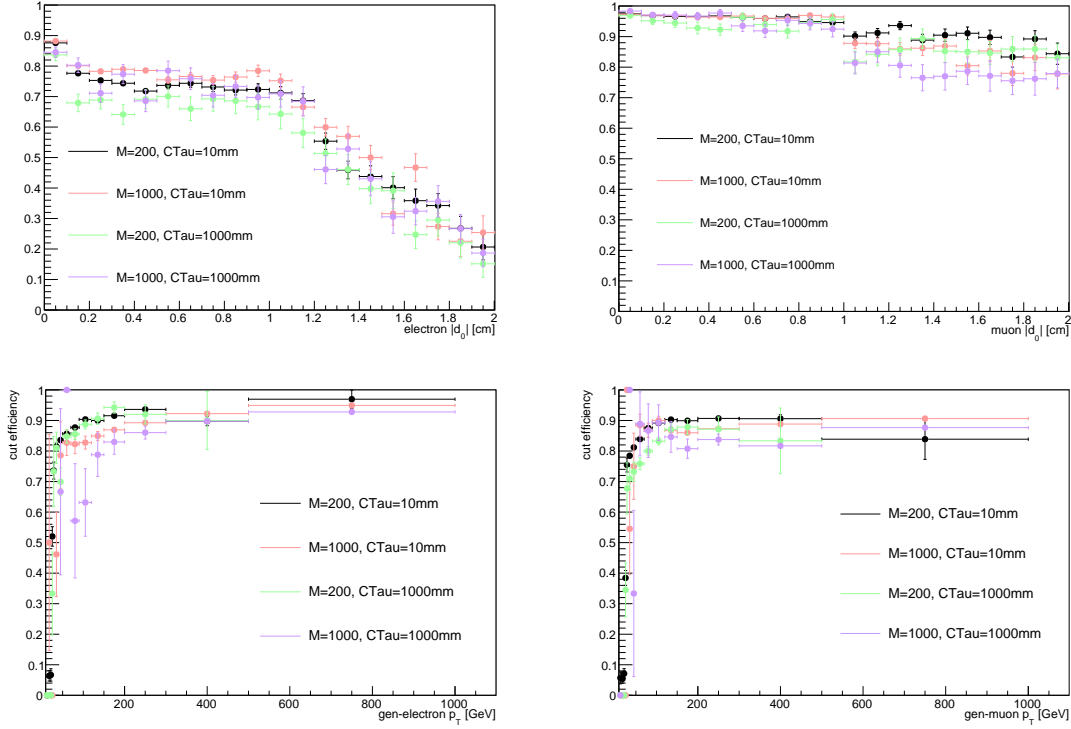


Figure 6.1: Reconstruction efficiency as a function of generated lepton d_0 for the electrons (top left) and for the muons (top right) and selection efficiency as a function of generated lepton p_T for the electrons (bottom left) and for the muons (bottom right), for four samples with different $m_{\tilde{t}}$ and $\langle c\tau_{\tilde{t}} \rangle$.

Figure 6.1 depicts the reconstruction efficiencies (top) and the selection efficiencies (bottom) of a single electron (left) and muon (right) for four different samples. To make the graph easily readable, the efficiencies of only four samples out of the twelve are shown. Inspecting the four graphs of Figure 6.1, it seems that all samples seem to agree with each other within roughly 10%. Keeping in mind that the goal of this study is to get a rough estimate of the yield, this agreement is sufficient. The biggest disagreement comes from the low p_T bins of the electron selection efficiency for the sample with a $m_{\tilde{t}}$ of 1000 GeV and $\langle c\tau_{\tilde{t}} \rangle$ of 1000 mm. However, the statistical uncertainties are big. This is to be expected for this sample as high $\langle c\tau_{\tilde{t}} \rangle$ samples yield lower reconstruction efficiency and the low p_T bins are less likely to be filled for high $m_{\tilde{t}}$ samples.

An interesting trend can be observed in the muons reconstruction efficiency for d_0 larger than 1 cm. The efficiency for the sample with $m_{\tilde{t}}$ of 200 GeV and $\langle c\tau_{\tilde{t}} \rangle$ of 10 mm (black) is systematically and significantly higher than the efficiency for the sample with a top squark mass of 1000 GeV and a lifetime of 10 mm (red). A similar trend is observed for the selection efficiency for both leptons. In general, the reconstruction

and selection efficiencies are higher for low top squark mass and low top squark lifetime samples as compared to samples with higher top squark mass and lifetime. However, it is really important to keep in mind that, even if these trends might introduce a bias, the goal of the study is to provide to model builder an easy and fast way to allow them to get a rough estimate. For this purpose, the efficiencies are definitely close enough to each other to be used. Indeed, as it will be discussed in Section 6.1.4, the systematic uncertainty for these studies is typically quite big. The next step is to produce a single set of efficiency. The merging procedure used to achieve this is explained in the next section.

6.1.3 Results

As observed in the previous section, the efficiencies are similar for a wide range of $m_{\tilde{t}}$ and $\langle c\tau_{\tilde{t}} \rangle$ hypotheses. It would be confusing and redundant to publish one set of four efficiencies for each sample. In this section, the information of the twelve samples is used and is merged to give a single set of four efficiencies.

A priori, different ways of merging the efficiency curves are possible. The most straight forward way to proceed would be to calculate the efficiency by dividing the sum of the yield obtained in the Reconstructed stage with the sum of the yield in the Initial stage. However, since samples with low mass have a much larger cross-section this would result in a reconstruction efficiency largely driven by the low top squark mass samples. Since there is no obvious reason why certain samples should be preferred as compared to others, the numerator and the denominator histograms are weighted by one over the number of events in the denominator. The resulting efficiencies are defined as the ratio of the sum of all the numerators to the sum of all denominators. Hence, for each lepton, the reconstruction efficiency is

$$\varepsilon_{reco}^l(d_0) = \frac{\sum_i^M \sum_j^{LT} N_{Reconstructed}^{l,ij} W^{l,ij}}{\sum_i^M \sum_j^{LT} N_{Initial}^{l,ij} W^{l,ij}} \quad (6.12)$$

and the selection efficiency is

$$\varepsilon_{sel}^l(p_t) = \frac{\sum_i^M \sum_j^{LT} N_{Selected}^{l,ij} W^{l,ij}}{\sum_i^M \sum_j^{LT} N_{Reconstructed}^{l,ij} W^{l,ij}}, \quad (6.13)$$

where l labels the lepton flavour, i the mass of the top squark, j its lifetime and $W^{l,ij}$ one over the total number of entries of the corresponding histogram.

The resulting efficiencies are depicted in Figure 6.2. These four curves have been published [90, 91] and used to set limits on alternative models [92] as it will be discussed shortly in Section 6.2. In the next section, the validity and accuracy of the recipe will be assessed. This kind of test is commonly referred to as a "closure test".

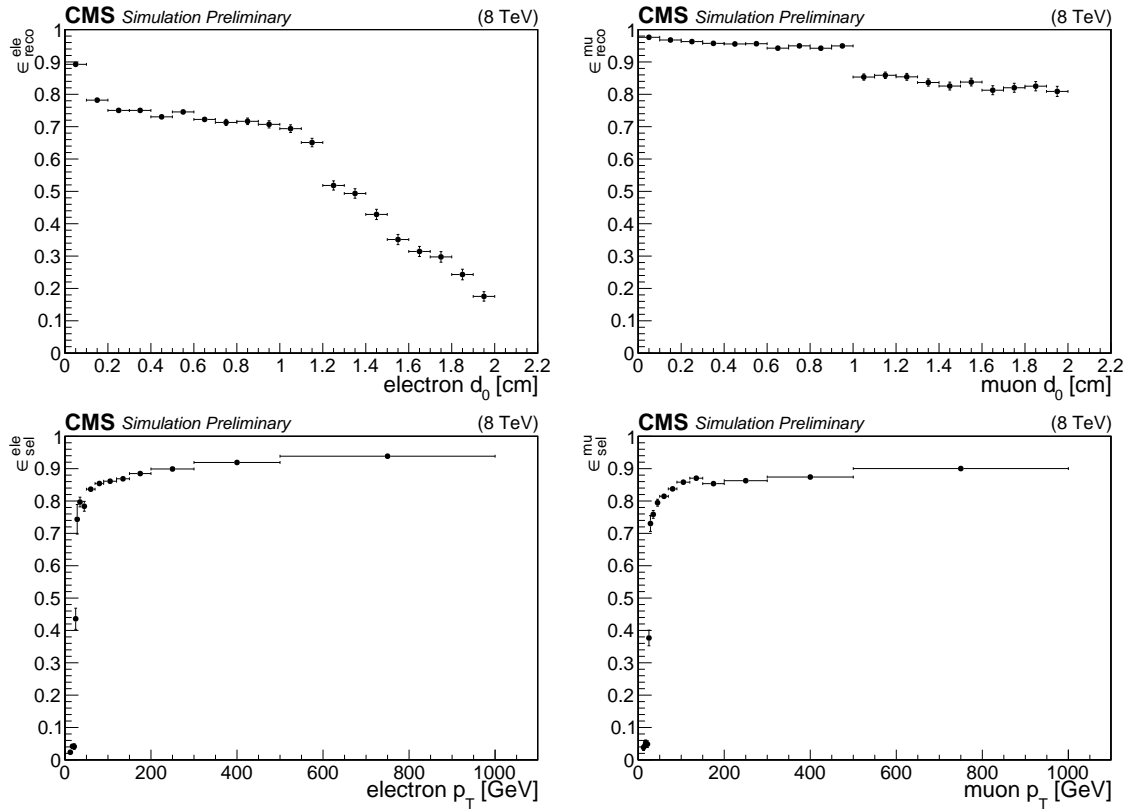


Figure 6.2: Average reconstruction efficiency as a function of generated lepton d_0 for the electrons (top left) and for the muons (top right) and average selection efficiency as a function of generated lepton p_T for the electrons (bottom left) and for the muons (bottom right), after merging the twelve samples used in this study.

6.1.4 Closure test

In Section 6.1.1, more specifically in Equation 6.4, it was claimed that the yield that would be observed in a real analysis with the CMS detector can be estimated using generated quantities and the set of efficiencies provided in the previous section. The goal of this section is to verify how accurate this claim is.

On the one hand, the yield is obtained by applying the preselection cuts to reconstructed quantities using the full CMS reconstruction simulation. On the other hand, the yield is obtained by applying the cuts on the generated quantities and by applying the weight given in Figure 6.2 which corresponds to the recipe available to models builders. A schematic of this procedure is shown in Figure 6.3.

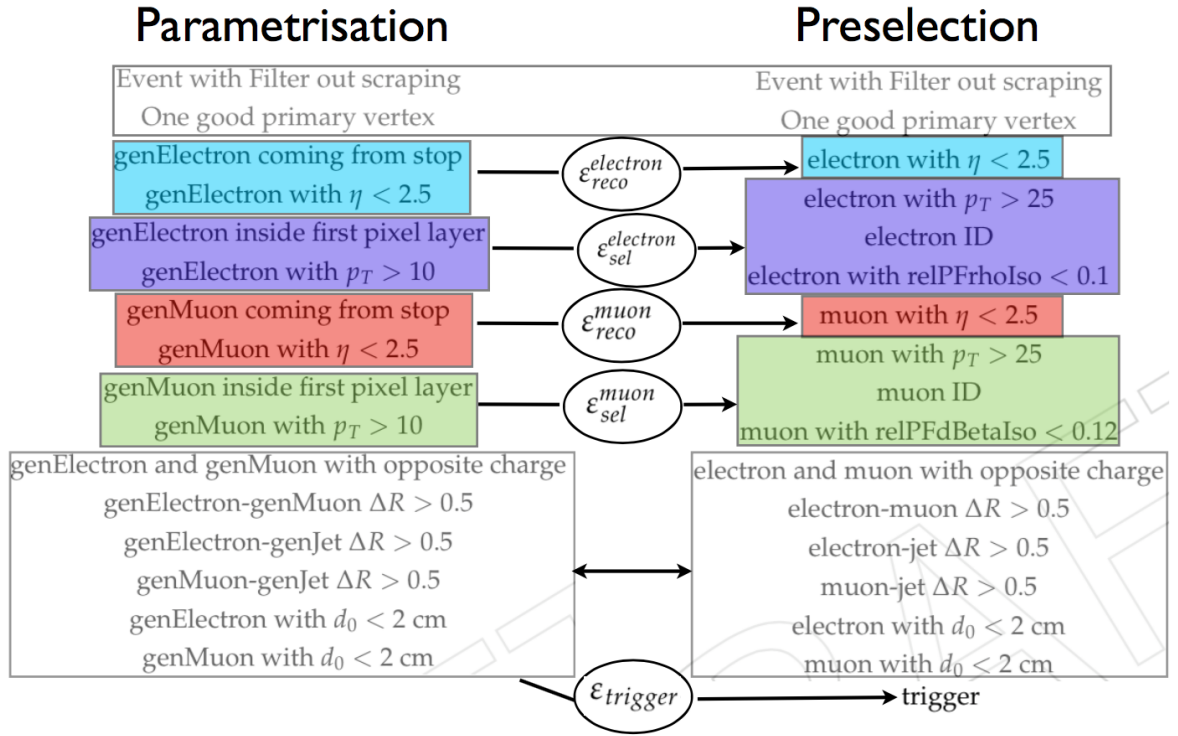


Figure 6.3: Schematics of the correspondence between the actual preselection applied on reconstructed quantities and its analogue applied on generated quantities.

Let R be the ratio between the yield obtained with cuts applied on simulated quantities and the yield obtained with cuts applied on reconstructed quantities. A ratio of one corresponds to the case where the recipe gives the exact same yield as the actual estimation from the full CMS reconstruction algorithm while a ratio bigger than one corresponds to the case where it overestimates the yield. The ratio obtained for all the signal samples is shown in Figure 6.4. A figure of merit (FOM) is now introduced to quantify the overall agreement as,

$$FOM = \frac{\sqrt{\sum_i (R_i - 1)^2}}{N}, \quad (6.14)$$

where i runs over all of the samples and N is the number of samples. With this formula, an overall agreement of 17% is observed which is good enough for that kind of studies. By comparing the four values of the ratio for a fixed mass with the same four values with a bigger lifetime, a clear trend is observed. The ratio is increasing with the increase of $m_{\tilde{t}}$. This observation is compatible with the trend observed in Figure 6.2. Because of this bias, the user of this parametrisation is suggested to take a conservative uncertainty of 25%. While this uncertainty may seem fairly large, one has to keep in mind that the intention of this parametrisation is to allow model builders to get an approximate yield on some models without actually performing a dedicated search. For that purpose, this uncertainty is reasonable and comparable to similar studies.

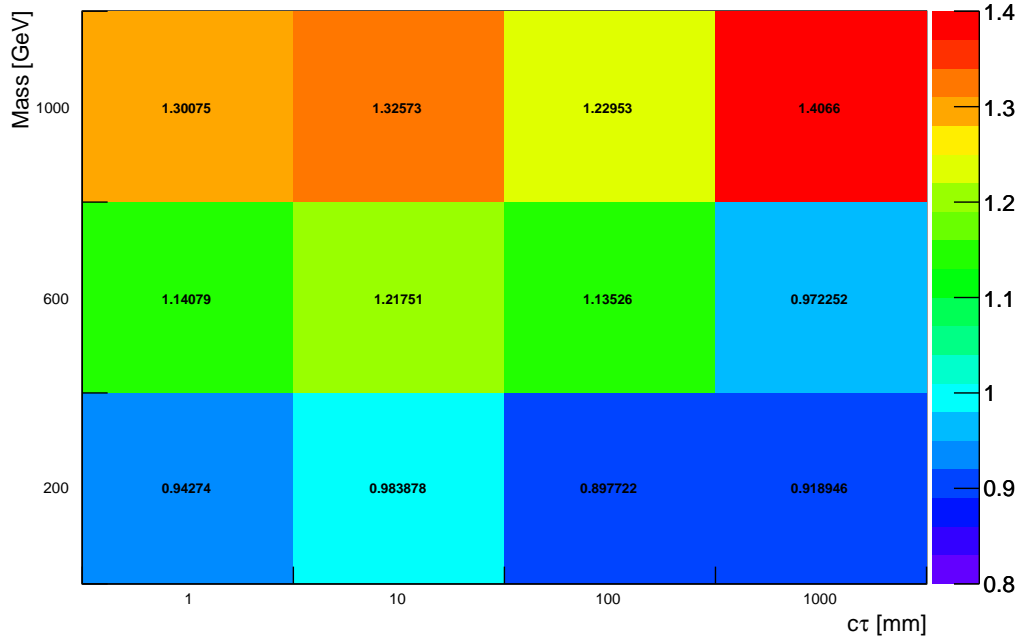


Figure 6.4: Ratio between the yield obtained with generator level quantities and with the standard preselection for all the signal samples considered in this study.

6.2 Parametrisation: use example

When new models are created by theoretical physicists, the constraints on these are typically very weak. If each of these models would require a dedicated search, it would take a very long time to put strong constraints on all of them. In that regard, it is crucial that constraints on a specific model can be translated into constraints on other models, which is precisely the goal of creating tools such as the one described in the previous section. In this section, a specific example where the results presented in Chapters 5–6 have been used by theorists outside the CMS community to set limits on various models will be reviewed. All the graphs shown in the following section are directly extracted from the paper entitled "Long-Lived Staus and Displaced Leptons at the LHC" [92]. This study is shortly summarised in this thesis in order to show the power of the parametrisation.

Firstly, some models, to which some of the LHC searches are sensitive, will be listed, in Section 6.2.1. In Section 6.2.2, using the recasting tools provided by these searches, the current limits on long-lived staus will be assessed.

6.2.1 Description of models giving rise to long-lived staus

A lot of models such as gauge-mediated SUSY breaking [93], RPV SUSY [27], and mini-split SUSY [94] can give rise to a final state containing some leptons with macroscopic displacement. Generally, these models are well constrained by dedicated LHC searches. However, the constraints on models predicting leptons which are the only visible object (solitary leptons) are almost unconstrained. Solitary leptons can arise in many models, for example in gauge-mediated SUSY breaking models. In this case, the right-handed stau, $\tilde{\tau}_R$, can be the next-to-lightest supersymmetric particle (NLSP) while the gravitino, \tilde{G} , is the lightest supersymmetric particle. The lifetime of a stau decaying to a tau and a gravitino, $\tilde{\tau} \rightarrow \tau \tilde{G}$, can be approximated by

$$c\tau_{\tilde{\tau}} \approx 100 \mu m \left(\frac{100 \text{ GeV}}{m_{\tilde{\tau}}} \right)^5 \left(\frac{\sqrt{F}}{100 \text{ TeV}} \right)^4, \quad (6.15)$$

where \sqrt{F} is the SUSY-breaking scale. As it can be seen in the previous equation, even low SUSY-breaking scale yields macroscopic displacement that can potentially be resolved by LHC searches. Obviously, depending on the SUSY-breaking scale, the lifetime of the stau can vary greatly. Several benchmark models are considered in [92] for the production of the long-lived stau.

- Direct $\tilde{\tau}_R$ production where the stau is the only next-to-lightest supersymmetric particle.
- Direct slepton production where all the sleptons are nearly degenerate. The assumption made here is that the selectron and the smuon have the same mass while the stau is slightly heavier. More specifically, they satisfy the following equations: $m_{\tilde{e}_R} = m_{\tilde{\mu}_R} = m_{\tilde{\tau}_R} + 10 \text{ GeV}$.

- Higgsino production with prompt decays $\tilde{H}^\pm \rightarrow \tilde{\tau}_R^\pm \nu$, and $\tilde{H}^0 \rightarrow \tilde{\tau}_R^\pm \tau^\mp$.
- Top squark production with prompt decay $\tilde{t} \rightarrow b\tilde{H}^+ \rightarrow b\nu\tilde{\tau}_R^\pm$.
- Majorana gluino production with prompt decay $\tilde{g} \rightarrow \tilde{t}\bar{t} \rightarrow \bar{t}bH^+ \rightarrow \bar{t}b\nu\tilde{\tau}_R^+$.

6.2.2 Current limits on long-lived staus

The following four analyses are the most sensitive to next-to-lightest supersymmetric particle stau: CMS disappearing tracks (DT) search [84], ATLAS disappearing tracks [85] search, CMS Heavy stable charged particle (HSCP) search [86], and the Displaced $e\mu$ search described in this thesis. Using the results and the recasting tools provided by these four analyses, limits are set on the long-lived staus produced by the benchmark models introduced in the previous section. As it can be seen in Figure 6.5, the limits set by these analyses are complementary. Indeed, for low lifetime, $c\tau \approx 1$ cm, the Displaced $e\mu$ search from this thesis sets the strongest constraints, for moderate lifetime, $c\tau \approx 50$ cm, it is the DT searches that are the most sensitive, and finally, the most stringent limits are set by the HSCP search for longer lifetime, $c\tau \approx 1$ m. From these limits, one can conclude that the parameter space for long-lived staus is only sparsely covered. In order to improve the coverage for these kinds of models, an extended version of the analysis presented in Chapter 5 is exposed in the next chapter by extending to ee and $\mu\mu$ final states.

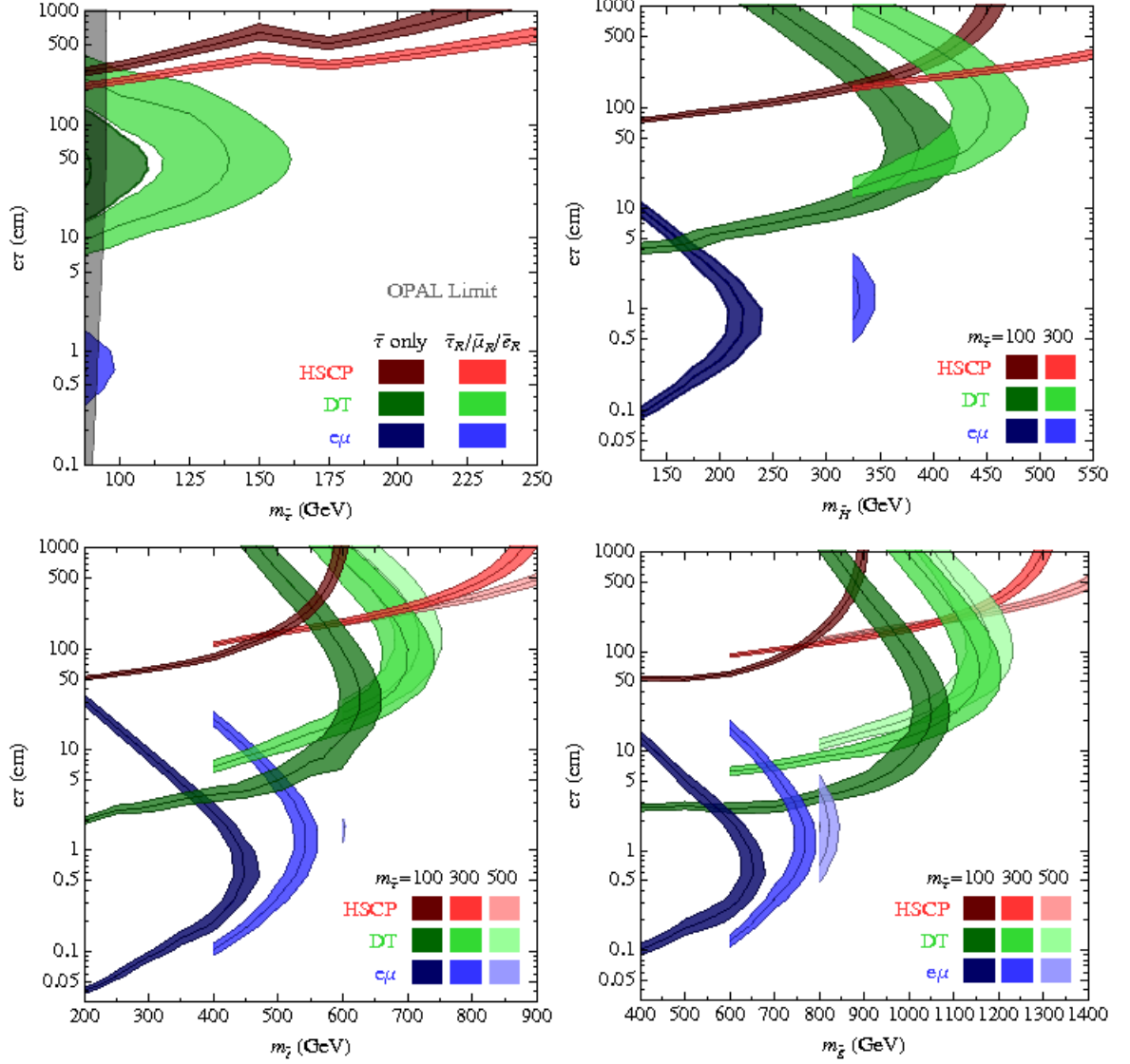


Figure 6.5: Constraints on long-lived staus with various production mechanism assumptions by the Displaced $e\mu$ search presented in Chapter 5 (blue), the DT searches (green), and the HSCP search (red) taken from [92]. **Top Left:** Constraints on direct production of stau next-to-lightest supersymmetric particle (dark shades) as well as for nearly degenerate sleptons (bright shades). **Top right:** Constraints on Higgsino production with a mass assumption of 100 GeV (dark shades) and 300 GeV (bright shades). **Bottom left:** Constraints on production right-handed top squarks with mass assumption of 100 GeV (dark shades), 300 GeV (bright shades), and 500 GeV (light shades). For all these scenarios the following assumption was made: $m_{\tilde{t}} = m_{\tilde{H}^+} + 50$ GeV. **Bottom right:** Constraints on production of Majorana gluinos with a mass assumption of 400 GeV (dark shades), 600 GeV (bright shades), and 800 GeV (light shades).

Search for Displaced Supersymmetry in events with same-flavour leptons with large impact parameters at 13 TeV

The search presented in Chapter 5 was the first LHC search optimised for the Displaced Supersymmetry model. A slightly improved version of this search was performed at 13 TeV in the $e\mu$ final state [95], hereafter referred to as the Displaced $e\mu$ search at 13 TeV. However, adding same-flavour final states is crucial to cover any gap left by the previous searches. Indeed, in the case where the signal would give rise to a final state with two muons or two electrons, the search presented in Chapter 5 would have no sensitivity. The purpose of this chapter is precisely to cover this gap. It is very similar¹ to the Displaced $e\mu$ search at 8 TeV with the important exception that final states with same-flavour leptons are examined. The search presented in this chapter will be further referred to as the Displaced same-flavour leptons search at 13 TeV and is sensitive to a broader range of models and will complement and is expected to significantly improve the limits obtained by the Displaced $e\mu$ search at 13 TeV.

Section 7.1 catalogues the list of samples used in this search. Section 7.2 describes all the corrections that have been applied to correct the simulated samples as well as some explanation on how these corrections were derived. The event selection is explained in Section 7.3. Section 7.4 exposes the background estimation techniques that have been used to assess the contribution of the Standard Model backgrounds. The effect of the systematic uncertainties on the final result is addressed in Section 7.5. Finally, the result is given in Section 7.6 where the limits on Displaced Supersymmetry are set.

¹Because of the similarities between this search and the one presented in Chapter 5, the focus will be on the differences of the two analyses.

7.1 Data and Monte Carlo simulation samples

Once again, the list of data samples can be divided into three categories: data, background and signal.

The data samples used are described in Section 7.1.1, the Standard Model background samples are listed in Section 7.1.2, and the signal samples are exposed in Section 7.1.3.

7.1.1 Data samples

This analysis uses proton-proton collision data collected by the CMS detector in 2015 at $\sqrt{s} = 13$ TeV. This corresponds to an integrated luminosity of 2.6 fb^{-1} which is roughly a factor seven less than the one in the previous search. However, due to the change of the centre-of-mass energy from 7 TeV to 13 TeV, the top squark production cross-section is significantly increased, as it will be detailed in Section 7.1.3. The `DoubleEG` (`DoubleMu`) primary dataset is used as the search sample for the ee ($\mu\mu$) final state. The `SingleElectron` and the `SingleMu` dataset are used to estimate the background contribution of the QCD multi-jet background. Trigger efficiencies are determined using the `MET` dataset. Finally, a study to estimate the tracking efficiency of displaced tracks was performed using the `NoBPTX` dataset.

These datasets, as well as their main purpose, are summarised in Table 7.1.

Table 7.1: List of data samples used for the analysis.

full name of the dataset	alias used	purpose
<code>DoubleEG_Run2015D-16Dec2015-v1_MINIAOD</code>	<code>DoubleEG</code>	discovery
<code>DoubleMuon_Run2015D-16Dec2015-v1_MINIAOD</code>	<code>DoubleMuon</code>	discovery
<code>SingleElectron_Run2015D-16Dec2015-v1_MINIAOD</code>	<code>SingleElectron</code>	QCD estimate
<code>SingleMuon_Run2015D-16Dec2015-v1_MINIAOD</code>	<code>SingleMuon</code>	QCD estimate
<code>MET_Run2015D-16Dec2015-v1_MINIAOD</code>	<code>MET</code>	trigger efficiency correction factor
<code>NoBPTX_Run2015D-16Dec2015-v1_MINIAOD</code>	<code>NoBPTX</code>	displaced tracking performance

7.1.2 Standard Model background from simulation

The backgrounds to be considered in this search are very similar to the ones considered in the search presented in Chapter 5. However, the background contribution from the Drell-Yan process is expected to be much higher in the same-flavour final states, at least in the prompt control region. Indeed, in the previous search, the contribution from Drell-Yan processes was coming from $Z \rightarrow \tau\tau$ decay followed by $\tau \rightarrow e + 2\nu$ and $\tau \rightarrow \mu + 2\nu$ which is roughly a factor 40 smaller than $Z \rightarrow \mu\mu$ or $Z \rightarrow ee$. One more

time, it is convenient to merge multiple processes into a composite dataset. All the QCD backgrounds samples are listed in Table 7.2 while all the non-QCD backgrounds samples are shown in Table 7.3.

Table 7.2: Full dataset names for simulated samples used to model QCD events.

Composite Dataset Name	Individual Dataset Name	Individual Dataset Full Name
<i>QCD MuEnriched</i>	<i>QCD Mu† p_T</i> 15 – 20	QCD_Pt-15to20_Mu†Pt5_vGT_PC_M
	<i>QCD Mu† p_T</i> 20 – 30	QCD_Pt-20to30_Mu†Pt5_vGT_PC_M
	<i>QCD Mu† p_T</i> 30 – 50	QCD_Pt-30to50_Mu†Pt5_vGT_PC_M
	<i>QCD Mu† p_T</i> 50 – 80	QCD_Pt-50to80_Mu†Pt5_vGT_PC_M
	<i>QCD Mu† p_T</i> 80 – 120	QCD_Pt-80to120_Mu†Pt5_vGT_PC_M
	<i>QCD Mu† p_T</i> 120 – 170	QCD_Pt-120to170_Mu†Pt5_vGT_PC_M
	<i>QCD Mu† p_T</i> 170 – 300	QCD_Pt-170to300_Mu†Pt5_vGT_PC_M
	<i>QCD Mu† p_T</i> 300 – 470	QCD_Pt-300to470_Mu†Pt5_vGT_PC_M
	<i>QCD Mu† p_T</i> 470 – 600	QCD_Pt-470to600_Mu†Pt5_vGT_PC_M
	<i>QCD Mu† p_T</i> 600 – 800	QCD_Pt-600to800_Mu†Pt5_vGT_PC_M
	<i>QCD Mu† p_T</i> 800 – 1000	QCD_Pt-800to1000_Mu†Pt5_vGT_PC_M
	<i>QCD Mu† p_T</i> 1000 – <i>Inf</i>	QCD_Pt-1000toInf_Mu†Pt5_vGT_PC_M
<i>QCD EMEnriched</i>	<i>QCD EM† p_T</i> 15 – 20	QCD_Pt-15to20_EM†_vGT_PC_M
	<i>QCD EM† p_T</i> 20 – 30	QCD_Pt-20to30_EM†_vGT_PC_M
	<i>QCD EM† p_T</i> 30 – 50	QCD_Pt-30to50_EM†_vGT_PC_M
	<i>QCD EM† p_T</i> 50 – 80	QCD_Pt-50to80_EM†_vGT_PC_M
	<i>QCD EM† p_T</i> 80 – 120	QCD_Pt-80to120_EM†_vGT_PC_M
	<i>QCD EM† p_T</i> 120 – 170	QCD_Pt-120to170_EM†_vGT_PC_M
	<i>QCD EM† p_T</i> 170 – 300	QCD_Pt-170to300_EM†_vGT_PC_M
	<i>QCD EM† p_T</i> 300 – <i>Inf</i>	QCD_Pt-300toInf_EM†_vGT_PC_M
<i>QCD bcToE</i>	<i>QCD bcToE p_T</i> 15 – 20	QCD_Pt_15to20_bcToE_vGT_PC_M
	<i>QCD bcToE p_T</i> 20 – 30	QCD_Pt_20to30_bcToE_vGT_PC_M
	<i>QCD bcToE p_T</i> 30 – 80	QCD_Pt_30to80_bcToE_vGT_PC_M
	<i>QCD bcToE p_T</i> 80 – 170	QCD_Pt_80to170_bcToE_vGT_PC_M
	<i>QCD bcToE p_T</i> 170 – 250	QCD_Pt_170to250_bcToE_vGT_PC_M
	<i>QCD bcToE p_T</i> 250 – <i>Inf</i>	QCD_Pt_250toInf_bcToE_vGT_PC_M

Global tag = PU25nsData2015v1_76X_mcRun2_asymptotic_v12 := GT_

Production Campaign = RunIIFall15MiniAODv2 := PC_

Format = MINIAODSIM := M

Enriched := †

Table 7.3: Full dataset names for simulated samples used to model non-QCD events.

Composite Dataset Name	Individual Dataset Name	Individual Dataset Full Name
<i>Diboson</i>	$WZ \rightarrow qqll\nu qq$	WZToLNu2QorQQ2L_vGT_PC_M
	$WW \rightarrow l\nu l\nu$	WWTo2L2Nu_vGT_PC_M
	$WZ \rightarrow l\nu\nu\nu$	WZTo1L3Nu_vGT_PC_M
	$WZ \rightarrow lll\nu$	WZTo3L3Nu_vGT_PC_M
	$ZZ \rightarrow qq\nu\nu$	ZZTo2Q2Nu_vGT_PC_M
	$ZZ \rightarrow llqq$	ZZTo2L2Q__vGT_PC_M
	$ZZ \rightarrow ll\nu\nu$	ZZTo2L2Nu_vGT_PC_M
	$ZZ \rightarrow llll$	ZZTo4L_vGT_PC_M
	$W\gamma \rightarrow l\nu\gamma$	WGToLNuG_vGT_PC_M
	$Z\gamma \rightarrow ll\gamma$	ZGTo2LG_vGT_PC_M
<i>W Jets</i>	$W \rightarrow l\nu$	WJetsToLNu_vGT_PC_M
<i>Drell – Yan</i>	$Z \rightarrow l^+ l^- M(50)$	DYJetsToLL_M-50_vGT_PC_M
<i>SingleTop</i>	<i>Single top (tW)</i>	ST_tW_top_5f_NoFullyHadronicDecays_vGT_PC_M
	<i>Single top ($\bar{t}W$)</i>	ST_tW_antitop_5f_NoFullyHadronicDecays_vGT_PC_M
<i>TT Jets</i>	$t\bar{t}$ (<i>fully leptonic</i>)	TTJets_DiLept_vGT_PC_M
	$t\bar{t}$ (<i>single lepton from t</i>)	TTJets_SingleLeptFromT_vGT_PC_M
	$t\bar{t}$ (<i>single lepton from \bar{t}</i>)	TTJets_SingleLeptFromTbar_vGT_PC_M
Global tag = PU25nsData2015v1_76X_mcRun2_asymptotic_v12 := GT_		
Production Campaign = RunIIFall15MiniAODv2 := PC_		
Format = MINIAODSIM := M		

7.1.3 Signal process simulation

In this search, samples of the process $pp \rightarrow \tilde{t}_1 \tilde{t}_1^*$, with the top squarks decaying via $\tilde{t}_1 \rightarrow bl$, are used as a benchmark model. These samples were produced using the same assumptions as the ones described in Section 5.1.3. The only difference lies in the production cross-section which is a function of the centre-of-mass energy. Table 7.4 shows the production cross-sections for each mass hypothesis which is calculated by the LHC SUSY Cross Section Working Group [96]. The comparison of Table 5.7 and Table 7.4 highlights the increase of the production cross-section for a higher centre-of-mass energy. For example, the increase of the production cross-section at 13 TeV from the production cross-section at 7 TeV is almost a factor four for $m_{\tilde{t}} = 200$ GeV, almost seven for $m_{\tilde{t}} = 600$ GeV, and more than 14 for $m_{\tilde{t}} = 1000$ GeV.

Table 7.4: Production cross-section of the signal processes.

Dataset Name	Cross-section(pb^{-1})
$\tilde{t}\tilde{t} \ M(200) \ c\tau(*)$	64.5085 ± 9.2955
$\tilde{t}\tilde{t} \ M(300) \ c\tau(*)$	8.51615 ± 1.18564
$\tilde{t}\tilde{t} \ M(400) \ c\tau(*)$	1.83537 ± 0.25142
$\tilde{t}\tilde{t} \ M(500) \ c\tau(*)$	0.51848 ± 0.06937
$\tilde{t}\tilde{t} \ M(600) \ c\tau(*)$	0.174599 ± 0.023060
$\tilde{t}\tilde{t} \ M(700) \ c\tau(*)$	0.0670476 ± 0.0089461
$\tilde{t}\tilde{t} \ M(800) \ c\tau(*)$	0.0283338 ± 0.0040152
$\tilde{t}\tilde{t} \ M(900) \ c\tau(*)$	0.0128895 ± 0.0019595
$\tilde{t}\tilde{t} \ M(1000) \ c\tau(*)$	0.00615134 ± 0.0010024
$\tilde{t}\tilde{t} \ M(1100) \ c\tau(*)$	0.00307413 ± 0.0005330
$\tilde{t}\tilde{t} \ M(1200) \ c\tau(*)$	0.00159844 ± 0.0002960
$< c\tau >$ in cm, either 0.1, 1, 10, or 100	

7.2 Corrections to Monte Carlo simulations

As already outlined in Section 3.4.2, it is known that the Monte Carlo simulation does not reproduce the data perfectly. To mitigate this difference, various corrective factors are applied to the Monte Carlo samples. These corrections are discussed in this section.

The correction factors that account for the difference in pileup scenarios will be exposed in Section 7.2.1. The lepton reconstruction and identification efficiencies corrections are discussed in Section 7.2.2. Finally, the trigger correction factor will be shown in Section 7.2.3.

7.2.1 Event pileup correction

The method used here is the same as the one explained in Section 3.4.2 and used in Section 5.2.1.

7.2.2 Lepton reconstruction and identification efficiencies corrections

As mentioned in Section 3.4.2.2 and, to avoid duplication of many months of work, the CMS collaboration publishes centrally produced correction factors for the whole collaboration for an agreed set of selection cuts. In the previous version of the analysis, using the tag and probe method described in Section 3.4.2.2, it was demonstrated that the correction factors without the cut related on the impact parameters were very similar to the values determined for the standard lepton selection. For that reason, those correction factors [97, 98] will be used in this analysis.

7.2.3 Trigger efficiency corrections

All the triggers used for the analysis are selecting on photons or muons. In order to remove potential biases, events collected from an orthogonal dataset are used to determine the efficiency. The $\text{jet}/E_{\text{T}}^{\text{miss}}$ data stream is an adequate candidate because there is no requirement applied to leptons or photons. As the background contribution coming from QCD is directly estimated from the data, one wants to have a sample depleted of QCD while still containing some leptons. Unlike the Displaced $e\mu$ search analysis presented in Chapter 5, the contribution from Drell-Yan processes is significant. For this reason, additional $t\bar{t}$ enriching cuts are not applied in this study. The standard analysis selection is applied with the exception that the p_{T} cuts are removed. Only triggers that are not prescaled and that are the same for Monte Carlo and data are used. These triggers are listed in Table 7.5.

Figure 7.1 shows the analysis trigger efficiency as a function of the lepton's p_{T} (top) and $|\eta|$ (bottom) for electrons (left) and muons (right). The trigger efficiency is calculated for $t\bar{t}$ Monte Carlo, Drell-Yan Monte Carlo, and data. In principle, the trigger correction factor is equated as the ratio of the data trigger efficiency to the Monte Carlo trigger efficiency. However, the statistical uncertainties are quite large,

Table 7.5: $\text{jet}/E_{\text{T}}^{\text{miss}}$ trigger names.

trigger name
HLT_PFMET170_v*
HLT_PFMET120_NoiseCleaned_BTagCSV0p72_v*
HLT_PFMET120_BTagCSV0p72_v*
HLT_CaloMHTNoPU90_PFMET90_NoiseCleaned_PFMHT90_IDTight_v*

and no clear conclusion can be drawn on the agreement between data and simulation. For this reason, correction factors related to the trigger efficiency are not applied in this search and differences are used as systematic uncertainties.

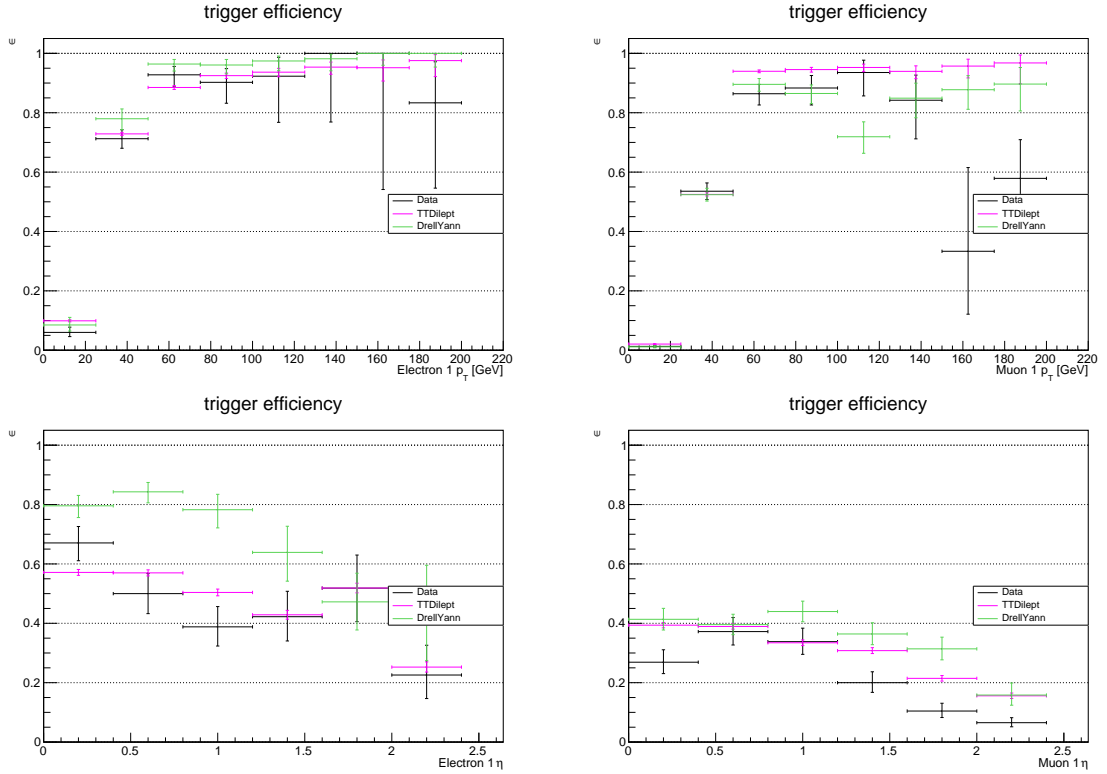


Figure 7.1: Analysis trigger efficiency calculated for $t\bar{t}$ Monte Carlo (purple), Drell-Yan Monte Carlo (green), and data (black). The trigger efficiencies are shown as function of the electron's p_{T} (top left), muon's p_{T} (top right), electron's $|\eta|$ (bottom left), and muon's $|\eta|$ (bottom right).

7.3 Event selection and definition of control and signal regions

Like in Chapter 5, various signal and background enriched regions are defined by applying different selection criteria. A list of regions have been defined and each one of them will be explained in details in the following sections. Table 7.6 summarises the list of all the regions defined in this analysis. It contains a short description, the name, the list of requirements, the purpose and the section where the regions are described. In this section, the first three regions will be exposed while the other will be discussed in the next one. These regions have similar requirements, but they differ in the displacement of their leptons.

Once again, a common selection called preselection is applied on the prompt control region, the displaced control region, and the signal regions. The exact definition of the preselection applied in this search has been slightly modified with respect to the previous one and is detailed in Section 7.3.1. The prompt control region is used to check the accuracy of the Monte Carlo simulation and is discussed in Section 7.3.2. The displaced control region, which definition has been slightly altered, aims at estimating the contribution from QCD in the signal regions and is exposed in Section 7.3.3. Finally, the signal region, which has been designed to contain as many events from the signal process while being depleted of background, is defined in Section 7.3.4. Figure 7.2 shows a schematic representation of the prompt control region, the displaced control region, and the signal region in the 2D plane of the leptons' d_0 . The differences between Figure 7.2 and Figure 5.10 are the following: first, the upper bound on the signal regions has been extended from 2 cm to 10 cm, secondly, the displaced control region is populated by events where both leptons' d_0 values are between 0.01 cm and 0.02 cm, and, finally, the hybrid control regions are not defined as they will not be used. All the events must have satisfied the preselection, and the difference between the regions only lies in the d_0 requirement.

7.3.1 Preselection

For the $\mu\mu$ final state, events are required to pass either the HLT_DoubleMu23NoFiltersNoVtxDisplaced trigger, which has been designed for this search by removing some d_0 related cuts, or the HLT_DoubleMu33NoFiltersNoVtx trigger. These two triggers yield a better efficiency for displaced muons [99] and, for that reason, the d_0 range has been extended up to 10 cm. The HLT_Photon36_R9Id85_OR_CaloId24b40e_Iso50T80L_Photon22_AND_HE10_R9Id65_Eta2_Mass15 trigger is used for the ee final state. Requiring two photons instead of two electrons considerably increases the efficiency for displaced electrons as the requirements on the track of the electrons are absent and at electromagnetic calorimeter-level photons and electrons are almost identical.

Stable particles, such as muons and electrons, are reconstructed with the particle-flow algorithm described in Section 3.2.2. Leptons are required to have their absolute pseudorapidity smaller than 2.4 in order to ensure that they are well inside the tracker.

Table 7.6: List of all the regions defined in this analysis. Each line contains a short description, the name, the list of requirements, the purpose and the section of description of the corresponding region.

description	name	selection	purpose	section
prompt lepton control region	PCR	preselection and $d_0 < 0.01$ cm	checks the accuracy of MC simulation	7.3.2
displaced control region	DCR	preselection and $0.01 < d_0 < 0.02$ cm	gets the normalisation of the QCD for the data-driven method	7.3.3
signal regions	SRs	preselection and $0.02 \text{ cm} < d_0$	signal enriched region, split in three sub-regions	7.3.4
$b\bar{b}$ + lepton control region	BBLCR	$b\bar{b}$ enriched cut	determines the transfer factors from QCD enriched d_0 distribution	7.4.1.1
Loose-iso displaced control region	LIDCR	preselection and $0.01 < d_0 < 0.02$ cm but with I_{rel} cut relaxed	validation of the QCD data-driven method (closure test)	7.4.1.4

Prompt Control Region (PCR):

2 Good leptons with both d_0 in $[0; 0.01]$ cm
 $\Delta R(\text{lepton1}, \text{lepton2}) > 0.5$; $q_1 \cdot q_2 = -1$

Displaced Control Region (DCR):

2 Good leptons with both d_0 in $[0.01; 0.02]$ cm
 $\Delta R(\text{lepton1}, \text{lepton2}) > 0.5$; $q_1 \cdot q_2 = -1$

Signal Region (SR):

2 Good leptons with both d_0 in $[0.02; 10]$ cm
 $\Delta R(\text{lepton1}, \text{lepton2}) > 0.5$; $q_1 \cdot q_2 = -1$

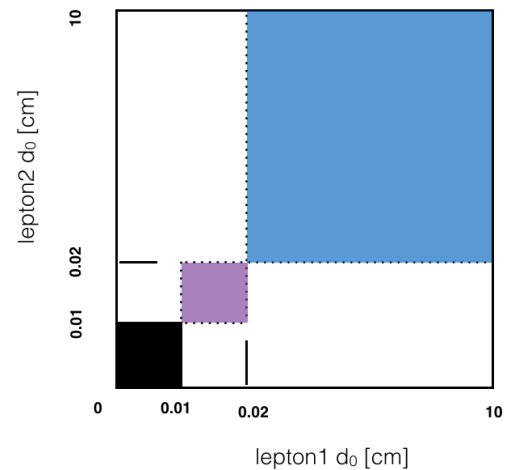


Figure 7.2: Schematic of various regions defined in the 2D plane of the leptons' d_0 after the standard preselection.

In addition, leptons must have their p_T well above the trigger thresholds. Electrons (muons) are selected if they have a p_T larger than 42 GeV (40 GeV). Finally, leptons should be well identified and isolated.

Electron candidates are required to pass the tight working point of the cuts recommended by the CMS collaboration [100] with the exception that the cuts related to the impact parameters have been removed. Additionally, electrons that have been seeded by a crystal close to the transition region between the endcap and the barrel detectors ($1.379 < |\eta_{SeedCrystal}| < 1.579$) are rejected. An electron is selected if its I_{rel} is smaller than 0.0354 (0.0646) for the electrons in the barrel (endcap), corresponding to the tight working point. For electrons, the FastJet [101] energy density (ρ) method is used to estimate the pileup contribution to the isolation. This algorithm assumes a certain density of energy per unit of area and computes the area of a jet. After the correction is applied, the average isolation does not depend on the number of interactions.

variable	requirement	
	Barrel	Endcap
full $5 \times 5 \sigma_{I_\eta I_\eta}$	< 0.0101	< 0.0279
$ \Delta\eta_{In} $	< 0.00926	< 0.00724
$ \Delta\phi_{In} $	< 0.0336	< 0.0918
$\frac{h}{E}$	< 0.0597	< 0.0615
$\frac{1}{E} - \frac{1}{p}$	< 0.012	< 0.00999
expected missing inner hits	≤ 2	≤ 1
pass conversion veto	true	true

Table 7.7: List of the cuts that define the tight electron identification selection where barrel is $|\eta_{SuCluster}| < 1.4442$ and endcap is ($1.5660 < |\eta_{SuCluster}| < 2.5$)

Muon candidates are reconstructed by combining information of the track parameters measured in the inner tracker and the muon detectors. Muons are required to pass the tight working point of the cut based muon identification [102]. Similarly to electrons, the cuts related to the muon's impact parameter have been removed in the analysis. The list of identification cuts applied in this analysis is shown in Table 7.8. For the muons, the method to estimate the pileup contribution in the isolation is the $\Delta\beta$ algorithm [103]. Using empirical evidence, the neutral pileup contribution is assumed to be half of the charged pileup contribution. The relative isolation of the muon has to be less than 0.15 to pass the tight working point.

Each event must contain at least two electrons (muons) passing all the criteria mentioned previously for the ee ($\mu\mu$) final state. In addition, the leptons are required to have opposite charge. The list of cuts applied to the electrons and muons is summarised in Table 7.9. Table 7.10 shows the list of cuts applied to the pair of leptons which are applied for the same reasons as the cuts presented in Section 5.3.1.

Once again, the d_0 variable will be used as the most discriminant variable between backgrounds and signal. Figure 7.3 illustrates the separation in the 2D plane of the second lepton d_0 and the first lepton d_0 between background processes and a signal sample with a mean decay length of 1 cm in the ee and $\mu\mu$ final state. By comparing

variable	requirement
Is a GlobalMuon and a TrackerMuon	true
Number of valid hits in the tracker	> 5
Number of hits in the muon stations	> 0
Number of pixel hits	> 0
Normalised χ^2 of track	< 10
Number of matched muon stations	> 1

Table 7.8: List of the cuts that define the tight muon identification selection.

Table 7.9: Summary of lepton related cuts

variable	electron	muon
$ \eta $	< 2.4	< 2.4
p_T	$> 42 \text{ GeV}$	$> 40 \text{ GeV}$
cut based ID	tight WP	tight WP
I_{rel}	< 0.0354 barrel < 0.0646 endcap	< 0.15
$ d_0 $	$< 10 \text{ cm}$	$< 10 \text{ cm}$

Table 7.10: Summary of lepton pair cuts

cut parameter	cut value
$\Delta R_{l_1, l_2}$	> 0.5
$q_{l_1} * q_{l_2}$	$= -1$

these two graphs, one can already appreciate the wider d_0 distribution for the electrons as compared to the muons. This difference is explained by the fact that, due to its lower mass, an electron will emit much more photons through bremsstrahlung than a muon. Because of this, the uncertainty on the direction of an electron, which is used to calculate its d_0 , is bigger than for a muon. This results in less good resolution for the electrons' d_0 as compared to the muons' d_0 , and, in turn, a wider d_0 distribution for the electrons. Depending on the transverse impact parameters of two leptons, the events passing the preselection are subdivided in various regions which will be discussed in the following sections.

7.3.2 Prompt lepton control region

Events populating the prompt control region must contain at least two electrons (muons) passing the preselection. In addition, the two electrons (muons) should both satisfy $d_0 < 0.01$ cm, which is the same definition as the prompt control region of the Displaced $e\mu$ search defined in 5.3.2. This region is dominated by prompt Standard Model background while being almost depleted of a signal. For that reason, this region is perfectly suited to compare the accuracy between the Monte Carlo simulations and the data. In all the graphs of this section, all corrections are applied according to the description in the previous section.

From now on, electron (muon) variables will always be shown in the ee ($\mu\mu$) final state. Figure 7.4 shows the p_T , η , and the azimuthal angle, ϕ , distributions for leptons, and Figure 7.5 depicts the invariant mass of lepton pairs. In both final states, the background is largely dominated by the Drell-Yan process while Diboson, $t\bar{t}$ and single top processes have almost negligible contributions. This is expected since Drell-Yan processes often decay into two leptons of the same flavour. The p_T distributions show minor discrepancies, but the agreement is never worse than about 20%. For the η and ϕ distributions, the agreement is better than 10%. Overall, these figures suggest that the Monte Carlo simulations are describing the data within roughly 10% accuracy, depending slightly on the variables. Figure 7.6 shows the leptons' d_0 distribution. The agreement in this figure is worse than for the other distributions. This effect has been observed many times and is known to be due to detector misalignment that is not correctly propagated to simulation. It can be worrying that the discriminating variable shows quite poor agreement, but, as it was already argued in Section 5.3.2, this effect is not important for large d_0 .

As it can be seen in Figure 7.5, the events coming from the Drell-Yan process peak around the mass of the Z -boson so that their contribution can easily be reduced without impacting the signal efficiency. To reduce the background from the Drell-Yan process, an additional cut is included in the preselection which vetoes events with invariant mass in a 10 GeV window around the Z -boson mass.

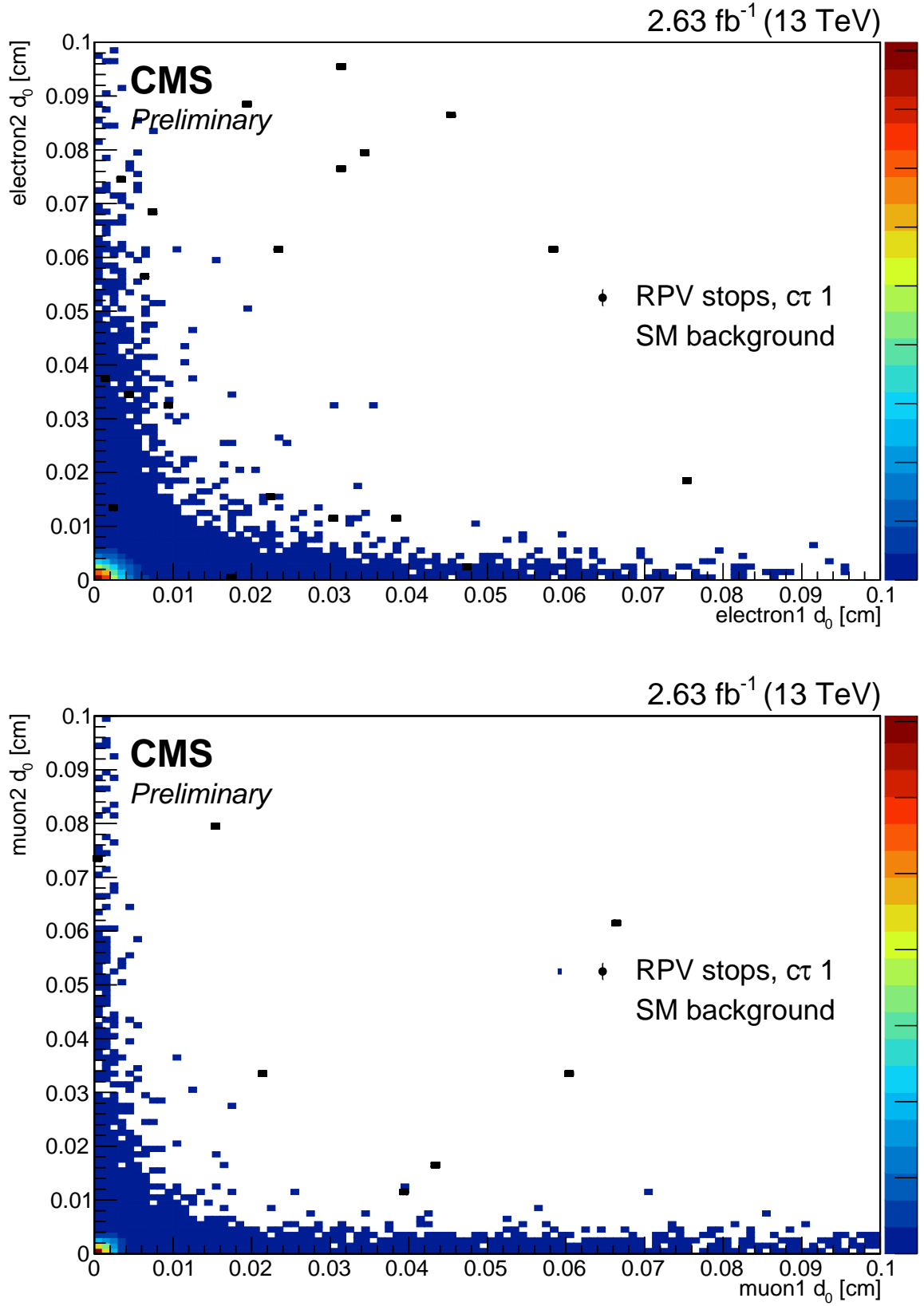


Figure 7.3: Distributions of signal and the backgrounds in the 2D plane of the leptons' d_0 for electrons (top) and muons (bottom).

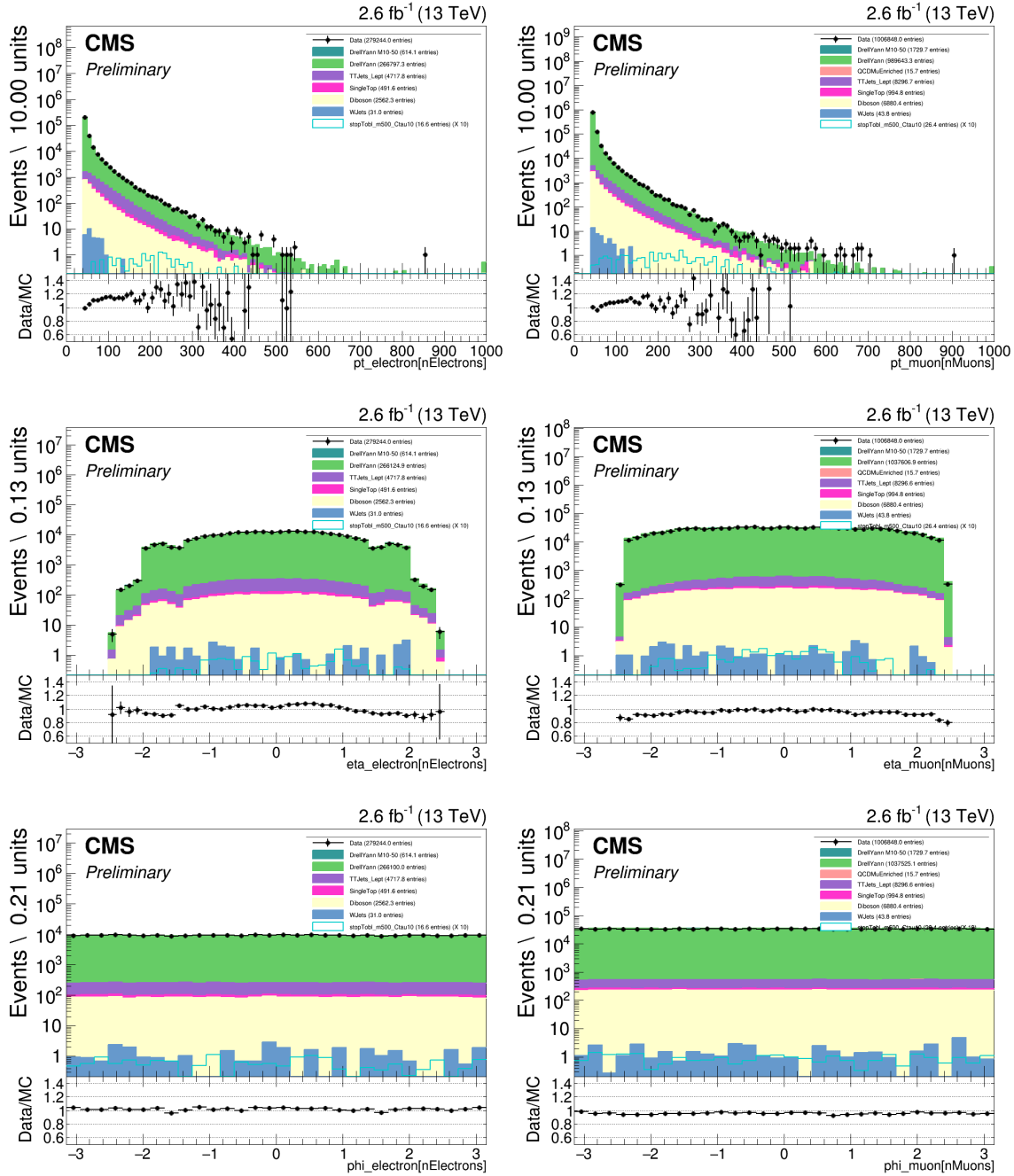


Figure 7.4: Lepton p_T (top), η (middle), and ϕ (bottom) in the prompt lepton control region, for electrons in the ee final state (left) and muons in the $\mu\mu$ final state (right). The data (black dots) is compared to the sum of expected Standard Model backgrounds split into different sources, Drell-Yann (green), TTJetsDilept (purple), SingleTop (magenta), Diboson (yellow), and WJets (blue). For comparison purposes, a signal sample with $m_{\tilde{t}} = 500$ GeV and $\langle c\tau_{\tilde{t}} \rangle = 1$ cm is overlaid, in blue. Its cross section has been scaled up by a factor ten.

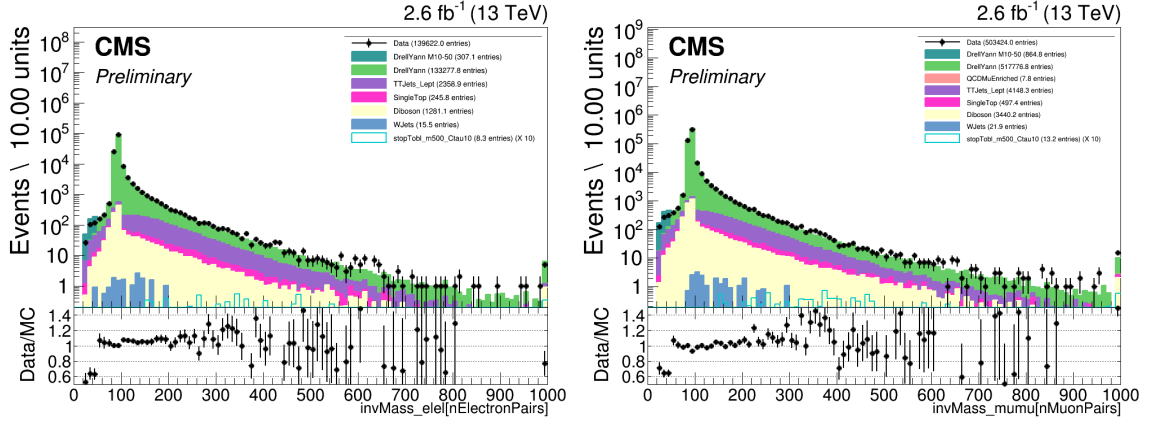


Figure 7.5: Dilepton invariant mass distributions in the prompt lepton control region for lepton pairs in the ee final state (left) and in the $\mu\mu$ final state (right). The data (black dots) is compared to the sum of expected Standard Model backgrounds split into different sources, Drell-Yann (green), TTJetsDilept (purple), SingleTop (magenta), Diboson (yellow), and WJets (blue). For comparison purposes, a signal sample with $m_{\tilde{t}} = 500$ GeV and $\langle c\tau_{\tilde{t}} \rangle = 1$ cm is overlaid, in blue. Its cross section has been scaled up by a factor ten.

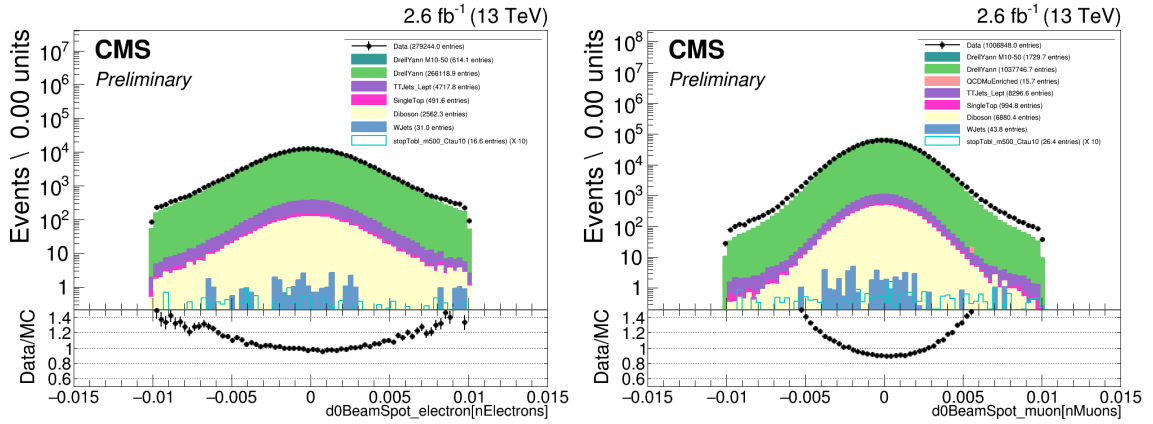


Figure 7.6: Lepton d_0 distribution in the prompt lepton control region, for the electrons in the ee final state (left) and for the muons in the $\mu\mu$ final state (right). The data (black dots) is compared to the sum of expected Standard Model backgrounds split into different sources, Drell-Yann (green), TTJetsDilept (purple), SingleTop (magenta), Diboson (yellow), and WJets (blue). For comparison purposes, a signal sample with $m_{\tilde{t}} = 500$ GeV and $\langle c\tau_{\tilde{t}} \rangle = 1$ cm is overlaid, in blue. Its cross section has been scaled up by a factor ten.

7.3.3 Displaced lepton control region

The displaced control region only differs from the prompt control region by the requirement made on the d_0 of the preselected leptons. Both leptons must have a d_0 between 0.01 cm and 0.02 cm which now define a square in the 2D plane of the leptons' d_0 , unlike the displaced control region described in 5.3.3. The lower value of this region corresponds to the upper value of the prompt control region while the signal region starts with a value of d_0 bigger than its upper edge as shown in Figure 7.2. As there is now an explicit displacement requirement on both leptons, one expects that the promptly decaying background will be drastically reduced. At that stage, only Standard Model processes which produce leptons with real lifetime will contribute significantly. Leptons coming from heavy flavour QCD such as B mesons and D mesons or from τ lepton decays are the important contributions. $Z \rightarrow \tau\tau$ can give rise to two displaced leptons, but the cut on the lepton p_T reduces this contribution to almost zero. Therefore most of the background will come from heavy flavour QCD. The QCD contribution will be derived using a data-driven technique that shall be exposed in Section 7.4.1.

7.3.4 Signal regions

The signal regions definition follows the same logic as the one used in the Displaced $e\mu$ search, which is explained in Section 5.3.5. Three inclusive signal regions, as well as three exclusive signal regions, are defined for the ee final state and for the $\mu\mu$ final state. Thanks to a newly designed trigger, the range of the search is extended up to $d_0 = 10$ cm. Figure 7.7 shows a schematic representation of the three inclusive signal regions (left) and the three exclusive signal regions (right) in the ee final state (top) and in the $\mu\mu$ final state (bottom).

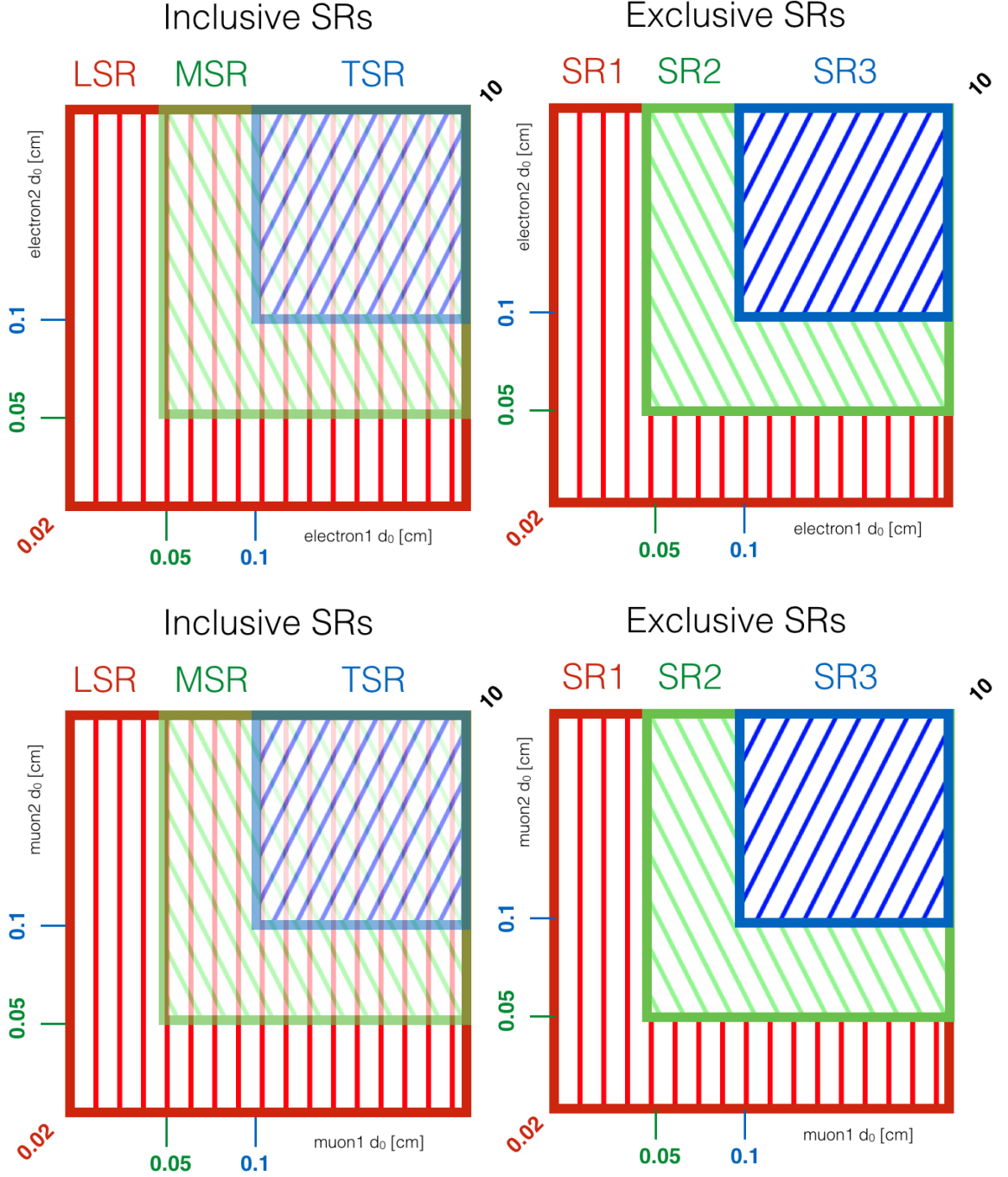


Figure 7.7: Schematic representation of the three inclusive signal regions (left) and the three exclusive signal regions (right) in the 2D plane of the leptons' d_0 in the ee final state (top) and in the $\mu\mu$ final state (bottom).

7.4 Background estimation techniques

The goal of this section is to estimate the background contribution in the signal region from various Standard Model processes, such as Drell-Yan, $t\bar{t}$, diboson, single top and leptonic decay from QCD. As mentioned already in Section 5.4, the contribution from QCD processes cannot reliably be estimated from Monte Carlo simulation only. The contribution from all the other backgrounds will be estimated with the same method as the one explained in Section 5.4.2.

The contribution from QCD will be derived using a data-driven technique which is explained in Section 7.4.1. For all the other Monte Carlo processes, the background will be estimated from Monte Carlo simulation directly with a method explained in Section 7.4.2.

7.4.1 Background contribution from data-driven technique

Since almost all the non-QCD backgrounds produce prompt leptons, it is expected that the QCD background will be the most significant contribution in the non-prompt regions. Due to the extremely high cross-section of the QCD processes, the limited number of simulated events and the uncertainties on QCD models, it is often hard to confidently trust the prediction from the simulation. For that reason, the contribution from QCD is derived using a data-driven technique.

The method used in this section differs from the ABCD method used in the previous search for two reasons. Firstly, this method was assuming that signal events would appear only with opposite sign leptons. While this assumption holds for the Displaced Supersymmetry scenario, it makes the search less model independent. Secondly, when the same method was tried as a first estimate, all the regions defined in the ABCD method were almost completely depleted of events which would have led to an unreliable estimate².

In the following subsections, the new method used to determine the number of QCD events in each signal region is exposed. The assumption is that one can get the estimate of the yield from QCD in any region, defined in the 2D plane of the leptons d_0 , by multiplying the yield from QCD in a region, also defined in that plane, with a transfer factor (TF) that accounts for the difference in d_0 distribution. Details on the method are exposed in Section 7.4.1.3.

In order to compute the transfer factor, it is necessary to get the d_0 distribution of the leptons coming from a QCD process. To achieve this, new regions enriched in QCD events were defined by inverting the isolation cut of the preselection. By doing so, the number of QCD events populating the newly defined regions is considerably enhanced. The definition of these regions will be detailed in Section 7.4.1.1

²There are two reasons why the event yield has decreased in this search with respect to the previous one. First, the integrated luminosity is about 6 times smaller in this search and, second, the recommendations for the tight identification of the leptons have been slightly updated and the efficiency is slightly lower.

As the selection applied in the $b\bar{b} + \text{lepton}$ control region differs significantly from the one in the signal regions, one can question the introduction of potential bias. More specifically, the d_0 distributions used to compute the transfer factors are calculated in a non-isolated region and are assumed to be similar in a isolated region. The validity of this assumption will be briefly discussed in Section 7.4.1.2.

7.4.1.1 $b\bar{b} + \text{electron (muon) control region}$

Two new regions will be defined in this section. The first (second) one aims at determining the electron (muon) d_0 distribution in events from QCD. In QCD events, a lepton typically comes within a jet. It is precisely for that reason that the requirement of the isolation was inverted with respect to the standard preselection.

In principle, $b\bar{b}$ events will contain two b-jets so one can require two b-tagged jets in the events. However, since the impact parameter is an important input variable in the b-tagging identification, this would certainly introduce a bias. For that reason, only one b-tagged jet is required. The other jet, referred to as the probe jet, is usually well separated from the first one, so is required to be nearly back to back in the transverse plane, ($|\Delta\phi| > 2.5$), with the b-jet. The lepton of interest should be near the probe jet ($|\Delta R| < 0.2$). The selection on the electron (muon) is the same as the one described in Section 7.3.1 with the important exception that the isolation is inverted, ($0.15 < I_{rel} < 1.5$). The list of the requirements that defines these regions is summarised in Table 7.11.

Figure 7.8 shows the Monte Carlo data agreement in the $b\bar{b} + \text{electron (muon)}$ control region (BBLCR). From these figures, it is clear that a control region almost pure in QCD and where the key distributions are well modelled by the Monte Carlo simulation was created. The relatively bad agreement in few bins in the ee final state figures is explained by the fact that, even in a QCD enriched region, the expected number of QCD events is quite low which implies that its statistical uncertainty is high.

Table 7.11: $b\bar{b} + \text{lepton}$ selections

	$b\bar{b} + \text{muon Selection}$	$b\bar{b} + \text{electron Selection}$
Trigger	HLT_Mu28NoFiltersNoVtx_CentralCalo.Jet40_v	HLT_Ele27_WPLoose_Gsf_v
Lepton selection	1 good muon with iso inverted	1 good electron with iso inverted
jet selection	jet loose ID & $ \eta < 2.4$ & $p_T \geq 30$ GeV	
b-jet selection	jet selection & medium CSV tag	jet selection & tight CSV tag
event selection	probe jet-b-tagged jet $\Delta\phi > 2.5$ lepton-probe jet $\Delta R < 0.2$	

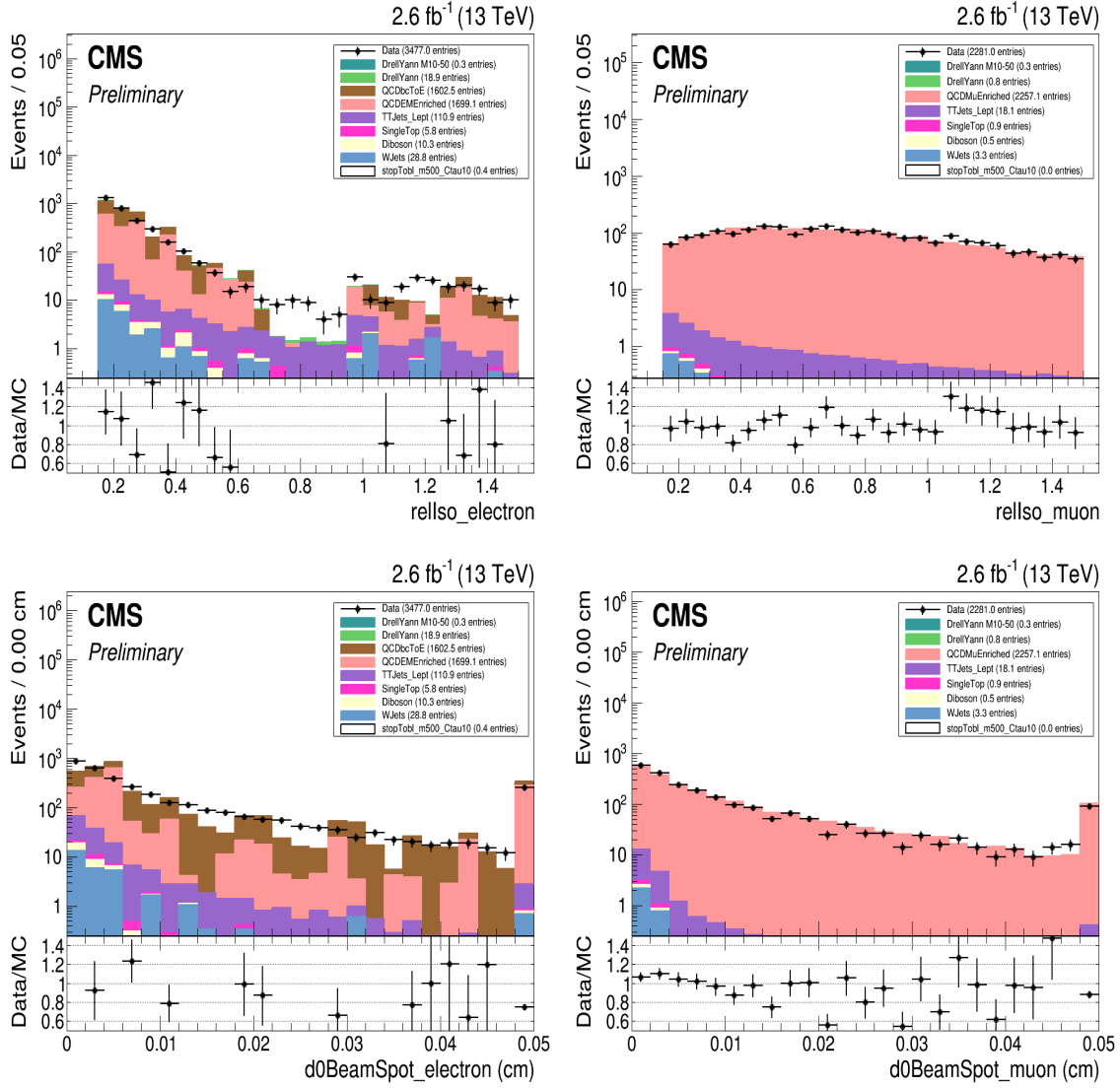


Figure 7.8: Distributions of the relative isolation of the lepton (top) and the d_0 of the lepton (bottom) in the $b\bar{b} + \text{electron}$ (left) and in the $b\bar{b} + \text{muon}$ (right) control region. The data (black dots) is compared to the sum of expected Standard Model backgrounds split into different sources, QCD EMEnriched (left) or QCD MuEnriched (right) is in pink, QCD bcToE (brown), Drell-Yan (green), TTJetsDilept (purple), SingleTop (magenta), Diboson (yellow), and WJets (blue). For comparison purposes, a signal sample with $m_{\tilde{t}} = 500$ GeV and $\langle c\tau_{\tilde{t}} \rangle = 1$ cm is overlaid, in blue. Its cross section has been scaled up by a factor ten.

7.4.1.2 $b\bar{b}$ + electron (muon) control region validation

This section aims at proving that the leptons from the $b\bar{b}$ + lepton control region have similar properties as the ones in the signal regions. Most importantly, the d_0 distributions of the leptons are supposed to be similar in the $b\bar{b}$ + lepton control region and in the signal regions. The most important difference between these two regions is that leptons are required to be isolated in the signal regions while they are required to be non-isolated in the $b\bar{b}$ + lepton control region. It is then essential to show that the d_0 distributions are similar for non-isolated and isolated leptons. In order to allow the comparisons of the d_0 distributions, a new region is defined.

This region, called the isolated $b\bar{b}$ + lepton control region, has the same definition as the $b\bar{b}$ + lepton control region one with the important change that the isolation requirement on the leptons is the same as the one in the signal regions. This comparison has been done in the Displaced $e\mu$ search at 13 TeV and can be used here as the definition of the regions are identical. Figure 7.9 compares the d_0 distributions of the leptons in the isolated $b\bar{b}$ + lepton control region and in the $b\bar{b}$ + lepton control region. The distributions are normalised to unit area in order to allow the comparison of the shape of the d_0 distributions.

As it can be seen in the ratio plots, the two distributions display similar shapes. Indeed, out of the nine non-zero bins, six of them are compatible with zero. The largest disagreement is found in the third bin of the ratio plot of the muons d_0 distributions and amounts to about 30%. However, as it will be discussed in Section 7.5.1, various $b\bar{b}$ + lepton control region regions are defined using different b-tagging working points in order to assess the systematic uncertainty related to this method. More specifically, as it can be seen in Table 7.17, the systematic uncertainty in the tight signal region for the $\mu\mu$ final state is 33% which is larger than the discrepancy found in the ratio plot. For these reasons, one can conclude that the discrepancies between the d_0 distributions in the isolated $b\bar{b}$ + lepton control region and in the $b\bar{b}$ + lepton control region are covered by the systematic uncertainties related to this method.

7.4.1.3 QCD background estimation methodology

As described previously, the QCD contribution in any region, referred to as the target (T) region, can be deduced from another region, referred to as the normalisation (N) region. Formally, one can write

$$\text{QCD}[T] = \text{QCD}[N] * TF_{N \rightarrow T} \quad (7.1)$$

where [T] is the region in which one wants to estimate the QCD yield, [N] is the normalisation region in which the QCD yield is known and transfer factor is the transfer factor that accounts for the difference in d_0 distribution. The transfer factor is the product of two transfer factors (one per lepton) and the value depends on the bounds of the region. The first transfer factor (TF1) is calculated using the bounds of the two regions on the first lepton only and similarly for the second transfer factor (TF2). Let the first lepton of the normalisation region be bounded by $tl1^3$ and $tu1$ and the first

³The convention here is the following. The first letter indicates if it is the normalisation (n) or the target (t) region, the second letter indicates if it is a lower (l) or an upper (u) bound, and finally the

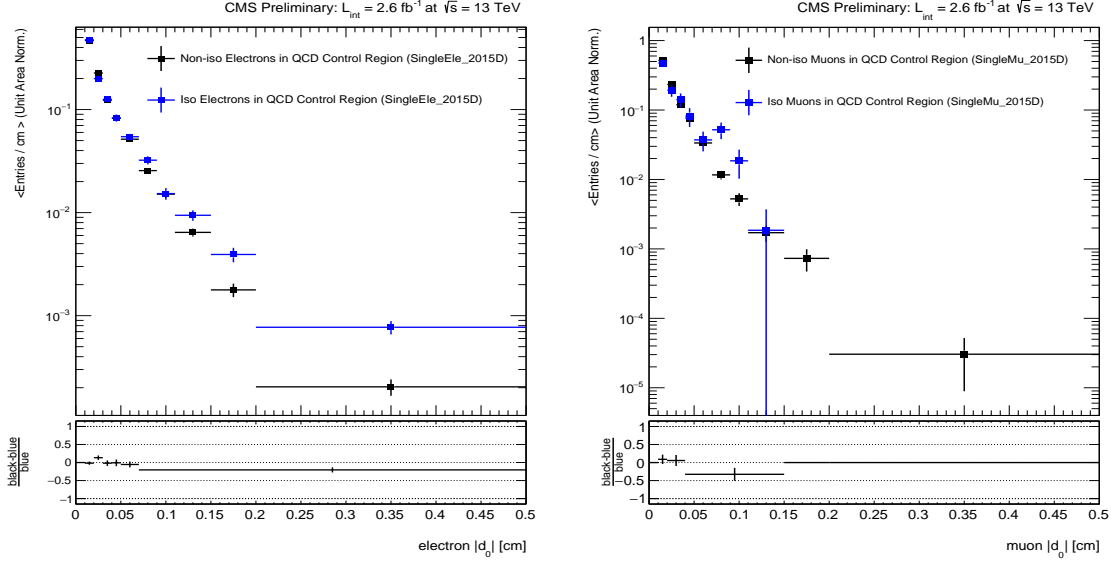


Figure 7.9: Comparison of the d_0 distributions of the electrons (left) and the muons (right) in the isolated $b\bar{b} + \text{lepton}$ control region (blue) and in the $b\bar{b} + \text{lepton}$ control region (black). All the distributions are normalised to unity in order to allow the comparison of the shape of the distributions.

lepton of the region N be bounded by $nl1$ and $nu1$ like it is depicted in Figure 7.10.

The first transfer factor is defined as follows

$$TF1_{N \rightarrow T} = \frac{\int_{tl1}^{tu1} d_0(l)}{\int_{nl1}^{nu1} d_0(l)}. \quad (7.2)$$

where the integral is performed over the d_0 distribution of the relevant lepton of the $b\bar{b}$ control region. Similarly the second transfer factor is defined as

$$TF2_{N \rightarrow T} = \frac{\int_{tl2}^{tu2} d_0(l)}{\int_{nl2}^{nu2} d_0(l)}. \quad (7.3)$$

Combining eqs. (7.1) to (7.3) together, one gets

$$\text{QCD}[T] = \text{QCD}[N] \frac{\int_{tl1}^{tu1} d_0(l)}{\int_{nl1}^{nu1} d_0(l)} \frac{\int_{tl2}^{tu2} d_0(l)}{\int_{nl2}^{nu2} d_0(l)}. \quad (7.4)$$

To get the yield estimate in any of the signal regions, the displaced control region is used as the normalisation region. In the normalisation region, the QCD yield is taken to be the difference between the data and the sum of all the non-QCD background. The number of QCD events in the displaced control region is found to be 0.1 ± 2.5 (5.4 ± 2.6) in the ee ($\mu\mu$) final state.

The validation of this method has been performed by doing a closure test in a dedicated control region as exposed hereafter.

number indicates which lepton it is.

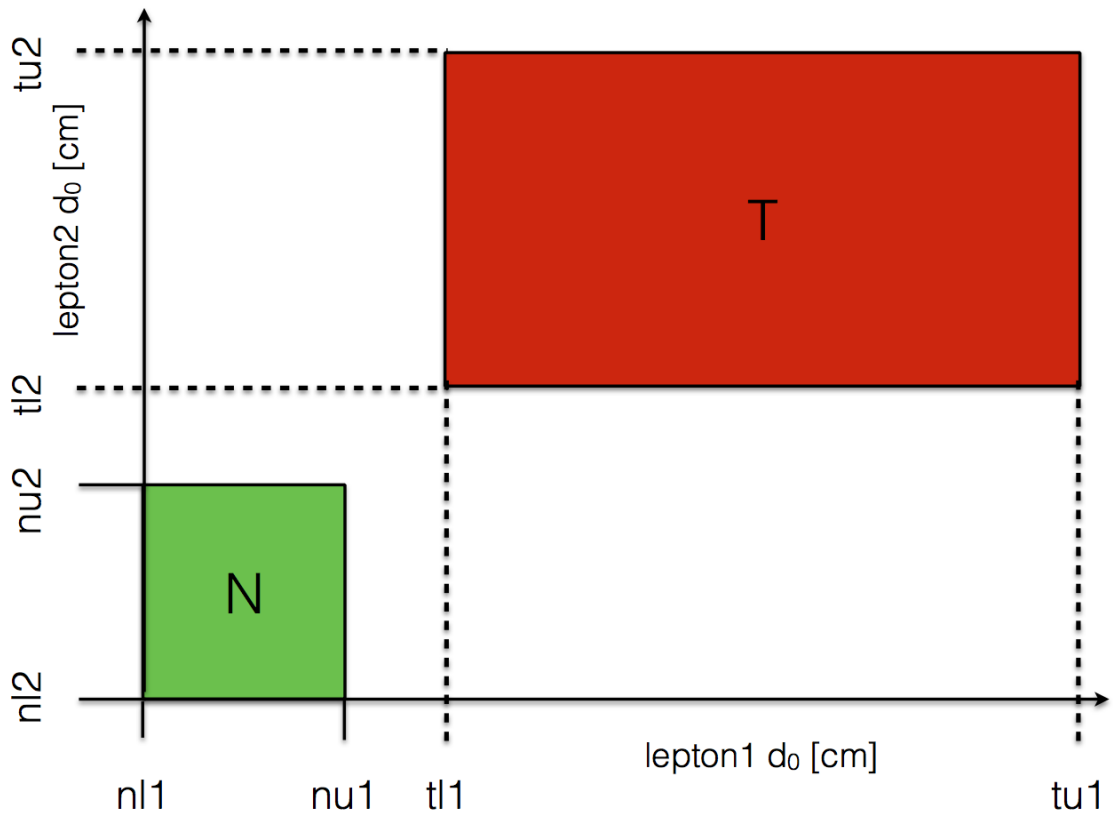


Figure 7.10: Schematic representation of the normalisation region and the target region which are used to define the transfer factors.

7.4.1.4 QCD closure test

To validate the data-driven method used to estimate the QCD contribution, a closure test is performed. It is clear that such a test needs to be done in a region where the QCD contribution is non-negligible. For that matter, a new region, enriched in QCD events, is defined. The displaced control region is used but the cut on the I_{rel} is relaxed, hence defining the loosely isolated displaced lepton Control Region (LIDCR), in order to get a meaningful number of QCD events. In the loosely isolated displaced control region, the background is largely dominated by events coming from QCD process.

As explained in Section 7.4.1.3, the method requires a normalisation region to get the estimate in another region, called the target region. The QCD contribution in the target region will be given by data minus the non-QCD (hereafter referred to as direct count) in one hand, and on the other hand, it will be estimated using the data-driven method explained before through Equation 7.4.

Different normalisation-target region pairs are defined. For each pair, the following four requirements will be satisfied.

- 1) For both leptons, the lower bound of the normalisation region ($nl1$ and $nl2$) is fixed to be the beginning of the displaced control region, namely $nl := nl1 = nl2 = 0.01 \text{ cm}$.
- 2) For the first lepton, the upper bound of the normalisation region ($nu1$) will always coincide with the lower bound of the target region ($tl1$), namely $b1 := nu1 = tl1$.
- 3) For the second lepton, the upper bound of the normalisation region ($nu2$) will always coincide with the lower bound of the target region ($tl2$), namely $b2 := nu2 = tl2$.
- 4) For both leptons, the upper bound of the target region ($tu1$ and $tu2$) is fixed to be the end of the displaced control region, namely $tu := tu1 = tu2 = 0.02 \text{ cm}$.

After these constraints, the regions are fully defined by picking a value of $b1$ and a value of $b2$ as depicted in Figure 7.11. By taking three values of $b1$ and three values of $b2$, nine normalisation-target region pairs are defined. The results obtained with the two methods in the nine region pairs are reported in Table 7.12 (7.13) for the ee final state ($\mu\mu$ final state). For the ee case, the agreement between the two methods is quite good, so the data-driven estimate is behaving as expected. However, one should note that the uncertainty attached to the estimated yield is always quite high due to the low event count and most of the predictions are compatible with zero within one standard deviation.

Furthermore, in the last two rows the background prediction from the direct count is negative. While it does not have a meaningful physics interpretation, this can occur when the non-QCD background is higher than the data. In the $\mu\mu$ case, the data-driven method systematically overestimates the number of expected backgrounds from QCD processes. For all the regions but the first two, the estimated yield from the direct method is compatible with zero. The data-driven estimate is however consistently above zero which is a clear hint that the method might be inaccurate. However, since the data-driven estimate also converges towards zero in the control region defined in this section and that the signal regions are even more displaced, one can expect that the discrepancies will get smaller. In addition, the data-driven prediction is still more accurate than taking prediction directly from Monte Carlo simulation, as events coming from QCD events typically have a very large uncertainty.

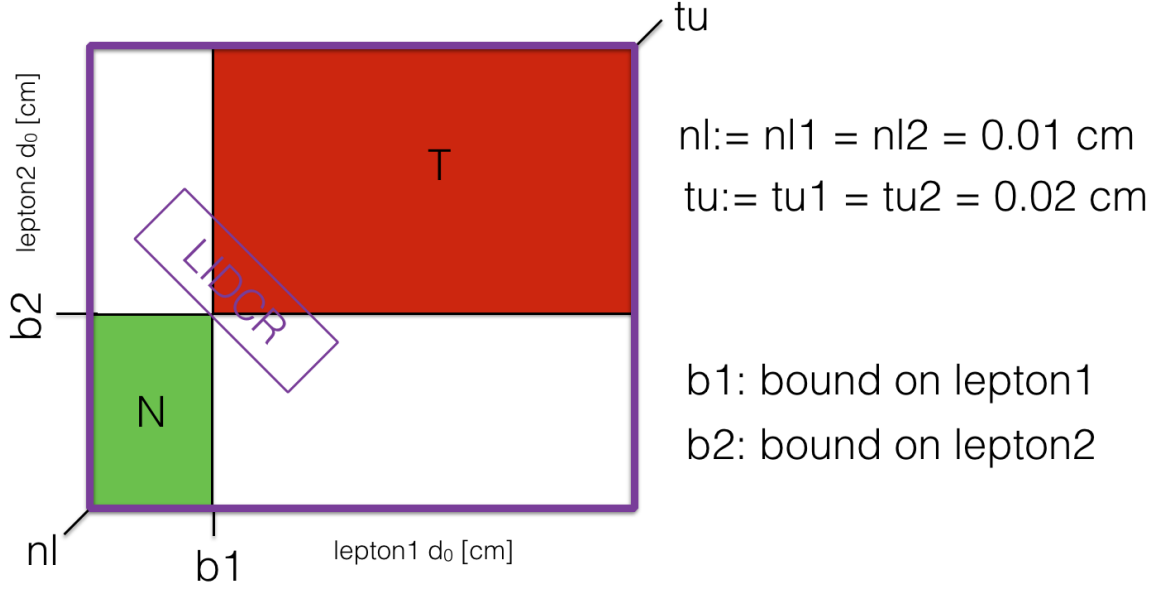


Figure 7.11: Schematic representation of the normalisation region and the target region which are used to define the transfer factors.

Table 7.12: Comparison of the yield estimate from QCD-processes between the two methods in the loosely isolated displaced control region in the ee final state.

b1 ; b2	direct yield	data-driven yield
0.012 ; 0.012	9 ± 4	17 ± 22
0.012 ; 0.015	2.3 ± 2.5	8 ± 7
0.012 ; 0.018	0.7 ± 1.4	2.1 ± 1.9
0.015 ; 0.012	5.0 ± 3.0	5 ± 6
0.015 ; 0.015	1.1 ± 1.8	3.5 ± 2.3
0.015 ; 0.018	0.3 ± 1.0	1.0 ± 0.6
0.018 ; 0.012	2.0 ± 1.7	1.4 ± 1.8
0.018 ; 0.015	-0.31 ± 0.13	1.1 ± 0.7
0.018 ; 0.018	-0.11 ± 0.07	0.32 ± 0.18

Table 7.13: Comparison of the yield estimate from QCD-processes between the two methods in the loosely isolated displaced control region in the $\mu\mu$ final state.

b1 ; b2	direct yield	data-driven yield
0.012 ; 0.012	3.3 ± 2.0	32 ± 17
0.012 ; 0.015	1.7 ± 1.4	14 ± 6
0.012 ; 0.018	-0.08 ± 0.08	3.2 ± 1.5
0.015 ; 0.012	0.4 ± 1.0	12 ± 6
0.015 ; 0.015	0.7 ± 1.0	6.0 ± 2.3
0.015 ; 0.018	-0.08 ± 0.08	1.5 ± 0.6
0.018 ; 0.012	0.0 ± 0	3.3 ± 1.5
0.018 ; 0.015	0.0 ± 0	1.5 ± 0.6
0.018 ; 0.018	0.0 ± 0	0.39 ± 0.16

7.4.2 Background contribution from Monte Carlo simulation

As stated previously, for non-QCD events, the Monte Carlo simulation can be trusted and the background contribution in each signal region will be estimated using these. However, since a very tight requirement is made on both leptons at the same time, the probability to pass this cut gets extremely small. For many samples, the contribution of the non-QCD background will fall to zero. While reducing the background as much as possible is a good thing, it is always hard to quantify the uncertainty on a zero events prediction. For that reason, the factorisation method explained in Section 5.4.2 is used again.

For each sample, after applying the standard preselection, the efficiency for an electron (muon) to pass a certain d_0 cut is calculated. These efficiencies are shown in Figure 7.12 on the left-hand side for electrons and on the right-hand side for muons.

For this technique to work, the efficiency of the first lepton to pass a given d_0 requirement should be uncorrelated with the one of the second lepton. The correlation factors between the d_0 of the two leptons are calculated for all the backgrounds and both final states. The average of the absolute value of the correlation factors is 0.082, and the largest correlation factor is -0.21 for the WJets background in the ee final state. These values suggest that little to no correlation is observed between the d_0 of the two leptons, which validates the assumption required for this method to work. Furthermore, a validation of this method is performed by comparing the background predicted with the factorisation method with the background predicted from applying the d_0 cut directly.

Figure 7.13 shows the comparison between the two methods in the ee final state (left) and in the $\mu\mu$ final state (right). For the ee final state, a good agreement between the two methods is observed across the whole d_0 range except for the Diboson dataset. In that case, the factorisation method seems to overestimate the yield in the loose signal region by more than a factor ten. Similar behaviour was already observed in the previous search, more specifically in Figure 5.24 and it was argued that this effect will have a negligible impact on the results. The background estimate is taken from the factorisation yielding a conservative estimate. For the $\mu\mu$ final state, the agreement between the two methods is good across the full d_0 range except for the Drell-Yan and the $t\bar{t}$ composite datasets. For the Drell-Yan composite dataset, the factorisation method underestimates the background by roughly a factor 10 in the loose signal region. However, even with the cut and count method, the background estimate is about 0.1 event which is small compared to background contribution from QCD events as it will be shown in the next section. In every case, the non-zero prediction is significantly extended thanks to the factorisation method which is precisely why it was used.

In order to estimate the background in each signal region for each composite dataset, one can identify where the solid coloured line crosses the vertical dashed line corresponding to the desired signal region. The yield obtained in the three inclusive signal regions with this method is shown in Table 7.14 in the ee final state and in Table 7.15 in the $\mu\mu$ final state. The prediction from the factorisation method is used for the limit settings because it gives non-zero prediction over a wider range of d_0 . Even if the agreement between the two methods is not perfect, the dominant background is coming from QCD processes so that the disagreement is expected to have a negligible

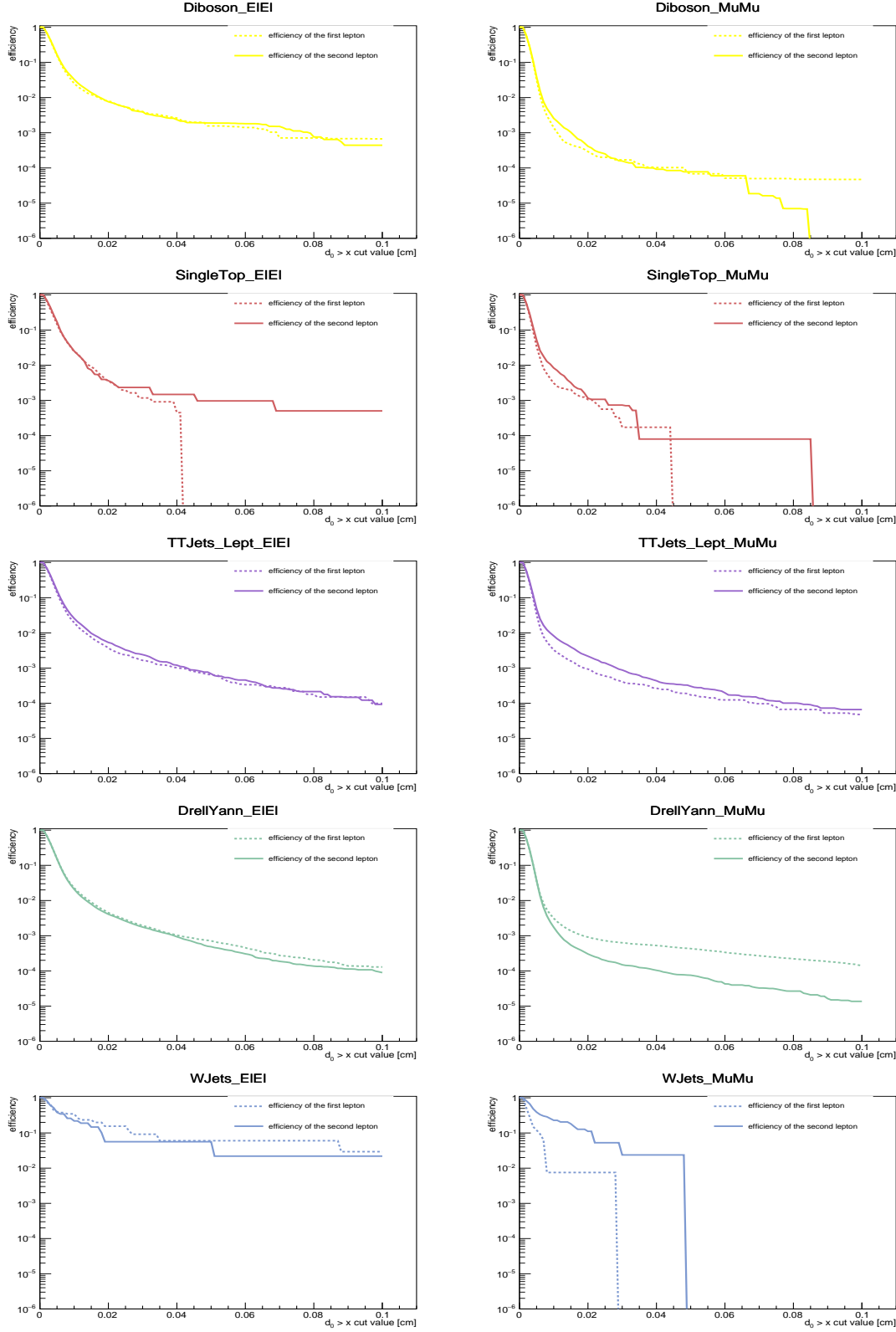


Figure 7.12: Efficiencies for the two electrons (left) and muons (right) in the prompt control region to pass a cut on d_0 for the five composite datasets considered in this analysis. The efficiency of the highest p_T lepton is shown in a solid line and the lowest p_T lepton is a dashed line.

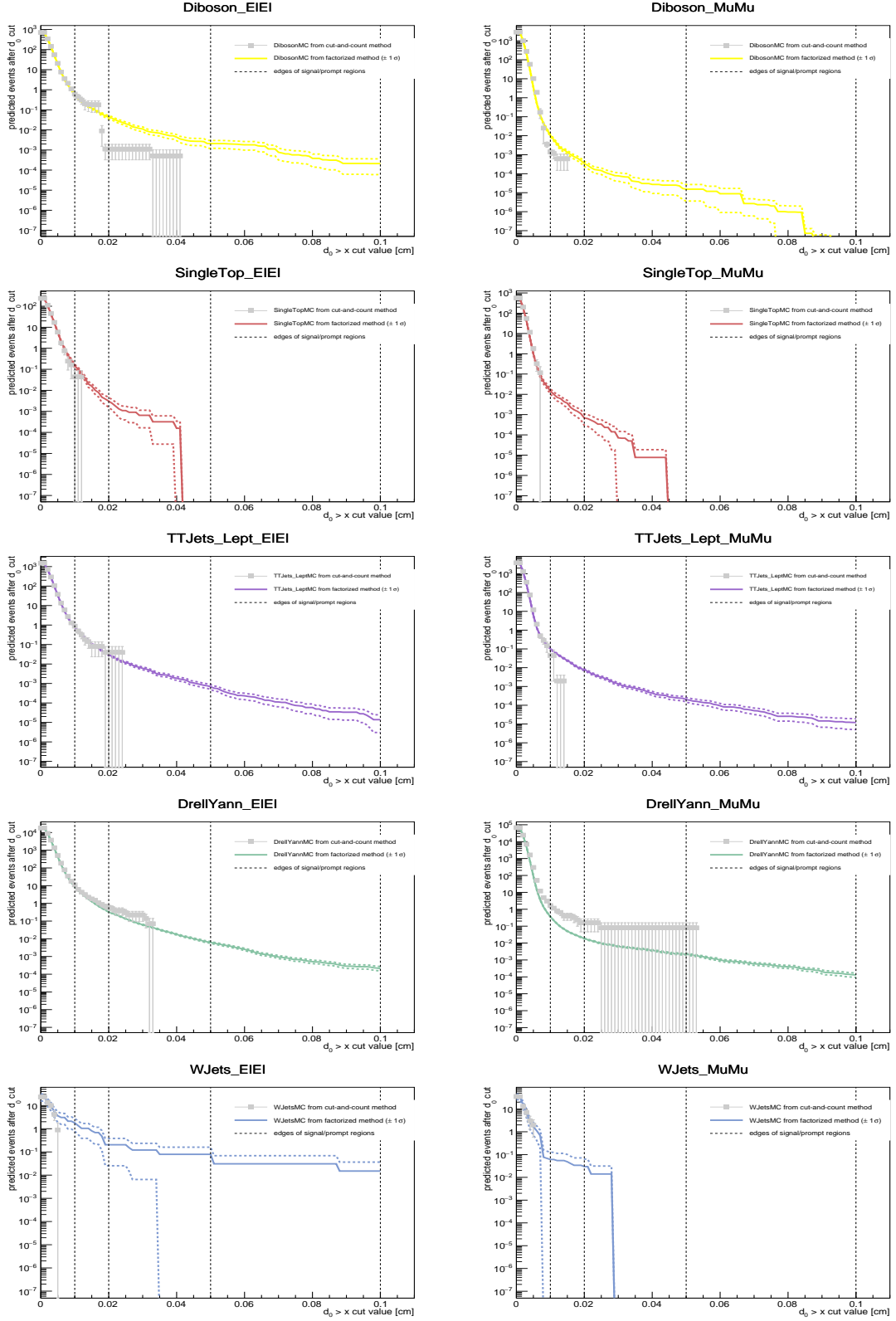


Figure 7.13: Comparison between the cut and count method (grey dots) and the factorisation method (solid line) for the five composite datasets considered in this analysis in ee final state (left) and the $\mu\mu$ final state (right). The coloured dashed line represents the upper and lower one σ statistical fluctuation on the factorisation method. The vertical black dashed line represents the transition from various control regions and signal regions.

contribution and will not influence the conclusion.

Table 7.14: Yield estimated with the factorisation method in the three inclusive signal regions for each non-QCD composite dataset in the ee final state.

background source	LSR	MSR	TSR
WJets	0.20 ± 0.18	0.08 ± 0.08	0.015 ± 0.021
Diboson	0.043 ± 0.008	0.0021 ± 0.0009	0.00021 ± 0.00015
SingleTop	0.0031 ± 0.0015	0.0 ± 0.0	0.0 ± 0.0
TTJets_Lept	0.0303 ± 0.0033	0.00068 ± 0.00019	0.000014 ± 0.000011
Drell-Yan	0.334 ± 0.014	0.0063 ± 0.0007	0.00021 ± 0.00006
Sum	0.61 ± 0.18	0.09 ± 0.08	0.015 ± 0.021

Table 7.15: Yield estimated with the factorisation method in the three inclusive signal regions for each non-QCD composite dataset in the $\mu\mu$ final state.

background source	LSR	MSR	TSR
WJets	0.030 ± 0.033	0.0 ± 0.0	0.0 ± 0.0
Diboson	0.00035 ± 0.00011	0.000015 ± 0.000012	$0.000000016 \pm 0.000000014$
SingleTop	0.0007 ± 0.0004	0.0 ± 0.0	0.0 ± 0.0
TTJets_Lept	0.0078 ± 0.0009	0.00020 ± 0.00006	0.000012 ± 0.000007
Drell-Yan	0.0186 ± 0.0013	0.00219 ± 0.00028	0.00013 ± 0.00004
Sum	0.057 ± 0.034	0.00240 ± 0.00029	0.00014 ± 0.00004

7.5 Systematic uncertainties

In this section, the list of all the systematic uncertainties affecting the background estimate is discussed. It includes all the systematic uncertainties discussed in Section 7.2. In addition, systematic uncertainties related to the data-driven method are also assessed.

The systematic uncertainty related to data-driven method used to estimate the background contribution from QCD processes is outlined in Section 7.5.1. A brief overview of the study performed to estimate the systematic uncertainty related to the displaced track efficiency is described in Section 7.5.2. Finally, in Section 7.5.3, the list of standard systematic uncertainties is given along with the resulting systematic uncertainties.

7.5.1 Data-driven estimate systematic uncertainty

To estimate the background coming from QCD events, transfer factors were calculated using the d_0 distribution of leptons coming from a control region enriched in QCD events. In the definition of this QCD enriched region, the $b\bar{b}$ + lepton control region, at least one of the jets was required to be tagged as a b-jet. The number of events populating this region depends on the b-tagging efficiency and hence on the working point used. As a consequence, the d_0 distribution in the $b\bar{b}$ + lepton control region might change with different working points yielding to different values of the transfer factors and of the background estimate in each signal region. Figure 7.14 shows the value of the transfer factors for each signal region and b-tagging working point. For the electron case, the differences between the values of the transfer factor with respect to the b-tagging working point increase with the tightening of the signal region. For the muon case, this trend is less obvious.

In order to assess the systematic uncertainty of the QCD yield in each signal region, the transfer factor is calculated for the three available b-tagging working points, and the relative systematic uncertainty is defined as:

$$\frac{\max(TF_{wp}) - \min(TF_{wp})}{\text{mean}(TF_{wp})}. \quad (7.5)$$

The resulting systematic uncertainties are given for each signal region in Table 7.16 for the ee final state and in Table 7.17 for the $\mu\mu$ final state. For the electron case in the tight signal region, the systematic uncertainty is about 82%. While this number seems big enough to have a significant impact on the final result, it is good to discuss some of its features. First, the total uncertainty on the QCD estimate is largely dominated by the statistical uncertainty so that the systematic uncertainty will have a negligible impact on the final result. Second, the total number of events from QCD processes in the tight signal region is at least two orders of magnitude below one so that the absolute uncertainty is hence still quite small. Finally, given the very large weight for QCD events, this uncertainty remains quite small compared to when the estimate

would have been calculated using Monte Carlo simulation instead of the data-driven method.

Table 7.16: Values of the transfer factors for different b-tagging working points and the resulting systematic uncertainty in the ee final state in each signal region.

Region	LSR	MSR	TSR
Loose	0.86 ± 0.05	0.213 ± 0.016	0.034 ± 0.004
Medium	0.85 ± 0.08	0.177 ± 0.022	0.025 ± 0.005
Tight	0.82 ± 0.11	0.154 ± 0.027	0.014 ± 0.004
mean	0.84 ± 0.11	0.181 ± 0.027	0.025 ± 0.005
Systematic uncertainty	4.79 %	32.32 %	82.08 %

Table 7.17: Values of the transfer factors for different b-tagging working points and the resulting systematic uncertainty in the $\mu\mu$ final state in each signal region.

Region	LSR	MSR	TSR
Loose	0.61 ± 0.06	0.031 ± 0.005	0.00089 ± 0.00032
Medium	0.65 ± 0.08	0.033 ± 0.007	0.00063 ± 0.00033
Tight	0.63 ± 0.10	0.038 ± 0.010	0.0008 ± 0.0005
mean	0.63 ± 0.10	0.034 ± 0.010	0.0008 ± 0.0005
Systematic uncertainty	6.0 %	21.12 %	33.12 %

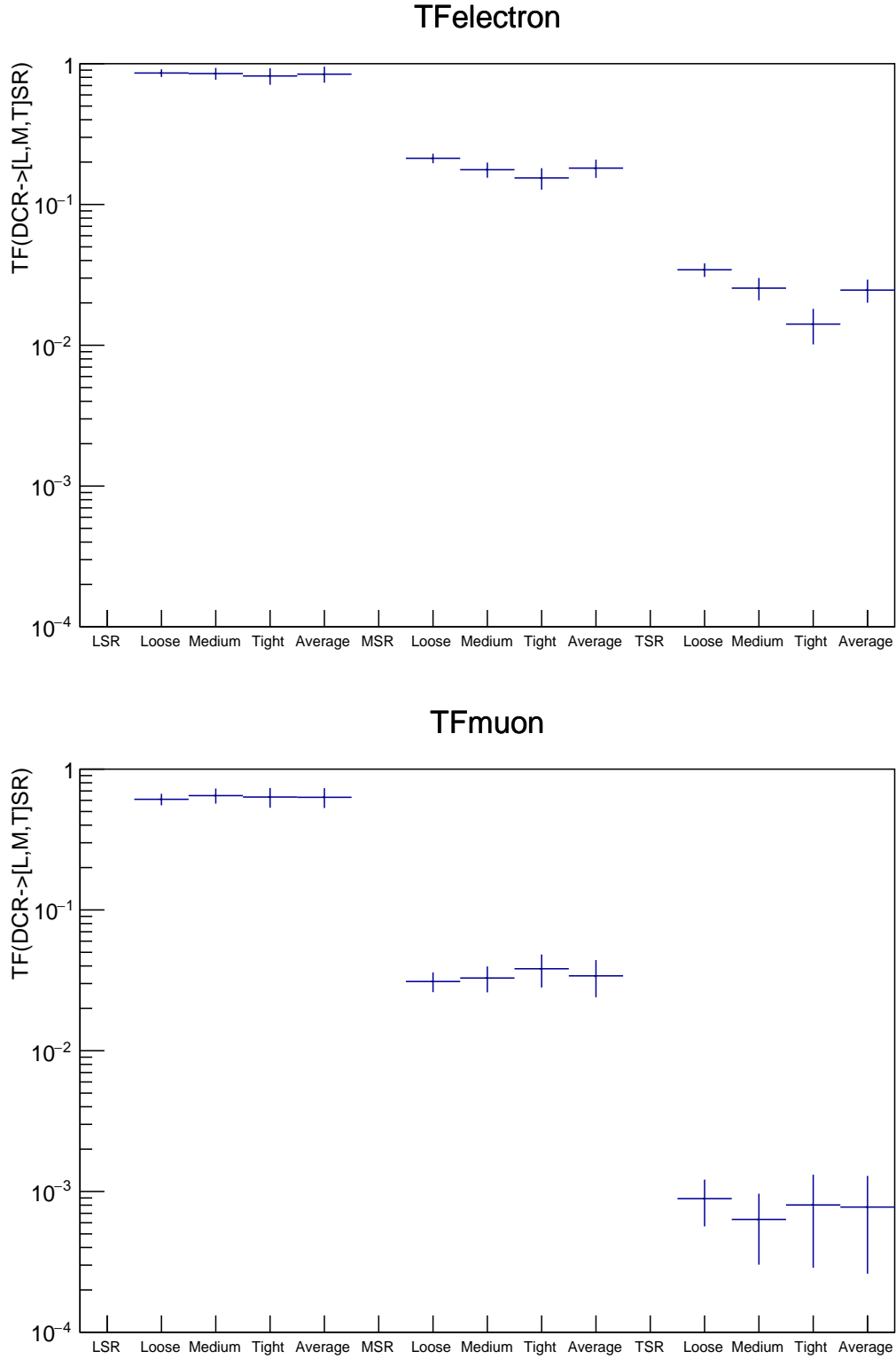


Figure 7.14: Value of the transfer factors to estimate the QCD background in the three inclusive signal regions in the ee final state (top) and in the $\mu\mu$ final state (bottom). For each signal region, the value of four transfer factors is displayed. The first three bins correspond to the loose, medium and tight working point of the b-tagging algorithm, and the fourth is the average of the previous three.

7.5.2 Displaced tracking efficiency systematic uncertainty

To estimate the displaced tracking efficiency, a sample of muons produced by cosmic rays is used. In data, events from the "NoBPTX" dataset are used. This dataset is well suited for this study because it records events when collisions are not taking place. For Monte Carlo simulations, a sample of muons from cosmic rays was generated in order to match the condition of the data. The efficiency to reconstruct a track is defined by the ratio of the number of tracks associated with a muon over the number of muons. This efficiency is calculated in Monte Carlo simulations and in data as a function of d_0 and z_0 and the ratio of these efficiencies is used as the systematic uncertainty. Using the sample with the highest $\langle c\tau_i \rangle$ (which represents the most challenging scenario in term of tracking efficiency), the impact of the displaced tracking efficiency on selecting two muons yields a relative systematic uncertainty of 12%. Because this systematic uncertainty affects mostly events with displaced objects, it is used for signal samples only.

7.5.3 Overall systematic uncertainties

In addition to the two analysis-specific systematic uncertainties, the standard systematic uncertainties are also considered. However, the methods on how to derive them have been already discussed in Section 3.4.2 and are not repeated here. The list of all the relative systematic uncertainties considered in this analysis is reported in Table 7.18 for the ee final state and in Table 7.19 for the $\mu\mu$ final state. The right-most column corresponds to the total relative systematic uncertainty and is largely dominated by the trigger systematic uncertainty. Since this search is largely dominated by the statistical uncertainties, it is expected that the impact of the total systematic uncertainty on the limits is negligible.

Table 7.18: List of the systematic uncertainties for each non-QCD background considered in this search in the ee channel.

Dataset	XS	PU	iso	id	L_{int}	trigger	track	total
WJets	3.84 %	4.8 %	4.62 %	4.44 %	5.0 %	20.0 %	-	22.45 %
Diboson	2.5 %	11.4 %	3.65 %	4.84 %	5.0 %	20.0 %	-	24.45 %
SingleTop	5.02 %	0.23 %	4.75 %	5.56 %	5.0 %	20.0 %	-	22.44 %
TTJetsDilept	6.11 %	7.76 %	5.23 %	4.9 %	5.0 %	20.0 %	-	23.96 %
Drell-Yan	1.73 %	0.15 %	2.03 %	3.75 %	5.0 %	20.0 %	-	21.12 %

Table 7.19: List of the systematic uncertainties for each non-QCD background considered in this search in the $\mu\mu$ channel.

Dataset	XS	PU	iso	id	L_{int}	trigger	track	total
WJets	3.84 %	3.64 %	0.18 %	0.39 %	5.0 %	10.0 %	-	12.38 %
Diboson	2.5 %	5.41 %	0.19 %	0.43 %	5.0 %	10.0 %	-	12.68 %
SingleTop	5.02 %	2.27 %	0.2 %	0.48 %	5.0 %	10.0 %	-	12.47 %
TTJetsDilept	6.11 %	7.42 %	0.2 %	0.47 %	5.0 %	10.0 %	-	14.76 %
Drell-Yan	1.73 %	3.69 %	0.15 %	0.26 %	5.0 %	10.0 %	-	11.9 %

7.6 Results

7.6.1 Event yields

The resulting yield in each exclusive signal region is shown in Table 7.20 for the ee final state and in Table 7.21 for the $\mu\mu$ final state. When the predicted events yield is zero, the value from the first non-zero preceding region is used as a conservative estimate. Both tables also contain the expected yield for a signal with a mass hypothesis of 500 GeV and with three different average lifetimes.

Table 7.20: Event yields of the background, the observation, and three different signal hypotheses in each exclusive signal region in the ee final state. The uncertainty is statistical only.

Event source	SR1	SR2	SR3
Background			
Drell-Yan	0.270 ± 0.012	0.0054 ± 0.0007	0.00021 ± 0.00006
Diboson	0.036 ± 0.007	0.0019 ± 0.0009	0.00021 ± 0.00015
QCD	0.1 ± 2.1	0.0 ± 0.4	0.00 ± 0.06
SingleTop	0.0024 ± 0.0013	0.0024 ± 0.0013	0.0024 ± 0.0013
TTJets_Lept	0.0236 ± 0.0028	0.00056 ± 0.00016	0.00014 ± 0.00011
WJets	0.17 ± 0.17	0.016 ± 0.031	0.015 ± 0.021
Background Sum	0.6 ± 2.1	0.0 ± 0.4	0.02 ± 0.07
Observation			
Data	2.0	0.0	0.0
Signal $gg \rightarrow \tilde{t}_1 \tilde{t}_1^*$ with $M = 500$ GeV			
$\langle c\tau \rangle = 0.1$ cm	11.26 ± 0.42	2.58 ± 0.20	0.430 ± 0.084
$\langle c\tau \rangle = 1.0$ cm	12.98 ± 0.46	10.46 ± 0.41	15.28 ± 0.50
$\langle c\tau \rangle = 10.0$ cm	1.45 ± 0.15	1.98 ± 0.18	6.51 ± 0.32

As can be seen in Table 7.21, the signal region 3 contains one observed event while the background expectation is 0.030. Because this may seem like an excess over the expected background, it is worth studying what is the probability of this to happen assuming that there is no signal. Using Equation 4.7, the p-value is $p = 0.0295$, which corresponds to 1.9 standard deviations. After correction for the number of categories in the analysis, also commonly referred to as the “look-elsewhere effect”, the probability is increased to 0.16 or equivalent to about one standard deviation. It results that no significant excess is observed over the background prediction and limits can be set on the signal processes cross-section.

Even if it has just been argued that one event is not a significant excess over the background expectation, it is insightful to scrutinise the properties of this event. Table 7.22 shows some variables of this event, and one can notice that the two muons have very similar properties. This feature is typical of a single muon produced by a cosmic ray, that is reconstructed as two muons by the reconstruction algorithm.

Table 7.21: Event yields of the background, the observation, and three different signal hypotheses in each exclusive signal region in the $\mu\mu$ final state. The uncertainty is statistical only.

Event source	SR1	SR2	SR3
Background			
Drell-Yan	0.0138 ± 0.0011	0.00194 ± 0.00026	0.000114 ± 0.000034
Diboson	0.00026 ± 0.00009	$(1.5 \pm 1.2)\text{e-}05$	$(1.6 \pm 1.4)\text{e-}08$
QCD	3.2 ± 1.7	0.18 ± 0.10	0.0042 ± 0.0034
SingleTop	0.0006 ± 0.0004	0.0006 ± 0.0004	0.0006 ± 0.0004
TTJets_Lept	0.0062 ± 0.0008	0.00017 ± 0.00005	0.00012 ± 0.000007
WJets	0.030 ± 0.033	0.030 ± 0.033	0.030 ± 0.033
Background Sum	3.3 ± 1.7	0.21 ± 0.11	0.035 ± 0.034
Observation			
Data	1.0	0.0	1.0
Signal $gg \rightarrow \tilde{t}_1 \tilde{t}_1^*$ with $M = 500$ GeV			
$\langle c\tau \rangle = 0.1$ cm	19.03 ± 0.56	4.50 ± 0.27	1.12 ± 0.13
$\langle c\tau \rangle = 1.0$ cm	25.5 ± 0.65	22.62 ± 0.61	45.08 ± 0.86
$\langle c\tau \rangle = 10.0$ cm	4.90 ± 0.28	6.22 ± 0.32	52.7 ± 0.94

Table 7.22: Comparison of some variables of the two muons in the event populating the signal region 3.

	muon 1	muon 2
p_T GeV	269.86	269.15
d_0 cm	-9.38	9.38
η	0.024	-0.025
ϕ	1.248	-1.894

An event display of this event, projected in the r - ϕ plane, is shown in Figure 7.15. The most striking property of the two muons of the event is that they are back to back, which is also typical of a single muon produced from a cosmic ray. This may suggest that an additional background should have been considered for the $\mu\mu$ final state. However, as already mentioned above, one event is not a significant excess, and limits are set in the next section.

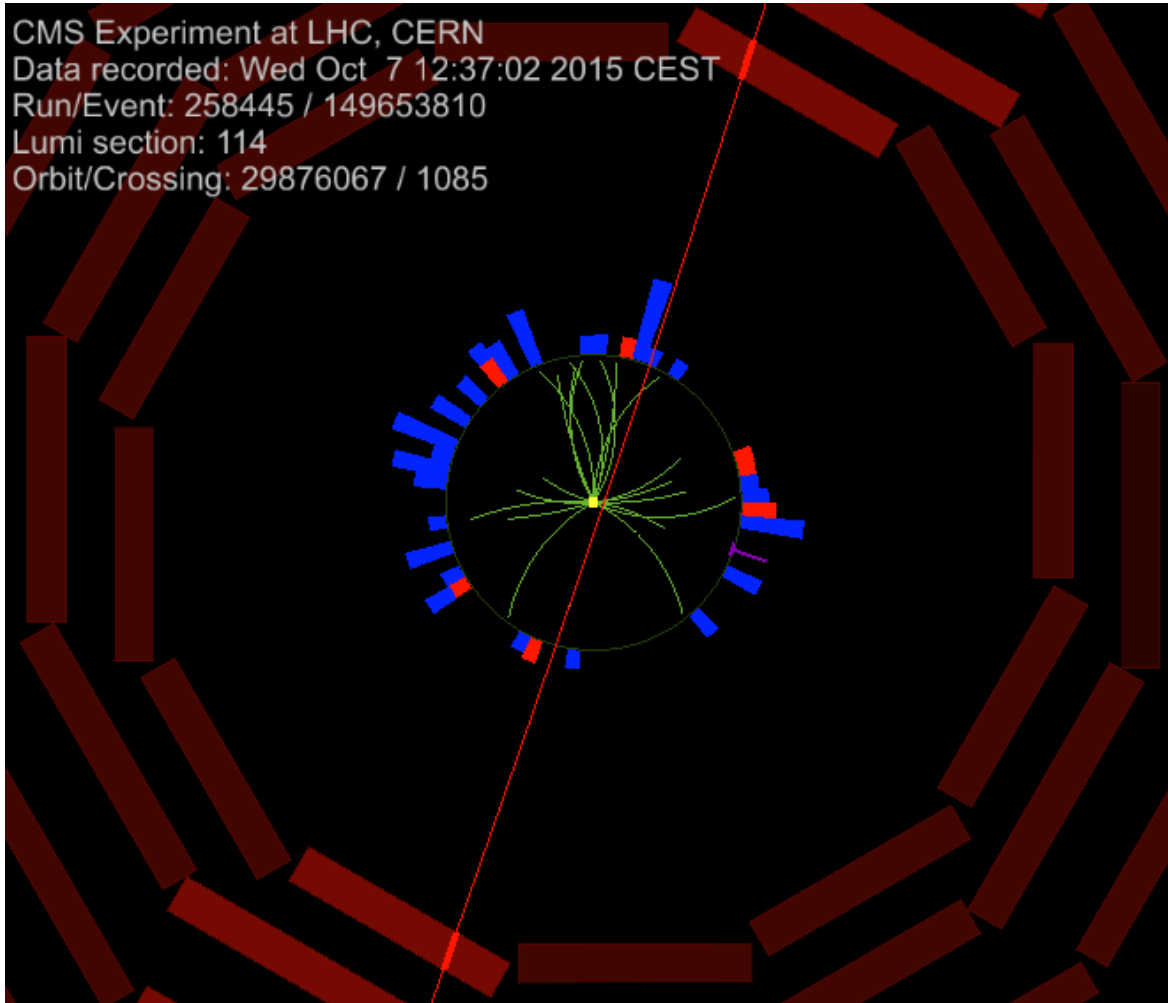


Figure 7.15: Event display of the event populating the signal region 3, projected in the r - ϕ plane. The tracks are in green, the hadronic calorimeter in blue, the electromagnetic calorimeter in light red, the missing transverse energy in purple, and the muons in dark red.

7.6.2 Limits

Since Table 7.20 and Table 7.21 show that no significant excess over the background prediction is observed, 95% confidence level limits are set on the production cross-section of top squark pair at 13 TeV. The limits extracted from each signal region are combined using the Higgs combine tool [89]. This time, the median significance is approximated using the “Asimov” data set instead of using Monte Carlo toys as it was done in Section 5.6.2. Thanks to this simplification, the computational time required to compute limits is reduced from about one week down to about 5 hours while yielding similar results. Indeed, it was shown that this approximation is very accurate except when both the expected background and the signal are simultaneously close to zero [73] which is not the case here as it can be seen in Tables 7.20 and 7.21.

The expected and observed limits are shown in Figure 7.16 for the ee final state and in Figure 7.17 for the $\mu\mu$ final state. This time, due to lack of time, the samples with intermediate lifetimes have not been generated like it was done in Section 5.6.1. As a consequence of that, the curves are just using four points (one for each different lifetime hypothesis) instead of forty points which explains why the curves look more "sharp".

For top squarks with a lifetime of $1\text{ cm}/c$, this search excludes top squark masses below 760 GeV (780 GeV) using the ee ($\mu\mu$) final state. In each final state separately, the most stringent limit is comparable to the Displaced $e\mu$ search at 8 TeV which excludes top squark masses below 790 GeV for a lifetime of $2\text{ cm}/c$. The lower luminosity for this search as compared to the previous one and the fact that both the ee final state and $\mu\mu$ final state have twice fewer events as compared to the $e\mu$ final state is compensated by the increase of energy which increases the production cross-section of the signals.

In parallel of the search presented in this chapter, the most straight forward extension of the search presented in Chapter 5 has been conducted at 13 TeV [95]. To make a fair comparison between the Displaced $e\mu$ search at 13 TeV and the Displaced same-flavour leptons search at 13 TeV, the ee and the $\mu\mu$ final states are combined. The combination and the comparison of the limits are discussed in the next section.

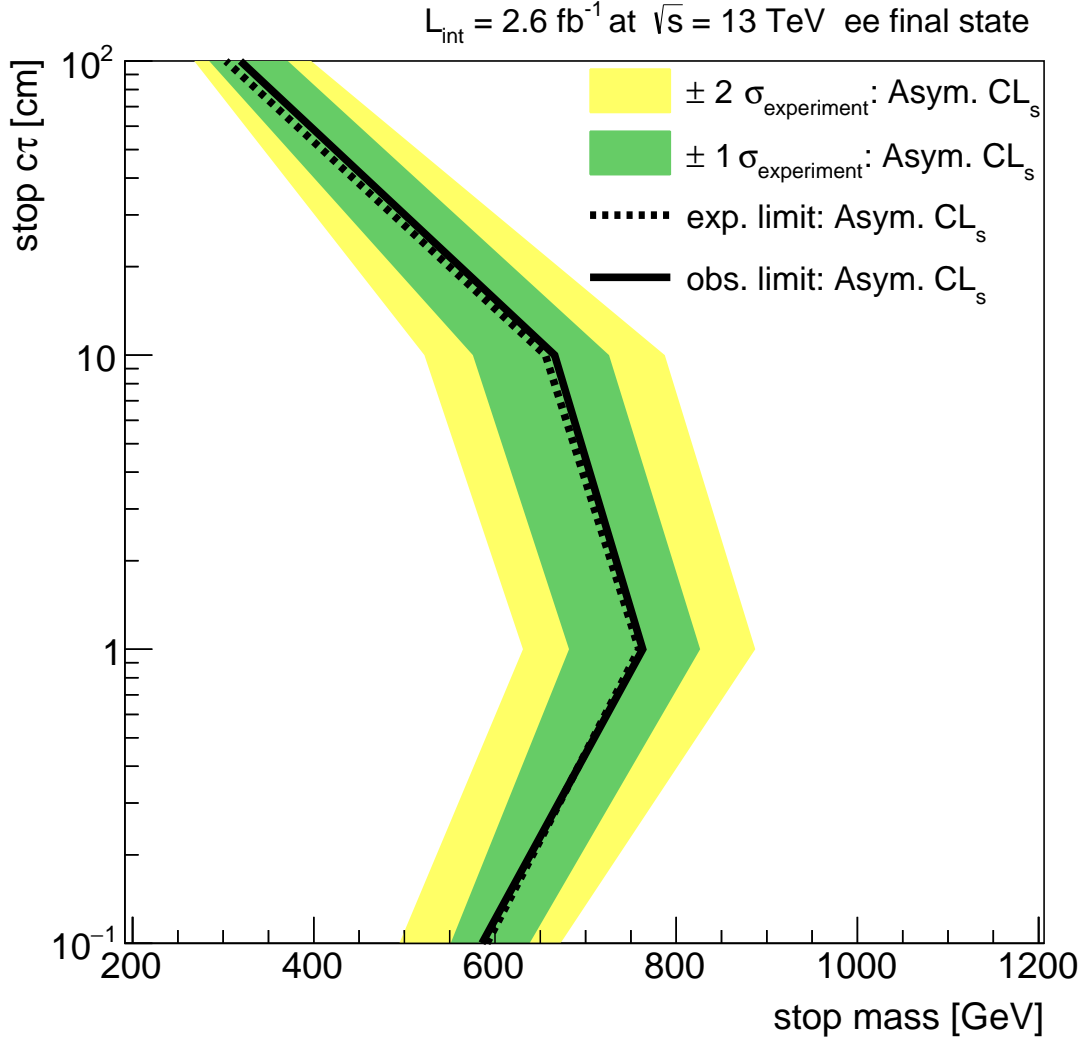


Figure 7.16: Expected and observed 95% CLs production cross-section exclusion contours for top squark pair in the $\langle c\tau_{\tilde{t}} \rangle$ versus $m_{\tilde{t}}$ plane. Using events in the ee final state, the region on the left of the contours is excluded by this search.

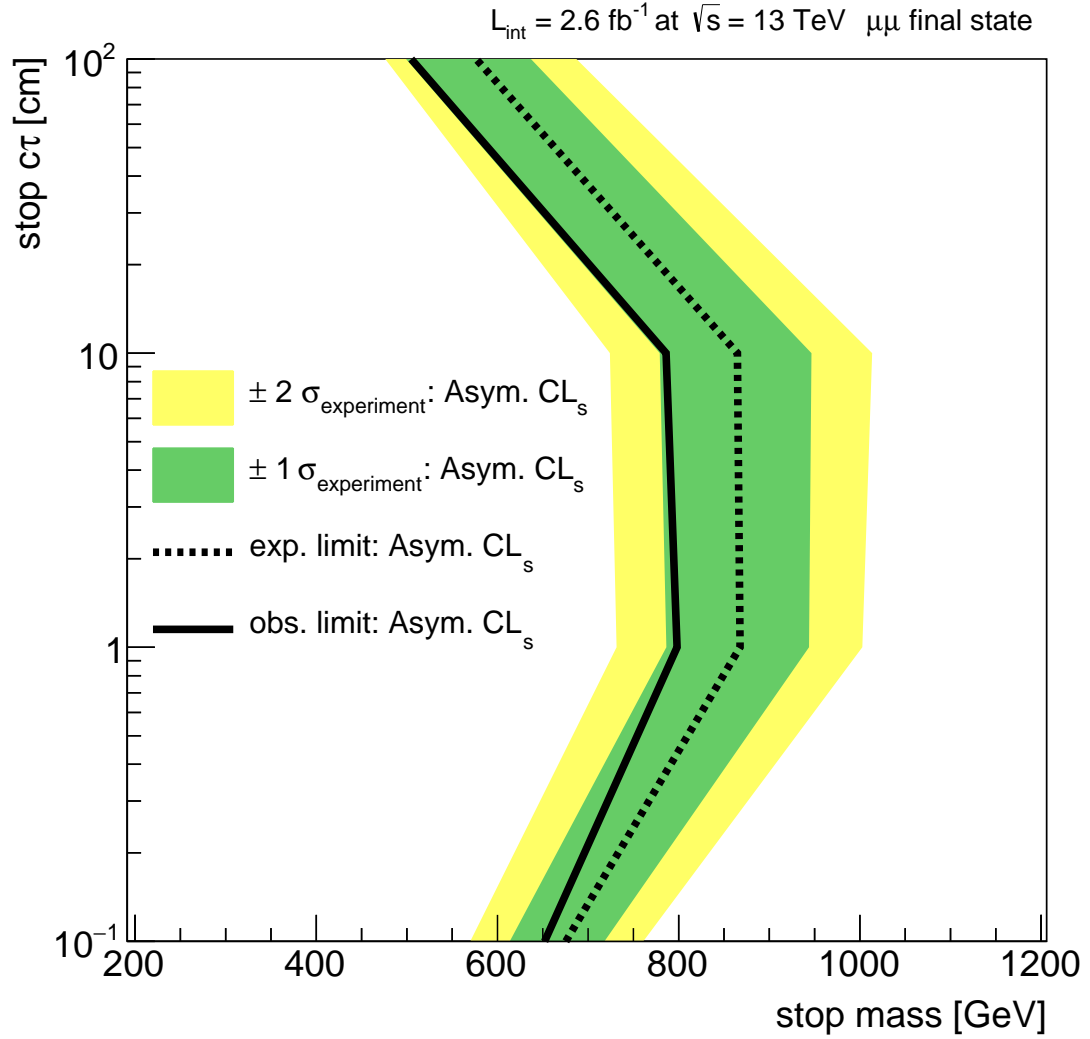


Figure 7.17: Expected and observed 95% CLs production cross-section exclusion contours for top squark pair in the $\langle c\tau_{\tilde{t}} \rangle$ versus $m_{\tilde{t}}$ plane. The region on the left of the contours is excluded by this search using events in the $\mu\mu$ final state.

7.6.3 Limits combination and comparison

In this section, three different aspects which might have an impact on the limits are considered. Firstly, the impact on the simultaneous change of the integrated luminosity at the centre-of-mass energy. Secondly, the impact of setting the limits with the asymptotic approximation instead of the Markov chain. Thirdly, the improvement of the limits provided by the combination of multiple channels.

Impact on the limits from the simultaneous change of integrated luminosity and centre-of-mass energy

For this study, it is useful to compare the Displaced $e\mu$ search at 8 TeV with the Displaced $e\mu$ search at 13 TeV. Indeed, these two searches use the same channel and the most important differences between them reside in the total integrated luminosity analysed as well as at the collision centre-of-mass energy. In addition, the method used to determine the QCD contribution has been revised in the Displaced $e\mu$ search at 13 TeV and is the same than one used in this chapter. Figure 7.18 compares the limits obtained of the Displaced $e\mu$ search at 8 TeV with the one of the Displaced $e\mu$ search at 13 TeV. For $\langle c\tau_{\tilde{t}} \rangle = 2 \text{ cm/c}$, top squark with mass of 790 GeV (870 GeV) by the Displaced $e\mu$ search at 8 TeV (13 TeV). This improvement is mostly explained by the higher centre of mass energy which implies larger top squark cross-section production.

Dependence of the limits on the method used to set the limits

For this study, a fair comparison can be made only if the two limits to be compared were produced using similar scenarios. For that matter, comparing the Displaced $e\mu$ search at 13 TeV and the Displaced same-flavour leptons search at 13 TeV seems reasonable. Indeed these two searches were performed using the same dataset⁴ and use the same method to estimate the background contribution. Furthermore, the combination of the ee and the $\mu\mu$ final states should yield the same amount of signal events than the $e\mu$ final state alone. Figure 7.19 compares the limits extracted from the Displaced $e\mu$ search at 13 TeV computed with the Markov chain with the limits extracted from the Displaced same-flavour leptons search at 13 TeV computed with asymptotic Cls. In this figure, one can observe that the expected limits are very close to each other for moderate $\langle c\tau_{\tilde{t}} \rangle$ (1 cm and 10 cm) but that they differ significantly for low $\langle c\tau_{\tilde{t}} \rangle$ (0.1 cm) and high $\langle c\tau_{\tilde{t}} \rangle$ (100 cm). This is explained by the fact that the approximation is accurate when the background and the signal yield is not simultaneously close to 0. Because the Displaced same-flavour leptons search at 13 TeV has a low background prediction in all the signal regions, it follows that the signal yield should be substantially higher than zero for that approximation to be accurate. As it can be seen in Tables 7.20 and 7.21, the signal yield is higher for intermediate $\langle c\tau_{\tilde{t}} \rangle$ as compared to low $\langle c\tau_{\tilde{t}} \rangle$ and high $\langle c\tau_{\tilde{t}} \rangle$. This means that the asymptotic Cls method yields trustworthy limits for $\langle c\tau_{\tilde{t}} \rangle$ values where the limits are the most stringent and works as predicted.

⁴It implies that the integrated luminosity, the centre of mass energy, the alignment scenario, the systematic uncertainties, the lepton selection are equal in both searches.

Improvement of the limits from the combination

As already mentioned in the introduction of this chapter, the Displaced same-flavour leptons search at 13 TeV does not only extend the Displaced $e\mu$ search at 13 TeV to new final states, but it can also improve the limits on the Displaced Supersymmetry model. For that matter, the three final states can be combined, and new limits are calculated using the asymptotic CLs method. Figure 7.20 shows the limits obtained from the combination of the $e\mu$, ee , and $\mu\mu$ final states. Comparing these limits with the ones obtained from the Displaced $e\mu$ search at 13 TeV, the improvement is obvious. For example, the expected limit for a top squark with $\langle c\tau_{\tilde{t}} \rangle = 1$ cm has increased from roughly 860 GeV to 980 GeV.

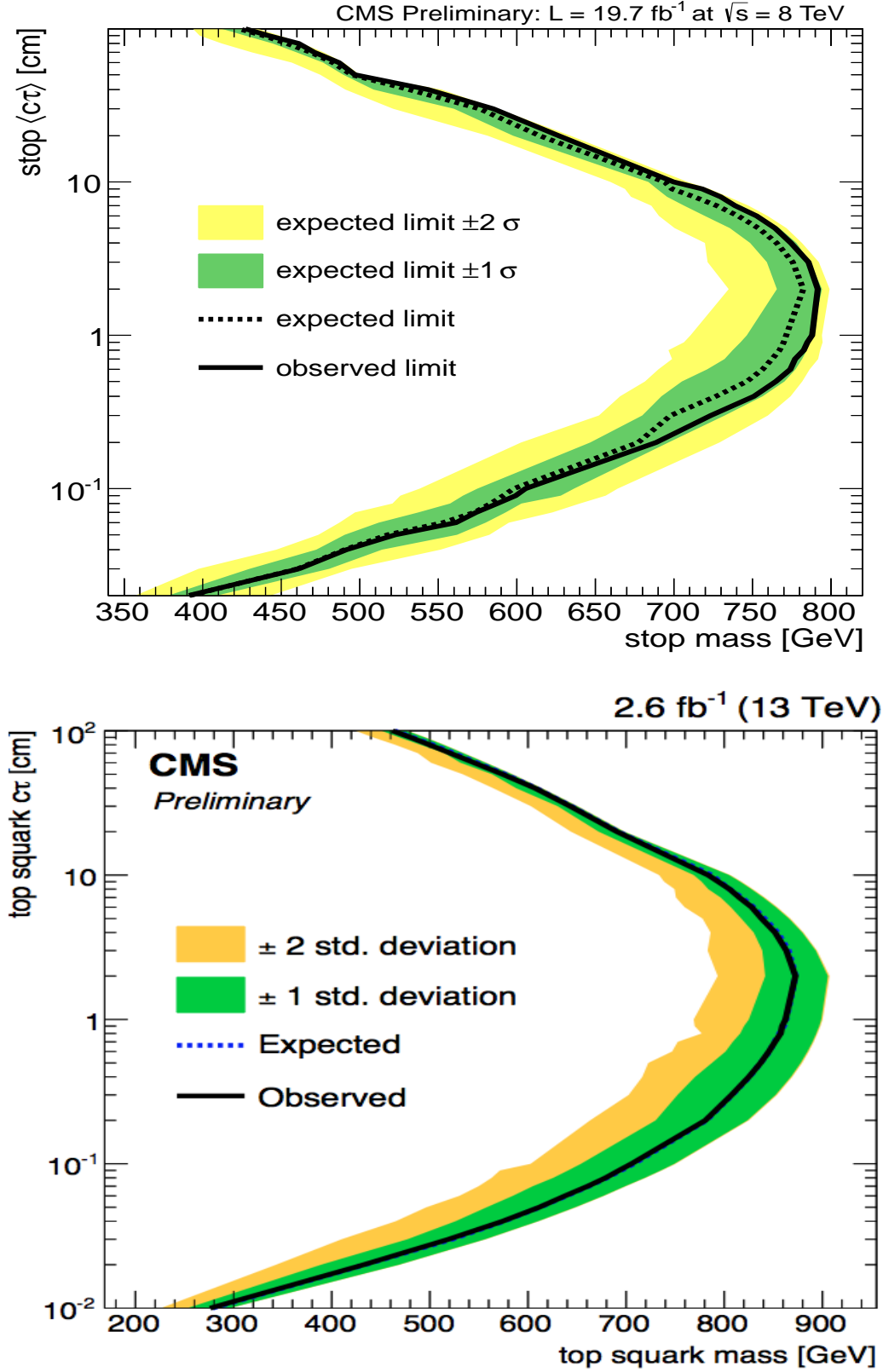


Figure 7.18: Expected and observed 95% CLs production cross-section exclusion contours for top squark pair in the $\langle c\tau_{\tilde{t}} \rangle$ versus $m_{\tilde{t}}$ plane. Using events in the $e\mu$ final state, the region on the left of the contours is excluded by Displaced $e\mu$ search at 8 TeV (top) and by the Displaced $e\mu$ search at 13 TeV (bottom).

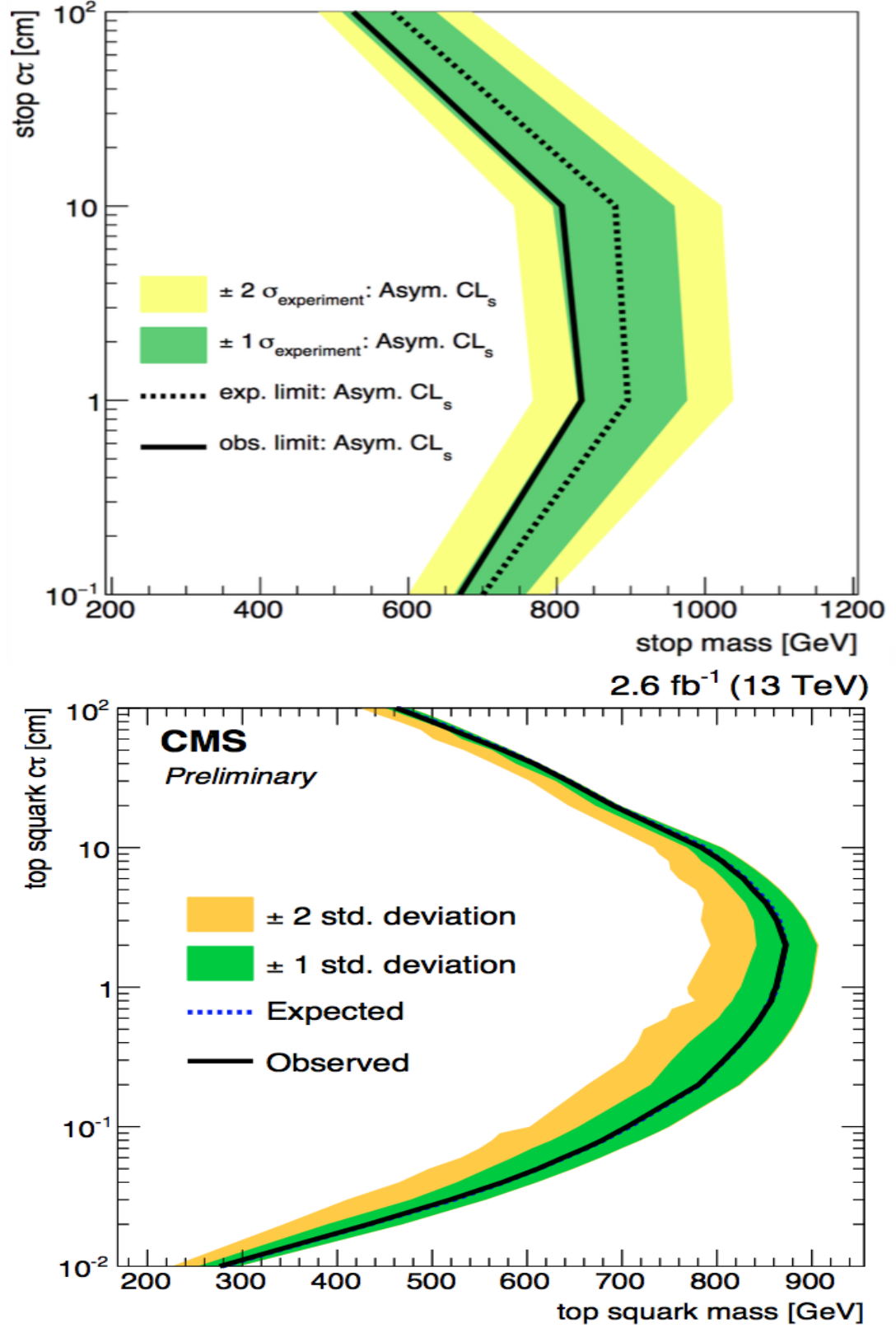


Figure 7.19: Expected and observed 95% CLs production cross-section exclusion contours for top squark pair in the $\langle c\tau_{\tilde{t}} \rangle$ versus $m_{\tilde{t}}$ plane. Using events in the $e\mu$ (ee and $\mu\mu$) final state(s), the region on the left of the contours is excluded by Displaced $e\mu$ search at 13 TeV (top) and by the Displaced same-flavour leptons search at 13 TeV (bottom).

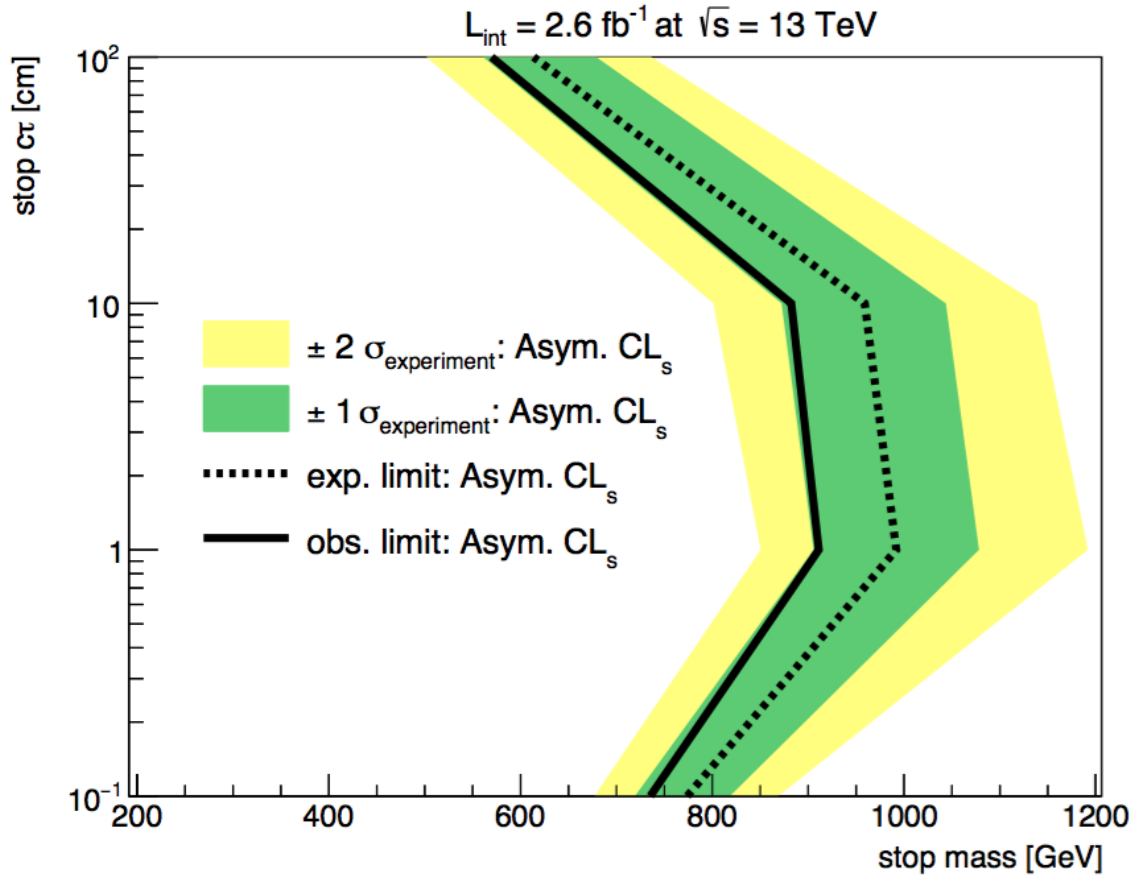


Figure 7.20: Expected and observed 95% CLs production cross-section exclusion contours for top squark pair in the $\langle c\tau_{\tilde{t}} \rangle$ versus $m_{\tilde{t}}$ plane. Using events in the $e\mu$, ee and $\mu\mu$ final states, the region on the left of the contours is excluded by the combination of the Displaced $e\mu$ search at 13 TeV and the Displaced same-flavour leptons search at 13 TeV.

Conclusion and prospects

For ages, human beings have expanded the boundary of their knowledge about the world surrounding them. However, it is only over the past two centuries that significant discoveries about the structure of matter have been made. The current knowledge of particle physics is embedded within a coherent theory, called the Standard Model. It has been formulated over decades and has proven to be an extremely accurate description of nature in numerous experiments. However, as some observational facts cannot be explained by the Standard Model, it is not believed to be the ultimate theory of everything, and extension of the Standard Model are being investigated. Among these theories, Supersymmetry is probably one of the most notorious one as it can solve some of the shortcomings of the Standard Model.

To test the validity of candidate theories, particle accelerators have been built in order to create highly energetic collisions in a controlled environment. The Large Hadron Collider at CERN is the most powerful particle accelerator ever built by humankind, and allows physicists to study matter at unprecedented energies. The debris of proton-proton collisions is studied by gigantic detectors, such as the Compact Muon Solenoid. The information collected by all the sub-detectors is combined using powerful algorithms in order to produce more comprehensible information. Finally, data and simulations are compared with each other and statistical tools are used in order to test the compatibility of new theories.

Extensive searches for any evidence of the minimal supersymmetric Standard Model have been conducted, and the constraints are becoming more and more stringent. However, alternative models in which the lightest supersymmetric particle has a lifetime of the order of few centimetres were essentially unconstrained in 2012. These scenarios can occur in various models, amongst which the Displaced Supersymmetry model. The most striking feature of Displaced Supersymmetry is that it predicts the existence of the lightest supersymmetric particle with significant lifetime so that its decay location will be measurably distant from its production location. For example, a proton-proton collision can produce a pair of top squarks, each of them can decay through R-parity violating interaction to a bottom quark and a lepton. In this case, two leptons and two b-jets are produced, and the impact parameter of the leptons can be used as a powerful variable to discriminate between signal and Standard Model background events. In this

thesis, two searches for Displaced Supersymmetry are presented as well as a recasting tool to reinterpret our results, as will be summarised in the next two sections.

8.1 Search for Displaced Supersymmetry in events with an electron and a muon with large impact parameters at 8 TeV

This search [1] uses proton-proton collision data collected in 2012 at $\sqrt{s} = 8$ TeV, corresponding to an integrated luminosity of 19.7 fb^{-1} . It is the first LHC search to target a specific set of models in which two leptons are displaced, have opposite sign and come from a different vertex. To reduce potential backgrounds from Drell-Yan processes, only different-flavour leptons are considered in the final state. No requirements on the b-jets are applied so that the analysis remains sensitive to a broad range of models which produced displaced leptons.

To end up in one of the signal regions, an event should contain exactly one well identified and isolated electron as well as exactly one well identified and isolated muon. The electron and the muon are required to have opposite charge. Three signal regions are defined according to the d_0 of the leptons in the events, each of those being the most sensitive for a different top squark lifetime assumption. The dominant background contribution comes from QCD processes, which is estimated with a data-driven method. This method assumes that the QCD contribution in the signal regions can be estimated from control regions with oppositely charged and/or anti-isolated leptons.

Limits are set on the top squarks pair production cross-section at 8 TeV using the Higgs combined tool. This search excludes top squark masses up to 790 GeV for a lifetime hypothesis of $2 \text{ cm}/c$ at 95% confidence level. When this search was published, these limits were the most stringent ones on Displaced Supersymmetry.

The search is sensitive to a broad range of models because it was intentionally designed not to apply cuts highly customised for Displaced Supersymmetry. To allow model builders to recast our results, the efficiencies to pass selection criteria which involve detector-specific variables are provided. The electron and muon reconstruction efficiencies are provided as a function d_0 , and their selection efficiencies are calculated as a function of p_T . These efficiencies are available to the wider scientific community [90, 91] and have been already used by theorists to set limits on long-lived staus [92].

8.2 Search for Displaced Supersymmetry in events with same-flavour leptons with large impact parameters at 13 TeV

In this section, the same-flavour version of the search presented in the previous section is discussed. It uses 2.6 fb^{-1} of proton-proton collision data collected by the CMS detector in 2015 at $\sqrt{s} = 13 \text{ TeV}$.

Leptons are required to be well identified and well isolated as in the previous search. However, an event can populate one of the signal regions if it contains exactly two muons or exactly two electrons. The signal regions are identical to the previous ones with the exception that the d_0 range of the most displaced signal region is extended from 2 cm to 10 cm. In this search, the background contribution in the signal regions from QCD processes is estimated by multiplying the number of QCD events in the displaced control region with some transfer factors. These transfer factors are a function of d_0 solely, which distributions are gotten from data in QCD-enriched control regions.

Since no significant excess is observed, 95% confidence limits are set on the top squarks pair production cross-section at 8 TeV using Higgs combined tool. This time, the asymptotic approximation is used to determine the likelihood ratio. Assuming $m_{\tilde{t}} = 1 \text{ cm}/c$, top squark masses below 760 GeV (780 GeV) are excluded using the ee ($\mu\mu$) final state. These limits are very close to the ones found in the $e\mu$ search at 8 TeV and slightly less stringent than the ones found in the $e\mu$ search at 13 TeV. Since there is no overlap between the events in the ee final state and in the $\mu\mu$ final state, limits are combined to achieve stronger limits.

8.3 Prospects

An easy extension of the search can be done by adding new final states in which leptons have the same charge. While this would not impact the limits on displaced supersymmetry it would render the analysis more generic and hence sensitive to a broader range of models.

The data-driven technique used to estimate the background contribution from QCD events might be slightly overestimating the QCD contribution and should probably be revised. It is not easy to redesign entirely a data-driven method and the method used in this thesis yields plausible results. In any case, even if the QCD estimate is slightly overestimated, the impact on the final limits will be very small because the background estimate is very close to zero, even in the loosest signal region. However, the same analysis is currently being done with much bigger integrated luminosity, and the potential overestimation of the background contribution from QCD events might

be more impactful.

Chapter 9

Acknowledgements

After spending almost a fifth of my life working on my PhD, it is an indescribable feeling to be writing this section just a few days before this journey ends. By no means, I will be able to express my gratitude to all the ones who have supported me during this extraordinary adventure, but I will still attempt to convey it.

I shall start by thanking my promotor, Freya Blekman, who initiates this once in a lifetime experience when she hired me. Throughout my PhD, I knew I could always count on her. She has been there to help to solve issues of any kind, explain to me many aspects of the CMS detector and collaboration, discuss physics, give me some coding advice, congratulate me when I was doing a good job and motivate me when I felt lost. She was also very understanding when I was going through hard times. She managed to find the very fine-tuned amount of pushing I needed to keep working without feeling overwhelmed. I am aware that I have required more attention than the average PhD student, and I am very grateful that she has always managed to find some time to support me.

I also wish to thank all the members of the jury: Jorgen D'Hondt, Stijn Buitink, Alberto Mariotti, Theo D'Hondt, Giacomo Bruno, and Philippe Mermod. They have scrutinised my work carefully, and their suggestions allowed me to improve the quality of my manuscript.

During my thesis, I had the great opportunity to collaborate with very kind people who were always keen to spend some time answering my never-ending questions: Jamie Antonelli introduced me to the wonders of coding from day one, James Keaveney taught me everything he knew about b-tagging, Nathalie Heracleous helped me building my own analysis framework, and Denys Lontkovski spent a lot of time discussing statistics with me. I have also benefited from the expertise of the following people on various occasions: Petra, Nadir, Caroline, Sezen, Lukas and Gregory.

I was also lucky to share a large office with a lot of people from different horizons and cultural backgrounds, and I found it to be a very enriching experience. We had most of our exciting exchanges at lunchtime (or Schmake Schmake time as I liked to call it) during which we conceptualised the BRAINZ project, among other things. I was also a member of the now very famous APNELEM United football team, and I can not describe how excited I was to play with my fellow teammates even though we were honestly pretty bad. For all these specials moments, I would like to thank An-nick, Isabelle, Isis, Liselotte, Kevin, Jarne, Simon, Kirill, Leonidas, Douglas, Dominic, Shimaa, Michael, Stijn, Seth, Gerrit, Giannis and Tomislav. I would also like to thank

the three secretaries, Audrey, Marleen and Merel, and the famously entertaining IT team: Abdel, Olivier, Romain Samir and Shkelzen. I also owe a big thank you to my psychologist, Maarten, for the very valuable help he has provided.

Thanks to my first flatmate and friend, Benedikt, I have also met very colourful people outside work. With no doubt, my PhD experience would have been completely different without you. Thank you Akis, Efi, Isabella, Iris, Hana, Kristel, Marion, Nicklas, Raphael, Rolf and Sylvain. Even if we are not living in the same country anymore, I know that we are still going to share very exciting adventures together! Among these people, Efaki mou deserves a special mention as I shared everything with her for many years. Efcharisto poli agaboobimene mou!

I also got support from my high school and university friends. I have shared with them a few memorable trips, futnet tournaments, festivals, PhD defences, and Risk games. It was always a big pleasure to spend some time with you whenever I was back in Switzerland for a few days. Thank you Belette, Bouatte, Crousti, Dixon, Desponzo, Gigi, Tamoufflette, Ting Tong and VKB.

I have also had the craziest moments of my life with my oldest friends from secondary school, aka the Kernel. I have met you more than twenty years ago, and for some unknown reasons, we are still friends! We have shared so many things together, mainly creepy jokes and beers. This group of friends has expanded over the years, and I would like to thank Andoo, Bangi, Constantin, Corpi, “l’enfant de la lune”, Joel, Julien, Neven, Piquette, Sebastien and Yann. Among these extraordinary chaps, a few of them have been especially supportive during the last year of my PhD. A big shout out to “le grand qui a la classe”, Kue, Nens and Pioupiou for hosting me, inviting me on holidays, the daily coaching, the amazing “Ping-Pong zinzin” sessions and cheering me up.

Je voudrais aussi remercier tous les membres de ma famille. Durant de nombreuses années, ils n’ont jamais cessé de m’encourager, chacun a leur manière. Mon père et sa compagne m’ont chaleureusement accueilli dans la maison où j’ai passé la majeure partie de mon enfance. Leur accueil m’a vraiment réchauffé le cœur. Un énorme merci à Arthur, Emilie, Louis, Françoise, Maria-Lena, Raymond, Stéphane, et Victor pour les parties d’échecs, les repas, les discussions, les nombreux jeux de mots, les cours d’introduction à l’agriculture, le support logistique ET TOUT! Je partage avec le petit Houfo une connexion particulière, et comme il le dit lui même à ses amis en parlant de moi “Il est comme moi, en plus con.” Fair enough, brother!

Besides all the things I have learnt related to my work, I have also learnt that I might have the most supportive friends ever. I was so moved when I noticed that so many people of my network spontaneously offered to help me when I was feeling the worst. I can not express how grateful I am to all these people! I can just let you know, that I will not forget what you have done for me and that I will be there for you if you need me!

Chapter 10

Summary

The Standard Model of particles physics describes the smallest known building blocks of matter and their interactions amongst each other. The predictive power of this theory has been astoundingly accurate, and the recent discovery of the long-sought Higgs boson is probably one of its most notorious predictions. However, despite its success, it is known that the Standard Model cannot be the ultimate theory of nature. Indeed, some experimental facts remain unexplained within the Standard Model. For example, it does not include the gravitational force and does not provide any description of dark matter. To expand the boundary of our knowledge, physicists have proposed new candidate theories describing the physics beyond the Standard Model. The predictions of some of these theories can be tested with the data collected by the detectors surrounding the Large Hadron Collider, the most powerful accelerator ever built by humankind, at CERN.

Supersymmetry is a very elegant theory that can solve many unanswered questions and in which all known particles are given a partner, called superpartner, or superparticle. Because there is still no evidence for the most simplistic assumption of Supersymmetry, the focus is placed on a specific model, called Displaced Supersymmetry, which predicts that the superpartners will acquire a longer lifetime. This will result in very striking signatures where the location of the superpartner's decay will be measurably distant from its production's location.

In this thesis, the data collected by the Compact Muon Solenoid detector is used, to test the validity of Displaced Supersymmetry. A first search is presented in Chapter 5 using data collected with a centre of mass energy of 8 TeV using one electron and one muon in the final state. A second search presented in Chapter 7 extends the first search by using same-flavour leptons final states. The combination of the two searches improves the constraints on the Displaced Supersymmetry model, on which tight constraints are placed. The searches are designed to be optimised for a lifetime of the order of few centimetres where the constraints were almost non-existent. However, a selection that is loose enough is applied so that the signatures predicted by other models with similar properties can be observed with a good probability. For that matter, efficiency curves that allow the results to be reused to put constraints on other models are provided.

Chapter 11

Samenvatting

Het Standaard Model van de deeltjesfysica beschrijft de kleinste bouwstenen van de materie en hun interacties. De voorspellende kracht van deze theorie is uitermate precies en de ontdekking van het lang gezochte Higgs boson in 2012 is waarschijnlijk één van de meest gekende successen van het Standaard Model. Ondanks deze ontdekking is het echter duidelijk dat het Standaard Model niet de ultieme theorie kan zijn. Het ontbreken van de zwaartekracht en de beschrijving van donkere materie zijn enkele van de niet verklaarde fenomenen in het Standaard Model. Fysici hebben nieuwe kandidaat theorieën voorgesteld om fysica buiten het Standaard Model te beschrijven en zo de grenzen van de kennis te verleggen. De voorspelling komende uit deze nieuwe theorieën kunnen worden getest met data verzameld door de experimenten by de Large Hadron Collider te CERN, de grootste deeltjesversneller ooit gebouwd door de mensheid.

Supersymmetrie is een theorie die kan worden gebruikt om veel onbeantwoorde vragen op te lossen, en waarbij alle gekende deeltjes een partner krijgen genaamd superpartner of superdeeltje. Doordat er nog steeds geen bewijs is voor de basisveronderstelling van Supersymmetrie, wordt de aandacht gelegd op een specifiek model, genaamd Verplaatste Supersymmetrie, dat super partners voorspelt met een langere levensduur. Deze eigenschap resulteert in een opvallend signaal waarbij de oorsprong van het verval van de super partner meetbaar verplaatst is ten opzichte van zijn plaats van ontstaan.

In deze thesis wordt data verzameld door het Compact Muon Solenoid experiment gebruikt om de validiteit van Verplaatste Supersymmetrie na te gaan en te beperken. Het onderzoek is gebaseerd op signaturen met een verplaatsing van een paar centimeter waar er nu zo goed als geen beperkingen op het model bestaan. We maken echter wel een selectie die los genoeg is zodat er ook een kans is om een signaal te zien met dezelfde eigenschappen, voorspeld door andere theorieën. Hierdoor hebben we een resultaat gecreëerd dat ook bruikbaar is om beperkingen op vele andere modellen op te leggen.

Bibliography

- [1] CMS Collaboration, “Search for Displaced Supersymmetry in events with an electron and a muon with large impact parameters”, *Phys. Rev. Lett.* **114** (2015), no. 6, 061801, [doi:10.1103/PhysRevLett.114.061801](#), [arXiv:1409.4789](#).
- [2] Muon g-2 Collaboration, “Measurement of the negative muon anomalous magnetic moment to 0.7 ppm”, *Phys. Rev. Lett.* **92** (2004) 161802, [doi:10.1103/PhysRevLett.92.161802](#), [arXiv:hep-ex/0401008](#).
- [3] C. Campagnari and M. Franklin, “The Discovery of the top quark”, *Rev. Mod. Phys.* **69** (1997) 137–212, [doi:10.1103/RevModPhys.69.137](#), [arXiv:hep-ex/9608003](#).
- [4] DONUT Collaboration, “Observation of tau neutrino interactions”, *Phys. Lett. B* **504** (2001) 218–224, [doi:10.1016/S0370-2693\(01\)00307-0](#), [arXiv:hep-ex/0012035](#).
- [5] ATLAS Collaboration, “Observation of a new particle in the search for the Standard Model Higgs boson with the ATLAS detector at the LHC”, *Phys. Lett. B* **716** (2012) 1–29, [doi:10.1016/j.physletb.2012.08.020](#), [arXiv:1207.7214](#).
- [6] CMS Collaboration, “Observation of a new boson at a mass of 125 GeV with the CMS experiment at the LHC”, *Phys.Lett.B* (2012) [arXiv:1207.7235](#).
- [7] ATLAS Collaboration, “Observation of a new particle in the search for the Standard Model Higgs boson with the ATLAS detector at the LHC”, *Phys.Lett.B* (2012) [arXiv:1207.7214](#).
- [8] Particle Data Group Collaboration, “Review of Particle Physics”, *Chin. Phys. C* **38** (2014) 090001, [doi:10.1088/1674-1137/38/9/090001](#).
- [9] LHCb Collaboration, “Observation of $J/\psi p$ Resonances Consistent with Pentaquark States in $\Lambda_b^0 \rightarrow J/\psi K^- p$ Decays”, *Phys. Rev. Lett.* **115** (2015) 072001, [doi:10.1103/PhysRevLett.115.072001](#), [arXiv:1507.03414](#).
- [10] S. L. Glashow, “Partial Symmetries of Weak Interactions”, *Nucl. Phys.* **22** (1961) 579–588, [doi:10.1016/0029-5582\(61\)90469-2](#).

- [11] S. Weinberg, “A Model of Leptons”, *Phys. Rev. Lett.* **19** (1967) 1264–1266, [doi:10.1103/PhysRevLett.19.1264](#).
- [12] A. Salam, “Gauge Unification of Fundamental Forces”, *Rev. Mod. Phys.* **52** (1980) 525–538, [doi:10.1103/RevModPhys.52.525](#). [Science210,723(1980)].
- [13] F. Englert and R. Brout, “Broken Symmetry and the Mass of Gauge Vector Mesons”, *Phys. Rev. Lett.* **13** (Aug, 1964) 321–323, [doi:10.1103/PhysRevLett.13.321](#).
- [14] P. W. Higgs, “Broken Symmetries and the Masses of Gauge Bosons”, *Phys. Rev. Lett.* **13** (Oct, 1964) 508–509, [doi:10.1103/PhysRevLett.13.508](#).
- [15] ATLAS, CMS Collaboration, “Combined Measurement of the Higgs Boson Mass in pp Collisions at $\sqrt{s} = 7$ and 8 TeV with the ATLAS and CMS Experiments”, *Phys. Rev. Lett.* **114** (2015) 191803, [doi:10.1103/PhysRevLett.114.191803](#), [arXiv:1503.07589](#).
- [16] H. Yukawa, “On the Interaction of Elementary Particles I”, *Proc. Phys. Math. Soc. Jap.* **17** (1935) 48–57, [doi:10.1143/PTPS.1.1](#). [Prog. Theor. Phys. Suppl.1,1(1935)].
- [17] Virgo, LIGO Scientific Collaboration, “GW151226: Observation of Gravitational Waves from a 22-Solar-Mass Binary Black Hole Coalescence”, *Phys. Rev. Lett.* **116** (2016), no. 24, 241103, [doi:10.1103/PhysRevLett.116.241103](#), [arXiv:1606.04855](#).
- [18] RENO Collaboration, “Observation of Reactor Electron Antineutrino Disappearance in the RENO Experiment”, *Phys. Rev. Lett.* **108** (2012) 191802, [doi:10.1103/PhysRevLett.108.191802](#), [arXiv:1204.0626](#).
- [19] Daya Bay Collaboration, “A side-by-side comparison of Daya Bay antineutrino detectors”, *Nucl. Instrum. Meth. A* **685** (2012) 78–97, [doi:10.1016/j.nima.2012.05.030](#), [arXiv:1202.6181](#).
- [20] Y. Oyama, “Results from K2K and status of T2K”, in *Proceedings, NATO Advanced Research Workshop on Nuclear Science and Safety in Europe: Yalta, Crimea, Ukraine, September 10-16, 2005*, pp. 113–124. 2006. [arXiv:hep-ex/0512041](#). [doi:10.1007/978-1-4020-4965-1_9](#).
- [21] K. G. Begeman, A. H. Broeils, and R. H. Sanders, “Extended rotation curves of spiral galaxies - Dark haloes and modified dynamics”, **249** (apr, 1991) 523–537, [doi:10.1093/mnras/249.3.523](#).
- [22] V. Trimble, “DARK MATTER IN THE UNIVERSE: WHERE, WHAT, AND WHY?”, *Contemp. Phys.* **29** (1988) 373–392, [doi:10.1080/00107518808213765](#).

- [23] Planck Collaboration, “Planck 2013 results. XVI. Cosmological parameters”, *Astron. Astrophys.* **571** (2014) A16, [doi:10.1051/0004-6361/201321591](#), [arXiv:1303.5076](#).
- [24] S. Martin, “A Supersymmetry Primer”, [arXiv:hep-ph/9709356](#).
- [25] CMS Collaboration, “Search for GMSB supersymmetry in events with at least one photon and missing transverse momentum in pp collisions at $\sqrt{s} = 13$ TeV”, CMS Physics Analysis Summary CMS-PAS-MET-16-046, 2017.
- [26] CMS Collaboration, “Search for new physics in final states with two opposite-sign, same-flavor leptons, jets, and missing transverse momentum in pp collisions at $\sqrt{s} = 13$ TeV”, *JHEP* **12** (2016) 013, [doi:10.1007/JHEP12\(2016\)013](#), [arXiv:1607.00915](#).
- [27] P. Graham, D. Kaplan, S. Rajendran, and P. Sarawat, “Displaced Supersymmetry”, *Journal of High Energy Physics* **149** (2012) [doi:10.1007/JHEP07\(2012\)149](#), [arXiv:1204.6038](#).
- [28] The Super-Kamiokande Collaboration, “Search for Proton Decay through $p \rightarrow \bar{\nu} K^+$ in a Large Water Cherenkov Detector”, *Phys. Rev. Lett.* **83** (Aug, 1999) 1529–1533, [doi:10.1103/PhysRevLett.83.1529](#).
- [29] L. Evans and P. Bryant, “LHC Machine”, *JINST* **3** (2008) S08001, [doi:10.1088/1748-0221/3/08/S08001](#).
- [30] CMS Collaboration, “CMS physics: Technical design report”,.
- [31] “Design Report Tevatron 1 project”, Technical Report FERMILAB-DESIGN-1984-01, 1984.
- [32] ATLAS Collaboration, “The ATLAS Experiment at the CERN Large Hadron Collider”, *JINST* **3** (2008) S08003, [doi:10.1088/1748-0221/3/08/S08003](#).
- [33] LHCb Collaboration, “The LHCb Detector at the LHC”, *JINST* **3** (2008) S08005, [doi:10.1088/1748-0221/3/08/S08005](#).
- [34] ALICE Collaboration, “The ALICE experiment at the CERN LHC”, *JINST* **3** (2008) S08002, [doi:10.1088/1748-0221/3/08/S08002](#).
- [35] “Large Hadron Collider”,. https://en.wikipedia.org/wiki/Large_Hadron_Collider.
- [36] “CERN Accelerator complex”,. <http://www.stfc.ac.uk/research/particle-physics-and-particle-astrophysics/large-hadron-collider/cern-accelerator-complex/>.
- [37] L. Taylor, “The CMS detector design”,. <http://cms.web.cern.ch/news/cms-detector-design>.

- [38] CMS Collaboration, “Description and performance of track and primary-vertex reconstruction with the CMS tracker”, *JINST* **9** (2014), no. 10, P10009, [doi:10.1088/1748-0221/9/10/P10009](#), [arXiv:1405.6569](#).
- [39] L. Viliani, “CMS tracker performance and readiness for LHC Run II”, *Nuclear Instruments and Methods in Physics Research Section A: Accelerators, Spectrometers, Detectors and Associated Equipment* **824** (2016).
- [40] CMS Collaboration, “The CMS ECAL performance with examples”, *JINST* **9** (2014) C02008, [doi:10.1088/1748-0221/9/02/C02008](#).
- [41] V. D. Elvira, “Measurement of the Pion Energy Response and Resolution in the CMS HCAL Test Beam 2002 Experiment”, Technical Report CMS-NOTE-2004-020, CERN, Geneva, Sep, 2004.
- [42] CMS Collaboration, “Performance of the CMS Hadron Calorimeter with Cosmic Ray Muons and LHC Beam Data”, *JINST* **5** (2010) T03012, [doi:10.1088/1748-0221/5/03/T03012](#), [arXiv:0911.4991](#).
- [43] CMS Collaboration, “CMS reconstruction improvement for the muon tracking by the RPC chambers”, *PoS RPC2012* (2012) 045, [doi:10.1088/1748-0221/8/03/T03001](#), [arXiv:1209.2646](#). [JINST8,T03001(2013)].
- [44] CMS Collaboration, “The CMS trigger system”, *JINST* **12** (2017), no. 01, P01020, [doi:10.1088/1748-0221/12/01/P01020](#), [arXiv:1609.02366](#).
- [45] R. Fruhwirth, “Application of Kalman filtering to track and vertex fitting”, *Nucl. Instrum. Meth. A* **262** (1987) 444–450, [doi:10.1016/0168-9002\(87\)90887-4](#).
- [46] P. Billoir, “Progressive track recognition with a Kalman like fitting procedure”, *Comput. Phys. Commun.* **57** (1989) 390–394, [doi:10.1016/0010-4655\(89\)90249-X](#).
- [47] R. Mankel, “A Concurrent track evolution algorithm for pattern recognition in the HERA-B main tracking system”, *Nucl. Instrum. Meth. A* **395** (1997) 169–184, [doi:10.1016/S0168-9002\(97\)00705-5](#).
- [48] A. Strandlie and W. Wittek, “Propagation of covariance matrices of track parameters in homogeneous magnetic fields in CMS”,.
- [49] J. R. Cash and A. H. Karp, “A Variable Order Runge-Kutta Method for Initial Value Problems with Rapidly Varying Right-hand Sides”, *ACM Trans. Math. Softw.* **16** (September, 1990) 201–222, [doi:10.1145/79505.79507](#).
- [50] CMS Collaboration, “Particle-flow reconstruction and global event description with the CMS detector”, *JINST* **12** (2017), no. 10, P10003, [doi:10.1088/1748-0221/12/10/P10003](#), [arXiv:1706.04965](#).

- [51] W. Adam, R. Frühwirth, A. Strandlie, and T. Todor, “Reconstruction of Electrons with the Gaussian-Sum Filter in the CMS Tracker at the LHC”, Technical Report CMS-NOTE-2005-001, CERN, Geneva, Jan, 2005.
- [52] M. Cacciari, G. P. Salam, and G. Soyez, “The Anti-k(t) jet clustering algorithm”, *JHEP* **04** (2008) 063, doi:10.1088/1126-6708/2008/04/063, arXiv:0802.1189.
- [53] CMS Collaboration, “Identification of b-quark jets with the CMS experiment”, *JINST* **8** (2013) P04013, doi:10.1088/1748-0221/8/04/P04013, arXiv:1211.4462.
- [54] M. A. Dobbs et al., “Les Houches guidebook to Monte Carlo generators for hadron collider physics”, in *Physics at TeV colliders. Proceedings, Workshop, Les Houches, France, May 26-June 3, 2003*, pp. 411–459. 2004. arXiv:hep-ph/0403045.
- [55] A. Buckley et al., “General-purpose event generators for LHC physics”, *Phys. Rept.* **504** (2011) 145–233, doi:10.1016/j.physrep.2011.03.005, arXiv:1101.2599.
- [56] A. I. A. L. e. a. Abramowicz, H., “Combination of measurements of inclusive deep inelastic ep scattering cross sections and QCD analysis of HERA data”, *Eur. Phys. J. C* **75** (2015) doi:10.1140/epjc/s10052-015-3710-4.
- [57] V. N. Gribov and L. N. Lipatov, “Deep inelastic e p scattering in perturbation theory”, *Sov. J. Nucl. Phys.* **15** (1972) 438–450. [*Yad. Fiz.*15,781(1972)].
- [58] Y. L. Dokshitzer, “Calculation of the Structure Functions for Deep Inelastic Scattering and e+ e- Annihilation by Perturbation Theory in Quantum Chromodynamics.”, *Sov. Phys. JETP* **46** (1977) 641–653. [*Zh. Eksp. Teor. Fiz.*73,1216(1977)].
- [59] G. Altarelli and G. Parisi, “Asymptotic Freedom in Parton Language”, *Nucl. Phys. B* **126** (1977) 298–318, doi:10.1016/0550-3213(77)90384-4.
- [60] B. Andersson, G. Gustafson, G. Ingelman, and T. Sjostrand, “Parton Fragmentation and String Dynamics”, *Phys. Rept.* **97** (1983) 31–145, doi:10.1016/0370-1573(83)90080-7.
- [61] CMS Collaboration, “Event generator tunes obtained from underlying event and multiparton scattering measurements”, *Eur. Phys. J. C* **76** (2016), no. 3, 155, doi:10.1140/epjc/s10052-016-3988-x, arXiv:1512.00815.
- [62] R. Field, “Min-Bias and the Underlying Event at the LHC”, *Acta Phys. Polon. B* **42** (2011) 2631–2656, doi:10.5506/APhysPolB.42.2631, arXiv:1110.5530.
- [63] CDF Collaboration, “The CDF-II detector: Technical design report”, technical report, 1996.

- [64] CMS Collaboration, “Measurement of the Underlying Event Activity at the LHC with $\sqrt{s} = 7$ TeV and Comparison with $\sqrt{s} = 0.9$ TeV”, *JHEP* **09** (2011) 109, [doi:10.1007/JHEP09\(2011\)109](https://doi.org/10.1007/JHEP09(2011)109), [arXiv:1107.0330](https://arxiv.org/abs/1107.0330).
- [65] J. Allison et al., “Geant4 developments and applications”, *IEEE Transactions on Nuclear Science* **53** (Feb, 2006) 270–278, [doi:10.1109/TNS.2006.869826](https://doi.org/10.1109/TNS.2006.869826).
- [66] T. Sjostrand, S. Mrenna, and P. Z. Skands, “PYTHIA 6.4 Physics and Manual”, *JHEP* **05** (2006) 026, [doi:10.1088/1126-6708/2006/05/026](https://doi.org/10.1088/1126-6708/2006/05/026), [arXiv:hep-ph/0603175](https://arxiv.org/abs/hep-ph/0603175).
- [67] J. Alwall et al., “MadGraph 5 : Going Beyond”, *JHEP* **06** (2011) 128, [doi:10.1007/JHEP06\(2011\)128](https://doi.org/10.1007/JHEP06(2011)128), [arXiv:1106.0522](https://arxiv.org/abs/1106.0522).
- [68] S. Alioli, P. Nason, C. Oleari, and E. Re, “A general framework for implementing NLO calculations in shower Monte Carlo programs: the POWHEG BOX”, *JHEP* **06** (2010) 043, [doi:10.1007/JHEP06\(2010\)043](https://doi.org/10.1007/JHEP06(2010)043), [arXiv:1002.2581](https://arxiv.org/abs/1002.2581).
- [69] S. Frixione and B. R. Webber, “Matching NLO QCD computations and parton shower simulations”, *JHEP* **06** (2002) 029, [doi:10.1088/1126-6708/2002/06/029](https://doi.org/10.1088/1126-6708/2002/06/029), [arXiv:hep-ph/0204244](https://arxiv.org/abs/hep-ph/0204244).
- [70] S. Jadach, J. H. Kuhn, and Z. Was, “TAUOLA: A Library of Monte Carlo programs to simulate decays of polarized tau leptons”, *Comput. Phys. Commun.* **64** (1990) 275–299, [doi:10.1016/0010-4655\(91\)90038-M](https://doi.org/10.1016/0010-4655(91)90038-M).
- [71] C. E. POG, “Electron Tag And Probe”,
<https://twiki.cern.ch/twiki/bin/view/CMSPublic/ElectronTagAndProbe>.
- [72] C. M. POG, “Muon Tag And Probe”,
<https://twiki.cern.ch/twiki/bin/view/CMS/MuonTagAndProbe>.
- [73] G. Cowan, K. Cranmer, E. Gross, and O. Vitells, “Asymptotic formulae for likelihood-based tests of new physics”, *Eur. Phys. J. C* **71** (2011) 1554, [doi:10.1140/epjc/s10052-011-1554-0](https://doi.org/10.1140/epjc/s10052-011-1554-0), [10.1140/epjc/s10052-013-2501-z](https://doi.org/10.1140/epjc/s10052-013-2501-z), [arXiv:1007.1727](https://arxiv.org/abs/1007.1727). [Erratum: *Eur. Phys. J. C* 73,2501(2013)].
- [74] L. J. Gleser, “[Setting Confidence Intervals for Bounded Parameters]: Comment”, *Statistical Science* **17** (2002), no. 2, 161–163.
- [75] P. Lenzi, S. Padhi, G. Retuerto, and F. Wuerthwein, “Standard model cross sections for CMS at 8 TeV”,
<https://twiki.cern.ch/twiki/bin/viewauth/CMS/StandardModelCrossSectionsat8TeV>.
- [76] N. Kidonakis, “Differential and total cross sections for top pair and single top production”, [arXiv:1205.3453](https://arxiv.org/abs/1205.3453).
- [77] M. Czakon, P. Fiedler, and A. Mitov, “The total top quark pair production cross-section at hadron colliders through $O(\alpha_S^4)$.”, *Phys. Rev. Lett.* **110** (2013) 252004, [doi:10.1103/PhysRevLett.110.252004](https://doi.org/10.1103/PhysRevLett.110.252004), [arXiv:1303.6254](https://arxiv.org/abs/1303.6254).

- [78] J. Beringer et al., “Review of Particle Physics”, *Phys. Rev. D* **86** (2012) 010001, [doi:10.1088/0954-3899/37/7A/075021](https://doi.org/10.1088/0954-3899/37/7A/075021).
- [79] T. Sjostrand, S. Mrenna, and P. Z. Skands, “A brief introduction to PYTHIA 8.1”, *Comput. Phys. Commun.* **178** (2008) 852–867, [doi:10.1016/j.cpc.2008.01.036](https://doi.org/10.1016/j.cpc.2008.01.036), [arXiv:0710.3820](https://arxiv.org/abs/0710.3820).
- [80] S. cross sections group, “SUSY cross sections for CMS at 8 TeV”, <https://twiki.cern.ch/twiki/bin/view/LHCPhysics/SUSYCrossSections8TeVstopsbottom>.
- [81] CMS Collaboration, “Muon ID and Iso efficiencies”, https://indico.cern.ch/event/257630/contributions/577156/attachments/452667/627631/Final_MuonID_and_Iso_eff_ReReco-22Jan2013.pdf.
- [82] CMS Collaboration, “Search for long-lived particles that decay into final states containing two electrons or two muons in proton-proton collisions at $\sqrt{s} = 8$ TeV”, *Phys. Rev. D* **91** (2015), no. 5, 052012, [doi:10.1103/PhysRevD.91.052012](https://doi.org/10.1103/PhysRevD.91.052012), [arXiv:1411.6977](https://arxiv.org/abs/1411.6977).
- [83] B. P. Roe et al., “Boosted decision trees, an alternative to artificial neural networks”, *Nucl. Instrum. Meth. A* **543** (2005), no. 2-3, 577–584, [doi:10.1016/j.nima.2004.12.018](https://doi.org/10.1016/j.nima.2004.12.018), [arXiv:physics/0408124](https://arxiv.org/abs/hep-ph/0408124).
- [84] CMS Collaboration, “Search for disappearing tracks in proton-proton collisions at $\sqrt{s} = 8$ TeV”, *JHEP* **01** (2015) 096, [doi:10.1007/JHEP01\(2015\)096](https://doi.org/10.1007/JHEP01(2015)096), [arXiv:1411.6006](https://arxiv.org/abs/1411.6006).
- [85] ATLAS Collaboration, “Search for charginos nearly mass degenerate with the lightest neutralino based on a disappearing-track signature in pp collisions at $\sqrt{s}=8$ TeV with the ATLAS detector”, *Phys. Rev. D* **88** (2013), no. 11, 112006, [doi:10.1103/PhysRevD.88.112006](https://doi.org/10.1103/PhysRevD.88.112006), [arXiv:1310.3675](https://arxiv.org/abs/1310.3675).
- [86] CMS Collaboration, “Searches for long-lived charged particles in pp collisions at $\sqrt{s}=7$ and 8 TeV”, *JHEP* **07** (2013) 122, [doi:10.1007/JHEP07\(2013\)122](https://doi.org/10.1007/JHEP07(2013)122), [arXiv:1305.0491](https://arxiv.org/abs/1305.0491).
- [87] CMS Collaboration, “Estimating Systematic Errors Due to Pileup Modeling 2012”, <https://twiki.cern.ch/twiki/bin/view/CMS/PileupSystematicErrors>.
- [88] S. Alekhin et al., “The PDF4LHC Working Group Interim Report”, [arXiv:1101.0536](https://arxiv.org/abs/1101.0536).
- [89] Higgs PAG, “Documentation of the RooStats-based statistics tools for Higgs PAG”, <https://twiki.cern.ch/twiki/bin/view/CMS/SWGuideHiggsAnalysisCombinedLimit>.

- [90] CMS Collaboration, “Displaced Susy parametrisation study for user”,
<https://twiki.cern.ch/twiki/bin/view/CMSPublic/DisplacedSusyParametrisationStudyForUser>.
- [91] CMS Collaboration, “Search for Displaced Supersymmetry in events with an electron and a muon with large impact parameters”,
<https://hepdata.net/record/ins1317640>.
- [92] J. A. Evans and J. Shelton, “Long-Lived Staus and Displaced Leptons at the LHC”, *JHEP* **04** (2016) 056, [doi:10.1007/JHEP04\(2016\)056](https://doi.org/10.1007/JHEP04(2016)056),
[arXiv:1601.01326](https://arxiv.org/abs/1601.01326).
- [93] G. F. Giudice and R. Rattazzi, “Theories with gauge mediated supersymmetry breaking”, *Phys. Rept.* **322** (1999) 419–499,
[doi:10.1016/S0370-1573\(99\)00042-3](https://doi.org/10.1016/S0370-1573(99)00042-3), [arXiv:hep-ph/9801271](https://arxiv.org/abs/hep-ph/9801271).
- [94] A. Arvanitaki, N. Craig, S. Dimopoulos, and G. Villadoro, “Mini-Split”, *JHEP* **02** (2013) 126, [doi:10.1007/JHEP02\(2013\)126](https://doi.org/10.1007/JHEP02(2013)126), [arXiv:1210.0555](https://arxiv.org/abs/1210.0555).
- [95] CMS Collaboration, “Search for displaced leptons in the e-mu channel”, CMS Physics Analysis Summary CMS-PAS-EXO-16-022, 2016.
- [96] SUSY cross sections group Collaboration, “SUSY cross sections for CMS at 13 TeV”,
<https://twiki.cern.ch/twiki/bin/view/LHCPhysics/SUSYCrossSections13TeVstopsbottom>.
- [97] CMS Collaboration, “ElectronScaleFactorsRun2”,
<https://twiki.cern.ch/twiki/bin/view/CMS/ElectronScaleFactorsRun2>.
- [98] CMS Collaboration, “MuonReferenceEffsRun2”,
<https://twiki.cern.ch/twiki/bin/viewauth/CMS/MuonReferenceEffsRun2>.
- [99] CMS Collaboration, “Muon Reconstruction and Identification Improvements for Run-2 and First Results with 2015 Run Data”,.
- [100] CMS Collaboration, “Cut-based electron identification for Run2”,
<https://twiki.cern.ch/twiki/bin/view/CMS/CutBasedElectronIdentificationRun2?rev=38>.
- [101] M. Cacciari and G. P. Salam, “Pileup subtraction using jet areas”, *Phys.Lett. B* **659** (2008) 119–126, [doi:10.1016/j.physletb.2007.09.077](https://doi.org/10.1016/j.physletb.2007.09.077),
[arXiv:0707.1378](https://arxiv.org/abs/0707.1378).
- [102] CMS Collaboration, “Soft ware guide for muon identification in Run2”,
<https://twiki.cern.ch/twiki/bin/view/CMS/SWGuideMuonIdRun2>.
- [103] CMS Collaboration, “Commissioning of the Particle-Flow reconstruction in Minimum-Bias and Jet Events from pp Collisions at 7 TeV”, Technical Report CMS-PAS-PFT-10-002, CERN, Geneva, 2010.